UNIVERSITY OF OKLAHOMA

GRADUATE COLLEGE

THEORETICAL AND EXPERIMENTAL STUDIES OF POWER-LAW FLUID

FLOW IN COILED TUBING

A DISSERTATION

SUBMITTED TO THE GRADUATE FACULTY

in partial fulfillment of the requirements for the

degree of

Doctor of Philosophy

By

YUNXU ZHOU
Norman, Oklahoma
2006

UMI Number: 3243499

UMI®

THEORETICAL AND EXPERIMENTAL STUDIES OF POWER-LAW FLUID
FLOW IN COILED TUBING

A DISSERTATION APPROVED FOR THE
MEWBOURNE SCHOOL OF PETROLEUM AND GEOLOGICAL
ENGINEERING

BY

—————————————————————
Dr. Subhash N. Shah, Chair

—————————————————————
Dr. Samuel Osisanya

—————————————————————
Dr. Ramkumar N. Parthasarathy

—————————————————————
Dr. Chandra S. Rai

—————————————————————
Dr. Djebbar Tiab

To the memory of my Father

To my Mother

ACKNOWLEGDEMENTS

TABLE OF CONTENTS

LIST OF TABLES

LIST OF FIGURES

ABSTRACT

Coiled tubing (CT) services is one of the fastest growing oilfield technologies. Yet, due to the small tubing diameter, there is excessive friction in coiled tubing. The excessive friction pressure is also due to the effect of secondary flow which is caused by centrifugal forces in coiled tubing. Predicting friction pressure in coiled tubing has been an engineering challenge. Literature survey indicated that there are no correlations that can be used to properly predict friction pressure of non-Newtonian fluids in coiled tubing. The current study is an effort to bridge this gap.

Following the approach of boundary layer approximation analysis taken by Ito, and Mashelkar and Devarajan, solutions of laminar flow of a power law fluid in coiled tubing were obtained for flow behavior index, n = 0.25, 0.30, …, 1.0. A new friction factor correlation of laminar flow in coiled tubing was developed and verified by comparing with Ito correlation (for n = 1) and experimental data. There was excellent agreement between the new correlation and experimental data. Similar approach was applied to turbulent flow of power law fluid in coiled tubing. Numerical solutions of turbulent coiled tubing flow for n = 0.25, 0.30, 0.40, …, 1.0 were obtained. A friction factor correlation for turbulent non-Newtonian fluid flow in coiled tubing was also developed and verified with Ito correlation for Newtonian turbulent flow and also with limited experimental data. For both laminar and turbulent flow of non-Newtonian fluid in coiled tubing, this study not only corrected the errors in Mashelkar and Devarajan's solutions for both laminar and turbulent flow

of non-Newtonian fluid in coiled tubing, but also extended Mashelkar and Devarajan's method to wider range of flow behavior indices.

An extensive experimental study was performed with polymer-based fluids using the field-scale and lab-scale flow loops which consist of an array of coiled tubing of ½, 1, 1-1/2, 1-3/4, and 2-3/8-in. diameter and of various tubing lengths and curvature ratios. Polymer fluids tested in this study included: xanthan, PHPA (partially hydrolyzed polyacrylamide), guar, HPG (hydroxypropyl guar), and HEC (hydroxyethyl cellulose) fluids at various polymer concentrations. It was found that coiled tubing curvature increased the friction pressure significantly. The maximum difference in friction factor between coiled tubing and straight tubing can be as high as 185%, depending on the tubing size, polymer concentration, and generalized Reynolds number. For Newtonian fluid (water), the difference in friction factor between coiled tubing and straight tubing is not as significant as for polymeric fluids. But, the friction factor difference still can be as high as 30%. Based on friction pressure data of field-scale flow tests, empirical correlations of Fanning friction factor as functions of generalized Dean number have been developed for turbulent flow of polymer fluids in coiled tubing. These correlations can be used for coiled tubing hydraulics design.

Data analysis of friction pressure showed that drag reduction in coiled tubing is lower than in straight tubing. As curvature ratio increases, the drag reduction of polymer fluids in coiled tubing decreases. It was also found that the onset of drag reduction in coiled tubing is delayed due to curvature. A new correlation for

maximum drag reduction (MDR) asymptote was developed based on the drag reduction data from the ½-in. flow loop which has curvature ratios of 0.01, 0.019, 0.031, and 0.076. This correlation reduces to the well-known Virk's asymptote for dilute polymer solutions in straight pipes. Therefore, Virk's asymptote can be considered as a special case (zero curvature ratio) of the new correlation for coiled tubing. A new drag reduction envelope is also proposed. Examples have demonstrated that the new drag reduction envelope is a useful tool to analyze the drag reduction behavior of polymer solutions in coiled tubing.

The CFD software FLUENT was used to simulate the Newtonian laminar and turbulent flow, and non-Newtonian laminar flow in a 2-3/8-in. coiled tubing. The simulation results revealed essential features of fluid flow in coiled pipes, such as secondary flow effect and shifting of high velocity region toward the outer tubing wall.

CHAPTER 1

INTRODUCTION

The coiled tubing (CT) industry is one of the fastest growing segments of the oilfield services sector. CT growth has been driven by attractive economics, continual advances in technology, and utilization of CT to perform an ever-growing list of oilfield operations. Coiled tubing toady is a global, multi-billion dollar industry in the mainstream of energy extraction technology.[1] The total number of working units reported in February 2001 is roughly 850 units. In January 2004, slightly more than 1050 CT units were estimated to be available worldwide. According to the rig count of the ICoTA (the International Coiled Tubing Association), the total CT units were 1182 in January 2005, with the biggest increase of CT units in Canada – from 239 units in 2004 to 311 units in January 2005. The global fleet of CT units has more than doubled over the past decade. In Canada, the CT market has boasted at annual growth rate of 25% since 1997.[2]

Coiled tubing has been gaining popularity because it has a number of advantages. Since coiled tubing is a continuous string of tubing, it can be run into or out of a well at much faster speeds than jointed tubing. This fast trip speed results in tremendous cost saving. In addition, fluid can be circulated through the tubing while it is being inserted into or drawn from the well. This capability allows for work on a pressurized well without the need to kill the well and risk damage to the reservoir. This feature becomes attractive for underbalanced drilling. Since it was first developed, coiled

tubing has been used for well cleaning, acid stimulation, and other conventional applications. Conventional CT applications such as well cleanouts are generally referred to as the "bread & butter" of the industry, since these applications still account for more than three quarters of coiled tubing revenues. More recently, CT drilling (CTD) and CT fracturing have emerged as two of the fastest growth areas. Revenues from these two CT applications have grown from almost zero a decade ago, to approximately 15% in recent times. The benefits of CT fracturing are significant – more than 20 intervals can be fractured in a single day. In general, the capabilities of the tubing, the CT units, and CT tools have improved tremendously over the past decade.

In view of the various CT applications, it is seen that CT operations almost exclusively involve pumping fluids through coiled tubing – whether in CT well cleanouts or CT drilling or CT fracturing. In many cases, the excessive frictional pressure in coiled tubing string is often a limitation of CT applications. The excessive friction pressure is due to the small tubing diameter and the curvature effect. The coiled tubing diameter has to be small enough for the whole length of tubing string to be spooled on the reel. Mechanically, to avoid excessive stress, the tubing diameter can not be large. The most commonly used CT sizes are 1-1/2 in. and 2-3/8 in. These are much smaller than conventional tubing and pipes. When a fluid flows through coiled tubing, secondary flow occurs due to the effect of centrifugal forces. Secondary flow causes extra flow resistance. The effect of coiled tubing curvature is more pronounced with flow of polymer fluids such as many drilling and completion

fluids. The difference in friction factor of these fluids in coiled tubing and in straight tubing (ST) can be as high as 185%. Accurately predicting frictional pressure in coiled tubing has been a challenge for engineers in CT operations design. The available commercial CT softwares are not able to predict CT friction pressure satisfactorily. CT engineers have to rely on experience or add some correction factors to the softwares' predictions.[*]

The objective of this study is to theoretically and experimentally investigate the frictional pressure behavior of polymer fluids commonly used in CT applications to meet the industry's need for improved hydraulics design of CT operations.

In Chapter 2, we reviewed the coiled tubing applications in the oil and gas industry so that we could properly define our research content (especially experimental work) and experimental conditions would be representative of field conditions. In the second part of Chapter 2, we reviewed the previous studies on fluid flow in coiled pipes. This has proved very beneficial for this research.

In Chapter 3, we took the approach of boundary layer approximation analysis of Barua,[3] Ito,[4] and Mashelkar and Devarajan,[5] and extended the work of Mashelkar and Devarajan to wider range of flow behavior index (n). Mashelkar and Devarajan only obtained solutions of boundary layer analysis for n = 0.5, 0.75, 0.9, and 1.0. We extended the solutions to n = 0.25, 0.30, …, 1.0. A new friction factor correlation for non-Newtonian laminar flow in coiled tubing was developed and verified by comparing with Ito correlation and with experimental data. Our new correlation not

---

[*] Personal communications with Mr. Bernt Olson of Cudd Pressure Control and Mr. Michael Bailey of Halliburton.

only matched the Ito correlation well, but was also in excellent agreement with experimental data.

In Chapter 4, we followed the similar approach as in Chapter 3 to consider the turbulent flow of non-Newtonian fluid in coiled tubing. A friction factor correlation for turbulent flow of power law fluid was developed based on the numerical solutions of non-Newtonian fluid flow in coiled tubing. Comparison with Ito correlation and Mashelkar and Devarajan correlation as well as experimental data was also provided.

Experimental investigation is an important part of this study. Starting from Chapter 5 through Chapter 7, we present results of extensive flow experiments in both coiled tubing and straight tubing, and rheological studies of various test fluids. More specifically, Chapter 5 describes the experimental setup in detail. It first describes the field-scale and lab-scale flow loops which include an array of coiled tubing reels, straight tubing sections, fluid mixing and pumping equipment as well as data acquisition system. Besides the equipment for flow tests, Chapter 5 also presents apparatuses for rheological characterization of the test fluids.

Chapter 6 presents experimental results of systematic and extensive flow tests of polymer fluids in coiled tubing. Throughout the chapter, wherever possible, we tried to compare the flow behavior in coiled tubing and straight tubing and their fundamental differences. Based on the data analysis, several important observations have been made concerning the flow behavior of water and non-Newtonian polymeric fluids. Empirical friction factor correlations have been developed based on the flow test data from the field-scale flow loop.

In Chapter 7, we explored the characteristics of drag reduction phenomena in coiled tubing. Observations of this chapter are expected to provide some insights into the unique friction behavior in coiled tubing. One of the major efforts of Chapter 7 is the development of the maximum drag reduction (MDR) asymptote in coiled tubing and the proposal of the drag reduction envelope for coiled tubing. The new MDR asymptote can be reduced to the well-known Virk's asymptote for straight pipes. It is found that drag reduction in coiled tubing is lower than in straight tubing. The larger the curvature ratio, the lower the drag reduction in coiled tubing. The coiled tubing curvature also delays the onset of drag reduction.

In Chapter 8, we initiated the effort of simulating fluid flow in coiled tubing using CFD software – FLUENT. A CT model of 2-3/8-in. coiled tubing on 111-in. diameter reel was constructed and grid mesh was created. Solutions of Newtonian laminar and turbulent flow, and non-Newtonian laminar flow were obtained. Essential flow features in coiled tubing were observed, such as shifted velocity profiles and secondary flows.

Study of complex non-Newtonian fluids such as drilling, completion, and stimulation fluids flowing in coiled tubing still faces many challenges and unanswered questions. These potential research issues will be addressed in the final chapter where we summarized our conclusions of the present study and recommendations for future research.

CHAPTER 2
LITERATURE REVIEW

This chapter presents literature reviews in two parts. Part 1 reviews the development of coiled tubing technology, CT advantages, and CT applications in the oil and gas industry. This will help us to identify the technical challenges and industry needs and make sure our research effort is of interest to the industry. Part 2 reviews the previous studies on fluid flow through curved or coiled pipes, both theoretical and experimental. This is essential for understanding the complex flow phenomenon of fluid flow in coiled tubing and taking the right approaches for the present study.

2.1   CT Applications in the Oil and Gas Industry

2.1.1   Coiled Tubing

Coiled tubing (CT) is a continuously-milled tubular product manufactured in lengths that require spooling onto a take-up reel during the manufacturing process. During CT application, the coiled tubing is straightened prior to being inserted into the wellbore and is recoiled for spooling back onto the service reel. Compared with conventional jointed tubing, the most important feature of CT is that the whole CT string is continuous and has no connections.

To run the CT into wellbore or pull it out of hole, a CT unit is required. As illustrated in Fig. 2.1, a typical CT unit consists of the following elements:

Fig. 2.1—Trailer mounted CT unit and crane.[1]

- Coiled tubing reel;

- Injector head;

- Power pack;

- Wellhead blowout preventer (BOP);

- Control cabin.

Coiled tubing reel is for storage and transport of CT string. The spooling capacity of CT reels depends on the CT diameter and core diameter. Single CT lengths can be in excess of 30,000 ft. The injector head is used to provide the surface drive force to run and retrieve the CT, to control the running rate, and to support the suspended tubing weight. The injector head is equipped with an arc roller system called tubing guide or gooseneck. The BOP stack consists of several hydraulically-operated rams and provides well pressure control. The stuffing box connected to the BOP stack

provides the dynamic high pressure sealing around the CT. The power pack is used to generate hydraulic and pneumatic power required to operate the CT unit. The control cabin, also called control console, includes all the controls and gauges for CT operators to monitor and operate the CT unit components.

2.1.2 Brief History of CT Technology

The modern coiled tubing technology can be traced back to the project PLUTO (Pipe Line Under The Ocean) by the Allied engineering teams during World War II.[6] Prior to the Allied invasion of Normandy, British engineers developed and laid very long continuous pipelines across the English Channel to fuel the Allied armies. Seventeen pipelines of total length of 30 miles were deployed. These pipelines were spooled onto 40-ft diameter reels and deployed by towing the reel behind a ship. In the early stages of CT technology, coiled tubing units were built to perform primarily sand cleanouts and nitrogen jet services. Unfortunately, the success rate of coiled tubing was poor and a reputation for limited reliability followed the coiled tubing development for some years in the early 1960s. Through the late 1970s and early 1980s, numerous revisions on equipment design and maintenance schedules were made for coiled tubing units built by Bowen Tools, Hydra Rig Inc., and Otis Engineering. These modifications were successful in improving the performance and reliability of surface equipment and significantly reducing equipment failure rates. Although surface equipment modifications increased coiled tubing reliability, the most dramatic improvements came as a result of new continuous tubing manufacturing methods and introduction of quality control.

Currently, there are two coiled tubing manufacturers providing all of the coiled tubing used by the CT service contractors worldwide.[1] These companies are Quality Tubing, Inc. (QTI) and Precision Tube Technology (PTT), each having manufacturing facilities in Houston, TX. New advancements in CT technology are being explored by each of these pipe manufacturers. Greater strength is achieved through changes in steel chemistry or treatment such as quenching and tempering. CT material advancements will play a significant role in continued progress in many of the leading edge CT applications. The CT industry has continued to make technical advancements in every aspects – tubing design and manufacturing, CT units, and various reliable CT tools. The technical progress has served to make CT an even more appealing solution for many applications.

2.1.3   Advantages of CT

Compared to conventional jointed tubing and pipes, coiled tubing has many advantages.[6] First, CT can be run in hole or pulled out of hole (RIH/POOH) easily and quickly. This can save a lot of workover time and therefore result in great cost savings. Second, when compared with conventional rig, the coiled tubing unit is relatively light and easy to move. Therefore, CT units are applicable to remote or environment sensitive situations. Third, the ability of CT to circulate fluids allows its use in many well workover operations such as well unloading or sand washout. In addition, CT has much higher tensile strength than wireline and can replace wireline operations in certain applications. The following is a brief list of CT advantages.

- Faster trip time;

- Faster rig (CT unit) mobilization and demobilization;

- Smaller environmental footprint;

- Safer and more effective operations in underbalanced conditions;

- More effective in positioning tools in horizontal wells;

- Ability to circulate fluid while RIH/POOH;

- Reduced crew/personnel requirement;

- Cost may be significantly reduced;

- Minimal well shut-in time.

Figs. 2.2 and 2.3 show that the CT mast units can be easily rigged up and rigged down for mobilization.

2.1.4 CT Applications in the Oil and Gas Industry

Traditionally, CT has been used in wellbore sand or fill cleanout, well unloading,[7] stimulation (matrix acidizing), cement squeeze, CT assisted well logging and perforating, [8] fishing, spoolable gas lift system, and others. [9] While well service/workover applications still account for more than 75% of CT use, technical advancements have increased the utilization of CT drilling and completion applications. CT drilling (CTD) and CT fracturing, practically unknown a decade ago, now make up nearly 15% of CT revenue.[2]

Fig. 2.2—A coiled tubing mast unit is rigged up.†

Fig. 2.3—A coiled tubing mast unit is rigged down.‡

2.1.4.1 Sand and Solids Washing

One of the main applications of coiled tubing is the removal of sand or similar fill from a wellbore.[10-14] Fig. 2.4 illustrates a typical process of coiled tubing sand

---

† Thanks to Mr. Michael Bailey of Halliburton for sharing this photo.
‡ Thanks to Dr. Steven Hill of Schlumberger for sharing this photo.

washing operation. Here, a sand bridge at 10,000 ft is being cleaned out. The operation involves circulation of a fluid through the CT to the sand face where the sand is picked up by the jetting action of the nozzles. The sand is then transported to the surface through the annulus between the CT and production tubing or casing.
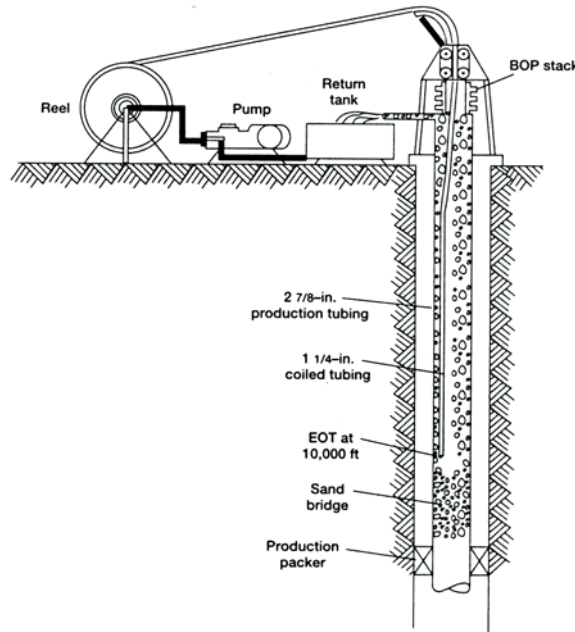
Fig. 2.4—Schematic of sand cleanout process using CT.[6]

An important consideration in designing sand cleanout operations is the proper selection of the fluid and pump rate.[15-17] They should be chosen so that sand can be effectively carried out to the surface while maintaining proper bottomhole pressure. Both Newtonian fluids, such as water and brines, and non-Newtonian fluids have been used in CT sand cleanouts. When washing sand inside casing, viscous non-Newtonian fluids such as biopolymer or gelled oil systems may have to be used. This is because the velocity between CT and casing is reduced and more viscosity is required to suspend the sand particles in the annular flow. Since the fluid pressure

should not exceed the allowable working pressure of the CT, wash fluids with friction-reducing properties are desired.

2.1.4.2 Well Unloading

Using CT to unload a well with nitrogen is a quick and cost-effective method to regain sustained production of wells with liquid load problems. Some wells stop production because of the hydrostatic pressure overbalance which prevents the reservoir fluids from flowing into the wellbore. The liquid load can be due to workover fluids from workover operations or liquid produced from reservoir, such as water accumulation in wellbore in low pressure gas wells. In these cases, lighter fluids such as nitrogen (N_2) can be used to unload (or kick off) these "load-up" wells.[6] The working principle of well unloading is the same as gas lift. The coiled tubing can be run into or out of a well at a speed of 100 to 200 ft/min. Nitrogen can be circulated at different depths to achieve a smooth and efficient unloading.[18] For hydraulically fractured wells, CT conveyed nitrogen can be used to lift the fracturing fluid and clean out frac sand left in the wellbore. Recently, coiled tubing in conjunction with downhole jet pump was used to dewater gas wells.[19] CT gas lift may be more cost-effective than conventional gas lift system.[20] Analysis and design of well unloading operations requires computer simulators to simulate the transient process. [15,21]

2.1.4.3 Coiled Tubing Drilling (CTD)

CT drilling can be divided into two main categories: directional and non-directional drilling. Non-directional drilling uses a fairly conventional drilling assembly in

conjunction with a downhole motor. Directional drilling requires the use of an orienting device to steer the well trajectory. Application of CTD is especially attractive for drilling shallow gas wells in Canada.[22] Drilling shallow gas wells with CT can be more efficient and economical than conventional rigs. Canada accounts for over 90% of worldwide CT drilling.[23] Fig. 2.5 shows the annual growth of coiled tubing drilled wells in Canada. The most active CTD contractor is Precision Drilling in Canada. Comparing the minimum location size (footprint) of CT units with small conventional drilling rigs, CT clearly has the size advantage: well sites are only one-quarter to one third the size of a conventionally drilled pad. Fig. 2.6 shows an example of CT drilling site. Along with smaller footprints, fewer loads are required to deliver equipment.
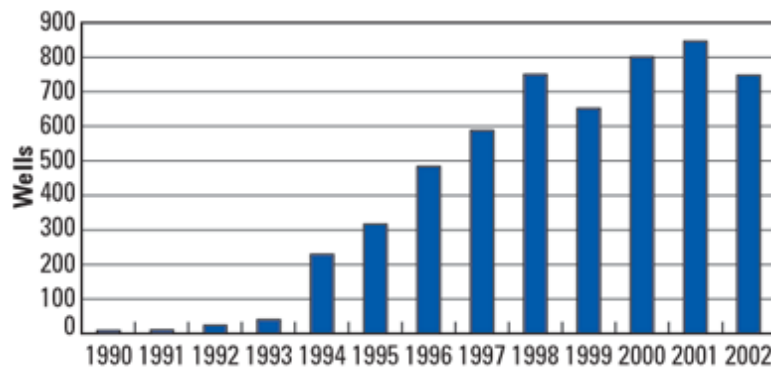
Fig. 2.5—Annual coiled tubing drilled wells.[23]

Fig. 2.6—Coiled tubing drilling wellsite.[§]

In Alaska, especially Prudhoe Bay, drilling sidetracks using coiled tubing has been successful drilling practice.[6] Drilling sidetracks through tubing involves milling windows through tubing and casings. In the UK North Sea, CTD proved a viable sidetracking technique on platforms in mature field to recover bypassed reserves. [6] Common tubing sizes for CTD are 2 in. and 2-3/8 in. To reduce frictional pressure in coiled tubing and annulus, a low-solids polymer drilling fluid is normally used. Coiled tubing is also useful for drilling multilaterals or re-entry drilling from existing wells.[24] Coiled tubing is especially useful for underbalanced drilling in low pressure reservoirs.[25] Slim-hole[26] or re-entry drilling,[27] microhole drilling, [22] and horizontal drilling[24,25,28] with coiled tubing are gaining increased interest in the new technology development.

15

2.1.4.4 CT Fracturing

Hydraulic fracturing through CT has become an effective stimulation technique for multizone oil and gas wells.[29-31] Hydraulic fracturing via CT is also an attractive production enhancement technique for mutliseam coalbed methane wells.[32] Fig. 2.7 shows a CT unit is being used for hydraulic fracturing.

Fig. 2.7—CT unit is used in hydraulic fracturing.[**]

In CT hydraulic fracturing, proppant such as sand is conveyed through the continuous string of coiled tubing as transport conduit to fractured formation. Compared with conventional tubing conveyed hydraulic fracturing, CT hydraulic fracturing has a number of advantages. In particular, CT provides the ability to quickly move in the hole (or be quickly repositioned) when fracturing multiple zones in a single well. CT also provides the ability to fracture or accurately spot the treatment fluid to ensure complete coverage of the zones of interest when used in

---

[**] Source: www.technicoilcorp.com.

conjunction with appropriate bottomhole assembly tools such as straddle packers. This is particularly important for stimulation of multiple zones or bypassed zones or horizontal wellbores. At the end of the formation treating operation, CT can be used to remove any sand plugs used in the treating process, and to lift the well to be placed on production.

2.1.4.5 CT Used in Acidizing

Coiled tubing has been used as an effective acid injection tool for acidizing horizontal or highly deviated carbonate wells.[33−38] In horizontal wells or long interval carbonate wells, conventional bullheading of acid could result in very uneven acid coverage and low stimulation efficiency, since acid would follow paths of the least resistance and flow into areas of highest permeability. CT conveyed acidizing can provide necessary mechanical isolation and diversion for uniform acid coverage along wellbore. The process involves pumping acid through CT and pumping an inert fluid through the annulus between the CT and the well. While acid is being injected through the CT, the CT is withdrawn gradually at a withdrawal rate contingent on the stimulation fluid injection rate and the desired volumetric coverage. Due to the unique capability of "pumping while-in-motion" of CT, acid can be spotted at any specific point along the treatment interval. At the end of acid stimulation, the well can be unloaded with CT to minimize the time that spent acid remains in the well.

2.1.4.6 Cement Squeeze

Coiled tubing has been successfully used to perform non-rig cement squeeze workovers.[39-45] The motivation of using CT to squeeze cement is economics: the reduction in workover costs in an environment where rig mobilization and operating costs are becoming prohibitive. In Prudhoe Bay, CT cement squeeze can be performed for about 25% of the cost for an equivalent rig squeeze, and CT cement squeezes have been performed: (1) to shut-off unwanted gas or water production, (2) to repair faulty primary cement jobs, and (3) to modify injection or production profiles. CT cementing was also used in a platform abandonment program in North Sea to plug wells. [46]

2.1.4.7 Other Applications

Logging with CT. CT is useful in conveying logging tools in highly-deviated, extended reach, and horizontal wells where gravity conveyed wireline logging is not suitable. The electric wireline can be installed during CT manufacturing or can be inserted into coiled tubing prior to logging. [47] One advantage of CT assisted logging is that it would minimize the "slip-stick" motion common to wireline-conveyed tools. Another advantage is that fluid such as N_2 can be pumped through CT to initiate or promote flow for production logging.

Fishing with CT. Compared with wireline fishing, CT fishing has advantages of high tensile strength and the unique capability to circulate wash fluids such as N_2 and acid at the fish to remove sand, mud, scale or other debris off the top of the fish. [48-51] Therefore, CT fishing is specially useful for fishing in highly-deviated and horizontal

wells, or fishing debris covered fish, or jarring and/or pulling a fish that is too heavy for wireline.

In most of the CT applications briefly reviewed above, fluids are pumped through the coiled tubing string either in drilling, fracturing, or wellbore cleanouts. Due to the limitation of CT tubing size, fluids with less friction pressure are desired. These fluids such as biopolymer solutions are non-Newtonian and drag reducing. Therefore, investigating friction pressure of polymer fluids in coiled tubing has become one of the objectives of this study.

2.2 Studies of Fluid Flow in Coiled Pipes

2.2.1 Introduction

Accurate prediction of frictional pressure losses when pumping fluids through coiled tubing has remained a challenge in hydraulics design, mainly due to the lack of adequate friction loss correlations and proper understanding of the complex flow phenomena of fluids (especially non-Newtonian fluids) in coiled tubing. Since the classic work of Dean,[52,53] the flow of Newtonian fluids in coiled pipes has been extensively studied; in contrast, the flow of non-Newtonian fluid in coiled pipes has remained relatively unstudied.

The objective of this part of the chapter is to review both theoretical and experimental studies on the flow of Newtonian and non-Newtonian fluids in coiled pipes. The mathematical formulation and the general characteristics of the secondary flow are first introduced in order to prepare for discussion of various theoretical

studies. The available friction factor correlations will be compared and evaluated for their accuracy and applicability.

2.2.2 Flow of Newtonian Fluid in Coiled Pipe

2.2.2.1 *Governing Equations*

Fig. 2.8 shows the toroidal coordinate system that has been often used in studying fluid flow in coiled pipes. We denote the radius of the pipe by *a* and the radius of the coil as *R*. C is the center of the pipe cross section, ϕ is the angle that the cross-section makes with a fixed axial plane. OZ is the axis of the coil. The flow is assumed in the direction of increasing ϕ under a driving pressure gradient. The velocity components u, v, and w are in the directions of r, α, and ϕ respectively.
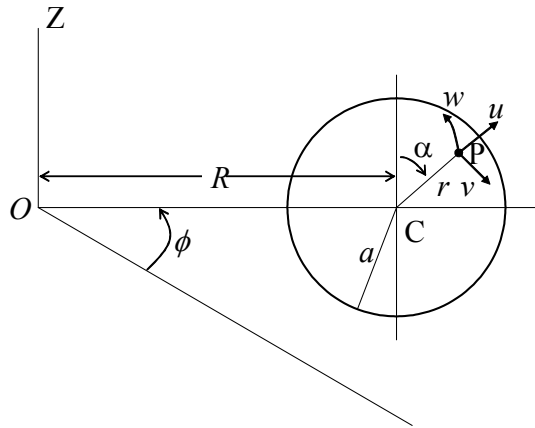
Fig. 2.8—Toroidal coordinate system.

The equations of momentum and continuity[52,53] are:

$$u\frac{\partial u}{\partial r}+\frac{v}{r}\frac{\partial u}{\partial \alpha}-\frac{v^2}{r}-\frac{w^2\sin\alpha}{R+r\sin\alpha}=-\frac{\partial}{\partial r}\left(\frac{p}{\rho}\right)-\upsilon\left(\frac{1}{r}\frac{\partial}{\partial \alpha}+\frac{\cos\alpha}{R+r\sin\alpha}\right)\left(\frac{\partial v}{\partial r}+\frac{v}{r}-\frac{1}{r}\frac{\partial u}{\partial \alpha}\right). \quad \text{...................}(2.1)$$

$$u\frac{\partial v}{\partial r}+\frac{v}{r}\frac{\partial v}{\partial \alpha}+\frac{uv}{r}-\frac{w^2\cos\alpha}{R+r\sin\alpha}=-\frac{1}{r}\frac{\partial}{\partial \alpha}\left(\frac{p}{\rho}\right)+\upsilon\left(\frac{\partial}{\partial r}+\frac{\sin\alpha}{R+r\sin\alpha}\right)\left(\frac{\partial v}{\partial r}+\frac{v}{r}-\frac{1}{r}\frac{\partial u}{\partial \alpha}\right). \quad \text{.................}(2.2)$$

20

$$u\frac{\partial w}{\partial r}+\frac{v}{r}\frac{\partial w}{\partial\alpha}+\frac{uw\sin\alpha}{R+r\sin\alpha}+\frac{vw\cos\alpha}{R+r\sin\alpha}=-\frac{1}{R+r\sin\alpha}\frac{\partial}{\partial\phi}\left(\frac{p}{\rho}\right)+\upsilon\left[\left(\frac{\partial}{\partial r}+\frac{1}{r}\right)\left(\frac{\partial w}{\partial r}+\frac{w\sin\alpha}{R+r\sin\alpha}\right)+\frac{1}{r}\frac{\partial}{\partial\alpha}\left(\frac{1}{r}\frac{\partial w}{\partial\alpha}+\frac{w\cos\alpha}{R+r\sin\alpha}\right)\right] \quad (2.3)$$

$$\frac{\partial u}{\partial r}+\frac{u}{r}+\frac{u\sin\alpha}{R+r\sin\alpha}+\frac{1}{r}\frac{\partial v}{\partial\alpha}+\frac{v\cos\alpha}{R+r\sin\alpha}=0\ . \quad ....\ (2.4)$$

The above equations plus adequate boundary conditions define a steady flow problem in a coiled tube. If the flow is assumed to be fully-developed, then u, v, and w will be independent of ϕ and pressure gradient in the axial direction (ϕ) will be constant:

$$-\frac{1}{R}\frac{\partial p}{\partial\phi}=G\ \text{(constant)}...\ (2.5)$$

Obviously, Eqs. (2.1) to (2.4) form a coupled, non-linear problem and are difficult to be solved analytically without invoking simplifying assumptions.

2.2.2.2 *Dean's Work and Dean Number*

The pioneering work of Dean[52,53] on the theoretical aspect of the coiled tube flow has been of significant importance in most of the later development. By assuming that the curvature of the pipe is small, that is, a/R is small, and that the flow is slow motion, Dean simplified the governing equations, Eqs. (2.1) to (2.4), and then, using a successive approximation method, obtained an analytical solution which is essentially an approximate solution obtained through perturbation over the Poiseuille flow of straight pipe.

21

As for the effect of pipe curvature on the flux, Dean's first paper[52] failed to show that the relation between pressure gradient and the flow rate is dependent of the curvature. In his second paper,[53] he derived the following flux expression:

$$\frac{Q_c}{Q_s} = 1 - \left(\frac{K}{576}\right)^2 (0.03058) + \left(\frac{K}{576}\right)^4 (0.01195), \quad \text{...}(2.6)$$

where Q_c and Q_s are the flow rates through coiled and straight pipes, and K is a dynamic similarity parameter and will be discussed below. Eq. (2.6) is valid only for very small K values.

One important contribution of the Dean's work is the introduction of non-dimensional parameter K which is called Dean number. According to Dean's original definition,

$$K = \frac{2W_0^2 a^3}{v^2 R}, \quad \text{...}(2.7)$$

where W_0 is the maximum axial velocity in the cross-section and v is the kinematic viscosity. There have been several versions of definition of Dean number,[54,55] but most researchers prefer the following definition:

$$N_{De} = N_{Re}\left(\frac{a}{R}\right)^{\frac{1}{2}}, \quad \text{...}(2.8)$$

where N_{Re} is Reynolds number. It can be shown that K and N_{De} are related by $K = 2(N_{De})^2$. Another definition of Dean number[56] is:

$$D = \sqrt{\left(\frac{2a^3}{v^2 R}\right)} \frac{Ga^2}{\mu}, \quad \text{...(2.9)}$$

where G is axial pressure gradient, v is kinematic viscosity, and μ is dynamic viscosity. Here, D and K are related by $D = 4\sqrt{K}$.

The Dean number provides a fundamental parameter in developing flow resistance correlations for flow in curved pipes. It has been found that at low Dean number, the law of resistance can be correlated with N_{De} only. For high Dean number, both N_{De} and curvature ratio (a/R) will be required.

2.2.2.3 Characteristics of Secondary Flow

The unique feature of the flow structure in coiled pipes is the secondary flow that is superimposed on the primary flow in the axial direction. Mathematically, the cause of the secondary flow is due to the two centrifugal force terms in the momentum equations for the r and α directions. Since the centrifugal force is perpendicular to the axial direction, there is no such a term in the ϕ momentum equation.

Fig. 2.9 illustrates the flow lines in the cross-section of a coiled pipe from Dean's solution which indicate that in the cross-section, the secondary flow streamlines form a pair of symmetrical vortices which have been called Dean vortices by later researchers. Dean[52] pointed out that the secondary flows of the spiral form are superimposed on the axial primary flow.
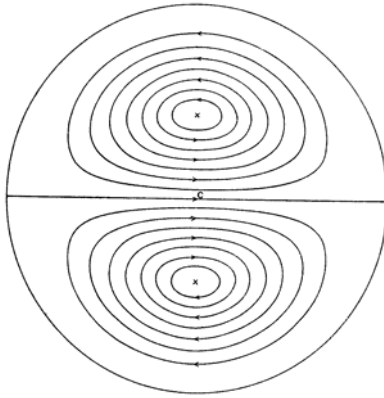
Fig. 2.9—Streamlines of secondary flow.[52]

Experimental observations of the secondary flow phenomena date back to 1910 when Eustice [57,58] did experiments of water flow in curved pipes. Eustice used filaments of six different colors to trace the paths of secondary flow streamlines and observed "the extremely beautiful effects due to the interacting of the colored bands."

Figs. 2.10 and 2.11 show the axial velocity profiles and contours in a cross-section of a coiled pipe obtained by Adler.[59] The curvature ratio was a/R = 1/100, and Reynolds number N_{Re} = 2050. It can be seen that the maximum axial velocity was shifted to the outer side of the coil and the velocity profile is very different from the parabolic profile for straight pipe.

Figs. 2.12 through 2.15 show the theoretical results of McConalogue and Srivastava,[56] and Collins and Dennis[60] for Dean number D = 96, 481, 2,000, and 5,000 respectively. These results show that as Dean number increases, the secondary flow becomes more confined to a thin area near the pipe wall. This characteristic supports the basic assumption of the boundary layer approximation methods.
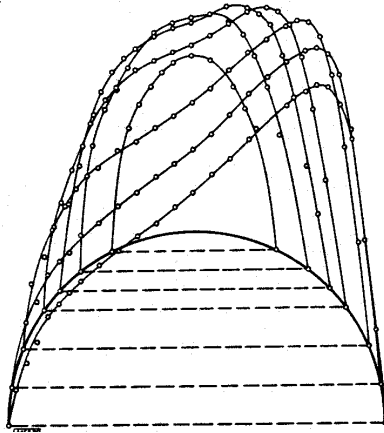
Fig. 2.10—Axial velocity profile, a/R = 0.01, N_{Re} =2050.[59]
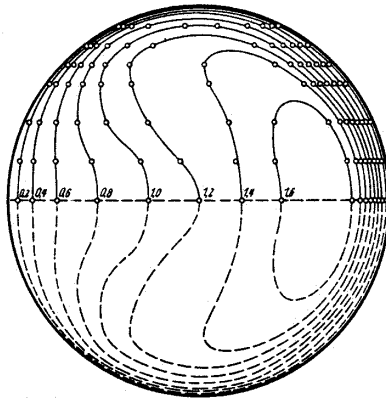
Fig. 2.11—Contours of axial velocity, a/R = 0.01, N_{Re} = 2050.[59]
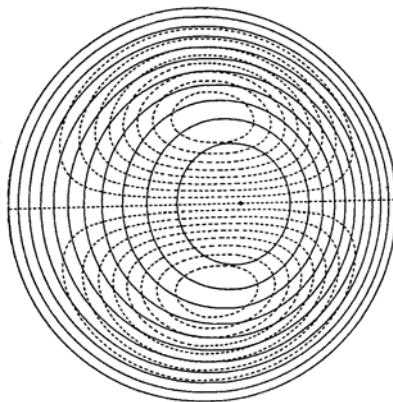
Fig. 2.12—Secondary flow streamlines and axial velocity contours (D = 96).[56]
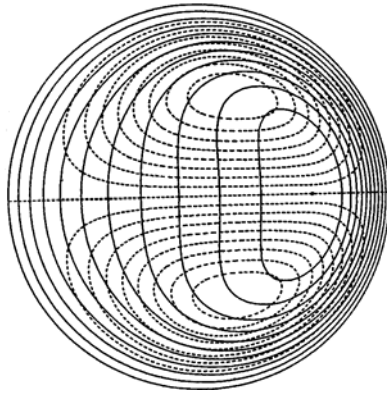
Fig. 2.13—Secondary flow streamlines and axial velocity contours (D = 481).[56]
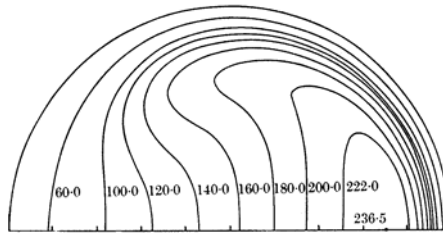
Fig. 2.14—Contours of axial velocity (D = 2000).[60]
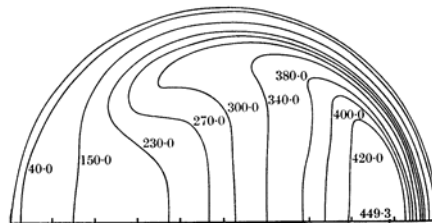
Fig. 2.15—Contours of axial velocity (D = 5000).[60]

2.2.2.4 Theoretical Methods

The complexity of the flow geometries and the equations of fluid flow in coiled pipes

attracted the attention of theoreticians as well as engineers. Various theoretical

methods have been developed. These theoretical methods can be roughly grouped as

26

analytical solutions for small Dean number, numerical methods, and boundary layer approximation methods for large Dean number.

Analytical solutions

For loosely coiled tubes (a/R is small) and small Dean number, the governing equations can be simplified and reduced to equations about a stream-function (ψ) and the axial velocity (w). Since the Dean number is small (therefore the deviation from the straight pipe flow is expected to be slight), it is appropriate to expand the solutions of the stream-function and axial velocity component in power series of the Dean number:

$$w = w_0 + w_1 K + w_2 K^2 + \cdots, \quad\quad\quad\quad\quad\quad\quad\quad\quad\quad\quad\quad\quad (2.10)$$

$$\psi = \psi_1 K + \psi_2 K^2 + \cdots, \quad\quad\quad\quad\quad\quad\quad\quad\quad\quad\quad\quad\quad\quad (2.11)$$

where $w_0, w_1, \psi_1, \psi_2, w_2,\ldots$ are functions of r and α. By substituting these expressions into the ψ and w equations and equating coefficients of the powers of K, Dean obtained the series solution by successively solving for $w_0, w_1, \psi_1, w_2, \psi_2, \ldots$ Note that w_0 is the solution for Poiseuille flow in straight pipe.

The similar approach was followed by Jones[61] for Rivlin-Reiner fluid model, and by Thomas and Walters[62,63] for elastico-viscous liquids in a curved pipe of circular and elliptic cross-sections respectively. Power series was also used by Larrain and Bonilla,[64] Topakoglu,[65] and Robertson and Muller.[66]

Van Dyke[54] extended the Dean's series by computer to 24 terms. But, his result has caused controversies due to the fact that his correlation of friction factor ratio is not in agreement with other studies.[67]

In addition to power series, Fourier-series development has also been used for series solutions. McConalogue and Srivastava's[56] results cover a range of Dean number of D from 96 to over 600. Dennis and Ng's[68] Fourier-series solution covers the range of Dean number D = 96 – 5000. It is found that for D < 956, the secondary flow consists of a symmetrical pair of counter-rotating vortices. For D > 956, the secondary flow has a four-vortex pattern consisting of two symmetrical pairs. Daskopoulos and Lenhoff[69] expressed their solution using Fourier series in the angular direction (α) and Chebychev polynominals in radius r.

Most studies of series solutions assumed negligible pitch of coil and neglected the effect of torsion. But, Germano[70,71] and Kao[72] studied the effect of torsion as well as curvature ratio.

Numerical Methods

If the curvature ratio (*a/R*) is small, the flow in curved pipe depends on a single parameter, the Dean number. This is not the case if (*a/R*) is not very small. The Navier-Stokes equations for fluid flow in coiled pipes can be solved numerically. Generally, a finite difference scheme has been adopted. These studies include Truesdell and Adler,[73] Greenspan,[74] Patankar *et al.*,[75] Collins and Dennis,[60] Joseph *et al.*,[76] Dennis,[77] and Hsu and Patankar,[78] *etc*. In these studies, the Navier-Stokes equations were simplified as stream-function/axial velocity or stream-

function/vorticity forms. Soh and Berger[79] used a finite-difference scheme and the value of curvature ratio can be arbitrary. Austin and Seader[80] solved the Navier-Stokes equations in the stream-function/vorticity form numerically using finite difference. A few studies have been reported for simulation of turbulent flows such as Patankar et al.[81] and Lai et al.[82] The challenges of numerical studies are accurate and efficient numerical scheme, grid system, and computational algorithms.

Boundary Layer Approximation Methods

The thickness of the boundary layer will become thinner with increasing Dean number. This feature has been shown by experiments[59] and numerical simulations.[60,68,77] According to the theory of the boundary layer approximation, the tube cross-section can be divided into two regions: the central inviscid core region and the thin boundary layer where the viscous effect is significant. Studies of this category include: Adler,[59] Ito,[4, 83] Barua,[3] Mori and Nakayama,[84] Mashelkar and Devarajan,[5,85,86] and Riley.[87]

To use the boundary layer approximation method, order of magnitude analysis is carried out with the boundary layer and the forms of velocity distributions are assumed. The potential difficulty with this method is the boundary layer separation at the inner side of the coil.[4] Fortunately, for the purpose of correlating flow resistance, the boundary layer models are probably sufficient and their accuracy has been verified by the experimental data.[4,83] This is probably because the contribution of the shear stress from the area at the inner bend is not significant to the circumferential averaged shear stress.

2.2.2.5 Experimental Studies

Experimental investigation of fluid flow in coiled pipes began as early as 1910s. Eustice[57,58] used colored filaments to observe the streamline flow of water in curved glass tubes and described the secondary flow streamlines. White[88] used the Dean number to correlate his experimental data on pressure drop through coiled pipes. He observed that the flow in curved pipe could be maintained laminar for a much higher Reynolds number than in straight pipes. This claim was verified by Taylor[89] in his experiments on the criterion of turbulence in curved pipes.

Adler[59] closely examined the velocity distributions by experiments, and found that a velocity profile of laminar flow differs greatly from the parabolic distribution and a thin boundary layer was assumed. Ito[83] measured the frictional pressure losses of turbulent flow in smooth curved pipes using water and drawn-copper tubing at various curvature ratios. Mori and Nakayama[84] measured velocity and temperature profiles of hot air in a curved pipe.

Srinivasan et al.[90] measured pressure drops of water and fuel oil in both helical tubes (with constant curvature) and spiral tubes (with variable curvature). Experimental values were used to develop equations to predict friction factors for laminar, transition, and turbulent regions. Equations were also given to predict critical Reynolds number for regime changes.

Mishra and Gupta[91] investigated pressure drop in coils of various diameters and pitches. Their data covered laminar flow and turbulent flows, and corresponding empirical correlations were proposed.

In addition to the gross flow experiments of measuring the flow resistance and flow rate, experiments were also made to understand the instability and flow regime transition, as discussed below.

2.2.2.6 Flow Regime Transition

It is a known fact that the transition from laminar to turbulent flow in coiled pipes occurs at a higher Reynolds number than in straight pipe. White[88] found that plots of flow resistance coefficient versus Dean number fall on a single line predicted by the Dean correlation at low Dean number. But, at high Dean numbers, data points of different curvature ratios deviated from the Dean correlation which was based on the streamline motion assumption. It was concluded that a flow state that was different than streamline occurred with curved pipes and the onset of turbulence was delayed with increase of curvature. These claims were confirmed experimentally by Taylor[89] whose test result with a curved pipe of curvature ratio of 1/18 indicated that streamline motion persisted up to a Reynolds number of 5,830, i.e., 2.8 times Reynolds' criterion for a straight pipe.

Ito[83] proposed the following empirical correlation for the critical Reynolds number:

$$N_{\mathrm{Re}c} = 20,000 \left(\frac{a}{R} \right)^{0.32} \quad \text{...(2.12)}$$

This equation provided good agreement with experimental results in the range of $15 < R/a < 8.6 \times 10^2$. For $R/a > 8.6 \times 10^2$, the critical Reynolds number for a curved

pipe practically coincides with that for a straight pipe. Mishra and Gupta[91] reported

that Eq. (2.12) is in good agreement with their experiments. But, as pointed out by

Srinivasan *et al.*,[90] Ito's[83] correlation will not give N_{Rec} = 2100 for a straight tube

where a/R = 0. Therefore, a new correlation was proposed based on the experiments

by Srinivasan *et al.*[90]:

$$N_{\mathrm{Re}c} = 2100\left[1+12\left(\frac{a}{R}\right)^{0.5}\right].$$ ....(2.13)

The previous observations and correlations were based on measurements of

global parameters such as friction factor. Due to the secondary flow effect, the

transition behavior on the plots of friction factor vs. Reynolds number is very gradual.

Actually, it is very difficult to accurately identify when the onset of the turbulence

occurs. If the fluid is non-Newtonian fluid, this transition would be even more

gradual.[92]

Sreenivasan and Strykowski[93] found that the characteristics of the transition

regime was dependent on the location in the pipe cross-section. Using hot wire

anemometers placed one quarter of the radius from the inner and outer walls, they

found that turbulence near the inner wall emerged by the gradual superposition of

higher order frequencies on the fundamental frequency. In contrast, near the outer

wall, turbulence emerged by high frequency "bursts". The sinusoidal oscillations at

the inner wall always preceded the turbulent bursts at the outer wall. Recently,

Webster and Humphrey[94] provided quantitative time-dependent point measurements

of velocity with a non-intrusive laser-Doppler velocimeter (LDV) and indicated that

the pipe curvature tends to dampen high frequency turbulent fluctuations, hence the manner of "transition to turbulence" in a coiled pipe is ambiguous.

All the above experimental observations indicate that much higher Reynolds number is needed to maintain turbulence in coiled pipes than in straight pipes.

2.2.2.7 Friction Factor Correlations

Based on the literature survey, the available correlations for laminar Newtonian fluids in curved pipes are summarized in Table 2.1 for the reference convenience. In this table, f_{SL} and f_{CL} are Fanning friction factors for laminar flow in straight and coiled pipes respectively. To evaluate these correlations, we first compared the correlations of White,[88] Srinivasan et al.,[90] Hasson,[95] Mishra and Gupta,[91] and Majuwar and Rao[96] that were developed from experimental data. It was found that except for the Mujawar and Rao[96] correlation, other four correlations are in excellent agreement. Therefore, it is appropriate to believe that the four of them are more trustful. Since the Mishra and Gupta[91] correlation covers the widest range of N_{De}, it is therefore used to further evaluate the other theoretical correlations.

Generally, all the boundary layer approximation methods are very close to the Mishra and Gupta[91] correlations for large Dean number, say, $N_{De} > 100$, except Adler[59] correlation which is significantly lower for $N_{De} < 2000$. The friction factor predicted by Mori and Nakayama[84] correlation is slightly higher than the others.

The Dean correlation is only valid for very small Dean number. The Topakoglu[65] correlation fails to be close to any correlation. Fig. 2.16 shows that van Dyke[54] correlation deviates from the rest when $N_{De} > 200$. Ito correlation is slightly

33

Table 2.1—Friction Factor Correlations of Laminar Newtonian Flow

No.	Authors	Correlations	Notes
1	Dean	$\dfrac{f_{CL}}{f_{SL}} = \left[1 - \left(\dfrac{K}{576}\right)^2 (0.03058) + \left(\dfrac{K}{576}\right)^4 (0.01195)\right]^{-1}$	K < 576
2	White	$\dfrac{f_{CL}}{f_{SL}} = \left\{1 - \left[1 - \left(\dfrac{11.6}{N_{De}}\right)^{0.45}\right]^{1/0.45}\right\}^{-1}$	$12 < N_{De} < 2000$
3	Adler	$\dfrac{f_{CL}}{f_{SL}} = 0.1064[N_{De}]^{1/2}$	Large N_{De}, say, $N_{De} > 10^2$
4	Barua	$\dfrac{f_{CL}}{f_{SL}} = \dfrac{(1.122)^3}{4N_{De}}\left\{1.181 + \left[(1.181)^2 + \dfrac{N_{De}}{\sqrt{6}}\right]^{1/2}\right\}^3$	Large N_{De}, say, $10^2 < N_{De} < 10^4$
5	Hasson	$\dfrac{f_{CL}}{f_{SL}} = 0.0969 N_{De}^{1/2} + 0.556$	$30 < N_{De} < 2000$
6	Mori and Nakayama	$\dfrac{f_{CL}}{f_{SL}} = \dfrac{0.108 N_{De}^{1/2}}{1 - 3.253 N_{De}^{-1/2}}$	Lagre Dean number, say, $N_{De} > 100$
7	Topakoglu	$\dfrac{f_{CL}}{f_{SL}} = \left\{1 - \dfrac{1}{48}\left(\dfrac{a}{R}\right)^2\left[\dfrac{1.541}{67.2}\left(\dfrac{N_{Re}}{6}\right)^4 + 1.1\left(\dfrac{N_{Re}}{6}\right)^2 - 1\right]\right\}^{-1}$	Small N_{De}

Table 2.1—Friction Factor Correlations of Laminar Newtonian Flow (continued)

No.	Authors	Correlations	Notes
8	Ito	$\frac{f_{CL}}{f_{SL}} = 0.1033 N_{De}^{1/2} \left[\left(1 + \frac{1.729}{N_{De}} \right)^{1/2} - \frac{1.315}{N_{De}^{1/2}} \right]^{-3}$	Large N_{De}, say, $N_{De} > 100$
9	Srinivasan et al.	$\frac{f_{CL}}{f_{SL}} = 0.41875 N_{De}^{0.275}$	$30 < N_{De} < 300$, $0.0097 < a/R < 0.135$
10	Collins and Dennis	$\frac{f_{CL}}{f_{SL}} = 0.1028 N_{De}^{1/2} \left\{ 1 + 3.7 N_{De}^{-1/2} \right\}$	$17 < N_{De} < 370$
11	Van Dyke	$\frac{f_{CL}}{f_{SL}} = 0.47136 N_{De}^{1/4}$	Large N_{De}, say, $N_{De} > 30$
12	Mishra and Gupta	$\frac{f_{CL}}{f_{SL}} = 1 + 0.033 \left(\log N_{De} \right)^{4.0}$	$1 < N_{De} < 3000$
13	Mujawar and Rao	$\frac{f_{CL}}{f_{SL}} = 0.26 \left(N_{De} \right)^{0.36}$	$35 < N_{De} < 2200$, $0.01 < a/R < 0.0695$
14	Liu and Masliyah	$\frac{f_{CL}}{f_{SL}} = 1 + \dfrac{\left[0.0908 + 0.0233 \left(\frac{a}{R} \right)^{1/2} \right] N_{De}^{1/2} - 0.132 \left(\frac{a}{R} \right)^{1/2} + 0.37 \left(\frac{a}{R} \right) - 0.2}{1 + 49/N_{De}}$	$0 < a/R < 1$, $N_{De} < 5000$
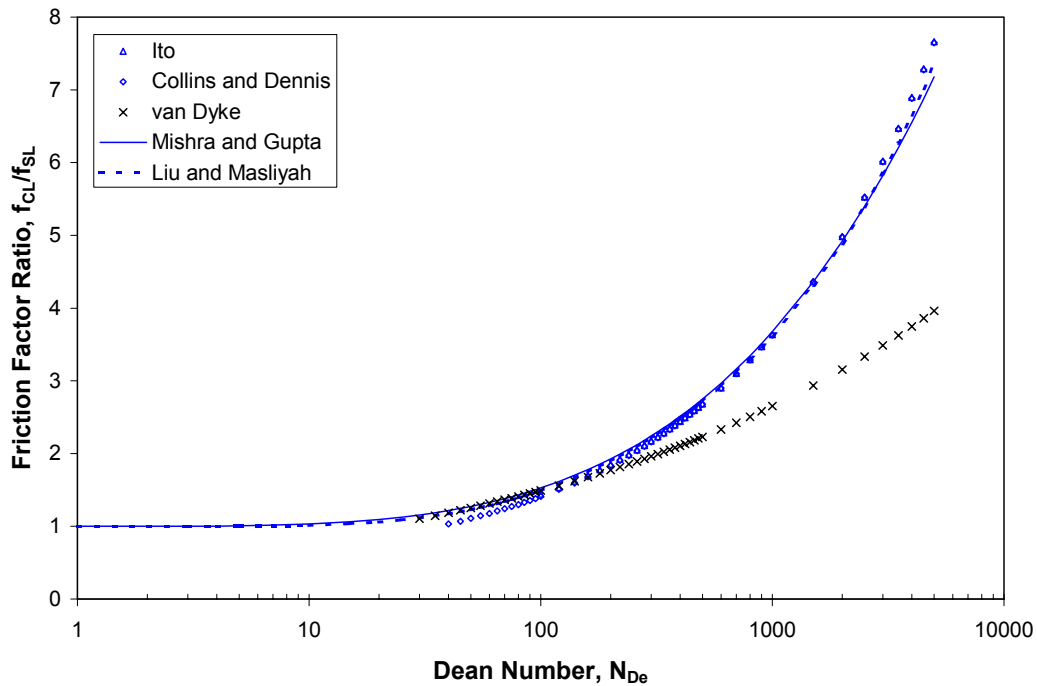
Fig. 2.16—Comparison of friction factor correlations of laminar Newtonian flow in coiled pipe.

lower when $N_{De} < 100$. Interestingly, all four correlations − Ito (for $N_{De} > 100$), Collins and Dennis,[60] Liu and Masliyah,[97] and Mishra and Gupta[91] are in close agreement over a large range of Dean number.

A few turbulent flow correlations are listed in Table 2.2. There is close agreement between them. In Table 2.2, f_{ST} and f_{CT} are Fanning friction factors of turbulent flow in straight and coiled pipes respectively. N_{Dec} is the critical Dean number for turbulent flow in coiled pipe.

36

Table 2.2—Friction Factor Correlations of Newtonian Turbulent Flow

No.	Authors	Correlations	Notes
1	Ito	$f_{CT} = \frac{1}{4}\left(\frac{a}{R}\right)^{\frac{1}{2}}\left\{0.029 + 0.304\left[N_{Re}\left(\frac{a}{R}\right)^2\right]^{-0.25}\right\}$	$300 > N_{Re}\left(\frac{a}{R}\right)^2 > 0.034$ $0.0012 < a/R < 0.067$
2	Srinivasan et al.	$f_{CT} = \dfrac{0.084\left(\dfrac{a}{R}\right)^{0.2}}{N_{De}^{0.2}}$	$N_{Dec} < N_{De} < 14000$ $0.0097 < a/R < 0.135$
3	Mishra and Gupta	$f_{CT} = f_{ST} + 0.0075\left(\dfrac{a}{R}\right)^{1/2}$, $f_{ST} = \dfrac{0.079}{N_{Re}^{0.25}}$	$4500 < N_{Re} < 10^5$ $0.003 < a/R < 0.15$

2.2.3 Flow of Non-Newtonian Fluid in Coiled Pipe

The complex rheological behavior of non-Newtonian fluids adds another dimension of complexity to the flow phenomena in coiled pipes. The flow of non-Newtonian fluids in coiled pipes has remained a much less studied area than Newtonian fluids.

Jones[61] considered the theoretical problem of the flow of a non-Newtonian, visco-inelastic Reiner-Rivlin fluid in a coiled tube. A number of investigators[62,63,98-100] have reported studies on the effect of elasticity on fluid flow in coiled pipes. Jones and Davies's[99] experiments showed that minute amounts of polymer could significantly delay departure of flow rate from Poiseuille flow, a phenomenon called "drag reduction in the laminar region".

Tsang and James[100] noted that polymer additives caused a reduction of the secondary motion and tried to explain the drag reduction by estimating the cross-sectional stresses based on Dean's solution and several molecular models.

Among the various studies of non-Newtonian flow in coiled pipes, those by Mashelkar and Devarajan[5,85,86] deserve special attention. Following Ito's[4] boundary layer approximation approach for Newtonian fluids, Mashelkar and Devarajan theoretically analyzed and numerically solved the flow equations for a power-law fluid in both laminar and turbulent flows. An empirical correlation for laminar flow was developed based on the numerical solutions and another correlation for visco-elastic fluids in terms of Weissenberg number based on data of flow tests.

Mishra and Gupta[91] have also measured friction factors of non-Newtonian fluids in coiled pipes and empirical correlations have been obtained.

In recent years, the rapid increase of coiled tubing applications in the oil and gas industry has driven the research activities of coiled tubing hydraulics using full-scale facilities. Azouz et al.[101] measured frictional pressure losses of linear guar gum, hydroypropyl guar (HPG), and borate-crosslinked guar gum in 1-1/2-in. coiled tubing reels. McCann and Islas[102] generalized the Srinivasan et al.[90] correlation for Newtonian turbulent flow to non-Newtonian fluids and compared the generalized correlation with the full-scale tests of six fluids prepared using bentonite and lime.

Shah and Zhou[92] discussed the characteristics of drag reduction of polymer solutions in coiled tubing and affecting parameters such as curvature, tubing ID, and polymer concentration. More recently, Shah et al.[103] experimentally investigated the flow behavior of hydraulic fracturing slurries in coiled tubing. An empirical correlation of slurry friction factor as affected by sand concentration was developed. The possible mechanisms of tubing erosion in typical fracturing operations have been addressed.

As with the case of Newtonian fluids, we have summarized the available friction factor correlations of non-Newtonian fluids in coiled tubing in Table 2.3. In this table, n is the flow behavior index of power law fluid, and N_{Reg} is the generalized Reynolds number. The Dean number, D_e is defined as:

$$D_e = \frac{(2a)^n v_m^{2-n} \rho}{K} (a/R)^{0.5} ,$$ .... (2.14)

Table 2.3—Friction Factor Correlations of Non-Newtonian Fluid (Laminar and Turbulent)

No.	Authors	Correlations	Notes
1	Mashelkar and Devarajan	$f_{CL} = \left(9.069 - 9.438n + 4.374n^2\right)\left(\dfrac{a}{R}\right)^{0.5} D_e^{(-0.768+0.122n)}$	$70 < D_e < 400$, $0.01 < a/R < 0.135$
2	Mishra and Gupta	$f_{CL} = f_{SL}\left[1 + 0.033\left(\log N_{De2}\right)^{4.0}\right]$	$f_{SL} = \dfrac{16}{N_{Re2}}$
3		$f_{CT} = f_{ST} + 0.0075\left(\dfrac{a}{R}\right)^{1/2}$	$f_{ST} = \dfrac{0.079}{N_{Red}^{0.25}}$
4	McCann and Islas	$f_{CT} = \dfrac{1.06a'}{N_{Reg}^{0.8b'}}\left(\dfrac{a}{R}\right)^{0.1}$	$a' = \dfrac{\log_{10}(n)+3.93}{50}$ $b' = \dfrac{1.75-\log_{10}(n)}{7}$

where ρ is fluid density, v_m is mean velocity, and K is consistency index of fluid. N_{Red} is Reynolds number based on differential viscosity and N_{Re2} is Reynolds number based on pseudoshear viscosity.[91] N_{De2} is defined as: $N_{De2} = N_{Re2}(a/R)^{0.5}$.

The present review shows that, compared with its counterpart of Newtonian fluids, the flow of non-Newtonian fluids has remained very much unstudied, either theoretically or experimentally. Yet, most fluids used with coiled tubing operations in the oil and gas industry are non-Newtonian, for example, polymer-based solutions, and surfactant-based solutions. Slurries and foam fluids are also used with coiled tubing. The available correlations are not appropriate for predicting friction pressure losses in these applications. Further systematic research is required.

CHAPTER 3
THEORETICAL ANALYSIS OF LAMINAR FLOW
OF POWER-LAW FLUID IN COILED TUBING

3.1   Introduction

When a fluid flows through a curved pipe, there exits a secondary flow by the action of centrifugal forces and the resultant secondary flow is in a double spiral form. Previous studies[3,59,84] showed that when the Dean number, $N_{De} = N_{Re}(a/R)^{0.5}$, is large, the secondary flow is mainly confined to a thin layer near the tubing wall. Ito[4] (1969) applied the approach of boundary layer approximation analysis and obtained solution to the laminar flow of Newtonian fluid in curved pipe. Mashelkar and Devarajan[5] extended the Ito's method to the laminar flow of non-Newtonian fluid in coiled tube and obtained a friction factor correlation based on the numerical analysis. Yet, they only obtained numerical solutions for four values of power law flow behavior index, i.e., n = 0.5, 0.75, 0.9, and 1.0. Therefore, the range of fluid properties is rather limited. Furthermore, as several authors[78,96] have pointed out, the Mashelkar and Devarajan[5] correlation does not match the Ito's laminar flow correlation[4] as it is supposed to when the flow behavior index is set to unity.

   In this study, we closely followed the approach of boundary layer approximation analysis taken by Ito, and Mashelkar and Devarajan, and extended the work of Mashelkar and Devarajan to numerical solutions of power law fluids in coiled tubing with much wider range of flow behavior index (n = 0.25, 0.30, …, 1.0 in steps of

0.05). A new friction factor correlation has been developed based on numerical analysis.

The general procedures of analysis and solution are as follows. First, we apply the boundary layer approximation approach and order of magnitude analysis to obtain simplified flow equations in both the boundary layer and the core region of the tubing cross section. After setting the appropriate boundary conditions for the boundary layer, we integrated the boundary layer flow equations to obtain equations of boundary layer momentum integrals. The velocity profiles in the boundary layer were then solved numerically by assuming appropriate forms of velocity distribution across the boundary layer. Once the flow field was solved, the friction factor correlation can be derived.

3.2   Mathematical Formulation

3.2.1   Governing Equations

The toroidal coordinate system, shown in Fig. 3.1, is used to represent the flow geometry of fluid flow in coiled tubing. Here, u, v, and w represent velocity components in the directions of r, θ, and ϕ respectively. a and R are the radii of the coiled tubing and the tubing reel respectively. The ratio, a/R, is called the curvature ratio.

Several assumptions have been made as follows:

a.   The flow is steady and fully-developed laminar flow;

b.   The curvature ratio (a/R) is small;

43

c. The Dean number is large, and therefore, only viscous forces are important in a thin boundary layer near the tubing wall, and the flow outside the boundary layer is influenced by the inertial and pressure forces alone.
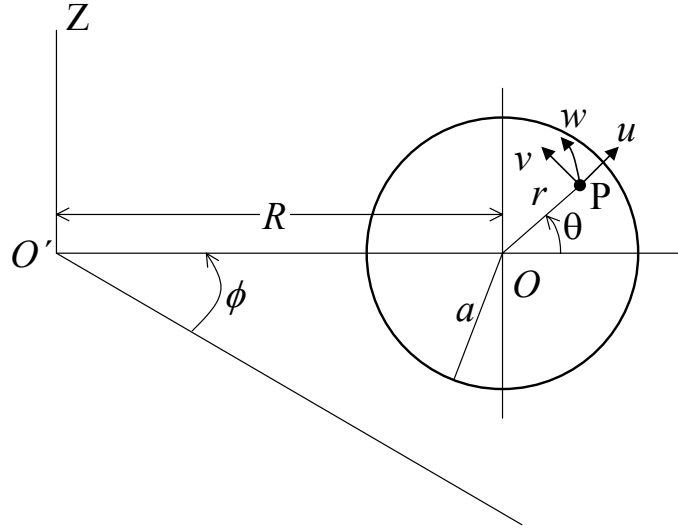
Fig. 3.1—Toroidal coordinate system.

d. The rheological behavior of the fluid can be described by a power law model.

The equations of motion and continuity are as follows[5]:

$$\rho\left(u\frac{\partial u}{\partial r}+\frac{v}{r}\frac{\partial u}{\partial\theta}-\frac{v^2}{r}-\frac{w^2\cos\theta}{R}\right)=-\frac{\partial p}{\partial r}-\left(\frac{\partial\tau_{rr}}{\partial r}+\frac{1}{r}\frac{\partial\tau_{r\theta}}{\partial\theta}+\frac{\tau_{rr}-\tau_{\theta\theta}}{r}\right) \quad\text{.................} \quad (3.1)$$

$$\rho\left(u\frac{\partial v}{\partial r}+\frac{v}{r}\frac{\partial v}{\partial\theta}+\frac{uv}{r}+\frac{w^2\sin\theta}{R}\right)=-\frac{1}{r}\frac{\partial p}{\partial\theta}-\left(\frac{\partial\tau_{r\theta}}{\partial r}+\frac{1}{r}\frac{\partial\tau_{\theta\theta}}{\partial\theta}+\frac{2}{r}\tau_{r\theta}\right) \quad\text{.....................} \quad (3.2)$$

$$\rho\left(u\frac{\partial w}{\partial r}+\frac{v}{r}\frac{\partial w}{\partial\theta}\right)=-\frac{1}{R}\frac{\partial p}{\partial\phi}-\left(\frac{\partial\tau_{r\phi}}{\partial r}+\frac{1}{r}\frac{\partial\tau_{\theta\phi}}{\partial\theta}+\frac{2\tau_{r\phi}\sin\theta}{R}\right) \quad\text{...............................} \quad (3.3)$$

$$\frac{\partial u}{\partial r}+\frac{u}{r}+\frac{1}{r}\frac{\partial v}{\partial\theta}=0 \quad\text{...} \quad (3.4)$$

44

$$-\frac{\partial p}{\partial \phi} = C \;. \dotfill (3.5)$$

where ρ is fluid density, p is pressure, and τ_{rr}, $\tau_{\theta\theta}$, $\tau_{r\theta}$, $\tau_{r\phi}$, and $\tau_{\theta\phi}$ are stress terms. The second index of these stresses indicates the direction of stress and the first index indicates the plane of the stress. For example, $\tau_{r\phi}$ indicates stress in the direction of ϕ on a plane that is normal to direction of r.

The overall flow through the tubing cross-section can be divided into two regions: a central inviscid core and a thin boundary layer adjacent to the tubing wall, schematically shown in Fig. 3.2. The central part of the fluid will be driven towards the outer wall due to the centrifugal force. The fluid entering the boundary layer will be pushed back along the wall toward the inner side. This will result in the double vortical motion in the cross-section of the tubing.
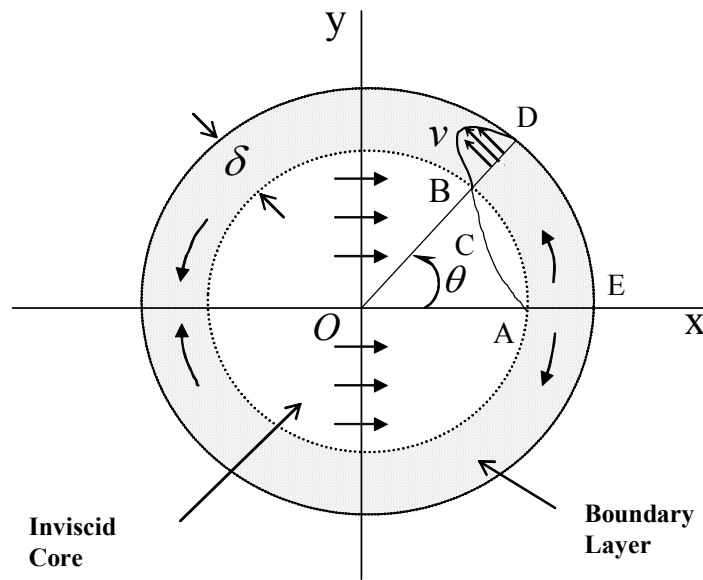
Fig. 3.2—Flow model showing the inviscid core and boundary layer.

3.2.2   Flow Equations outside the Boundary Layer

In the region outside the boundary layer, the axial velocity distribution is more uniform than in the boundary layer, and therefore, the secondary velocity components u and v may be small compared with the primary component w, i.e., u, v << w. Then, Eqs. (3.1) to (3.3) reduce to:

$$-\frac{w^2 \cos\theta}{R} = -\frac{1}{\rho}\frac{\partial p}{\partial r} \quad\text{..} \quad (3.6)$$

$$\frac{w^2 \sin\theta}{R} = -\frac{1}{\rho r}\frac{\partial p}{\partial\theta} \quad\text{..} \quad (3.7)$$

$$u\frac{\partial w}{\partial r} + \frac{v}{r}\frac{\partial w}{\partial\theta} = \frac{C}{\rho R} \quad\text{..} \quad (3.8)$$

Noting that

$$\sin\theta\frac{\partial}{\partial r} + \frac{\cos\theta}{r}\frac{\partial}{\partial\theta} = \frac{\partial}{\partial y} \quad\text{..} \quad (3.9)$$

and if p is eliminated from Eqs. (3.6) and (3.7), we have

$$\frac{\partial w}{\partial y} = 0 \quad\text{..} \quad (3.10)$$

which gives

$$w = F(x), \quad\text{..} \quad (3.11)$$

where F is an arbitrary function of x.

From Eq. (3.4), we can introduce a stream function ψ so that

$$u = \frac{1}{r}\frac{\partial \Psi}{\partial \theta} , \quad v = -\frac{\partial \Psi}{\partial r} \ . \ \dots\dots\dots\dots\dots\dots\dots\dots\dots\dots\dots\dots\dots\dots\dots\dots\dots\dots \quad (3.12)$$

Inserting Eqs. (3.11) and (3.12) into Eq. (3.8) and integrating, we have

$$\Psi = \frac{Cy}{\rho R F'(x)} + const. \ . \ \dots\dots\dots\dots\dots\dots\dots\dots\dots\dots\dots\dots\dots\dots\dots\dots\dots \quad (3.13)$$

where F′(x) = dF/dx. The function F(x) will be determined later from the condition of

continuity of the secondary flow between the core and the boundary layer.

3.2.3   Boundary Layer Equations

In the boundary layer, the axial velocity component w will be reduced from a value,

w_1 (here the subscript 1 denotes the edge of the boundary layer) at the edge of the

boundary layer to zero at the wall (no-slip boundary). Therefore, the secondary flow

component v becomes comparable with w. In order to obtain simplified equations for

the boundary layer, we conduct order of magnitude analysis:

$$u \sim O(\delta) \quad v, w \sim O(1) \quad \frac{\partial}{\partial r} \sim O(\delta^{-1}) \quad \frac{\partial}{\partial \theta}, \frac{\partial}{\partial \phi} \sim O(1), \ \dots\dots\dots\dots\dots\dots\dots\dots\dots \quad (3.14)$$

where δ is the boundary layer thickness.

Eqs. (3.1) to (3.4) then reduce to[5,104]:

$$-\frac{v^2}{a} - \frac{w^2 \cos\theta}{R} = -\frac{1}{\rho}\frac{\partial p}{\partial r} \ \dots\dots\dots\dots\dots\dots\dots\dots\dots\dots\dots\dots\dots\dots\dots \quad (3.15)$$

$$u\frac{\partial v}{\partial r} + \frac{v}{a}\frac{\partial v}{\partial \theta} + \frac{w^2 \sin\theta}{R} = -\frac{1}{\rho a}\frac{\partial p}{\partial \theta} - \frac{1}{\rho}\frac{\partial \tau_{r\theta}}{\partial r} \ \dots\dots\dots\dots\dots\dots\dots\dots\dots \quad (3.16)$$

$$u\frac{\partial w}{\partial r}+\frac{v}{a}\frac{\partial w}{\partial \theta}=-\frac{1}{\rho R}\frac{\partial p}{\partial \phi}-\frac{1}{\rho}\frac{\partial \tau_{r\phi}}{\partial r} \quad\text{..} \quad (3.17)$$

$$\frac{\partial u}{\partial r}+\frac{1}{a}\frac{\partial v}{\partial \theta}=0 \; . \quad\text{..} \quad (3.18)$$

Next, Eqs. (3.16) and (3.17) will be further simplified. Eq. (3.15) indicates that the pressure variation over the boundary layer is only of order δ, and can be neglected. Therefore, we have $p(r,\theta,\phi)=p_1(\theta,\phi)$ where the subscript 1 denotes the edge of the boundary layer. Hence, from Eq. (3.7),

$$\frac{\partial p}{\partial \theta}=-\rho\frac{a}{R}w_1^2\sin\theta \quad\text{..} \quad (3.19)$$

Eq. (3.16) then becomes:

$$u\frac{\partial v}{\partial r}+\frac{v}{a}\frac{\partial v}{\partial \theta}=\frac{w_1^2-w^2}{R}\sin\theta-\frac{1}{\rho}\frac{\partial \tau_{r\theta}}{\partial r} \quad\text{..} \quad (3.20)$$

Further order of magnitude analysis[4,5,104] shows that the first term on the right hand side of Eq. (3.17) can be neglected and hence Eq. (3.17) can be simplified as:

$$u\frac{\partial w}{\partial r}+\frac{v}{a}\frac{\partial w}{\partial \theta}=-\frac{1}{\rho}\frac{\partial \tau_{r\phi}}{\partial r} \quad\text{..} \quad (3.21)$$

If a power law rheological model is assumed, Eqs. (3.20) and (3.21) can be written as:

$$u\frac{\partial v}{\partial r}+\frac{v}{a}\frac{\partial v}{\partial \theta}=\frac{w_1^2-w^2}{R}\sin\theta+\frac{K}{\rho}\frac{\partial}{\partial r}\left[\left(-\frac{\partial w}{\partial r}\right)^{n-1}\left(\frac{\partial v}{\partial r}\right)\right] \quad\text{...................} \quad (3.22)$$

$$u \frac{\partial w}{\partial r} + \frac{v}{a} \frac{\partial w}{\partial \theta} = \frac{K}{\rho} \frac{\partial}{\partial r} \left(-\frac{\partial w}{\partial r} \right)^{n-1} \left(\frac{\partial w}{\partial r} \right),$$ .... (3.23)

where n and K are the flow behavior index and consistency index of the power law model. In Eqs. (3.22) and (3.23), we neglected the effect of ($\partial v / \partial r$) on the total shear rate, since $(\partial v / \partial r)^2 \ll (\partial w / \partial r)^2$ for a/R ≪ 1.

For boundary conditions, we shall have approximately[4,5]

$$r = a - \delta, \ v \cong 0, \ \frac{\partial v}{\partial r} \cong 0$$ .... (3.24)

$$r = a - \delta, \ w = w_1, \ \left(\frac{\partial w}{\partial r} \right)_1 \cong 0$$ .... (3.25)

3.2.4 Continuity of the Secondary Flow

In Fig. 3.2, let A and B be the points on the outer edge of the boundary layer. Using Eq. (3.13), the flux across a curve ACB drawn outside the boundary layer is:

$$\int_A^B d\Psi = \Psi_B - \Psi_A = \frac{Ca \sin \theta}{\rho R F'(x)}$$ .... (3.26)

Across AE, v = 0 for reasons of symmetry. Across BD, the flux is $\int_0^\delta v \, d\xi$, where

$$\xi = a - r.$$ .... (3.27)

We have then

$$\frac{Ca \sin \theta}{\rho R F'(x)} = \int_0^\delta v \, d\xi$$ .... (3.28)

Considering x ≈ acosθ in the thin boundary layer, we have

$$F'(x) = \frac{dw}{dx} = -\frac{1}{a\sin\theta}\frac{dw_1}{d\theta} \quad \text{..} \quad (3.29)$$

From Eqs. (3.28) and (3.29), it follows that

$$\frac{dw_1}{d\theta} = -\frac{Ca^2\sin^2\theta}{\rho R\int_0^\delta v\,d\xi} \quad \text{..} \quad (3.30)$$

Considering the force balance for a cylindrical volume of length $Rd\phi$ and radius a, we have

$$2\int_0^\pi \int_0^a \left[p - \left(p + \frac{\partial p}{\partial\phi}d\phi \right) \right] r\,dr\,d\theta = Rd\phi 2a\int_0^\pi \tau_{r\phi}d\theta \quad \text{.........................} \quad (3.31)$$

Hence,

$$C = -\frac{\partial p}{\partial\phi} = \frac{2R}{\pi a}\int_0^\pi \tau_{r\phi}d\theta \quad \text{..} \quad (3.32)$$

3.2.5   Boundary Layer Momentum Integrals

Integrating Eq. (3.22) over the boundary layer thickness δ and using Eqs. (3.18) and (3.24), we have

$$\frac{a}{\rho}\tau_{r\theta}\bigg|_{\xi=0} = -\frac{d}{d\theta}\int_0^\delta v^2 d\xi + \frac{a}{R}\sin\theta\int_0^\delta (w_1^2 - w^2)d\xi \quad \text{.............................} \quad (3.33)$$

Similarly from Eq. (3.23), we have

$$\frac{a}{\rho}\tau_{r\phi}\bigg|_{\xi=0} = w_1\frac{d}{d\theta}\int_0^\delta v\,d\xi - \frac{d}{d\theta}\int_0^\delta vw\,d\xi \quad \text{...} \quad (3.34)$$

50

3.2.6 Application of the Pohlhausen Method

The Pohlhausen's approximation method is followed for solving the velocity distributions in the boundary layer. We are looking for solutions of v and w in the boundary layer that satisfy the following boundary conditions:

$$\xi = 0: \text{v} = 0, \; -\frac{w_1^2 \sin\theta}{R} = \frac{K}{\rho} \frac{\partial}{\partial r}\left[\left(-\frac{\partial w}{\partial r}\right)^{n-1}\left(\frac{\partial v}{\partial r}\right)\right] \quad\text{(3.35)}$$

$$\xi = \delta: \text{v} = 0, \; \frac{\partial v}{\partial \xi} = 0 \quad\text{(3.36)}$$

$$\xi = 0: \text{w} = 0, \; \frac{\partial^2 w}{\partial \xi^2} = 0 \quad\text{(3.37)}$$

$$\xi = \delta: \text{w} = w_1, \; \frac{\partial w}{\partial \xi} = 0 \quad\text{(3.38)}$$

The above conditions can be satisfied by the following velocity profiles[5]:

$$v = \left(\frac{2}{3}\right)^{n-1} \frac{\rho \sin\theta}{KR} \delta^{n+1} w_1^{3-n} g(\eta) + Sh(\eta) \quad\text{(3.39)}$$

and

$$w = w_1 k(\eta), \quad\text{(3.40)}$$

where,

$$g(\eta) = \frac{1}{6}\left(2\eta - 3\eta^2 + \eta^4\right) \quad\text{(3.41)}$$

$$h(\eta) = \frac{1}{6}\left(\eta - 3\eta^3 + 2\eta^4\right) \quad\text{(3.42)}$$

$$k(\eta) = \frac{1}{2}\left(3\eta - \eta^3\right) \dotfill (3.43)$$

and

$$\eta = \frac{\xi}{\delta} \cdot \dotfill (3.44)$$

S can be considered as a shape factor of v-velocity component and is a function of angle θ. Now our task becomes solving for δ, w_1, and S from the two boundary layer momentum integral equations [Eqs. (3.33) and (3.34)] and the boundary layer continuity equation [Eq. (3.30)] as well as the boundary conditions.

To reduce Eqs. (3.33), (3.34) and (3.30) to non-dimensional form, the following dimensionless variables are defined:

$$\delta_o = \left(\frac{\delta}{a}\right) D_{e0}^{1/(n+1)} \dotfill (3.45)$$

$$S_o = \frac{S}{w_{10}}\left(a/R\right)^{-1/2} \dotfill (3.46)$$

$$w_o = \frac{w_1}{w_{10}}, \dotfill (3.47)$$

where,

$$D_{e0} = N'_{Reg}\sqrt{a/R} \dotfill (3.48)$$

and w_{10} is the value of w_1 at $\theta = 0$. N'_{Reg} is defined as:

$$N'_{Reg} = \frac{(a)^n w_{10}^{2-n}\rho}{K} \dotfill (3.49)$$

Since the specific expressions for g(η), h(η), and k(η) are already given in Eqs. (3.41) to (3.43), the integrals and the terms of $\tau_{r\theta}|_{\xi=0}$ and $\tau_{r\phi}|_{\xi=0}$ in Eqs. (3.33) and (3.34) can be evaluated. The final differential equations in a non-dimensional form are obtained as the following:

$$\frac{d}{d\theta}\left[\frac{17}{315}\left(\frac{2}{3}\right)^{2(n-1)}\delta_o^{2(n+1)+1}w_o^{2(3-n)}\sin^2\theta + \frac{101}{1260}\left(\frac{2}{3}\right)^{n-1}\delta_o^{n+2}w_o^{3-n}S_o\sin\theta + \frac{19}{630}\delta_o S_o^2\right]$$

$$=6\left[\frac{38}{35}\delta_o w_o^2\sin\theta - \left(\frac{2}{3}\right)^{1-n}\frac{S_o w_o^{n-1}}{\delta_o^n}\right] \dots\dots\dots\dots\dots\dots\dots\dots\dots\dots\dots\dots\dots\dots\dots\dots\dots\dots\dots\dots (3.50)$$

$$w_o\frac{d}{d\theta}\left[\frac{1}{3}\left(\frac{2}{3}\right)^{n-1}\delta_o^{n+2}w_o^{3-n}\sin\theta + \frac{S_o\delta_o}{4}\right] - \frac{d}{d\theta}\left[\frac{3}{16}\left(\frac{2}{3}\right)^{n-1}\delta_o^{n+2}w_o^{4-n}\sin\theta + \frac{25}{168}\delta_o w_o S_o\right]$$

$$=10\left(\frac{2}{3}\right)^{-n}\frac{w_o^n}{\delta_o^n} \dots\dots\dots\dots\dots\dots\dots\dots\dots\dots\dots\dots\dots\dots\dots\dots\dots\dots\dots\dots\dots\dots\dots\dots\dots\dots (3.51)$$

$$\frac{dw_o}{d\theta} = -\frac{120\alpha\sin^2\theta}{\left[4\left(\frac{2}{3}\right)^{n-1}\delta_o^{n+2}w_o^{3-n}\sin\theta + 3S_o\delta_o\right]}, \dots\dots\dots\dots\dots\dots\dots\dots\dots\dots\dots\dots\dots (3.52)$$

where,

$$\alpha = \frac{2}{\pi}\left(\frac{2}{3}\right)^{-n}\int_0^\pi \frac{w_o^n}{\delta_o^n}d\theta \dots\dots\dots\dots\dots\dots\dots\dots\dots\dots\dots\dots\dots\dots\dots\dots\dots\dots\dots (3.53)$$

3.3   Solution Procedure

The task now becomes solving for δ_o, w_o, and S_o as function of θ from the coupled, nonlinear ordinary differential equations [Eqs. (3.50) to (3.53)]. This can be accomplished by integrating Eqs. (3.50) to (3.52) with the angle θ in the range of 0 −

π. A Runge-Kutta scheme was used to solve the system of ordinary differential equations. The initial condition (at $\theta = 0$) was determined following Ito's approach.[4] In the neighborhood of $\theta = 0$, let

$$\delta_o = \delta_{o0}\left(1 + \delta_{o2}\theta^2 + \cdots\right) \dotfill (3.54)$$

$$S_o = S_{o1}\theta\left(1 + S_{o3}\theta^2 + \cdots\right) \dotfill (3.55)$$

$$w_o = 1 + w_{o2}\theta^2 + \cdots \dotfill (3.56)$$

Substituting these expansions into Eqs. (3.50) and (3.51) leads to two equations about δ_{o0} and S_{o1} with the flow behavior index (n) of the power law model as a parameter.

$$68\left(\frac{2}{3}\right)^{2(n-1)} + 101\left(\frac{2}{3}\right)^{n-1}\frac{S_{o1}}{\delta_{o0}^{n+1}} + 38\left(\frac{S_{o1}}{\delta_{o0}^{n+1}}\right)^2 = \frac{108}{\delta_{o0}^{2(n+1)}}\left[38 - 35\left(\frac{2}{3}\right)^{1-n}\frac{S_{o1}}{\delta_{o0}^{n+1}}\right] \dotfill (3.57)$$

$$49\left(\frac{2}{3}\right)^{n-1} + 34\frac{S_{o1}}{\delta_{o0}^{n+1}} = 3360\left(\frac{2}{3}\right)^{-n}\frac{1}{\delta_{o0}^{2(n+1)}} \dotfill (3.58)$$

Therefore, for a given value of n, the initial condition can be determined by solving the above two equations. To evaluate α from numerical solutions of w_o and δ_o, the Simpson's rule was employed for the numerical integration in Eq. (3.53).

Note that in order to solve for δ_o, w_o, and S_o numerically, the value of α must be known, see Eq. (3.52). But Eq. (3.53) indicates that α depends on the solutions of δ_o and w_o. Therefore, a trial-and-error method is needed. First, with an assumed value of α, Eqs. (3.50) to (3.52) were numerically integrated. Then δ_o and w_o thus determined were substituted into Eq. (3.53) and a new value of α was found. The calculation

procedure was repeated until the difference between the assumed value and the calculated value of α satisfied a specified convergence criterion.

Once the solutions for dimensionless variables δ_o, w_o, and S_o are obtained, the velocity field both in the boundary layer and the central core can be defined by using Eqs. (3.11) to (3.13), (3.29), (3.30), (3.39), (3.40), and (3.45) to (3.47). Friction factor correlations can be developed, as will be shown later.

3.4   Results and Discussion

3.4.1   Numerical Solutions of Eqs. (3.50) to (3.52)

Numerical solutions of the governing equations, Eqs. (3.50) to (3.52), were obtained for a wide range of flow behavior index (n) – from 0.25 to 1.0 in steps of 0.05. Figs. 3.3 to 3.5 show the solutions for n = 1.0, 0.9, 0.7, 0.5, and 0.3 respectively. To check the accuracy of the calculation method, the results of the Newtonian fluid (n = 1) were compared with the Ito's solution. Our results were in excellent agreement with Ito's result.

Fig. 3.6 shows the profiles of boundary layer thickness (normalized as δ/a) for flow behavior index n = 0.95 and 0.5, and Dean number D_e = 200 and 500 respectively. It can be seen that as the Dean number increases, the boundary layer becomes thinner. As n decreases from 0.95 to 0.5, the boundary layer adjacent to the outer wall becomes thinner while it is becoming thicker at the inner side of the tubing wall. This implies that as the flow behavior index n decreases, the high velocity will shift more and more toward the outer wall, whereas the cross-sectional area near the

inner wall will contribute less and less to the total flux. This flow feature may have practical implications. For example, the faster flow velocity near the outer wall may cause more severe erosion at the extados of the coiled tubing than at the intrados.[29]
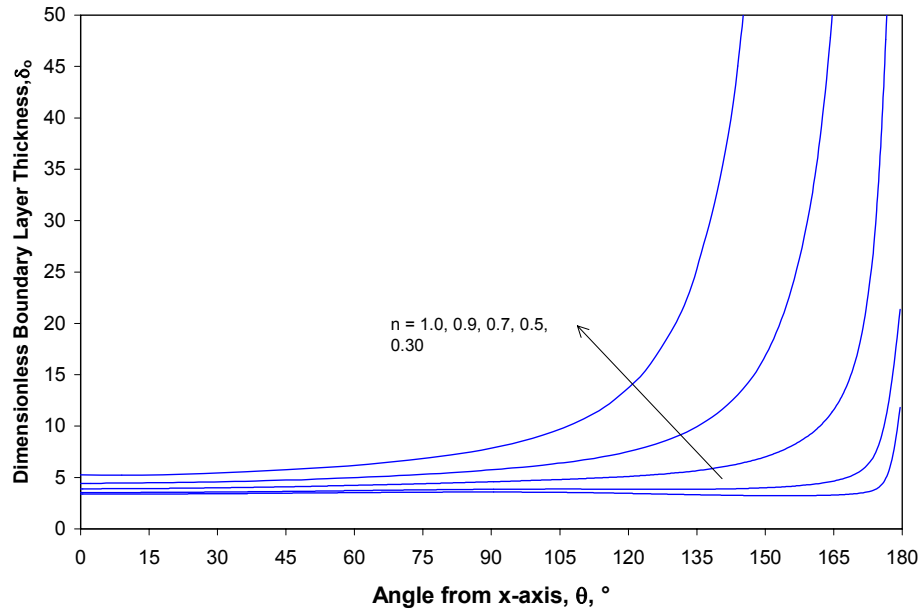
Fig. 3.3—Dimensionless boundary layer thickness, δ_o.

3.4.2   Development of New Friction Factor Correlation

The Fanning friction factor, f, can be defined as[3-5]:

$$ f = \frac{\left[-\left(\dfrac{\partial p}{R \partial \phi}\right)\right](2a)}{4\left(\dfrac{1}{2}\rho v_m^2\right)} \quad\text{...} \quad (3.59) $$

The pressure gradient $(\partial p / \partial \phi)$ is related to the flow field through Eq. (3.32). The following equation can be derived from Eqs. (3.59) and (3.32) (see Appendix A):

56
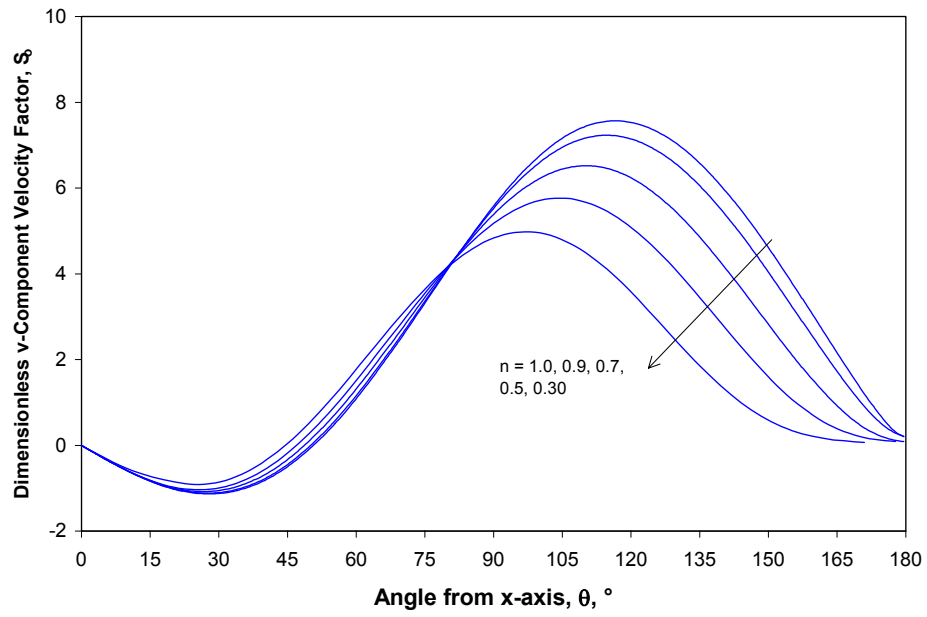
Fig. 3.4—Dimensionless v-velocity component factor, S_o.
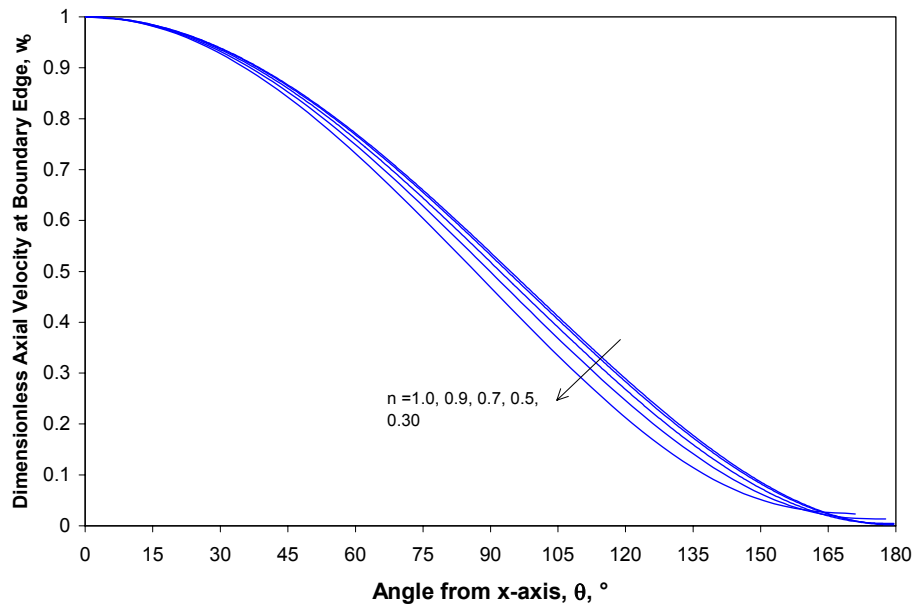
Fig. 3.5—Dimensionless axial velocity at the outer edge of the boundary layer, w_o.
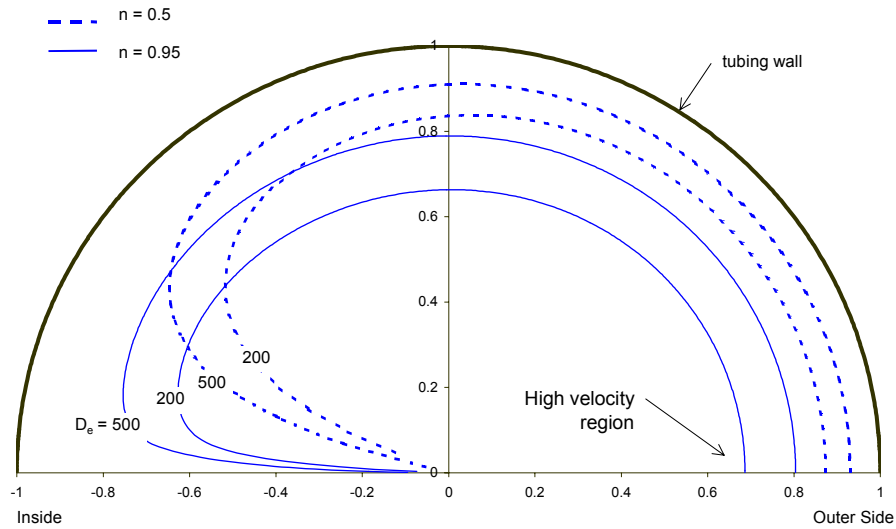
Fig. 3.6—Effects of flow behavior index and Dean number on the profiles of the boundary layer thickness.

$$f = 2^{\frac{n}{n+1}} \alpha D_e^{-1/(n+1)} \left(\frac{a}{R}\right)^{1/2} \left(\frac{v_m}{w_{10}}\right)^{-\frac{3n}{n+1}} , \dotfill (3.60)$$

where α is determined from Eq. (3.53).

Therefore, if (v_m/w_{10}) is known, the Fanning friction factor can be calculated. In fact, (v_m/w_{10}) can be determined from the numerical solution of fluid velocities and the equation for (v_m/w_{10}) can be derived as following.

The total flow rate, Q, through the tubing cross section can be calculated by integrating velocity in the core region and the boundary layer region:

$$Q = 2\int_{-a}^{a} w_1 \sqrt{a^2 - x^2}\, dx - 2a\int_{0}^{\pi}\int_{0}^{\delta} (w_1 - w)\, d\xi d\theta \dotfill (3.61)$$

The mean axial velocity is expressed as[4]:

$$v_m = \frac{Q}{\pi a^2} = \frac{2}{\pi}\int_0^\pi w_1 \sin^2\theta d\theta - \frac{3}{4\pi a}\int_0^\pi w_1 \delta d\theta \quad\text{...}\ (3.62)$$

This can be written in non-dimensional form as

$$\frac{v_m}{w_{10}} = \frac{2}{\pi}\int_0^\pi w_o \sin^2\theta d\theta - \frac{3}{\pi}2^{-(n+2)/(n+1)}De^{-1/(n+1)}\left(\frac{v_m}{w_{10}}\right)^{(2-n)/(n+1)}\int_0^\pi w_o\delta_o d\theta$$

or

$$\frac{v_m}{w_{10}} = \beta - \gamma De^{-1/(n+1)}\left(\frac{v_m}{w_{10}}\right)^{(2-n)/(1+n)} \quad,\text{...}(3.63)$$

in which

$$\beta = \frac{2}{\pi}\int_0^\pi w_o \sin^2\theta d\theta \quad\text{...}\ (3.64)$$

$$\gamma = \frac{3}{\pi}2^{-(n+2)/(n+1)}\int_0^\pi w_o\delta_o d\theta \quad\text{...}(3.65)$$

Eq. (3.63) indicates that once the flow field (w_o, δ_o, and S_o) are solved, the term (v_m/w_{10}) can be determined for a given Dean number, D_e, since β and γ can be calculated from the numerical solution. Table 3.1 shows the solutions of (v_m/w_{10}) for various D_e and n values.

Based on Table 3.1, the following empirical correlation can be developed:

$$\frac{v_m}{w_{10}} = c_1 + \frac{c_2}{D_e} + c_3 n + \frac{c_4}{D_e^2} + c_5 n^2 + c_6 \frac{n}{D_e} , \dots\dots\dots\dots\dots (3.66)$$

where $c_1 = 0.420946436$, $c_2 = -4.559282473$, $c_3 = 0.215446172$, $c_4 = 146.8544113$, $c_5 = -0.15279169$, and $c_6 = -4.409221412$.

Table 3.1—Values of (v_m/w_{10}) Calculated Based on Numerical Solutions

D_e	Flow Behavior Index							
	0.25	0.3	0.35	0.4	0.45	0.5	0.55	0.6
50	0.39843	0.40824	0.41192	0.41455	0.41589	0.41584	0.41428	0.41163
100	0.42284	0.43235	0.43662	0.43988	0.44206	0.44289	0.44256	0.44122
150	0.43308	0.44253	0.44717	0.45082	0.45347	0.45482	0.45516	0.45455
200	0.43886	0.44832	0.45321	0.45714	0.46012	0.46182	0.46261	0.46248
250	0.44262	0.45211	0.45719	0.46132	0.46455	0.46651	0.46763	0.46785
300	0.44529	0.45481	0.46004	0.46434	0.46775	0.46992	0.47129	0.47179
350	0.44729	0.45684	0.46220	0.46663	0.47020	0.47252	0.47410	0.47483
400	0.44885	0.45843	0.46390	0.46843	0.47213	0.47459	0.47635	0.47725
450	0.45011	0.45971	0.46527	0.46990	0.47371	0.47629	0.47819	0.47925
500	0.45114	0.46077	0.46641	0.47112	0.47502	0.47770	0.47973	0.48092
550	0.45201	0.46167	0.46737	0.47215	0.47614	0.47891	0.48104	0.48236
600	0.45275	0.46243	0.46819	0.47304	0.47710	0.47995	0.48218	0.48360
650	0.45339	0.46309	0.46891	0.47381	0.47794	0.48086	0.48317	0.48468

Table 3.1—Values of (v_m/w_{10}) Calculated Based on Numerical Solutions (Continued)

D_e	Flow Behavior Index							
	0.65	0.7	0.75	0.8	0.85	0.9	0.95	1
50	0.40788	0.40366	0.39835	0.39269	0.38652	0.38001	0.37311	0.36591
100	0.43893	0.43611	0.43238	0.42824	0.42361	0.41859	0.41318	0.40742
150	0.45307	0.45101	0.44817	0.44487	0.44109	0.43692	0.43235	0.42740
200	0.46154	0.46000	0.45774	0.45501	0.45180	0.44819	0.44419	0.43980
250	0.46731	0.46614	0.46431	0.46200	0.45923	0.45604	0.45246	0.44847
300	0.47155	0.47068	0.46918	0.46720	0.46476	0.46190	0.45866	0.45499
350	0.47483	0.47420	0.47298	0.47126	0.46909	0.46650	0.46352	0.46013
400	0.47746	0.47703	0.47603	0.47454	0.47259	0.47023	0.46748	0.46431
450	0.47963	0.47937	0.47856	0.47726	0.47551	0.47334	0.47079	0.46780
500	0.48145	0.48134	0.48070	0.47956	0.47798	0.47598	0.47360	0.47078
550	0.48301	0.48303	0.48254	0.48154	0.48011	0.47825	0.47603	0.47336
600	0.48437	0.48450	0.48414	0.48327	0.48197	0.48025	0.47816	0.47562
650	0.48556	0.48580	0.48555	0.48480	0.48362	0.48201	0.48004	0.47762

For each value of n, an α value can be calculated through Eq. (3.53). α can then be correlated with n:

$$\alpha = \left[a' + b' \ln(n)\right]^2, \quad \text{...} \quad (3.67)$$

in which a' = 0.669734019, and b' = -0.203276681.

Let $Y = (v_m/w_{10})$, then the Fanning friction factor can be written as:

$$f = 2^{\frac{n}{n+1}} \alpha D_e^{-1/(n+1)} \left(\frac{a}{R}\right)^{1/2} Y^{-\frac{3n}{n+1}}, \quad \text{...}(3.68)$$

where

$$Y = c_1 + \frac{c_2}{D_e} + c_3 n + \frac{c_4}{D_e^2} + c_5 n^2 + c_6 \frac{n}{D_e} \quad \text{.......................................} \quad (3.69)$$

Since the generalized Reynolds number has been widely used for non-Newtonian fluids, we introduced the following generalized Dean number based on generalized Reynolds number:

$$N_{DNg} = N_{\text{Re}g} (a/R)^{1/2} \quad \text{...} \quad (3.70)$$

It can then be shown that

$$D_e = 2^{3(n-1)} \left(\frac{3n+1}{4n}\right)^n N_{DNg} \quad \text{...} \quad (3.71)$$

where N_{Reg} is the generalized Reynolds number. Therefore, for a power law fluid with the rheological parameters (n and K_p) known, the Fanning friction factor through coiled tubing can easily be calculated using Eqs. (3.67) to (3.71).

3.4.3 Comparison with Previous Work

3.4.3.1 Comparison with the Ito, and Mashelkar and Devarajan Correlations (Newtonian Fluid)

For n = 1 (the Newtonian fluid case), the Ito[4] correlation can serve as a good check

for accuracy of the newly developed correlation.

Ito[4] correlation:

$$ f = 1.654 \left(\frac{a}{R}\right)^{1/2} N_{De}^{-1/2} \left[\left(1 + \frac{1.729}{N_{De}}\right)^{1/2} - \frac{1.315}{N_{De}^{1/2}}\right]^{-3} \quad \text{...} \quad (3.72) $$

Mashelkar and Devarajan Correlation:

$$ f = \left(9.069 - 9.438n + 4.374n^2\right)\left(a/R\right)^{0.5} D_e^{(-0.768+0.122n)} \quad \text{...................................} \quad (3.73) $$

Figs. 3.7 and 3.8 show the plots of Fanning friction factor vs. Dean number (D_e)

for Ito,[4] Mashelkar and Devarajan,[5] and the new correlation of this study at curvature

ratios of 0.01 and 0.03 respectively. It can be seen that there is an excellent agreement

between the new correlation and the Ito correlation. But, the Mashelkar and

Devarajan correlation fails to closely match the Ito correlation. The deviation between

the Mashelkar and Devarajan correlation, and the Ito correlation is 14 to 22%. This

discrepancy was pointed out previously by Hsu and Patankar,[78] and Mujawar and

Rao.[96]

3.4.3.2 Comparison with Mashelkar and Devarajan Correlation (Non-Newtonian Fluid)

Mashelkar and Devarajan[5] correlation is the only available correlation based on the

similar approach of approximate boundary layer analysis for non-Newtonian fluids

and it has been referenced in literature.[105] Therefore, it would be useful to compare our result with this correlation.
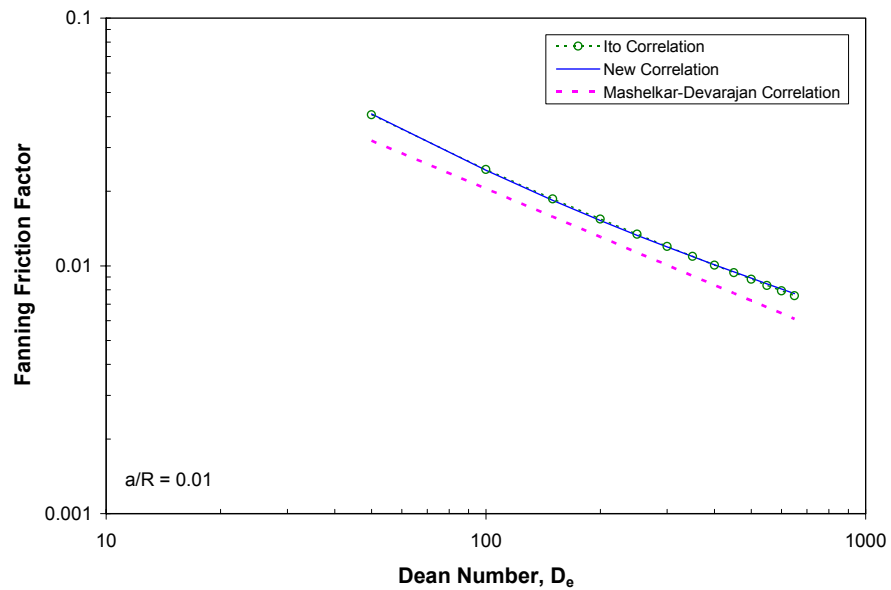
Fig. 3.7—Comparison with Ito correlation (n = 1, a/R = 0.01).
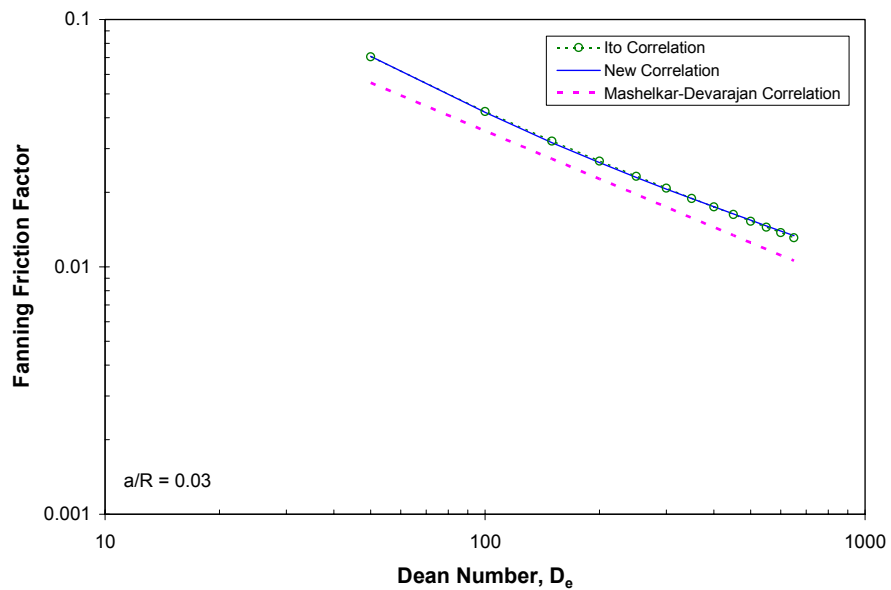
Fig. 3.8—Comparison with Ito correlation (n = 1, a/R = 0.03).

As already pointed out earlier, the Mashelkar and Devarajan[5] correlation could not match the Ito correlation for n = 1. As n decreases, the difference between the new correlation and the Mashelkar and Devarajan correlation becomes larger. Figs. 3.9 and 3.10 compare the two correlations for n = 0.6 at curvature ratios of 0.01 and 0.03 respectively. The increasing discrepancy between the two correlations is due to the fact that the Mashelkar and Devarajan correlation fails to properly describe the effect of the flow behavior index (n), as is shown in Fig. 3.11. Figs. 3.12 and 3.13 show the effect of flow behavior index according to the new correlation for curvature ratios of 0.01 and 0.03 respectively.

Furthermore, in their work, numerical solutions ware obtained only for four n values (n = 1.0, 0.9, 0.75, and 0.5). Since their correlation could not match the Ito correlation even for n = 1, the correlation based on the four n values is questionable.
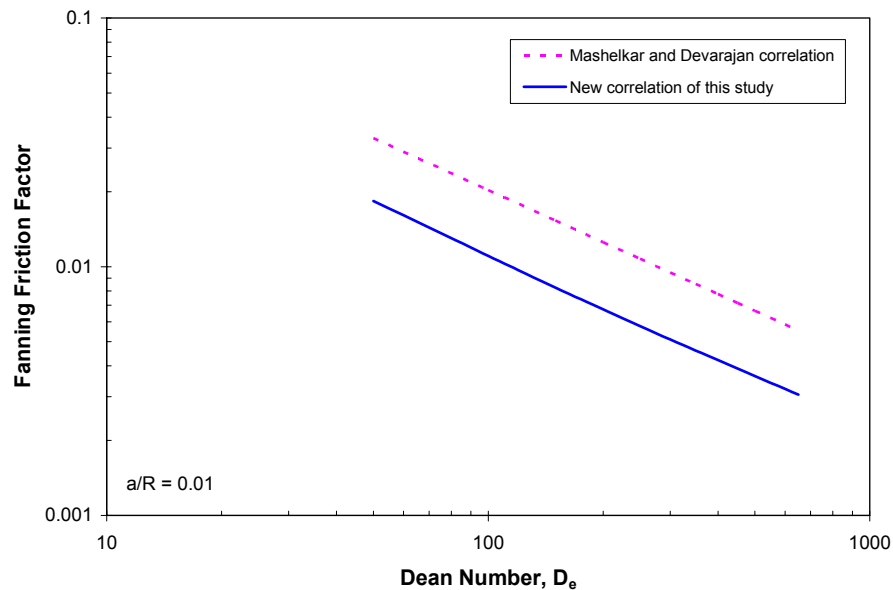
Fig. 3.9—Comparison between the new correlation and the Mashelkar and Devarajan correlation (n = 0.6, a/R = 0.01).
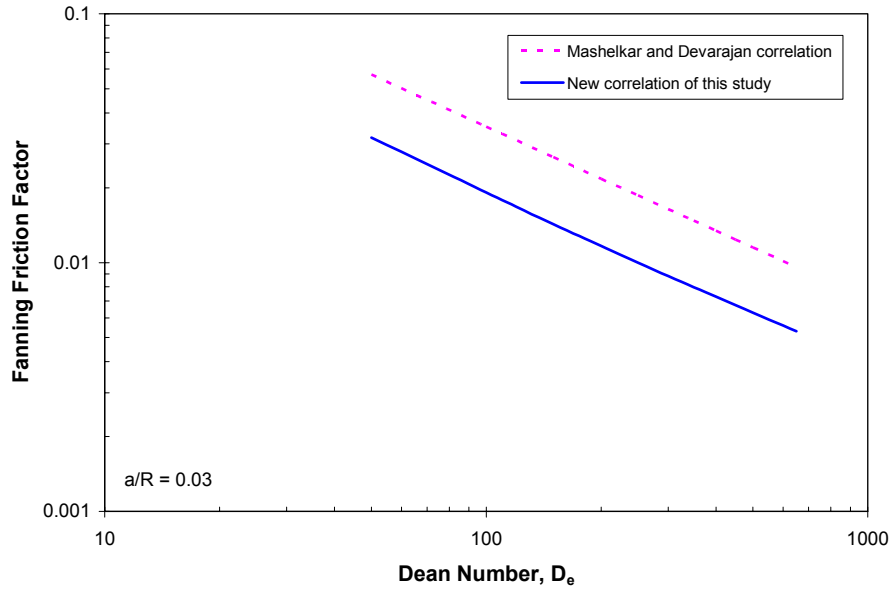
Fig. 3.10—Comparison between the new correlation and the Mashelkar and Devarajan correlation (n = 0.6, a/R = 0.03).
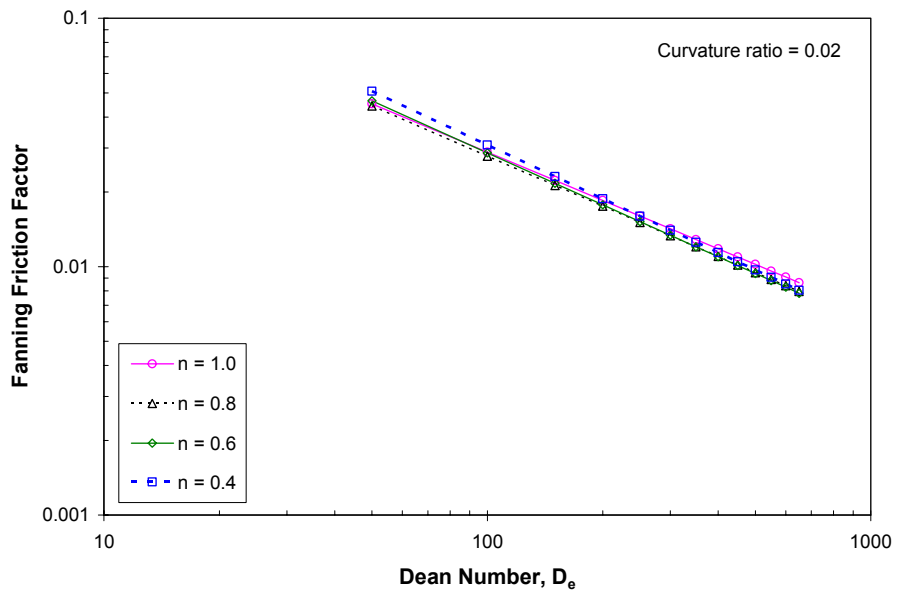
Fig. 3.11—Effect of flow behavior index by Mashelkar and Devarajan correlation.
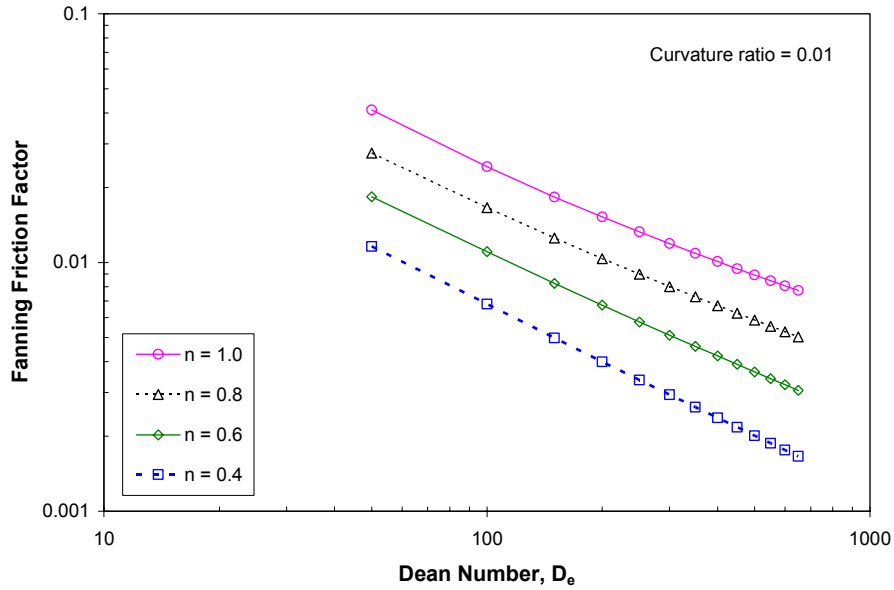
Fig. 3.12—Effect of flow behavior index by the new correlation (a/R = 0.01).
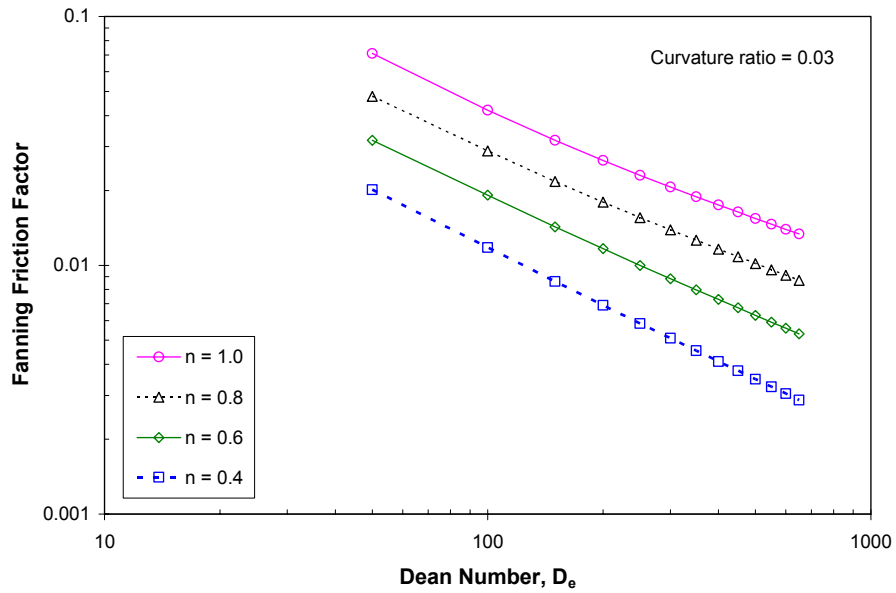
Fig. 3.13—Effect of flow behavior index by the new correlation (a/R = 0.03).

Our new correlation not only matches the Ito correlation for n = 1, but it is also based

on a much wider range of n, i.e., from 0.25 to 1.0 in steps of 0.05.

66

3.4.4 Comparison with Experimental Data

Experiments of fluid flow in coiled tubing have been conducted using a full-scale coiled tubing flow loop used for a joint industry project at the University of Oklahoma. The flow loop includes several reels of 1-in., 1-1/2-in., and 2-3/8-in. coiled tubing strings and straight tubing sections. The curvature ratio values for these coiled tubing reels are 0.0113, 0.0165, 0.0169, and 0.0185. Fluids tested are typical drilling, completion, and stimulation fluids used in the industry. These fluids are generally non-Newtonian and can be described by a power law model within the flow conditions investigated. The primary measured data include the flow variables such as frictional pressure drops across different tubing sections at various flow rates. More detailed description of the experimental facility and experimental procedures is discussed in Chapters 5 and 6. Although the flow rates in the majority of the tests were high enough to result in turbulent flow, the following test data can be used to evaluate the newly developed friction factor correlation for laminar flow in coiled tubing.

Example 1—Laminar Flow of 60 lb/Mgal HPG in 2-3/8-in. CT. A 60 lb/Mgal HPG (hydroxypropyl guar) gel was pumped through the 1000 ft long and 2-3/8-in. diameter coiled tubing reel to investigate the laminar flow behavior of non-Newtonian fluid in coiled tubing. Rheological properties were evaluated using a Model 35 Fann viscometer: $n = 0.314$ and $K_p = 0.1131$ $lb_f s^n/ft^2$. The experimental data and the predictions by our new correlation [Eq. (3.68)] are shown in Fig. 3.14. From the Srinivasan correlation [Eq. (2.13)], the critical Reynolds number for

Newtonian fluid in this coil is 5528. The critical Reynolds number for non-Newtonian fluids should be higher than this value.
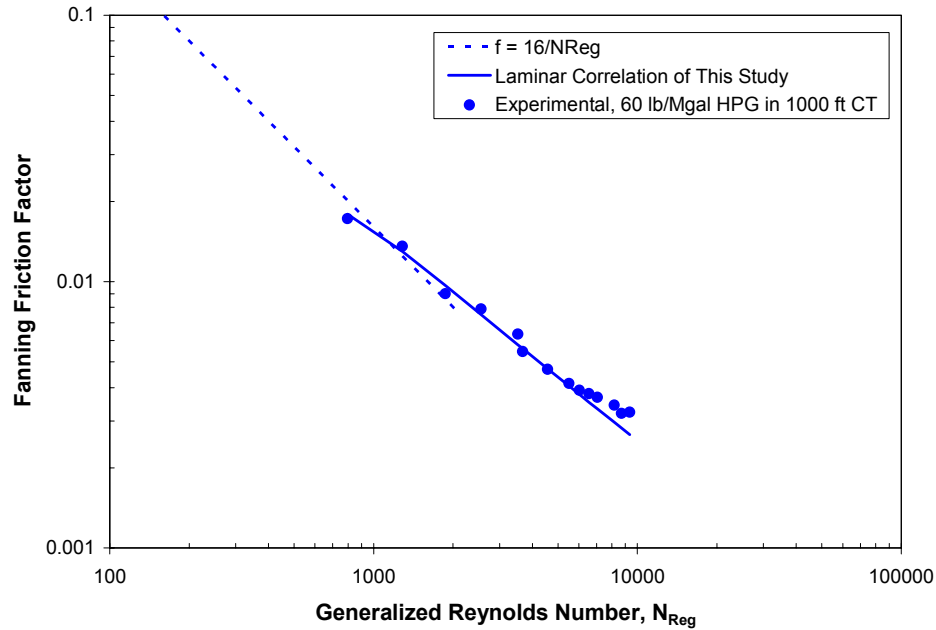
Fig. 3.14—Friction factor of 60 lb/Mgal HPG in 1000 ft, 2-3/8-in. OD coiled tubing.

It can be seen that the new laminar flow correlation of this study matches the experimental data reasonably well for the generalized Reynolds number up to 6000, with absolute deviation changing from 0.4% to 8.7% and an average absolute deviation of 4.3%. At generalized Reynolds number greater than 6000, the correlation begins to deviate from the experimental data points. As generalized Reynolds number increases from 6558 to 9349, the friction factor predicted from the correlation is 7.1 to 17.4% less than the experimental data. Considering the high accuracies of the pressure transducers and the flowmeters, as will be discussed in Chapter 5, the random errors in measurement are much smaller than the deviations observed above

(7.1 – 17.4%). Therefore, the reason for the deviation of the correlation with the friction factor data at Reynolds number greater than 6000 is most probably because the flow may have been in turbulent flow regime. Since one basic assumption of the boundary layer approximation approach is that the Dean number should be large, the new correlation is not recommended for $N_{DNg} < 100$. Fortunately, the flow conditions for field applications of coiled tubing would generally satisfy the requirement of large Dean number.

Example 2—30 and 40 lb/Mgal Guar Fluids in 2-3/8-in. Coiled Tubing. Fig. 3.15 shows the plots of Fanning friction factor vs. generalized Reynolds number for guar solution in 2-3/8-in. coiled tubing. It compares the experimental data and the predictions by the new correlation and by the Mashelkar and Devarajan correlation. The rheological properties of the guar fluids are: $n = 0.432$, $K_p = 0.0243$ $lb_f s^n/ft^2$ for 40 lb/Mgal guar solution, and $n = 0.527$, $K_p = 0.0079$ $lb_f s^n/ft^2$ for 30 lb/Mgal guar solution. It can be observed that there is a good agreement between the experimental data and the predictions by the new correlation of this study. It is found that the deviations between the predicted and the experimental friction factors are generally within 10%. Unfortunately, the Mashelkar and Devarajan correlation is much higher than the experimental data in this case.

Example 3—Oil-Based Drilling Mud in 2-3/8-in. Coiled Tubing. Fig. 3.16 compares the experimental data of an oil-based drilling mud in 2-3/8-in. coiled tubing with predictions by the two correlations. The power law parameters of this oil mud are: $n = 0.689$, $K_p = 0.0106$ $lb_f s^n/ft^2$. It is shown that the new correlation is very close

to the experimental data, only underestimating the friction factor by about 8%. The

Mashelkar and Devarajan correlation overpredicts the friction factor by about 37%.
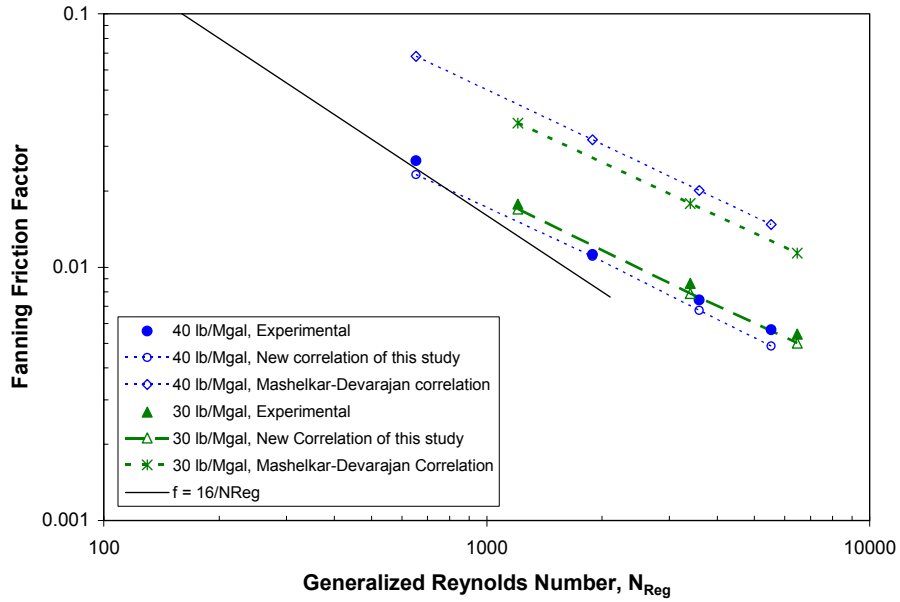
Fig. 3.15—Comparison between experimental data and correlations (30 and 40 lb/Mgal guar in 1000 ft 2-3/8-in. coiled tubing).
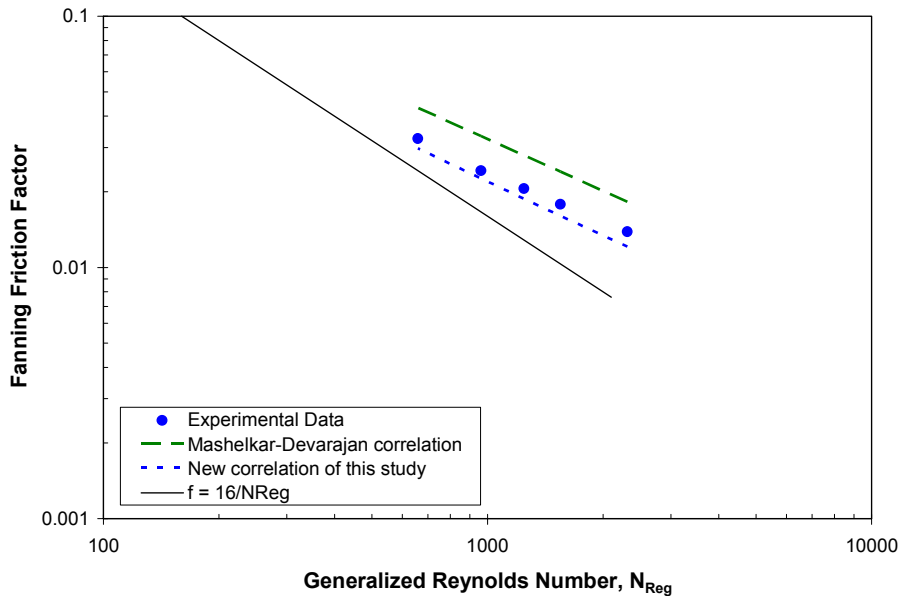
Fig. 3.16—Comparison between experimental data and correlations (oil-based drilling mud in 1000 ft 2-3/8-in. coiled tubing).

3.5   Summary

The boundary layer approximation method has been successfully applied to the theoretical and numerical analysis of non-Newtonian fluid flow in coiled tubing under laminar flow conditions and large Dean numbers. A new friction factor correlation of non-Newtonian laminar flow in coiled tubing has been developed based on extensive numerical analysis. The new correlation is expressed in an empirical form of Fanning friction factor as function of generalized Dean number, curvature ratio, and flow behavior index. There has been an excellent agreement between the new friction factor correlation and the experimental data obtained from experiments conducted in the full-scale coiled tubing flow loop. The Mashelkar and Devarajan correlation was also evaluated by comparing it with the experimental data, Ito correlation for $n = 1$ (Newtonian fluid), and the new correlation of this study. It was found that Mashelkar and Devarajan correlation failed to give any acceptable agreement with either the experimental data or the Ito correlation.

The present work not only corrects the errors in the Mashelkar and Devarajan correlation, but also extends the range of applicability of the new correlation to fluids with wider range of flow behavior index—$n = 0.25$ to 1.0 which would cover most fluids used in coiled tubing operations in the oil and gas industry.

CHAPTER 4

THEORETICAL ANALYSIS OF TURBULENT
FLOW OF POWER-LAW FLUID IN COILED
TUBING

4.1   Introduction

Among the various approaches of investigating fluid flow in coiled pipes, the boundary layer approximation method is especially useful for flow at high Dean number. This is because the effect of secondary flow at high-Dean number is largely confined in a thin boundary layer adjacent to the pipe wall. Under this condition, the tubing cross-section can be divided into two regions: the central inviscid core and the thin viscous boundary layer. This leads to much simplified flow equations for high-Dean number flows in curved geometry. This approach has been used by a number of researchers, for example, by Adler,[59] Barua,[3] Mori and Nakayama,[84] and Ito[4,83] for Newtonian fluids and by Mashelkar and Devarajan[5,86] for non-Newtonian fluids.

In the previous chapter, we applied the method of boundary layer approximation analysis and solved the laminar flow problem of a power law fluid in coiled tubing by extending the work of Mashelkar and Devarajan to fluids with wider range of flow behavior index. An empirical correlation of friction factor was obtained based on the theoretical analysis and numerical solutions. In fact, the same approach can be applied to the analysis of non-Newtonian turbulent flow in coiled tubing. First, the

flow model in coiled tubing was simplified and the tubing cross section was divided into inviscid core and a thin boundary layer. Then, the flow equations for the core and the boundary layer were simplified through order of magnitude approximations. The simplified momentum equations for the boundary layer were then integrated over the boundary layer thickness to obtain equations of momentum integrals. After assuming proper forms of velocity profiles for flow in the boundary layer, the equations of momentum integrals were converted to ordinary differential equations which could be solved numerically to get the solutions of velocity field. Similar to the case of non-Newtonian laminar flow in coiled pipe, the Fanning friction factor correlation was then obtained. The major contribution of this study is the extension of the work of Mashelkar and Devarajan to wider range of flow behavior index of power law model and the development of the new friction factor correlation for non-Newtonian turbulent flow in coiled tubing.

4.2   Mathematical Formulation

4.2.1   Coordinate System and Governing Equations

The difficulty in theoretical analysis of coiled tubing flow is mainly due to the complex flow geometry. For typical coiled tubing reels, the torsion which can be defined as the ratio of $h/(2\pi R)$ (h is the pitch of the coil and R is the radius of the reel drum) is small and its effect on the friction pressure can be neglected.[70,73] Therefore, the toroidal coordinate system, as shown in Fig. 4.1, can be used to represent the flow geometry of fluid flow in coiled tubing. This significantly reduces the complexity of

the problem. Here, u, v, and w are velocity components in the directions of r, θ, and φ respectively. "a" and "R" are the radii of the coiled tubing and coiled tubing reel. The ratio of a/R is the curvature ratio. For coiled tubing reels used in the oil and gas industry, the curvature ratio is in the order of 10^{-2} and therefore can be considered small.
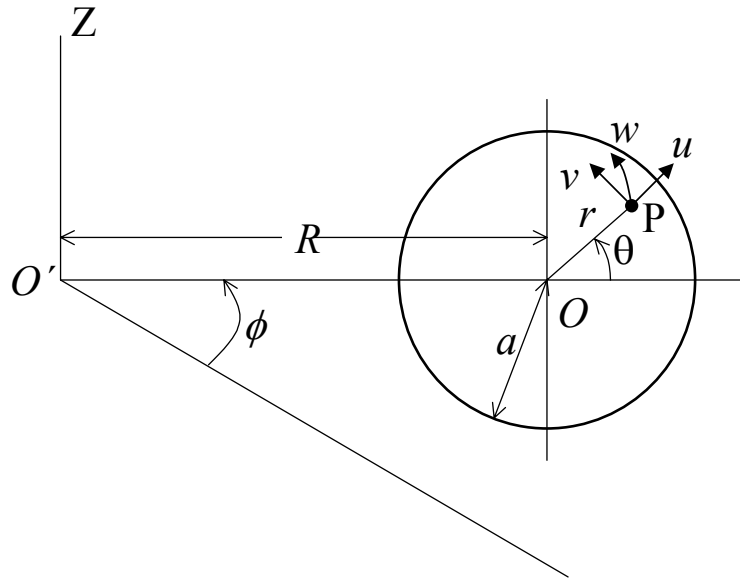
Fig. 4.1—Toroidal coordinate system.

In this study, we only consider the steady and fully-developed turbulent flow of a power law fluid in coiled tubing. The time-averaged equations of motion and continuity are as follows[86]:

$$\rho\left(\bar{u}\frac{\partial\bar{u}}{\partial r}+\frac{\bar{v}}{r}\frac{\partial\bar{u}}{\partial\theta}-\frac{\bar{v}^2}{r}-\frac{\bar{w}^2\cos\theta}{R}\right)=-\frac{\partial\bar{p}}{\partial r}-\left(\frac{\partial\bar{\tau}_{rr}}{\partial r}+\frac{1}{r}\frac{\partial\bar{\tau}_{r\theta}}{\partial\theta}+\frac{\bar{\tau}_{rr}-\bar{\tau}_{\theta\theta}}{r}\right)\quad\text{......................(4.1)}$$

$$\rho\left(\bar{u}\frac{\partial\bar{v}}{\partial r}+\frac{\bar{v}}{r}\frac{\partial\bar{v}}{\partial\theta}+\frac{\overline{uv}}{r}+\frac{\bar{w}^2\sin\theta}{R}\right)=-\frac{1}{r}\frac{\partial\bar{p}}{\partial\theta}-\left(\frac{\partial\bar{\tau}_{r\theta}}{\partial r}+\frac{1}{r}\frac{\partial\bar{\tau}_{\theta\theta}}{\partial\theta}+\frac{2}{r}\bar{\tau}_{r\theta}\right)\quad\text{..................(4.2)}$$

74

$$\rho\left(\bar{u}\frac{\partial \overline{w}}{\partial r} + \frac{\bar{v}}{r}\frac{\partial \overline{w}}{\partial \theta}\right) = -\frac{1}{R}\frac{\partial \overline{p}}{\partial \phi} - \left(\frac{\partial \bar{\tau}_{r\phi}}{\partial r} + \frac{1}{r}\frac{\partial \bar{\tau}_{\theta\phi}}{\partial \theta} + \frac{2\bar{\tau}_{r\phi}\sin\theta}{R}\right) \quad\dotfill(4.3)$$

$$\frac{\partial \bar{u}}{\partial r} + \frac{\bar{u}}{r} + \frac{1}{r}\frac{\partial \bar{v}}{\partial \theta} = 0 \quad\dotfill(4.4)$$

where ρ is fluid density, $\overline{p}$ is pressure, and $\bar{\tau}_{rr}$, $\bar{\tau}_{\theta\theta}$, $\bar{\tau}_{r\theta}$, $\bar{\tau}_{r\phi}$, and $\bar{\tau}_{\theta\phi}$ are stress terms. The index convention of the stresses is the same as in Chapter 3. Since the flow is steady and fully-developed, the axial pressure gradient is constant, i.e.,

$$-\frac{\partial \overline{p}}{\partial \phi} = C \quad\dotfill(4.5)$$

The tubing cross-section is divided into two regions: the central inviscid core and the thin boundary layer, as shown in Fig. 4.2. In the following, simplified equations for each region are obtained.
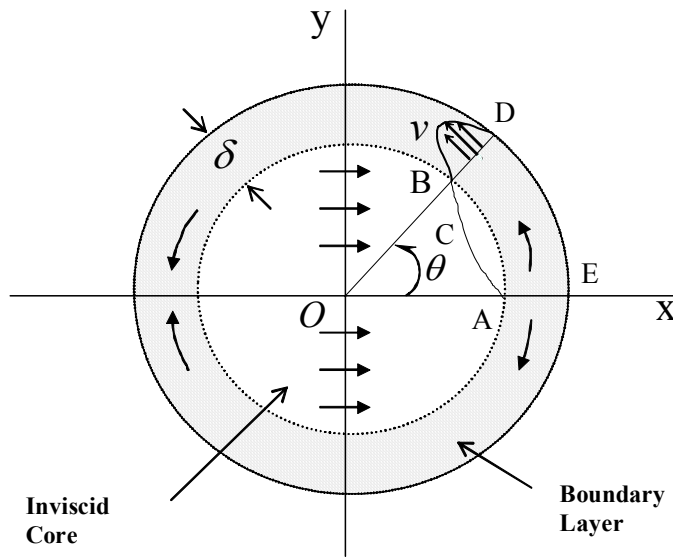
Fig. 4.2—Flow model showing the inviscid core and boundary layer.

4.2.2 Flow Equations for the Inviscid Core

In the central region of the coiled tubing cross section, the axial velocity distribution is more uniform than in the boundary layer. The secondary velocity components, $\bar{u}$ and $\bar{v}$, are small compared with the axial component $\bar{w}$, i.e., $\bar{u}$, $\bar{v} \ll \bar{w}$. Then, by neglecting the viscous effect, Eqs. (4.1) to (4.3) reduce to:

$$-\frac{\bar{w}^2 \cos\theta}{R} = -\frac{1}{\rho}\frac{\partial \bar{p}}{\partial r} \quad\text{..(4.6)}$$

$$\frac{\bar{w}^2 \sin\theta}{R} = -\frac{1}{\rho r}\frac{\partial \bar{p}}{\partial \theta} \quad\text{..(4.7)}$$

$$\bar{u}\frac{\partial \bar{w}}{\partial r} + \frac{\bar{v}}{r}\frac{\partial \bar{w}}{\partial \theta} = \frac{C}{\rho R} \quad\text{..(4.8)}$$

By eliminating $\bar{p}$ from Eqs. (4.6) and (4.7), we get

$$\sin\theta\frac{\partial \bar{w}^2}{\partial r} + \frac{\cos\theta}{r}\frac{\partial \bar{w}^2}{\partial \theta} = 0 \quad\text{..(4.9)}$$

For the coordinate systems shown in Fig. 4.1 and Fig. 4.2, the following relationship can be derived:

$$\sin\theta\frac{\partial}{\partial r} + \frac{\cos\theta}{r}\frac{\partial}{\partial \theta} = \frac{\partial}{\partial y} \quad\text{..(4.10)}$$

Thus, Eq. (4.9) can be written as

$$\frac{\partial \bar{w}}{\partial y} = 0 \quad\text{..(4.11)}$$

which indicates that $\bar{w}$ can be an arbitrary function of x, i.e.,

$$\overline{w} = F(x) \dotfill (4.12)$$

We can write

$$\overline{w} = A + Bx$$

or

$$\overline{w} = A + Br\cos\theta \dotfill (4.13)$$

The constants A and B in Eq. (4.13) will be determined later by considering the continuity between the core region and the boundary layer.

4.2.3   Flow Equations for the Boundary Layer

In the boundary layer, the axial velocity component $\overline{w}$ reduces drastically from a value ($\overline{w}_1$) at the boundary layer edge to zero at the tubing wall (no-slip boundary is assumed). Therefore, the angular velocity component $\overline{v}$ becomes comparable with $\overline{w}$. Similar to the case of laminar flow, order of magnitude analysis is made as the following:

$$\overline{u} \sim O(\delta); \ \overline{v}, \overline{w} \sim O(1); \ \frac{\partial}{\partial r} \sim O(\delta^{-1}); \ \frac{\partial}{\partial \theta}, \frac{\partial}{\partial \phi} \sim O(1) \dotfill (4.14)$$

where δ is the boundary layer thickness.

Eqs. (4.1) to (4.4) then reduce to[86,104]:

$$\frac{\overline{v}^2}{a} + \frac{\overline{w}^2 \cos\theta}{R} = \frac{1}{\rho} \frac{\partial \overline{p}}{\partial r} \dotfill (4.15)$$

$$\overline{u}\frac{\partial \overline{v}}{\partial r} + \frac{\overline{v}}{a}\frac{\partial \overline{v}}{\partial \theta} + \frac{\overline{w}^2 \sin\theta}{R} = -\frac{1}{\rho a}\frac{\partial \overline{p}}{\partial \theta} - \frac{1}{\rho}\frac{\partial \overline{\tau}_{r\theta}}{\partial r} \dotfill (4.16)$$

77

$$\bar{u}\frac{\partial \bar{w}}{\partial r}+\frac{\bar{v}}{a}\frac{\partial \bar{w}}{\partial \theta}=-\frac{1}{\rho R}\frac{\partial \bar{p}}{\partial \phi}-\frac{1}{\rho}\frac{\partial \bar{\tau}_{r\phi}}{\partial r} \quad\text{...(4.17)}$$

$$\frac{\partial \bar{u}}{\partial r}+\frac{1}{a}\frac{\partial \bar{v}}{\partial \theta}=0 \quad\text{..(4.18)}$$

Next, Eqs. (4.16) and (4.17) can be simplified by considering the three pressure gradient terms ($\partial\bar{p}/\partial r$, $\partial\bar{p}/\partial\theta$, and $\partial\bar{p}/\partial\phi$). Eq. (4.15) indicates that the pressure variation over the boundary layer is only of order δ, and therefore, can be neglected. The pressure inside the boundary layer can be assumed to be equal to the boundary layer edge pressure which can be determined from the core flow equation:

$$\frac{\partial \bar{p}}{\partial \theta}=-\rho\frac{a}{R}\bar{w}_1^2\sin\theta \quad\text{..(4.19)}$$

Eq. (4.16) then becomes

$$\bar{u}\frac{\partial \bar{v}}{\partial r}+\frac{\bar{v}}{a}\frac{\partial \bar{v}}{\partial \theta}=\frac{\bar{w}_1^2-\bar{w}^2}{R}\sin\theta-\frac{1}{\rho}\frac{\partial \bar{\tau}_{r\theta}}{\partial r} \quad\text{...(4.20)}$$

Through further order of magnitude analysis,[4,86,104] Eq. (4.17) can be simplified as

$$\bar{u}\frac{\partial \bar{w}}{\partial r}+\frac{\bar{v}}{a}\frac{\partial \bar{w}}{\partial \theta}=-\frac{1}{\rho}\frac{\partial \bar{\tau}_{r\phi}}{\partial r} \quad\text{...(4.21)}$$

4.2.4   Continuity of the Secondary Flow

According to Eq. (4.4), we can introduce a stream function Ψ such that

$$\bar{u}=\frac{1}{r}\frac{\partial \Psi}{\partial \theta} \quad\text{..(4.22)}$$

$$\bar{v}=-\frac{\partial \Psi}{\partial r} \quad\text{..(4.23)}$$

78

Inserting Eqs. (4.13), (4.22), and (4.23) into Eq. (4.8) and also noting that x = rcosθ, we have

$$\Psi = \frac{C}{\rho RB} r \sin\theta \quad\text{...(4.24)}$$

In Fig. 4.2, let A and B be two points on the outer edge of the boundary layer. Using Eq. (4.24), the flux across a curve ACB drawn outside the boundary layer is:

$$\int_A^B d\Psi = \Psi_B - \Psi_A = \int_0^\delta \bar{v}d\xi \quad\text{......................................(4.25)}$$

or

$$\frac{C}{\rho RB} r_B \sin\theta = \int_0^\delta \bar{v}d\xi \quad\text{...(4.26)}$$

where ξ = a – r and δ is the boundary layer thickness.

Since $r_B = a - \delta \approx a$, it follows that

$$B = \frac{Ca \sin\theta}{\rho R \int_0^\delta \bar{v}d\xi} \cdot \quad\text{...(4.27)}$$

and over the entire cross-section,

$$B = \frac{Ca}{\rho R} \frac{1}{\pi} \int_0^\pi \frac{\sin\theta d\theta}{\int_0^\delta \bar{v}d\xi} \quad\text{...(4.28)}$$

Eq. (4.28) establishes the link between the boundary layer flow and the core flow. Also note that at r = 0, $\overline{w}$ = v_m. Hence, from Eq. (4.13), A = v_m. Thus, the constants A and B can be determined.

4.2.4.1 Equations of Boundary Layer Momentum Integrals

The following boundary conditions can be applied to the boundary layer:

At r = a:

$$\overline{u} = \overline{v} = \overline{w} = 0 \quad\text{...(4.29)}$$

At r = a - δ:

$$\overline{v}_1 = 0, \left(\frac{\partial \overline{v}}{\partial r}\right)_1 = 0, \quad\text{..(4.30)}$$

$$\overline{w} = \overline{w}_1, \left(\frac{\partial \overline{w}}{\partial r}\right)_1 = 0, \quad\text{..(4.31)}$$

where the subscript 1 refers to the boundary layer edge. Integrating Eqs. (4.20) and (4.21) over the boundary layer thickness (δ) and making use of Eq. (4.18), we have

$$\frac{1}{a}\frac{d}{d\theta}\int_0^\delta \overline{v}^2 d\xi = \frac{\sin\theta}{R}\int_0^\delta \left(\overline{w}_1^2 - \overline{w}^2\right)d\xi - \frac{1}{\rho}\overline{\tau}_{r\theta}\big|_{\xi=0} \quad\text{..(4.32)}$$

$$-\frac{\overline{w}_1}{a}\frac{d}{d\theta}\int_0^\delta \overline{v}d\xi + \frac{1}{a}\frac{d}{d\theta}\int_0^\delta \left(\overline{v}\overline{w}\right)d\xi = -\frac{1}{\rho}\overline{\tau}_{r\phi}\big|_{\xi=0} \quad\text{..(4.33)}$$

To solve Eqs. (4.32) and (4.33), appropriate velocity distributions for $\overline{v}$ and $\overline{w}$ in the boundary layer are needed. In this aspect, we follow the arguments of

Mashelkar and Deverajan.[86,104] The assumed velocity distributions are as the following:

The axial component is

$$\overline{w} = \overline{w}_1 \left(\frac{\xi}{\delta} \right)^{\frac{\beta n}{2 - \beta(2-n)}} \quad \dots (4.34)$$

The angular component is

$$\overline{v} = D \left(\frac{\xi}{\delta} \right)^{\frac{\beta n}{2 - \beta(2-n)}} (1 - \xi/\delta), \dots (4.35)$$

where $\overline{w}_1$ is the value of w at the boundary layer edge. D is the amplitude of $\overline{v}$ and here it is called the characteristic angular velocity. β is one of the coefficients of the Dodge and Metzner[106,107] friction factor correlation for turbulent flow in straight pipe:

$$f = \frac{\alpha}{N_{Re,g}^{\beta}}, \dots (4.36)$$

where α and β are functions of flow behavior index of the power law fluid.

The shear stress expressions for $\overline{\tau}_{r\phi}$ and $\overline{\tau}_{r\theta}$ in Eqs. (4.32) and (4.33) are simplified as[86,104,107]:

$$\overline{\tau}_{r\theta} = \frac{\alpha(0.817)^{2-\beta(2-n)}}{2^{\beta n+1}} \gamma_1^{\beta} \rho^{1-\beta} \delta^{-\beta n} U^{2-\beta(2-n)} \frac{D}{\sqrt{D^2 + \overline{w}_1^2}}, \dots (4.37)$$

$$\overline{\tau}_{r\phi} = \frac{\alpha(0.817)^{2-\beta(2-n)}}{2^{\beta n+1}} \gamma_1^{\beta} \rho^{1-\beta} \delta^{-\beta n} U^{2-\beta(2-n)} \frac{\overline{w}_1}{\sqrt{D^2 + \overline{w}_1^2}}, \dots (4.38)$$

where

81

$$U = \sqrt{D^2 + \overline{w}_1^2}$$ ....(4.39)

Inserting Eqs. (4.34), (4.35), (4.37), and (4.38) into the boundary layer momentum integral equations [Eqs. (4.32) and (4.33)] and integrating, we get

$$f_1(n)\frac{\partial}{\partial\theta}\left[D^2\delta\right] = \left[1 - f_2(n)\right]\delta\overline{w}_1^2\,\frac{a}{R}\sin\theta - f_5(n)\frac{K^\beta}{\rho^\beta}a\delta^{-\beta n}D\overline{w}_1^{1-\beta(2-n)}$$ ....(4.40)

$$f_3(n)\frac{\partial}{\partial\theta}\left[\delta D\overline{w}_1\right] - f_4(n)\overline{w}_1\,\frac{\partial}{\partial\theta}\left[D\delta\right] = -f_5(n)\frac{K^\beta}{\rho^\beta}a\delta^{-\beta n}\overline{w}_1^{1-\beta(2-n)},$$ ....(4.41)

where f₁(n), f₂(n), f₃(n), f₄(n), and f₅(n) are functions of flow behavior index n and are given as the following:

$$f_1(n) = \frac{[2-\beta(2-n)]\left[4 - 8\beta + 4\beta n + 4\beta^2 - 4\beta^2 n + \beta^2 n^2\right]}{2(3\beta n - 2\beta + 2)(\beta n - \beta + 1)(8\beta n - 6\beta + 6)}$$ ....(4.42)

$$f_2(n) = \frac{[2-\beta(2-n)]}{[2+\beta(3n-2)]}$$ ....(4.43)

$$f_3(n) = \frac{[2-\beta(2-n)][2+\beta(n-2)]}{4[2+\beta(3n-2)][1+\beta(n-1)]}$$ ....(4.44)

$$f_4(n) = \frac{[2-\beta(2-n)][2+\beta(n-2)]}{[2+2\beta(n-1)][4+\beta(3n-4)]}$$ ....(4.45)

$$f_5(n) = \frac{\alpha(0.817)^{2-\beta(2-n)}}{2^{\beta n+1}}\left[8^{n-1}\left(\frac{3n+1}{4n}\right)^n\right]^\beta$$ ....(4.46)

Note that from Eq. (4.13), the axial velocity component at the boundary layer edge, $\overline{w}_1$, can be written as:

$$\overline{w}_1 = v_m + Ba\cos\theta$$ ....(4.47)

Then, the three equations [Eqs. (4.40), (4.41), and (4.47)] provide the required equations for the three unknowns—δ, D, and $\overline{w}_1$. Therefore, the problem becomes closed.

4.2.5 Non-Dimensionalization

Eqs. (4.40), (4.41), and (4.47) can be written in non-dimensional form by defining the following dimensionless variables:

$$\delta_o = \frac{\delta}{a\left[N^o_{\mathrm{Reg}}\left(a/R\right)^{1/2\beta}\right]^{\frac{\beta}{\beta n+1}}} \quad \text{...(4.48)}$$

$$D_o = \frac{D}{v_m\sqrt{a/R}} \quad \text{...(4.49)}$$

$$w_o = \frac{\overline{w}_1}{v_m}, \quad \text{...(4.50)}$$

where

$$N^o_{\mathrm{Reg}} = \frac{(2a)^n v_m^{2-n}\rho}{K}. \quad \text{...(4.51)}$$

Eqs. (4.40), (4.41), and (4.47) then become

$$f_1(n)\frac{\partial}{\partial\theta}\left[D_o^2\delta_o\right] = \left[1 - f_2(n)\right]\delta_o w_o^2 \sin\theta - f_5(n)2^{\beta n}\delta_o^{-\beta n}D_o w_o^{1-\beta(2-n)} \quad \text{.........................(4.52)}$$

$$f_3(n)\frac{\partial}{\partial\theta}\left[D_o w_o\delta_o\right] - f_4(n)w_o\frac{\partial}{\partial\theta}\left[D_o\delta_o\right] = -f_5(n)2^{\beta n}\delta_o^{-\beta n}w_o^{1-\beta(2-n)} \quad \text{.............................(4.53)}$$

$$w_o = 1 + \left(\frac{Ba}{v_m}\right)\cos(\theta) \quad \text{...(4.54)}$$

Noting that B is given in Eq. (4.28), it follows that

$$\frac{Ba}{v_m} = \frac{\alpha^*}{f_4(n)} \int_0^\pi \frac{\sin\theta \, d\theta}{D_o \quad \delta_o} \quad \dots\dots\dots\dots\dots\dots\dots\dots\dots\dots\dots\dots\dots\dots\dots\dots\dots\dots\dots\dots\text{(4.55)}$$

$$\alpha^* = f_5(n) 2^{\beta n + 1} \pi^{-1} \int_0^\pi w_o^{2-\beta(2-n)} \delta_o^{-\beta n} d\theta \quad \dots\dots\dots\dots\dots\dots\dots\dots\dots\dots\text{(4.56)}$$

4.3   Solution Procedure

Eqs. (4.52) to (4.54) completely defined the flow field for the boundary layer. The task now becomes solving the coupled, non-linear differential equations [Eqs. (4.52) to (4.54)] for solutions of δ_o, D_o, and w_o. This can be accomplished by integrating Eqs. (4.52) and (4.53) with angle θ in the range of $0 - \pi$. In order to start the numerical integration, the initial condition ($\theta = 0$) has to be determined. Ito's approach[4,83] is followed for this purpose. In the close neighborhood of $\theta = 0$, δ_o, D_o, and w_o can be expanded as the following:

$$\delta_o = \delta_{o0}\left(1 + \delta_{o2}\theta^2 + \dots\dots\right) \quad \dots\dots\dots\dots\dots\dots\dots\dots\dots\dots\dots\dots\dots\dots\dots\text{(4.57)}$$

$$D_o = D_{o1}\theta\left(1 + D_{o3}\theta^2 + \dots\dots\right) \quad \dots\dots\dots\dots\dots\dots\dots\dots\dots\dots\dots\dots\dots\text{(4.58)}$$

$$w_o = 1 + \frac{Ba}{v_m}\left(1 - \frac{\theta^2}{2!} + \frac{\theta^4}{4!} - \dots\dots\right) \quad \dots\dots\dots\dots\dots\dots\dots\dots\dots\dots\dots\text{(4.59)}$$

Inserting Eqs. (4.57) to (4.59) into Eqs. (4.52) and (4.53) and equating the terms of equal powers of θ, we have

$$\delta_{o0} = [f_5(n)]^{1/(\beta n+1)} 2^{\frac{\beta n}{\beta n+1}} \left\{ \frac{2f_1(n)}{[f_3(n)-f_4(n)]^2} - \frac{1}{f_3(n)-f_4(n)} \right\}^{\frac{1}{2(\beta n+1)}} [1-f_2(n)]^{-\frac{1}{2(\beta n+1)}} \left[1+\frac{Ba}{v_m}\right]^{-\frac{\beta(2-n)}{\beta n+1}} \quad ......(4.60)$$

$$D_{o1} = -\left[\frac{f_5(n)}{f_3(n)-f_4(n)}\right] 2^{\beta n} \left(1+\frac{Ba}{v_m}\right)^{1-\beta(2-n)} \delta_{o0}^{-(\beta n+1)} \quad ....(4.61)$$

The Runge-Kutta numerical scheme is used to solve Eqs. (4.52) to (4.54). Note that in order to solve for δ_o, D_o, and w_o, the value of $\left(\frac{Ba}{v_m}\right)$ must be known. But, Eqs. (4.55) and (4.56) indicate that $\left(\frac{Ba}{v_m}\right)$ itself depends on the solution of δ_o, D_o, and w_o. Therefore, a trial-and-error approach is needed. First, with an assumed value of $\left(\frac{Ba}{v_m}\right)$, Eqs. (4.52) to (4.54) are numerically integrated to obtain δ_o, D_o, and w_o. Then, the solutions of δ_o, D_o, and w_o are substituted into Eqs. (4.55) and (4.56), and a new value of $\left(\frac{Ba}{v_m}\right)$ is found. The numerical procedure is repeated until the old and new values of $\left(\frac{Ba}{v_m}\right)$ are close enough to meet the convergence criterion. In evaluating $\left(\frac{Ba}{v_m}\right)$ in Eqs. (4.55) and (4.56), a Simpson numerical integration scheme is used.

4.4　Results and Discussion

4.4.1　Numerical Solutions of Eqs. (4.52) to (4.54)

Numerical solutions of the three dimensionless variables – δ_o, D_o, and w_o, were obtained using the procedures described above for a wide range of flow behavior index – from 0.25 to 1.0, which would cover most fluids to be employed with coiled tubing operations in the oil and gas industry. By comparison, Mashelkar and

Devarajan[86] only obtained solutions for n = 1.0, 0.9, 0.75, and 0.5. Therefore, the use of their results is very limited. Figs. 4.3 to 4.5 show the dimensionless quantities δ_o, w_o, and D_o as functions of angle θ for n = 1.0, 0.9, …, 0.3 respectively. The solutions of δ_o, D_o, and w_o together with Eqs. (4.48) to (4.50) and Eq. (4.13) completely define the velocity field in the tubing cross-section. The numerical solutions can also be used to deduce the friction factor correlation, as will be elaborated below.
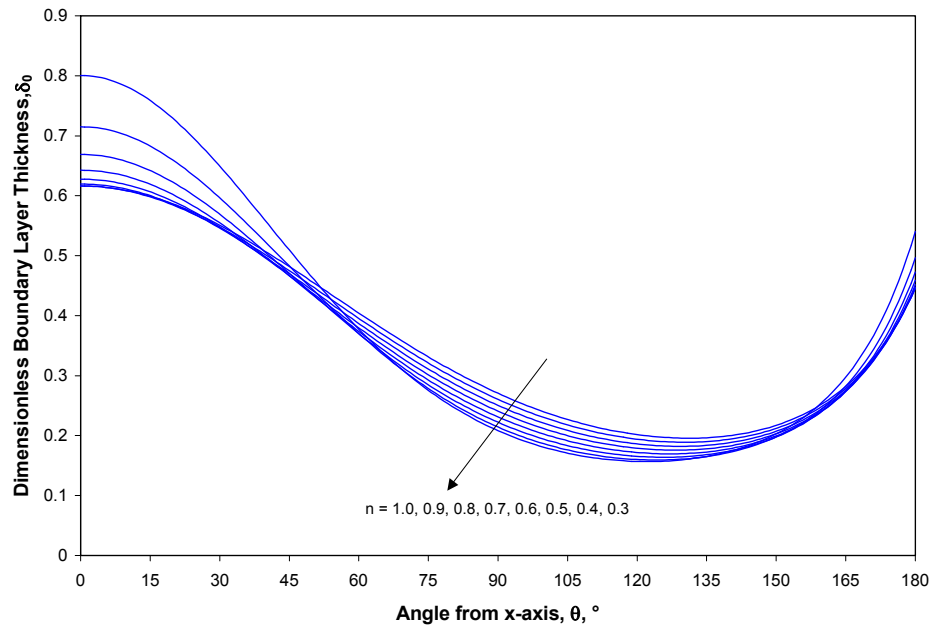
Fig. 4.3—Dimensionless boundary layer thickness, δ_o.
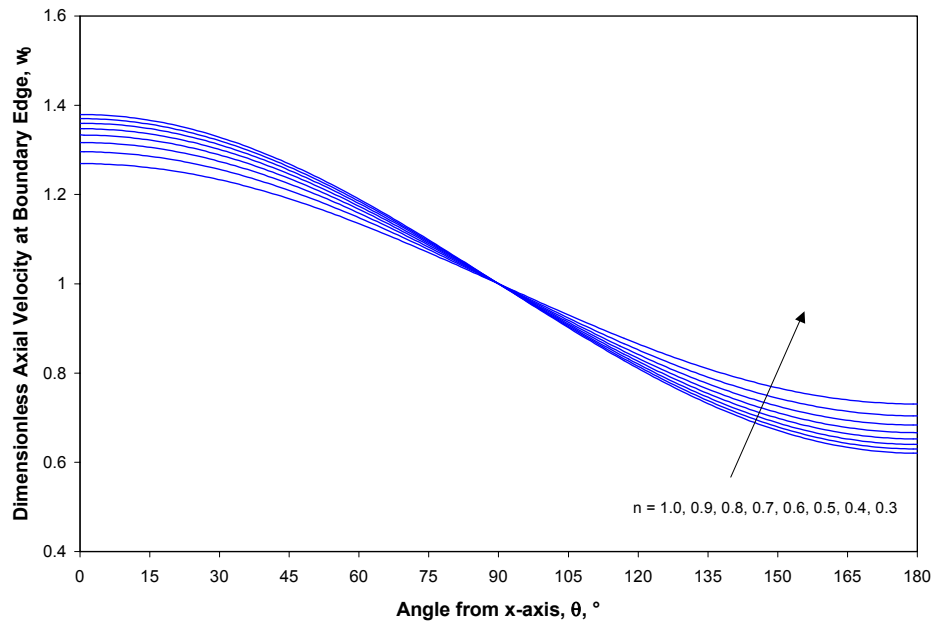
Fig. 4.4—Dimensionless axial velocity at boundary layer edge, w_o.
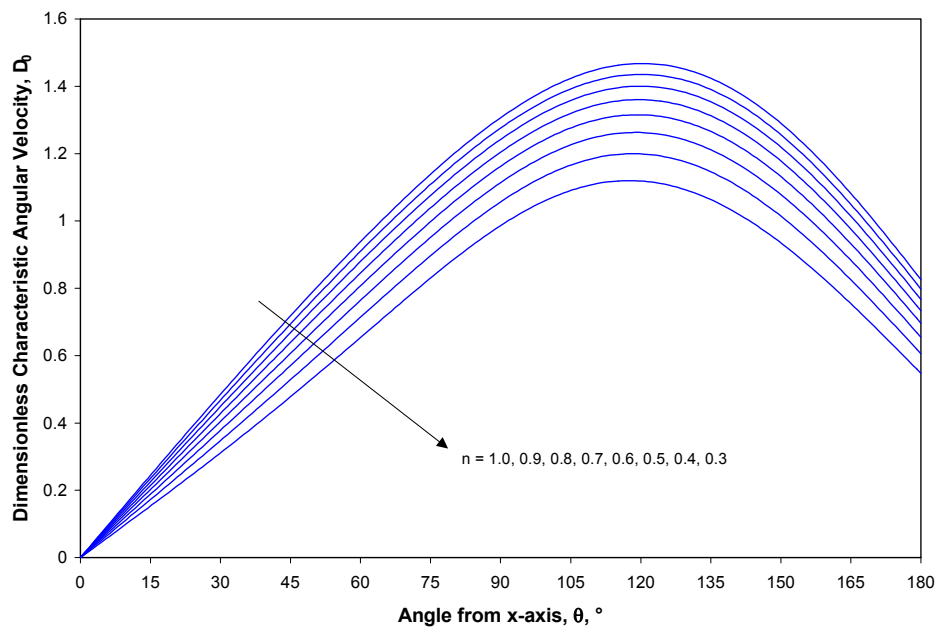
Fig. 4.5—Dimensionless characteristic angular velocity, D_o.

4.4.2   Development of Friction Factor Correlation

The Fanning friction factor in coiled tubing can be written as[3-5]:

$$f = \frac{\left(-\frac{\partial \overline{p}}{R \partial \phi}\right) a}{\rho v_m^2} = \frac{C\left(\frac{a}{R}\right)}{\rho v_m^2} \qquad (4.62)$$

Considering the force balance for a cylindrical volume of length $Rd\phi$ and radius a, we have

$$2 \int_0^\pi \int_0^\pi \int_0^a \left[\overline{p} - \left(\overline{p} + \frac{\partial \overline{p}}{\partial \phi} d\phi\right)\right] r dr d\theta = Rd\phi 2a \int_0^\pi \overline{\tau}_{r\phi}\Big|_{\xi=0} d\theta \qquad (4.63)$$

Hence,

$$C = -\frac{\partial \overline{p}}{\partial \phi} = \frac{2R}{\pi a} \int_0^\pi \overline{\tau}_{r\phi}\Big|_{\xi=0} d\theta \qquad (4.64)$$

Substituting Eqs. (4.64) and (4.38) into Eq. (4.62), and using Eqs. (4.48) to (4.50) for the definitions of dimensionless variables, the following correlation can be derived (see Appendix B):

$$f = \frac{\alpha^*\left(a/R\right)^{1/2}}{\left[2^{3(n-1)}\left(\frac{3n+1}{4n}\right)^n N_{Reg}\left(a/R\right)^{1/(2\beta)}\right]^{\beta/(\beta n+1)}}, \qquad (4.65)$$

where α^* is given in Eq. (4.56). Therefore, α^* is a function of flow behavior index n. Table 4.1 lists the values of α^* from the numerical solution of Eqs. (4.52) to (4.54) for a number of n values.

Table 4.1—Results of Numerical Solutions of Eqs. (4.52) to (4.54)

n	α^*	Ba/v_m
1.00	0.073297	0.379361
0.90	0.068524	0.370133
0.80	0.063679	0.359793
0.70	0.058728	0.347570
0.60	0.053668	0.333447
0.50	0.048454	0.316578
0.40	0.043024	0.295837
0.30	0.037259	0.269277
0.25	0.034181	0.252728

We can get the following correlation for α^*:

$$\alpha^* = c_1 + c_2 n^{c_3}, \dots\dots\dots\dots\dots\dots\dots\dots\dots\dots\dots\dots\dots\dots\dots\dots\dots\dots(4.66)$$

where c_1 = 0.0152513, c_2 = 0.058005016, and c_3 = 0.805882557. The correlation coefficient R^2 = 1.000. Fig. 4.6 shows the plot of α^* vs. flow behavior index n from this study.

The final friction factor correlation of turbulent flow of power law fluid in coiled tubing becomes:

$$f = \frac{\left(c_1 + c_2 n^{c_3}\right)\left(a/R\right)^{1/2}}{\left[2^{3(n-1)}\left(\frac{3n+1}{4n}\right)^n N_{\mathrm{Reg}}\left(a/R\right)^{1/(2\beta)}\right]^{\beta/(\beta n+1)}} \cdot \dots\dots\dots\dots\dots\dots\dots\dots\dots(4.67)$$

where β can be read from the chart of Dodge and Metzner[106] or calculated from the following curve-fitted correlation:

$$\beta = 1/\left(1.945 + 0.2504/n^{0.5}\right) \dots\dots\dots\dots\dots\dots\dots\dots\dots\dots\dots\dots\dots(4.68)$$
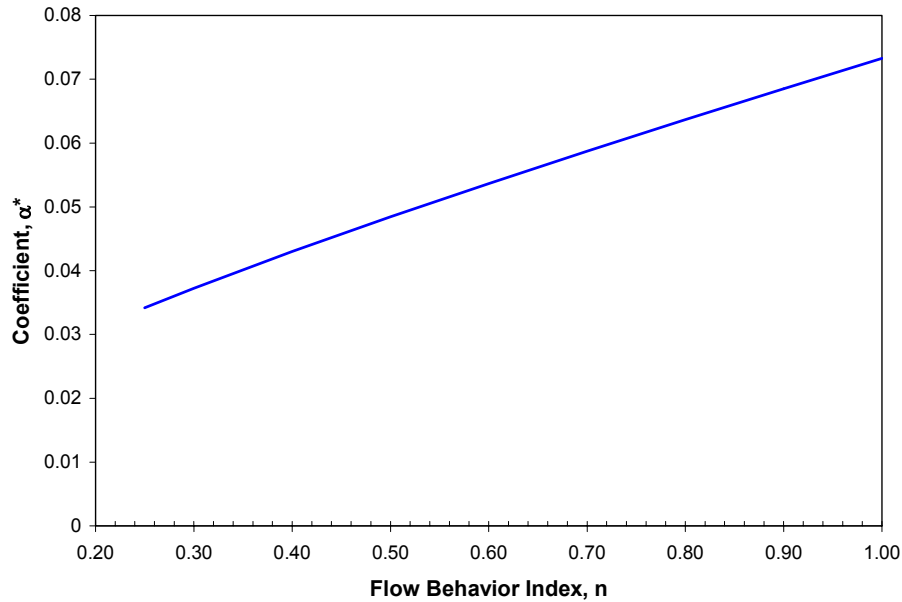
Fig. 4.6—Coefficient α* of the new non-Newtonian turbulent flow correlation.

4.4.3   Comparison with Previous Work

4.4.3.1   Comparison with the Ito, and Mashelkar and Devarajan Correlations (Newtonian Fluid)

Ito[83] applied the concept of boundary layer approximation to the turbulent flow of Newtonian fluid in curved pipes. By assuming the $1/7^{th}$-power velocity distribution, he obtained the following friction factor correlation for curved pipe:

$$f = \frac{0.0725(a/R)^{1/10}}{N_{\mathrm{Re}}^{1/5}} \quad \text{...(4.69)}$$

Eqs. (4.34) and (4.35) indicate that for the Newtonian case where n = 1 and β = 0.25, the assumed velocity distributions reduce to the $1/7^{th}$-power distributions. Therefore, the Ito correlation can be used to check the accuracy of our new correlation for the special case of n = 1.

Mashelkar and Devarajan did not provide any turbulent friction factor correlation in terms of flow behavior index n as they did for the laminar. They only obtained numerical solutions for n = 0.5, 0.75, 0.9, and 1.0, as shown in the following table.

Table 4.2—Numerical Results of Mashelkar and Devarajan for Non-Newtonian Turbulent Flow

n	β	α*	Ba/v_m
1.00	0.250	0.07185	0.37803
0.90	0.257	0.08186	0.36988
0.75	0.269	0.06566	0.31824
0.50	0.293	0.06325	0.26894

The friction factor can be calculated using Eq. (4.65).

Figs. 4.7 and 4.8 compare the friction factors predicted by the Ito, the Mashelkar and Devarajan correlation, and the new correlation of this study for curvature ratios of 0.01 and 0.03 respectively. The critical Reynolds numbers for turbulent flow at a/R = 0.01 and 0.03 are 4582 and 6512 respectively from the Ito's[83] criterion: N_{Rec} = 20000(a/R)$^{0.32}$. Therefore, we only calculated friction factors for N_{Re} > 4582 or N_{Re} > 6512. Figs. 4.7 and 4.8 show that there is a very close agreement between the new correlation and the Ito correlation, with the difference being less than 0.8%. The Mashelkar and Devarajan correlation also closely matches the Ito correlation, with deviation of about -0.9% (friction factor is just slightly underestimated). Therefore, practically both our new correlation and Mashelkar and Devarajan correlation are in close agreement with the Ito correlation.
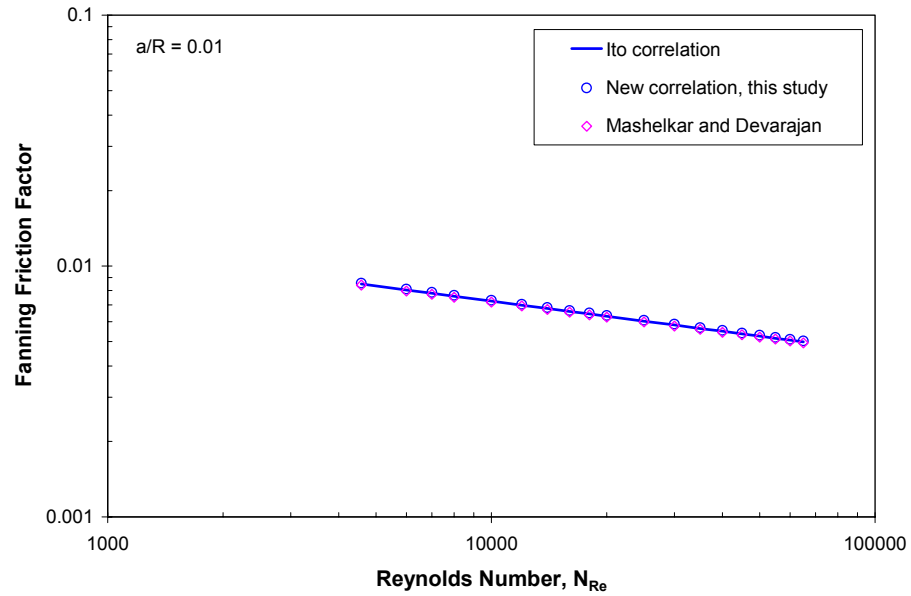
Fig. 4.7—Comparison of Mashelkar and Devarajan correlation, and the new correlation with Ito correlation for Newtonian fluid (n = 1, a/R = 0.01).
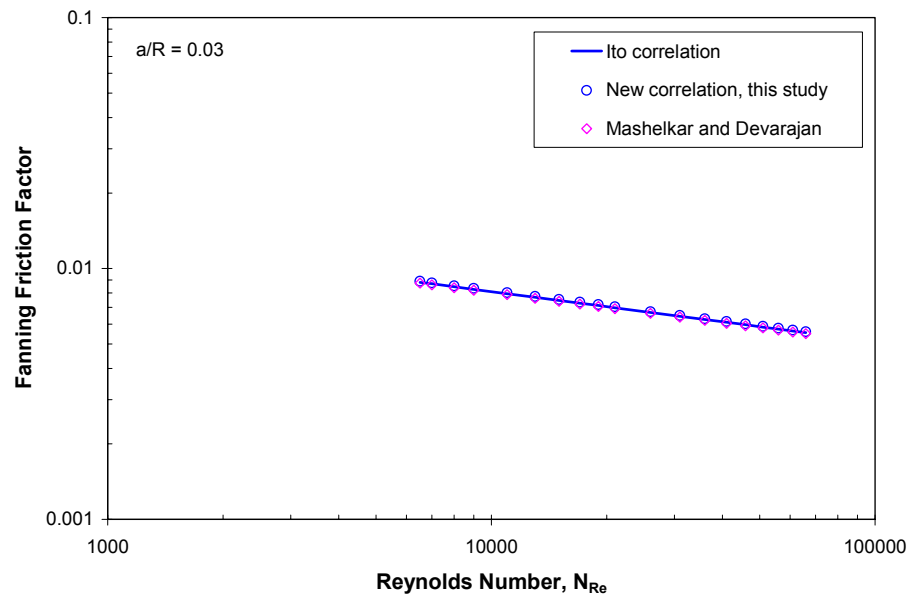
Fig. 4.8—Comparison of Mashelkar and Devarajan correlation, and the new correlation with Ito correlation for Newtonian fluid (n = 1, a/R = 0.03).

4.4.3.2 Comparison with Mashelkar and Devarajan Correlation (Non-Newtonian Fluid)

Figs. 4.9 and 4.10 show friction factors predicted by Mashelkar and Devarajan, and by the new correlation of this study for flow behavior index n = 0.5, 0.75, 0.9, and 1.0, respectively. In these two plots, the curvature ratio is assumed as 0.02. Similar plots of Fanning friction factor vs. generalized Reynolds number for other curvature ratio values such as a/R = 0.01 and 0.03, were also made. It was found that the friction behavior at a/R = 0.01 and 0.03 is similar to what is shown in Figs. 4.9 and 4.10. As indicated in Fig. 4.10, as flow behavior index decreases, the friction factor predicted by our new correlation is also decreased. This behavior is similar to non-Newtonian fluid flow in straight pipe. But, Fig. 4.9 indicated that Mashelkar and Devarajan method does not show consistent trend as far as the effect of flow behavior index is concerned. It can be seen that the friction factor for n = 0.9 is higher than the friction factor of Newtonian fluid. This is in conflict with the well-known behavior of power law fluid in pipe flow. The shear-thinning property of a power law fluid should lead to a lower friction factor than Newtonian fluid at corresponding Reynolds number.[106] The friction factors predicted by Mashelkar and Devarajan method for n = 0.5 and 0.75 are lower than the Newtonian friction factor.

Fig. 4.11 compares the friction factor predicted by the Mashelkar and Deverajan method and by the new correlation of this study respectively. At n = 0.5, 0.75, and 0.9, the friction factor predicted by the Mashelkar and Devarajan method is higher than our new correlation by approximately 32.2, 7.1, and 19.6% respectively.
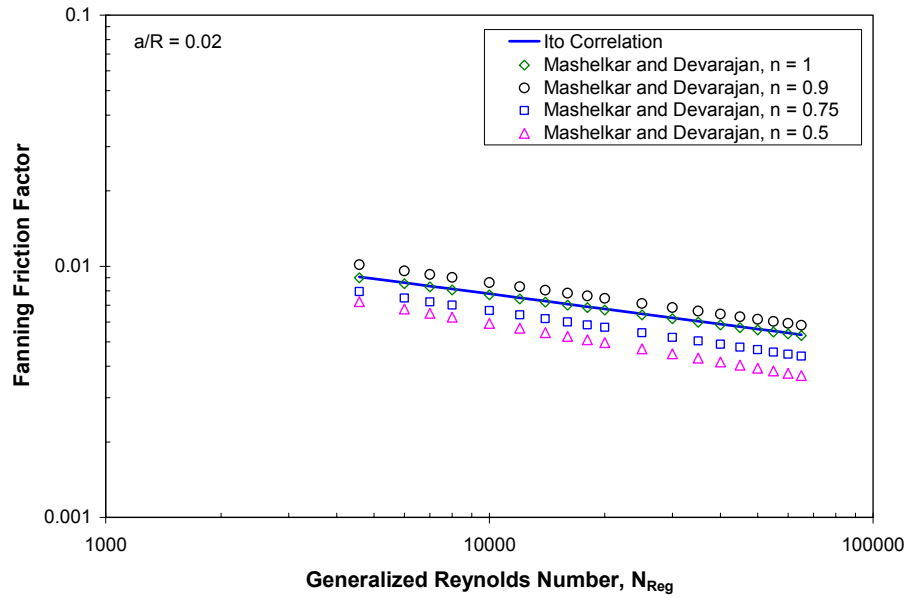
Fig. 4.9—Effect of flow behavior index on Fanning friction factor predicted by Mashelkar and Devarajan (a/R = 0.02).
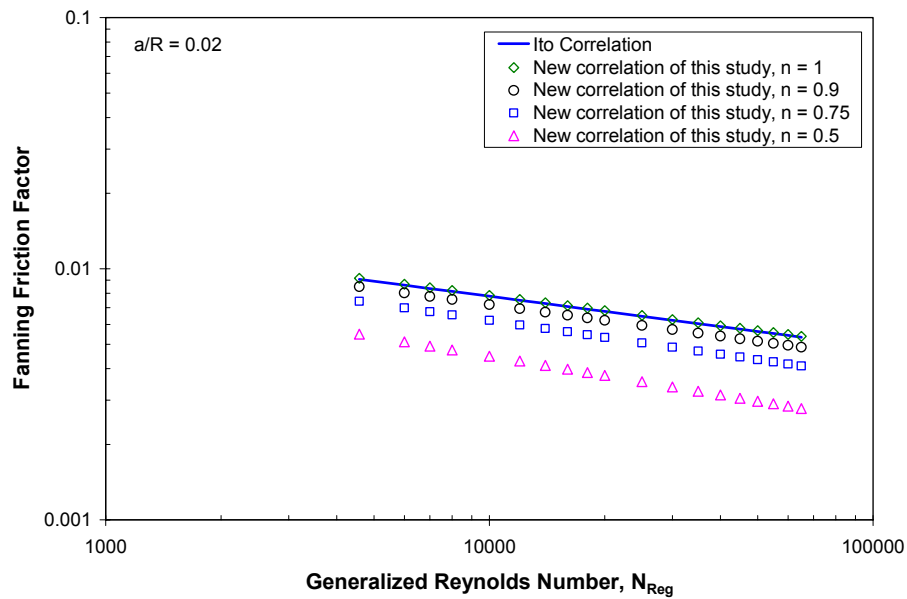
Fig. 4.10—Effect of flow behavior index on Fanning friction factor predicted by the new correlation of this study.
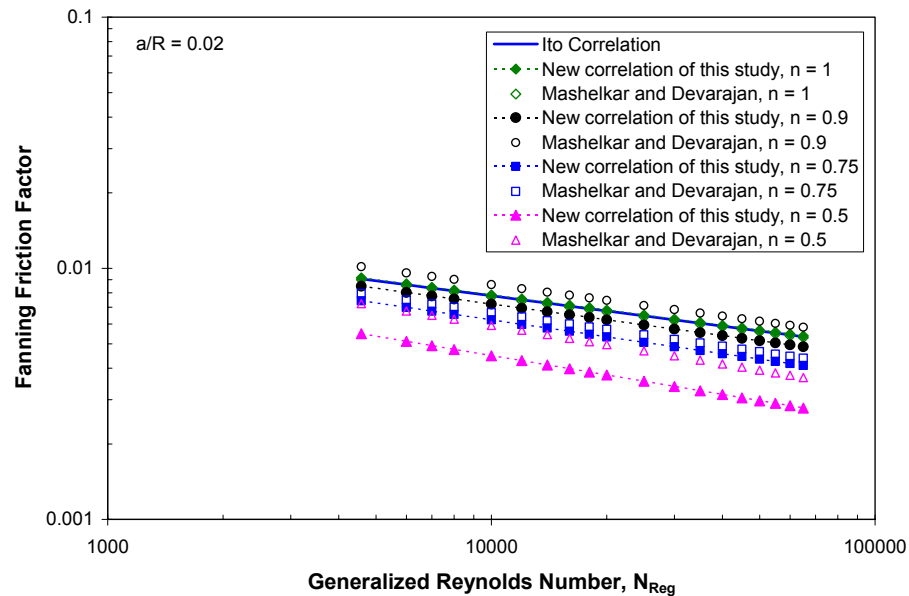
Fig. 4.11—Comparison between Mashelkar and Devarajan, and the new correlation of this study for non-Newtonian fluid.

4.4.4   Comparison with Experimental Data

Fig. 4.12 shows the friction factor of 35 lb/Mgal guar in 200 ft straight tubing and 1000 ft coiled tubing respectively. The tubing outside diameter is 2-3/8 in. Obviously, the friction factor in coiled tubing is greater than that in straight tubing due to the curvature effect. The prediction of the new correlation is seen to be close to the experimental data. Actually, for generalized Reynolds number in the range of 10,000 – 25,000, the match is very good. At lower Reynolds number, the correlation deviates from the experimental data. This is probably because at lower generalized Reynolds number, the flow regime does not reach fully turbulent flow.

95
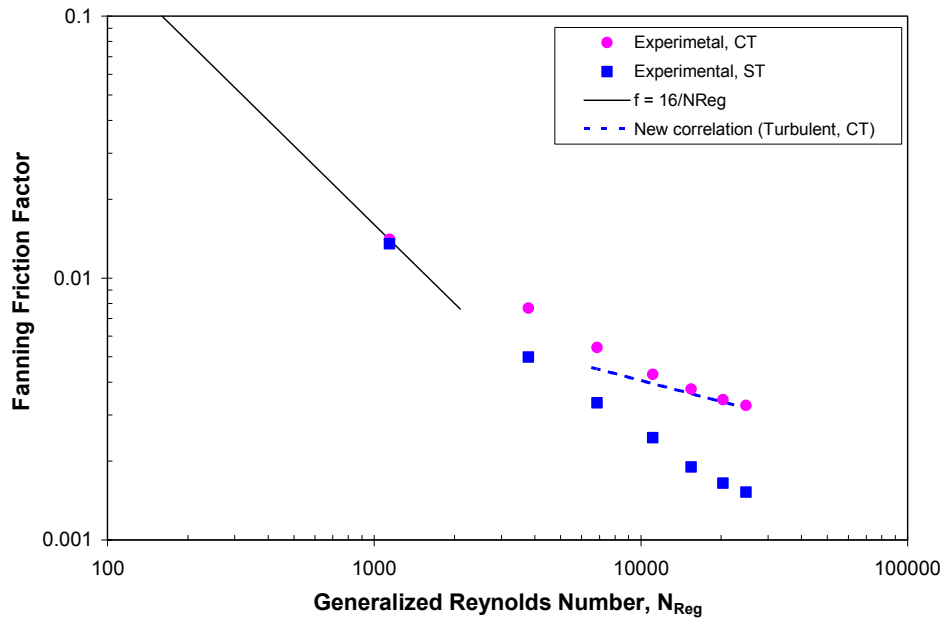
Fig. 4.12—Fanning friction factor vs. generalized Reynolds number (35 lb/Mgal guar in 1000 ft, 2-3/8-in. CT).

Fig. 4.13 shows the results of 25 lb/Mgal guar in 2-3/8-in. coiled tubing. In this case, the correlation gives good match with the generalized Reynolds number in a range around 9500. Yet, as the generalized Reynolds number increases, the correlation tends to overpredict the friction factor. Fig. 4.14 shows the comparison of experimental data and the new correlation for 20 lb/Mgal Xanthan in 2000 ft, 2-3/8-in. coiled tubing. Similarly, in a range of generalized Reynolds number around 12000, the match is quite good. For high Reynolds number, the correlation overpredicts the friction factor. One reason for this overprediction might be that at high Reynolds number, these fluids exhibit strong drag reduction. Our theoretical analysis and therefore the new correlation only considered purely viscous fluids that follow the

power law model. Therefore, the new correlation may not closely predict the correct

friction factors under highly drag-reducing flow conditions.
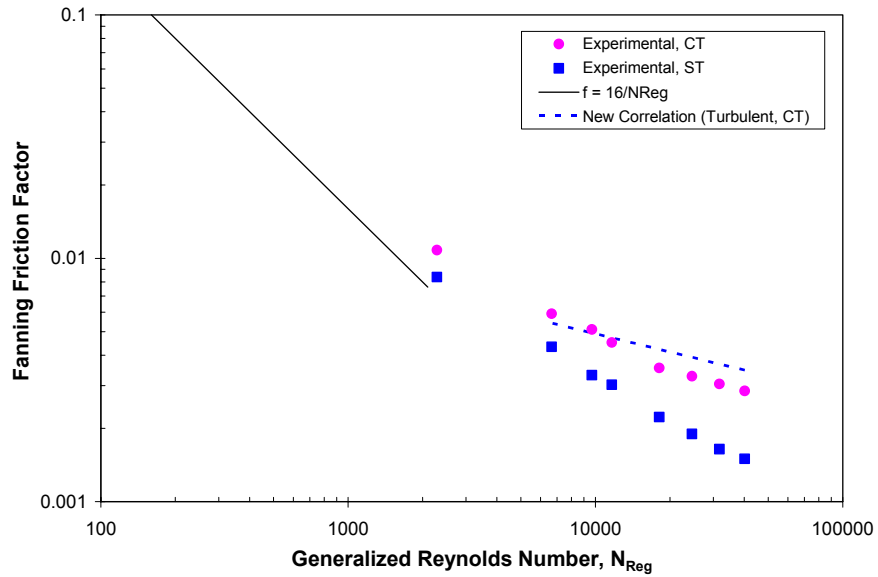
Fig. 4.13—Fanning friction factor vs. generalized Reynolds number (25 lb/Mgal guar in 1000 ft, 2-3/8-in. CT).
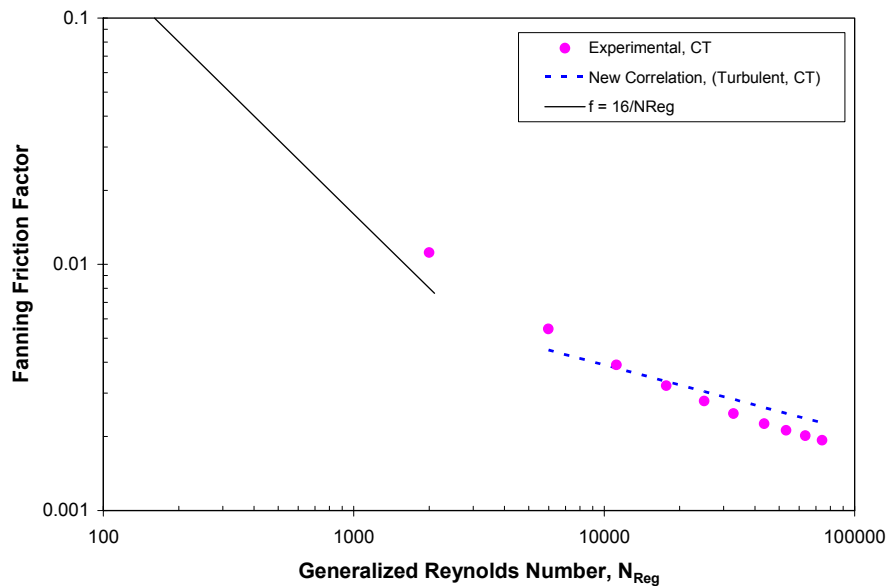
Fig. 4.14—Fanning friction factor vs. generalized Reynolds number (20 lb/Mgal xanthan in 2000 ft, 2-3/8-in. CT).

4.5   Summary

The boundary layer approximation method has been successfully applied to solve the steady, fully-developed turbulent flow of a power law fluid in coiled tubing. This study extended Mashelkar and Devarajan's work to fluids with wider range of flow behavior indices ($n = 0.25, 0.3, 0.4, …, 1.0$).

A new friction factor correlation for non-Newtonian fluid flow in coiled tubing has been developed based on the numerical analysis. This new correlation was verified by comparing with the Ito correlation and Mashelkar and Devarajan correlation for the special case of Newtonian fluid ($n = 1$). There is excellent agreement between the new correlation of this study and the Ito correlation. For non-Newtonian fluid, comparison was made with Mashelkar and Devarajan correlation. For $n = 0.75$, the difference between Mashelkar and Devarajan correlation and our new correlation is 7.1%. For $n = 0.75$ and 0.9, Mashelkar and Devarajan correlation is 32.2% and 19.6% higher than the new correlation. It has been shown that the Mashelkar and Devarajan correlation could not properly describe the effect of flow behavior index on friction factor of power law fluids. The new correlation was also evaluated with some full-scale experimental data. Under certain flow conditions and at certain generalized Reynolds number, there is a good agreement between the new correlation and the experimental results. It should be noted that the fluid model we had assumed in the numerical analysis is purely viscous power law model. Therefore, the new friction factor correlation based on the numerical analysis may overpredict friction factors if the fluids exhibit strong drag-reducing properties. For these drag

reducing fluids, the best approach of investigation is through flow experiments. This will be discussed in more details in later chapters.

CHAPTER 5

EXPERIMENTAL SETUP

5.1   Introduction

Experimental study constitutes an essential part of this research. The fluids we investigated in this study are polymer fluids typically used in drilling, completion, and stimulation applications. Their flow behavior in coiled tubing is rather complicated. Direct experimental measurement of fluid flow in coiled tubing is an effective method of investigation. Through the Coiled Tubing Consortium (CTC), a full-scale coiled tubing flow test facility has been established at the Well Construction Technology Center (WCTC), Mewbourne School of Petroleum & Geological Engineering, the University of Oklahoma. The experimental setup provided us unique capability to conduct flow test and investigate the flow behavior of various fluids in coiled tubing. An array of coiled tubing reels and straight tubing sections with various dimensions are available to meet the needs of experimental investigation. The advantage of full-scale tests is that the experimental results and friction pressure correlations based on full-scale test data can be used directly in field applications. The limitation of full-scale tubing tests is their high experimental expenses. These include costs of large amount of materials, operation of field-size equipment, and man-power. For this reason, a lab-scale coiled tubing flow loop was also built. This flow loop has been proven to be cost-effective. Further, the ease of handling the equipment

associated with the lab-scale loop results in better quality control in terms of fluid mixing and preparation. As will be seen later, the coiled tubing reels in the lab-scale tests cover wider range of curvature ratio of coiled tubing and the lab-scale test results complement the full-scale test results.

In addition to tubing flow experiments, characterization of the fluids' rheological properties is another important aspect of the experimental investigation. Fann Model 35 viscometers were used for rheological measurements at ambient temperatures.

This chapter presents the experimental flow loops, fluid mixing and pumping equipment, measurement instruments, data acquisition system, and rheometers. The functions and capabilities of various components of the experimental setup are described. The fluid systems and experimental procedures are also discussed.

5.2   Full-Scale Experimental Setup

In this research, majority of the experimental work was conducted using the full-scale flow loop. Fig. 5.1 shows the schematic of the coiled tubing flow loop, which is located at the Well Construction Technology Center. It consists of 9 coiled tubing reels, two 200-ft long straight tubing sections, six 30-ft straight tubing sections, fluid mixing and storage tanks, fluid pumping equipment, and data acquisition system. This flow loop was designed and built as part of the research for the joint-industry consortium on coiled tubing. The following describes the components of the flow loop.
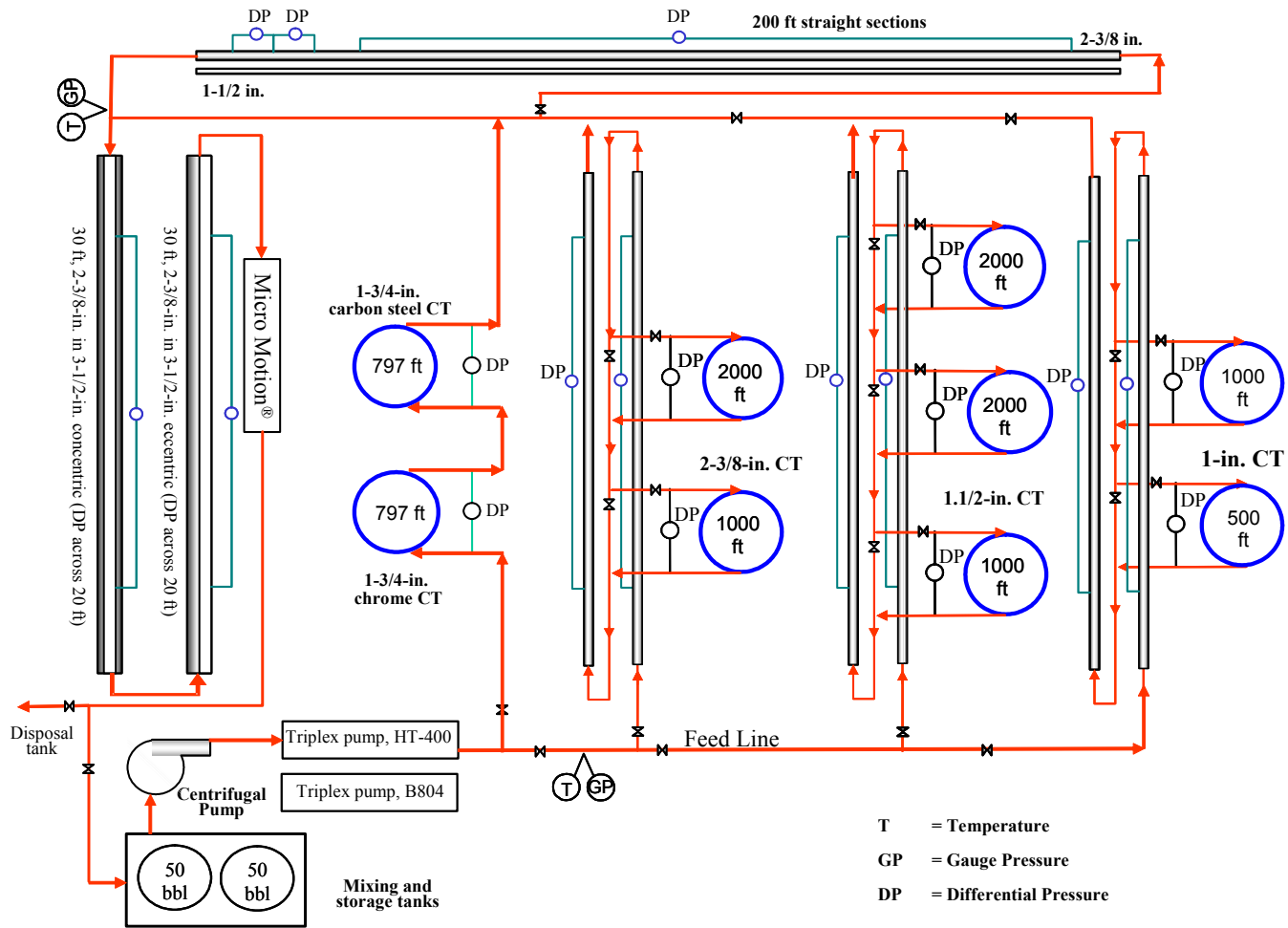
Fig. 5.1—Schematic of full-scale coiled tubing flow loop.

5.2.1　Coiled Tubing Reels

Coiled tubing reels are the unique components of this field-scale coiled tubing test facility. There are total of 9 coiled tubing reels that have been used at various stages of the experimental work. The dimensions of these coiled tubing reels are shown in Table 5.1. Fig. 5.2 shows the layout of the coiled tubing reels in the coiled tubing flow test facility.

Table 5.1—Dimensions of Coiled Tubing Reels in Full-Scale Flow Loop

Reel No.	OD (in.)	ID (in.)	Length (ft)	Reel Diameter (in.)
1	1	0.81	500	48
2	1	0.81	1000	72
3	1-1/2	1.188	1000	72
4	1-1/2	1.188	2000	72
5	1-1/2	1.188	2000	72
6	2-3/8	2.063	1000	111
7	2-3/8	2.063	2039	111
8	1-3/4	1.532	797	82
9	1-3/4	1.482	797	82

Reels 1 and 2, on the right in Fig. 5.2, have an outer diameter of 1 in. and are the smallest coiled tubing in the field-scale flow loop. Either reel can be put online. Or if both are online, pressure drop over a total length of 1500 ft can be measured. Note that Reel 1 and Reel 2 are spooled onto two drums of different diameters. They correspond to two curvature ratios – 0.0169 and 0.0113. Therefore, if fluid is pumped through both reels, the differential pressure measurement across both reels can provide a direct comparison on the effect of tubing curvature.

Fig. 5.2—Coiled tubing reels.

Reels 3 through 5, in the middle of Fig. 5.2, have an OD of 1-1/2 in. Their reel drum diameters are all 72 in. The curvature ratio of these three reels is 0.0165. Reels 6 and 7, in the upper-left corner of Fig. 5.2, have an outside diameter of 2-3/8 in. and are the largest tubing size in the facility. They are spooled onto reel drums of 111 in. diameter, corresponding to curvature ratio of 0.0185.

The other two coiled tubing reels used in this study, Reels 8 and 9, are shown in Fig. 5.3. They each have a nominal outside diameter of 1-3/4 in. and is 797 ft long. Reel 8 is a chrome tubing with wall thickness of 0.109 in. while Reel 9 is carbon steel tubing with wall thickness of 0.134 in. The original purpose of having these two tubing reels was to conduct slurry erosion test through these tubing reels. But before running extensive slurry erosion tests, water and guar gel were also pumped through these tubing strings to collect frictional pressure data.

Fig. 5.3—Chrome and carbon steel tubing reels.

5.2.2 Straight Tubing (ST) Sections

The purpose of including straight tubing sections in the flow loop is two-fold: (1) to compare frictional pressures between coiled tubing and straight tubing, and (2) to collect frictional pressure data of various fluids in straight tubing so that useful correlations of friction pressure can be developed. As indicated in Fig. 5.1, there are two 30-ft straight tubing sections at the upstream and downstream of CT reels for each tubing size of 1, 1-1/2, and 2-3/8 in. Pressure ports were made on each of these straight sections so that differential pressure across 20 ft can be measured.

Two 200-ft straight tubing sections, 1-1/2 in. and 2-3/8 in. in diameter, were later added to the flow loop. They were installed in the yard parallel to the fence, shown in Fig. 5.4. It is expected that longer tubing length could lead to more accurate measurement of differential pressure. On the long straight tubing sections, pressure ports were made across 160 ft. The first pressure port for the 160-ft segment is 30 ft

away from the tubing entrance, therefore, it is considered free of entrance effect. The second pressure port in the downstream side is 12 ft away from the exit end and it is also believed to be long enough to avoid exit effect. Additional ports were also drilled across the first two 10-ft segments at the entry end. Entrance effect can be investigated by measuring differential pressures over these entrance segments.

Fig. 5.4—200-ft long straight tubing sections.

5.2.3   Fluid Mixing and Pumping Equipment

Two 50-bbl capacity fluid mixing and storage tanks are located on a MX-5000 trailer unit, shown in Fig. 5.5. Each tank has individually-controlled hydraulically-driven agitator. One tank can be used to prepare and store test fluid while the other tank can be used to store water either for water test or to flush the system.

106

Fig. 5.5—50-bbl fluid mixing and storage tanks.

To prepare a test fluid, polymers and additives were added to one of the tanks. The solution was hydrated in the tank. The mixing tanks have pneumatic control panels to adjust the blending paddle speed and to operate valves for diverting test fluid or water from each tank into the flow loop. The control panel was manned during experiments to maintain uninterrupted supply of test fluid to the flow loop. A 150-bbl effluent tank is used to store the spent test fluid for later disposal.

The high pressure pumping equipment includes a Halliburton Energy Services HT-400 triplex plunger pump and a Schlumberger B804 triplex plunger pump, shown in Figs. 5.6 and 5.7 respectively. The HT-400 triplex pump is capable of pumping fluids up to 5000 psi pressure and 300 gallons per minute (7.1 bbl/min) flow rate. The Schlumberger B804 triplex pump can pump fluid up to 10,000 psi and 290 gpm (6.9

Fig. 5.6—Halliburton Energy Services HT-400 triplex plunger pump.

Fig. 5.7—Schlumberger B804 triplex plunger pump.

bbl/min) flow rate. For typical fluid tests, only one pump is used. For flow tests at very high flow rates, two triplex pumps can be used to deliver a total flow rate of

about 10 bbl/min. A Galigher 4×6 centrifugal pump, shown in Fig. 5.8, is used to boast the suction of the triplex pump(s). It takes fluid from the mixing tank and feeds the triplex plunger pump(s). The centrifugal pump also serves as an aid in fluid mixing.

Fig. 5.8—Galigher centrifugal pump.

5.3   Lab-Scale Experimental Setup

The schematic of the lab-scale flow loop is shown in Fig. 5.9. It mainly consists of four coiled tubing reels, one 10-ft straight tubing section, fluid mixing and pumping equipment, and data acquisition system. These components are parallel to those used in the full-scale flow loop, as discussed previously. Since the tubing size is only ½-in. OD, the requirements for the amount of fluid and pumping capacity are significantly reduced.
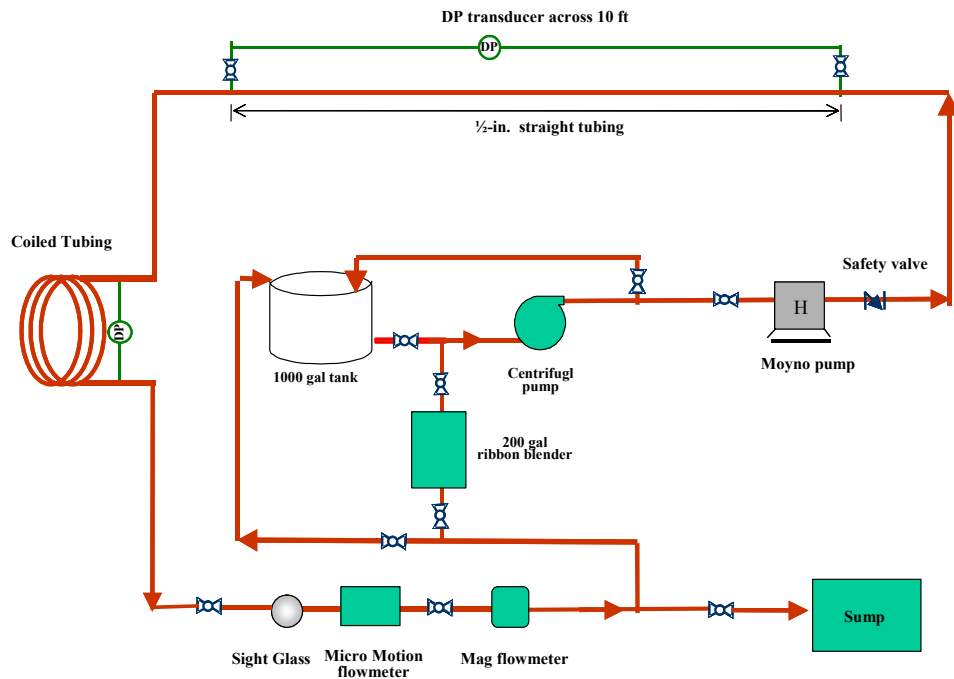
Fig. 5.9—Schematic of lab-scale flow loop.

5.3.1 Coiled Tubing Dimensions

Four coils of ½-in. coiled tubing, shown in Fig. 5.10, were used in this study. The tubing is ½-in. OD and 0.435-in. ID and is made of stainless steel. Their dimensions are given in Table 5.2. The coils were made by spooling straight stainless tubings onto drums with various diameters. Since the tubing diameter is fixed, decreasing the coil diameter (from Coil 1 through Coil 4) increases the curvature ratio. These four coils cover a wide range of curvature ratio – from 0.01 to 0.076. The typical range of curvature ratio encountered in the field applications is well within the range of the

110

four coils. The wide curvature ratio range of the present coils helps to investigate the effect of curvature ratio on friction pressure losses in coiled tubing. During flow tests, the four coils can be interchanged through quick connections.

Fig. 5.10—Photograph of four ½-in. stainless coils.

Table 5.2—Dimensions of Four ½-in. Coils

No.	Coil Diameter (in)	Tubing Length (ft)	Number of Turns	Curvature Ratio (a/R)
1	3.608	36.14	3	0.010
2	1.878	18.83	3	0.019
3	1.168	23.26	6	0.031
4	0.478	13.58	7	0.076

5.3.2   Fluid Mixing and Pumping Equipment

Fluid mixing and storage vessels include a 1000-gal polyethylene storage tank and a 200-gal ribbon blender. The 1000 gal storage tank serves as large volume source of test fluid. The 200 gal ribbon blender can be used to prepare slurry. Pumping is achieved by a Model 6P10 Moyno progressive cavity pump and a Model 5M Deming centrifugal pump. The Moyno pump with its indefinitely variable speed drive can deliver up to approximately 140 gpm at 600 psi. The centrifugal pump serves to boost the suction of the Moyno pump.

5.4   Measurement Instruments

The high pressure test environment required reliable and accurate measurement instruments. The main data collected in a flow test included: flow rate, differential pressures across various sections of straight and coiled tubing, fluid density, fluid temperature, and system pressure. The instrument used in this study included: Micro Motion flowmeters, Honeywell differential pressure transducers, and gauge pressure transducers. Auxiliary equipment also included mimiPumps that were used to purge the pressure lines for the differential pressure transducers and pressure gauges. The following describes these instruments and equipment.

5.4.1   Micro Motion Flowmeters

Micro Motion flowmeters work based on Coriolis effect. They are capable of making multi-variable measurement: mass flow rate, volumetric flow rate, density, and

temperature. Three Micro Motion flowmeters have been used in the research project. Table 5.3 summarizes their specifications.

Table 5.3—Specifications of Micro Motion Flowmeters

Item	Flowmeter 1	Flowmeter 2	Flowmeter 3
Model	DL200 S228SU	DS300 S157SU	CMF050M320NU
S/N	154891	251696	341151
Flow rate range, gal/min	0 - 420	0 - 840	0 - 30
Flow rate accuracy, %	± 0.15	± 0.15	± 0.05
Temperature accuracy, °C	± 0.1	± 0.1	± 1
Density accuracy, g/cm^3	± 0.0005	± 0.0005	± 0.0005
Operating pressure, psi	740	740	1475
Usage	Full-scale flow loop	Full-scale flow loop	Lab-scale flow loop

5.4.2   Differential Pressure and Gauge Pressure Transducers

Differential pressure transducers are the most important instrument for measuring frictional pressures across various tubing sections. Due to the nature of the field-scale testing, the system pressure during a flow test is very high. This presents special requirement for the differential pressure transducers – they should work in high pressure environment and yet have enough accuracy. Furthermore, since the tubing lengths of various tubing sections are widely different, from 10 ft to 2000 ft, their pressure drops vary significantly. Therefore, differential pressure transducers with different measurement ranges are needed. In this research project, Honeywell differential pressure transducers were chosen to measure frictional pressures across tubing sections.

113

Table 5.4 lists the differential pressure (DP) and gauge pressure transducers used for pressure measurement during this study.

5.4.3   Data Acquisition System

The data measured by the flowmeters, pressure transducers as well as pressure gauges were collected and transmitted to a computer where the data was displayed and saved for later analysis. This task was accomplished by the Fluke Hydra data acquisition system (Fluke Corporation, Everett, WA, Model 2625A). The Fluke Hydra system contains two hydras, each having 21 analog measurement channels. The sample rate is up to 10 samples per second. The Hydra data logger communicates with a host computer via a wireless modem radio link. The wireless tool can allow up to 1200 ft distance between the remote logger and the receiving computer. The remote operation is advantageous for this field-size test loop and high pressure environment.

The software of the data acquisition system provides the option of displaying the data signals graphically. This feature is useful for the operator to monitor the trends of measured variables and make proper decisions and adjustments during an experiment. By looking at the signals, the operator can determine whether the flow has reached steady state or when to change one flow rate to another flow rate. By observing the trends of the DP signals, the operator can also judge whether any pressure ports (or pressure lines) are blocked and need purging.

Table 5.4—Differential Pressure and Gauge Pressure Transducers Used in This Study

No.	Quantity	Model	Max Span (psi)	Min Span (psi)	Rating (psi)	Accuracy*	Usage
1	2	STD170V	0 - 3000	0 - 100	6000	± 0.15%	High pressure, field-scale CT.
2	1	STD170G	0 - 3000	0 - 100	3000	± 0.15%	Low pressure field-scale CT; 200 ft ST
3	2	(1) STD130V (1) YSTD130G	0 - 100	0 - 5	6000	± 0.075%	Field-scale 30-ft ST sections
4	4	(3) STD130G (1) STD130V	0 - 100	0 - 5	3000	± 0.075%	Field-scale annular sections; lab-scale coils and ST
5	2	STG120G	0 - 14.5	0 - 1 INH2O	3000	± 0.075%	10-ft segments in 200-ft ST
6	2	STG98LC	0 - 6000	0 - 500	9000	± 0.10%	System pressure

* expressed in percentage of calibration span.

5.5 Rheometers

Fann Viscometers. Fig. 5.11 shows two Fann Model 35 viscometers used in this study. Each viscometer consists of two cylinders: an outer cylinder, called rotor (or sleeve), and an inner cylinder, called bob. The annular space between the two cylinders contains the fluid sample to be tested. The shear is introduced by rotating the outer cylinder – the rotor. The torque is balanced by a helically wound precision spring where its deflection can be read on a calibrated dial at the top of the viscometer. For a given bob-rotor geometry and given torque spring, the rotational speed of the rotor (measured in rpm) can be converted to shear rate and the torque indicated by the dial reading can be converted to shear stress.

Fig. 5.11—Fann Model 35 viscometers.

The Fann viscometers used for this study have standard bob and rotor. The bob (B1) has a radius of 1.7245 cm and length of 3.8 cm, the rotor (R1) has a radius of

1.8415 cm. One of the Fann viscometers has six rotor speeds and a No. 1 torsion spring. The other viscometer has 12 rotor speeds and a No. 1/5th spring. For thin fluids, the No. 1/5th spring was used for better accuracy. Fann viscometers had been routinely used throughout this experimental study for rheological measurements at ambient temperatures. For rheological measurements at elevated temperatures, Bohlin CS-50 rheometer had been used.[108]

5.6   Fluid Systems

Table 5.5 shows the four types of polymer solutions tested on the field-scale flow loop. These are typical drilling and completion fluids suggested by the Coiled Tubing Consortium members. Table 5.6 lists the product name, generic description, and provider/manufacturer of each fluid.

Table 5.5—List of Fluids Tested with Field-Scale Flow Loop

No.	Viscosifier/Additive	Concentration
1	Xanthan	10, 20, 40 lb/Mgal
2	PHPA	20, 40 lb/Mgal
3	Guar	20, 30, 40 lb/Mgal
4	HEC	20, 30, 40 lb/Mgal

Table 5.7 shows three polymers and their concentrations used in the experiments with the lab-scale flow loop.

117

Table 5.6—Product Names, Generic Descriptions, and Provider/Manufacturers

Item	Product Name	Description	Provider/Manufacturer
Xanthan	XANVIS® L	Xanthan gum	Kelco Oil Field Group
PHPA	DRILLAID PA 469	Polymerized acrylamide	Baker Petrolite
Guar	WG-19	Guar gum	Halliburton Energy Services
HEC	NATROSOL	Hydroxyethyl cellulose	HERCULES INC.

Table 5.7—Rheological Parameters of Fluids Tested in the ½-in. Flow Loop

Fluids	Concentration lb/Mgal	n	K_p $lb_f s^n/ft^2$
Xanthan	10	0.717	0.00082
	15	0.403	0.00755
	20	0.365	0.01303
	30	0.310	0.03104
Guar	10	0.819	0.00019
	20	0.619	0.00268
	30	0.482	0.01168
HPG	10	0.805	0.00036
	20	0.598	0.00336
	30	0.485	0.01270

A brief description of each fluid is given in the following.

Xanthan. Xanthan gum is a high-molecular-weight biopolymer and is produced by bacterial fermentation of microorganism Xanthamonas compestris.[109-112] Xanthan gum solutions display remarkable shear-thinning properties. Its major application in drilling fluids is as a suspending agent due to its high viscosity at low shear rate. This shear-thinning property also makes it useful as completion and stimulation fluids. The xanthan polymer used in this study is Xanvis® L of Kelco Oil Field Group. It is a cream-colored fluid suspension.

PHPA. Partially hydrolyzed polyacrylamide (PHPA) is a synthetic water-soluble polymer. The primary benefits of synthetic polymers over natural polymers are increased temperature stability and contamination resistance.[113] PHPA polymer has been widely used in drilling fluids.[114] The PHPA polymer used in this study is in the form of white powder and was provided by Baker Petrolite.

Guar and HPG. Guar is a long-chain natural polymer composed of manmose and galactose sugars.[115] Guar gum comes from the endosperm of guar beans. The beans are removed from bean pod, processed to separate the endosperm from the bean hull and embryo, and ground into a powder. HPG (hydroxypropyl guar) is obtained by the reaction of propylene oxide with the guar molecules, creating a more temperature stable polymer. It was developed primarily to reduce the residue obtained from guar gum. Guar gum and HPG are the most widely used viscosifiers for water-based fracturing fluids. It is reported that over 70% of all fracturing treatments use guar or hydroxypropyl guar (HPG)-based aqueous fluids.[115] The guar polymer tested in this study is a WG-19 and is a product of Halliburton Energy Services.

HEC. Hydroxyethyl cellulose (HEC) is also a natural polymer. It is produced by chemically reacting ethylene oxide with cotton or wood-based cellulose. [109,116] It is nonionic water-soluble polymer and can be of various viscosity grades, made possible by changing the molecular weight of the cellulose backbone. The HEC polymer used in this study is a frac-grade HEC. Its viscosity is higher than those used as fluid loss additives.

5.7   Experimental Procedure

The experimental procedure began with proper fluid preparation. The fluid mixing procedures recommended by the product providers/manufacturers were followed. The general fluid mixing procedures are given in Appendix C. Fluid samples were taken and checked to ensure adequate mixing and hydration. After the fluid was prepared, water was pumped through the system as a system calibration check. The fluid was then pumped through the flow loop, and when the system was completely filled with gel, it was switched to recirculation. In order to reduce any heating or gel degradation due to extensive shearing, the test sequence used was to first pump fluid through 2-3/8-in. coiled tubing, followed by 1-1/2-in., and finally the 1-in. tubing. During each test, the fluid was pumped at various flow rates until either the pump rate reached the maximum capacity of the triplex pump or the system pressure reached a maximum pressure of 5,000 psi. At each flow rate, 2–3 minutes of steady flow was allowed to collect quality data. In the beginning and at the end of each test, fluid samples were taken from a sampling port in the flow loop and submitted to the Fann Model 35 viscometers for rheological measurements. In this way, any rheology changes due to heating or degradation can be taken into account during the data analysis. The experimental procedure for tests on the lab-scale loop is quite similar to that on the field-scale loop. The main difference is that once flow test was completed on one coil in the lab-scale flow loop, it had to be switched to another coil and repeat the same testing procedure with the same fluid.

It should be pointed out that only one fluid sampling port was constructed in the field-size flow loop. For safety consideration, this port was made downstream of the Micro Motion flowmeter. It is realized that the fluid properties could be different at various locations of the flow loop. For example, the property of fluid immediately after the pump may be different than the fluid at the downstream of the flow loop due to different shear histories. In the present study, Fann Model 35 viscometers were used. Due to the time lag between the time when the sample was taken and the time when the sample was tested on the viscometer, testing on the viscometer may not detect fluid dynamic property change. To understand the property change of fluid along the flow path of the flow loop, several sampling ports may be built and fluid properties should be measured dynamically online. This can be explored in future studies.

It should also be noted that the flow tests with both field-scale and lab-scale flow loops were conducted at ambient temperatures. For applications where fluid temperature may be elevated, such as cases where fluid is re-circulated in high temperature wells, it is suggested that the rheological properties of fluid at elevated temperature should be used in the friction pressure calculation using the correlations developed based on the ambient flow tests. Rheological properties at elevated temperatures can be evaluated using Bohlin rheometer.[108] In future studies, a number of flow tests at elevated temperatures can be performed using the lab-scale flow loop to verify the predictions of the friction factor correlations based on the ambient flow tests.

CHAPTER 6

EXPERIMENTAL STUDY OF FRICTION

BEHAVIOR OF NON-NEWTONIAN FLUID FLOW

IN COILED TUBING

6.1 Procedure of Data Analysis

Data reduction and analysis involved processing and analyzing rheological data from
measurements of Fann Model 35 viscometers and the tubing flow data of tests
conducted with the various tubing sizes and different fluids including water and
polymer solutions.

6.1.1 Data Reduction and Analysis of Rheological Data

The data reduction of Fann viscometer measurements is rather straightforward. The
shear rate and shear stress [for standard rotor-bob (R1-B1) combination] were
calculated using the following equations[117]:

$$\dot{\gamma}_w = 1.703(RPM) \quad\dotfill\quad (6.1)$$

and

$$\tau_w = 0.01066 N\theta_i, \quad\dotfill\quad (6.2)$$

where RPM is the rotational speed of the rotor in rpm (revolutions per minute); θ_i the
dial reading at "i" rpm; N the spring factor (= 1 for No. 1 spring, 0.2 for $1/5^{th}$ spring);
$\dot{\gamma}_w$ the shear rate at the bob surface, 1/sec; and τ_w the shear stress at the bob surface,

lb_f/ft^2. Once data of dial readings at various rpm were obtained, the proper rheological models can be chosen and model parameters can be calculated. As an example, Fig. 6.1 shows the plot of shear stress vs. shear rate for 40 lb/Mgal xanthan fluid sample taken before the flow test through the 2-3/8-in. coiled tubing.
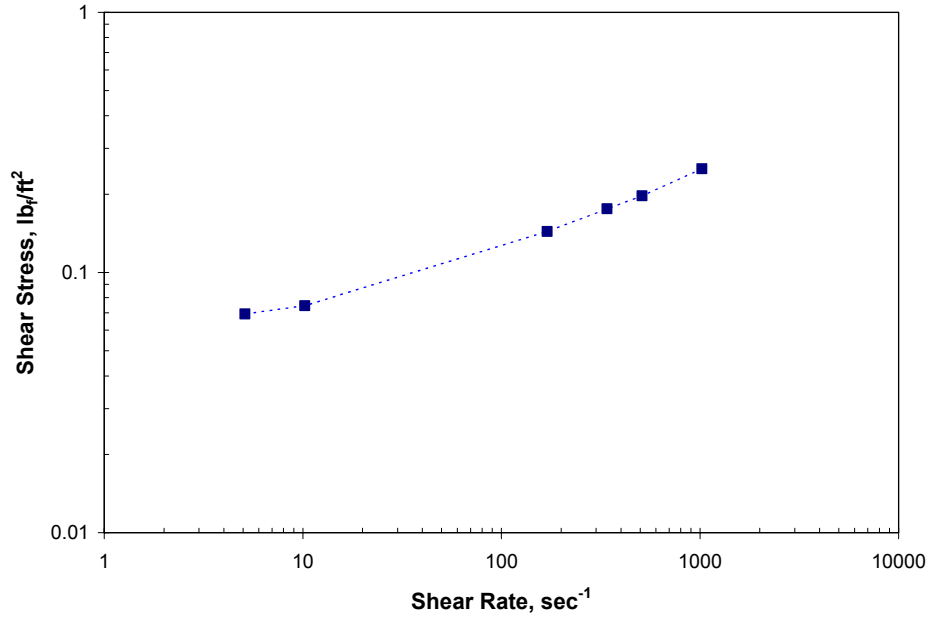
Fig. 6.1—Rheogram of 40 lb/Mgal xanthan sample taken before flow through 2-3/8-in. tubing.

Power law model can be applied to the data points to obtain flow behavior index (n) and consistency index (K_v). K_v is the consistency index from viscometer and can be converted into geometry-independent consistency index (K). K_v was also converted to consistency index for pipe flow, K_p, according to the following equation[117,118]:

$$\frac{K_v}{K_p} = \left(\frac{4n\lambda}{3n+1} \right)^n ,\dots\dots\dots(6.3)$$

123

where

$$\lambda = \left(\frac{s^{s/n}}{ns^2}\right)\left(\frac{s^2-1}{s^{s/n}-1}\right), \quad\text{..(6.4)}$$

in which

$$s = R_c/R_b, \quad\text{..(6.5)}$$

where R_c and R_b are the radii of the cup (the rotor) and the bob.

For certain thin fluids, the dial readings of Fann viscometer at 3 rpm and 6 rpm may not be accurate. Therefore, when calculating power law parameters, the data points at 3 rpm and 6 rpm were not included.

In Appendix D, Tables D.1 through D.4 list the values of flow behavior index and consistency index for various fluids at different stages of fluid testing. The table items are arranged in accordance to the order of testing. Generally, fluids were tested first through larger tubing size and then through smaller tubing size in order to minimize possible shear degradation of polymers.

6.1.2　Data Reduction and Analysis of Flow Test Data

The data recorded in flow tests with the data acquisition system consist of flow rate, pressure drop across straight and coiled tubings, fluid density, and fluid temperature, etc. The transient data points due to flow rate change or due to purging operations were removed so that only the steady state data points were used for the data analysis. Following the traditional approach of pipe flow analysis, plots of friction factor

versus Reynolds number (or generalized Reynolds number for non-Newtonian fluid) were analyzed.

The Fanning friction factor was calculated from the following relationship:

$$f = \frac{\tau_w}{\frac{1}{2}\rho v_m^2} \quad\text{..(6.6)}$$

in which the wall shear stress, τ_w, is calculated from:

$$\tau_w = \frac{d\Delta p}{4L} \quad\text{..(6.7)}$$

where d is the tubing inside diameter and Δp is the frictional pressure drop over a tubing length of *L*. For Newtonian fluid, Fanning friction factor is plotted with Reynolds number, N_{Re}:

$$N_{Re} = \frac{\rho d v_m}{\mu}, \quad\text{..(6.8)}$$

where ρ is fluid density, μ the dynamic viscosity, and v_m is the mean velocity.

The generalized Reynolds number, N_{Reg}, is used for non-Newtonian fluids:

$$N_{Reg} = \frac{d^n v_m^{2-n} \rho}{K_p 8^{n-1}} \quad\text{..(6.9)}$$

where n is the power law flow behavior index and K_p is the fluid consistency index for pipe viscometer. These values are determined using the Fann Model 35 viscometers, as discussed previously.

6.2 Water Tests

6.2.1 Objective

One of the objectives of water tests is for system check and calibration. Water data is often used as a baseline to compare with frictional pressure data of other fluids. In this study, extensive water tests have been conducted through both straight and coiled tubing of various sizes and lengths. These data have been analyzed and compared with published correlations.

6.2.2 Correlations Used in Water Data Analysis

For straight tubing, the following correlations were used.

Drew[119] correlation for smooth pipe:

$$f = 0.00140 + \frac{0.125}{N_{Re}^{0.32}} \quad \text{..(6.10)}$$

where f is the Fanning friction factor, and N_{Re} is Reynolds number. This correlation is applicable in the Reynolds number range of $2100 < N_{Re} < 3 \times 10^6$ and is for Newtonian turbulent flow in smooth pipes.

Chen[120] correlation for rough pipe:

$$\frac{1}{\sqrt{f}} = -4.0 \log \left\{ \frac{h_r}{3.7065d} - \frac{5.0452}{N_{Re}} \log \left[\frac{1}{2.8257} \left(\frac{h_r}{d} \right)^{1.1098} + \frac{5.8506}{N_{Re}^{0.8981}} \right] \right\}, \quad \text{..........(6.11)}$$

where h_r is the tubing roughness projection and d the tubing inside diameter. The Chen correlation can be used for Newtonian turbulent flow in straight pipes with roughness. The result of the Chen correlation is almost identical to the Colebrook[121]

equation for the range of N_{Re} from 4000 to 4×10^8 and (h_r/d) from 0.05 to 5×10^{-7}. Since the Chen equation is an explicit equation, it overcame the drawbacks of the Colebrook equation which is implicit and a trial-and-error method has to be used.

For Newtonian turbulent flow in smooth coiled tubing, Srinivasan[90] correlation can be used:

$$f = \frac{0.084(a/R)^{0.1}}{N_{Re}^{0.2}}, \dotfill (6.12)$$

where a/R is the coiled tubing curvature ratio, and a and R are the radii of tubing and reel drum. Eq. (6.12) is valid for $0.0097 < a/R < 0.135$. Srinivasan correlation is based on flow tests of Newtonian fluids (water and oil) in smooth coiled pipes.

Analyzing water flow data of coiled tubing with roughness has been a challenge. This is mainly because there is no published correlation on the effect of tubing roughness on friction factor in coiled tubing. In this study, we propose the following friction factor correlation for coiled tubing with roughness:

$$f_{rough} = \frac{0.084(a/R)^{0.1}N_{Re}^{0.12}}{(0.125+0.00140N_{Re}^{0.32})}\left[-4.0\log\left\{\frac{h_r}{3.7065d}\right.\right.$$
$$\left.\left.-\frac{5.0452}{N_{Re}}\log\left[\frac{1}{2.8257}\left(\frac{h_r}{d}\right)^{1.1098}+\frac{5.8506}{N_{Re}^{0.8981}}\right]\right\}\right]^{-2}, \dotfill (6.13)$$

where f_{rough} is the Fanning friction factor in rough coiled tubing. The above correlation was derived based on the assumption that the ratio of rough coiled tubing friction factor to the smooth coiled tubing friction factor is approximately equal to the corresponding ratio in straight tubing. Though the accuracy of this assumption is yet

to be verified, the experimental data of the present study seem to indicate that Eq. (6.13) can adequately describe the effect of tubing roughness on friction factor in coiled tubing, as will be discussed below.

In the data analysis, the correlation of water viscosity as function of temperature was used to correct the water viscosity.[122]

6.2.3   Water Tests in 1, 1-1/2, 1-3/4, and 2-3/8-in. Tubing

Figs. 6.2 through 6.5 show the plots of Fanning friction factor versus Reynolds number of water in 1, 1-1/2, 1-3/4, and 2-3/8-in. straight and coiled tubing. Shown also on the plots are the Chen correlation of friction factor for straight tubing and the Srinivasan correlation for smooth coiled tubing. Several observations can be made and discussed as follows.

First, the friction factor in coiled tubing for all tubing sizes (except the 1-3/4-in. tubing reels which have no corresponding straight sections) is significantly higher than in straight tubing. The maximum difference in friction factor can be as high as 30%. The extra flow resistance in coiled tubing is due to the effect of secondary flow in curved flow geometry. Furthermore, the extent of the secondary flow effect is a function of curvature ratio. This is evident by comparing the friction factors of the 500 ft and the 1000 ft 1-in. coiled tubing, as shown in Fig. 6.2. Note that the 500 ft CT string was spooled onto a smaller drum diameter (48 in.) than the 1000 ft CT string which was spooled onto a 72-in. diameter drum. The 500-ft CT reel has a greater curvature ratio (a/R = 0.0169) than the 1000-ft CT reel (a/R = 0.0113). The difference in friction factor between the 500-ft and 1000-ft CT reels can be as much

as 8%. Meanwhile, for the CT reels with same curvature ratios, their friction factors are approximately the same, as shown in Figs. 6.3 and 6.5.
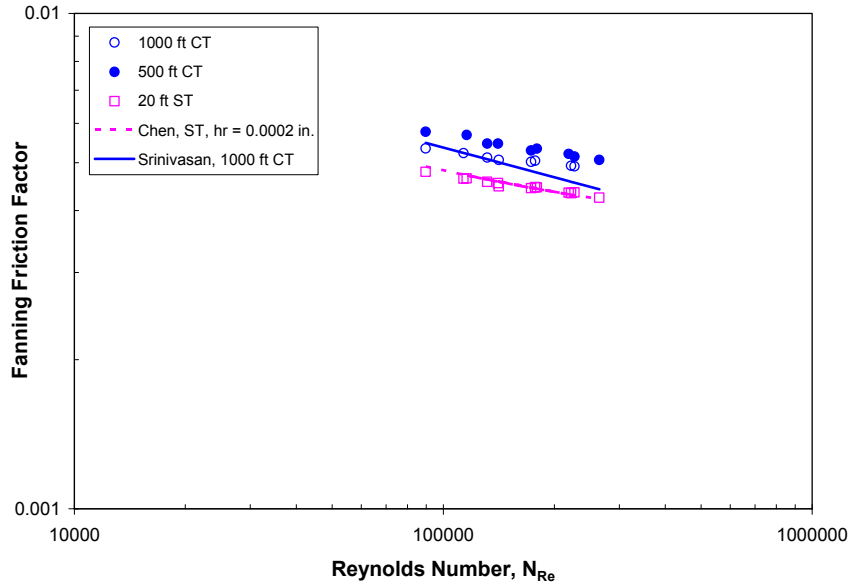
Fig. 6.2—Fanning friction factor versus Reynolds number of water in 1-in. straight and coiled tubing.
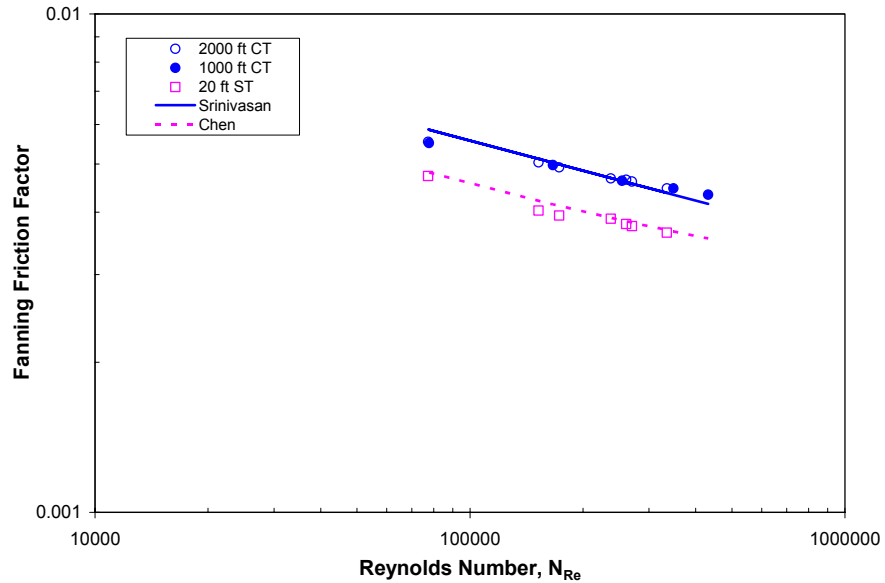
Fig. 6.3—Fanning friction factor versus Reynolds number of water in 1-1/2-in. straight and coiled tubing.
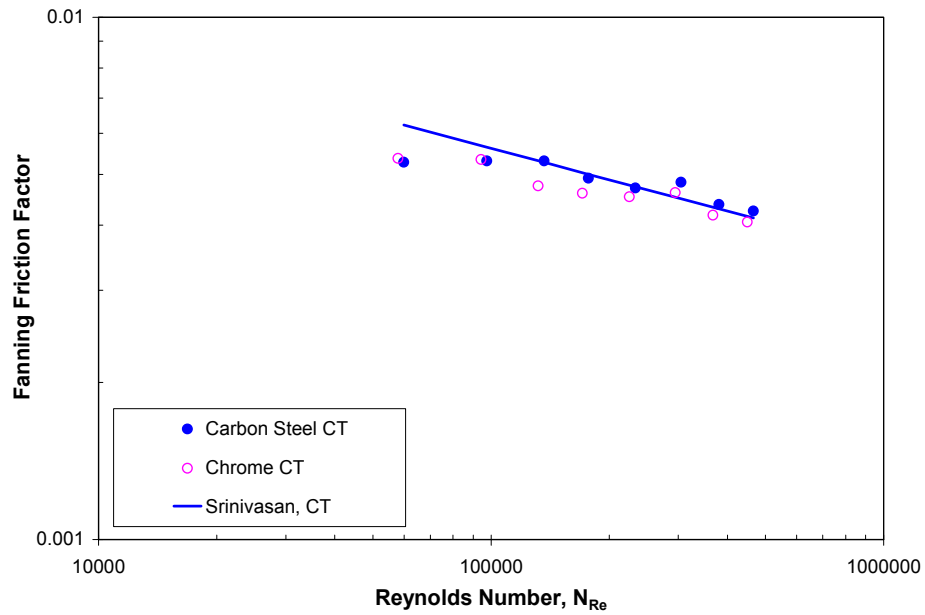
Fig. 6.4—Fanning friction factor versus Reynolds number of water in 1-3/4-in. chrome and carbon steel coiled tubing.
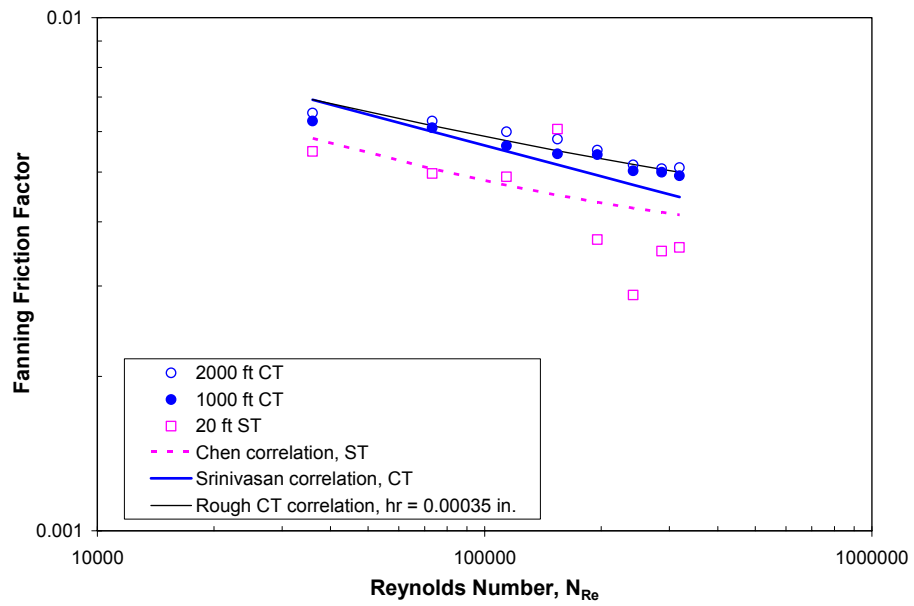
Fig. 6.5—Fanning friction factor versus Reynolds number of water in 2-3/8-in. straight and coiled tubing.

130

Second, Figs. 6.2 and 6.5 indicate that the friction factors in the 1-in. and 2-3/8-in. coiled tubing reels are higher than the Srinivasan correlation. Therefore, tubing roughness effect is evident in both CT sizes. To estimate the magnitude of possible tubing roughness, we applied the previously proposed correlations [Eq. (6.13)] to match the friction factor data of the 1-in. and 2-3/8-in. coiled tubing. Fig. 6.6 shows the result of the 1-in. CT reels. It is seen that the proposed correlation is able to match
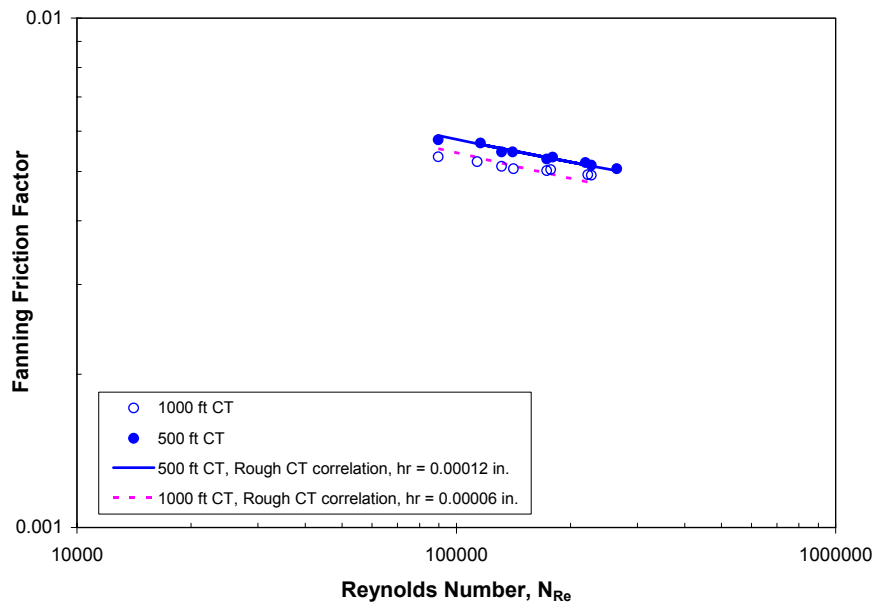
Fig. 6.6—Friction factor versus Reynolds number of 1-in. tubing, measured and predicted using the proposed rough CT correlation.

the friction factor data of the 500-ft and the 1000-ft coiled tubing with tubing roughness of 0.00012 in. and 0.00006 in. respectively. As indicated in Fig. 6.5, a tubing roughness of 0.00035 in. results in a very good match of the friction factor data with Eq. (6.13). It is encouraging to find out that these roughness values are very

close to the roughness data measured with Tuboscope's Hommel Surface Roughness Meter on similar coiled tubing. The measured average roughness for carbon steel coiled tubing is between 0.000025 to 0.000149 in.[††]

It is important to point out that the newly proposed correlation [Eq. (6.13)] can not only match the majority of the data on point-to-point basis, but, more importantly, also provide a good match to the trend of the data. This has been proven for both 1-in. and 2-3/8-in. tubing data sets, see Figs. 6.5 and 6.6 respectively. In these plots, it can be seen that the Srinivasan correlation has a steeper slope than those of the data points which exhibit flatter slopes. Recall the friction factor behavior of Newtonian fluid in straight pipes, such as the Moody[123] diagram of friction factor. The smooth pipe flow or "hydraulically smooth" pipe flow is characterized by steeper slopes than rough pipe flow, with slope depending on the magnitude of the Reynolds number. The flatter lines indicate more dominance of roughness at higher Reynolds numbers. The newly proposed correlation [Eq. (6.13)] is shown to be able to effectively adjust the slope of the Srinivasan correlation to better match the experimental data of coiled tubing with roughness.

In Fig. 6.3, it can be seen that the friction factor data of the 1-1/2-in. coiled tubing is very close to the Srinivasan correlation. But, this does not necessarily mean that the 1-1/2-in. CT reels are smooth. It is more likely that the inner diameter of the 1-1/2-in. tubing had been changed due to previous usage. Prior to this research project, the 1-1/2-in. CT reels had been used extensively for testing fracturing

---

[††] Thanks to Dr. Roderic Stanley of Quality Tubing, Inc. for providing this data and discussion.

132

slurries. These previous tests might have altered the tubing inner diameter (enlarged due to slurry erosion). It would be very tempting to have one parameter, either tubing ID or roughness measured independently so that the other parameter could be estimated from the water test data using the correlation we proposed, Eq. (6.13). But, neither measurement was available.

It is interesting to note that the friction factor in the 1-3/4-in. chrome coiled tubing is lower than the 1-3/4-in. carbon steel coiled tubing. It is therefore believed that the chrome tubing has less roughness effect. The friction factor of the chrome tubing is slightly lower than the Srinivasan correlation. By using the new correlation [Eq. (6.13)], the roughness in the 1-3/4-in. carbon steel coiled tubing is estimated as 0.00005 in.

Third, the friction factor data in straight tubing of all tubing sizes can be matched by Chen correlation with various tubing roughnesses. For the 1-in. straight tubing, a roughness of $h_r = 0.0006$ in. in Chen correlation results in good match with the data. In the 20-ft straight tubing of the 1-1/2-in. diameter, Chen correlation with roughness of 0.00006 in. matched the data well. As shown in Fig. 6.5, the data of the 20-ft straight tubing of 2-3/8-in. diameter show large scatter. For large tubing sizes (especially 2-3/8-in.), the data from tests on the 200-ft straight tubing sections are more reliable. This is evident from Fig. 6.7 which shows the result of friction factor versus Reynolds number for water in the 200-ft long and 2-3/8-in. diameter straight tubing section.
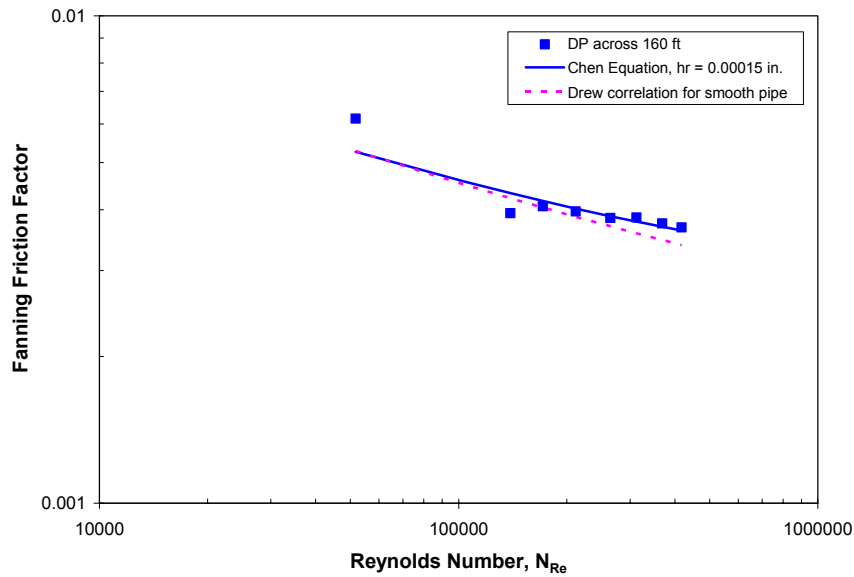
Fig. 6.7—Fanning friction factor versus Reynolds number of water in 200 ft straight tubing of 2-3/8-in. diameter (DP measured across 160 ft).

6.2.4   Water Tests in ½-in. Tubing

Fig. 6.8 presents the results of water tests in the four ½-in. coils and the 10-ft straight section in the lab-scale flow loop. The four coils have curvature ratios of a/R = 0.01, 0.019, 0.031, and 0.076 respectively. It can be clearly seen that as curvature ratio increases, the friction factor increases. The significance of the effect of curvature on friction pressure is thus demonstrated. The straight tubing data have been compared with Drew correlation and the coiled tubing data with the Srinivasan correlation. Since each coil has a different curvature ratio, the Srinivasan correlation has to be applied separately with each curvature ratio corresponding to each coil. For example, the comparison in Figs. 6.9 and 6.10 (for a/R = 0.01 and 0.031 respectively) shows that the friction factor data of straight tubing and the coils are in close agreement with the Drew correlation and the Srinivasan correlation respectively. The reason for the

134
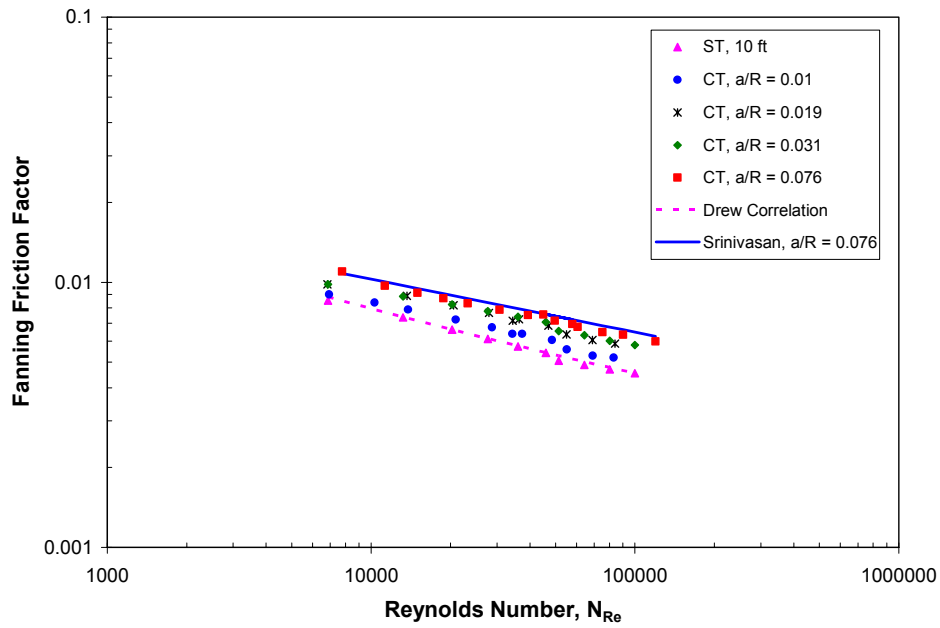
Fig. 6.8—Fanning friction factor versus Reynolds number of water in ½-in. straight and coiled tubing.
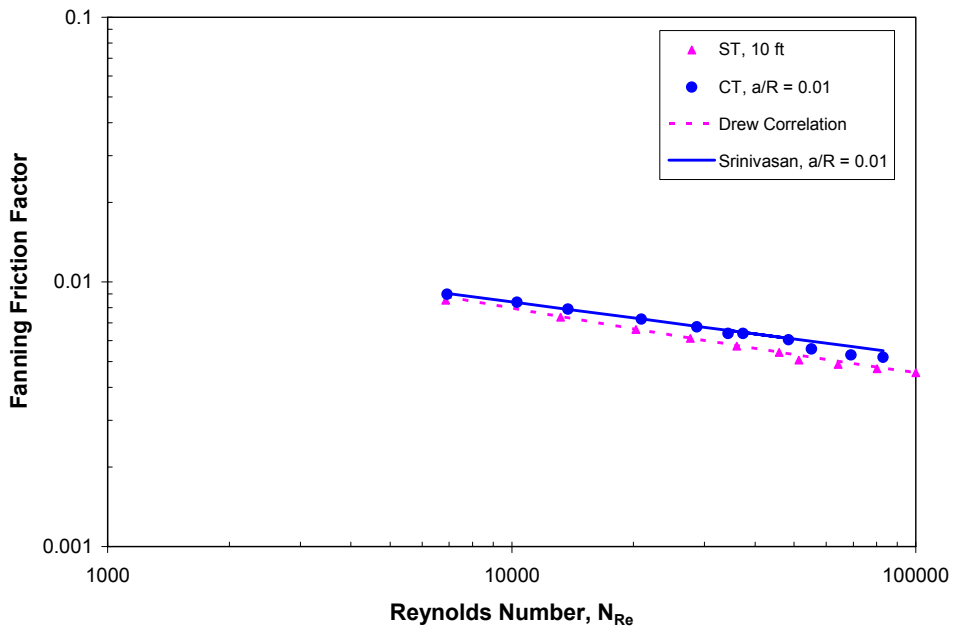
Fig. 6.9—Comparison of Fanning friction factor data of water with Drew and Srinivasan correlations for a/R = 0.01.

135
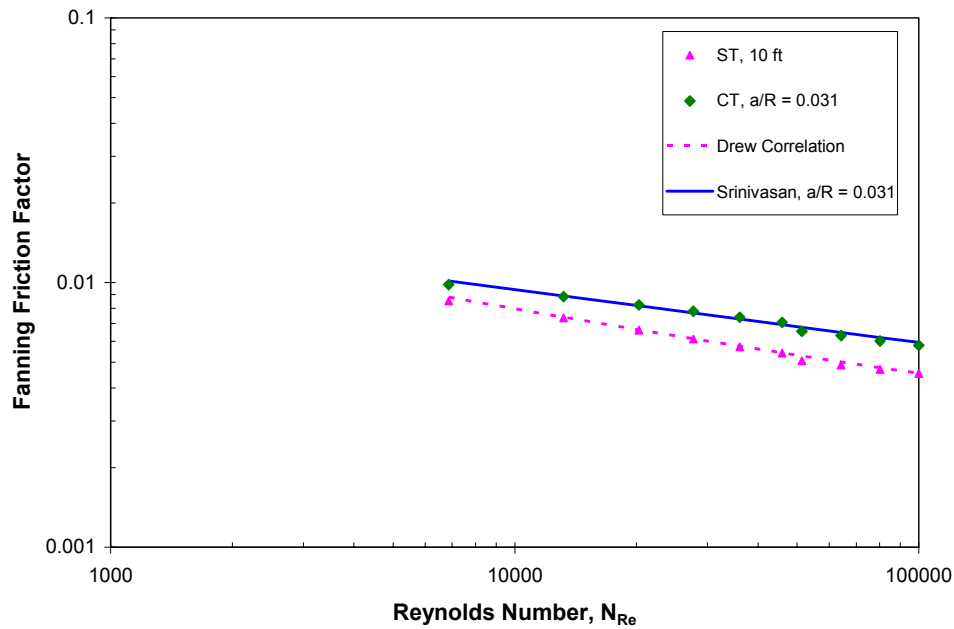
Fig. 6.10—Comparison of Fanning friction factor data of water with Drew and Srinivasan correlations for a/R = 0.031.

close agreement is because the straight tubing section and the four coils were made of stainless tubing. Therefore, they exhibit behavior of smooth tubing.

6.3   Flow Tests of Non-Newtonian Fluids in Field-Size Flow Loop

6.3.1   Flow Tests of Xanthan Fluids

Xanthan fluids at three polymer concentrations (10, 20, and 40 lb/Mgal) have been tested using the field-scale flow loop. Figs. 6.11 through 6.14 show the friction behavior on the traditional plots of Fanning friction factor versus generalized Reynolds number. On the these plots, we also plotted the Hagen-Poiseuille equation
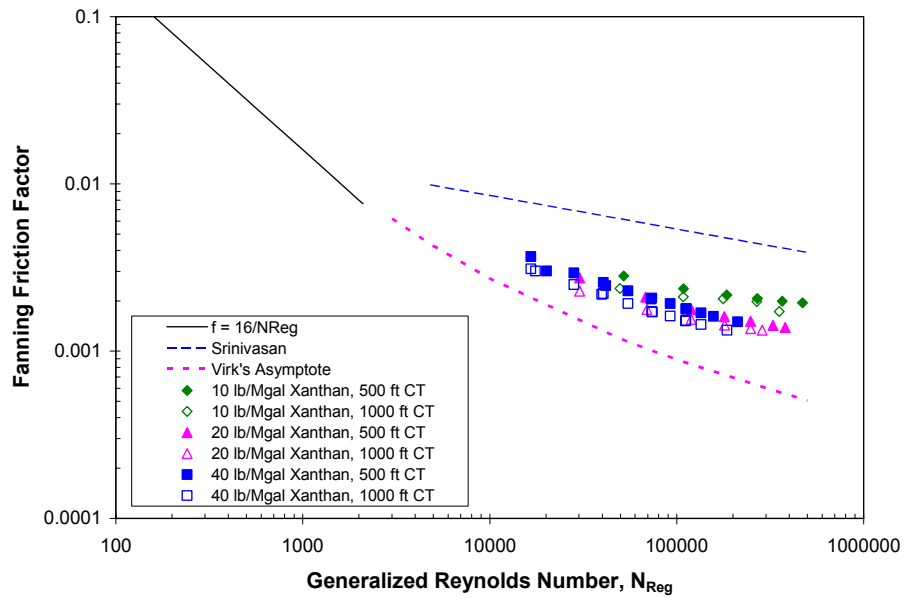
Fig. 6.11—Friction factor behavior of 10, 20, and 40 lb/Mgal xanthan in 1-in. coiled tubing.
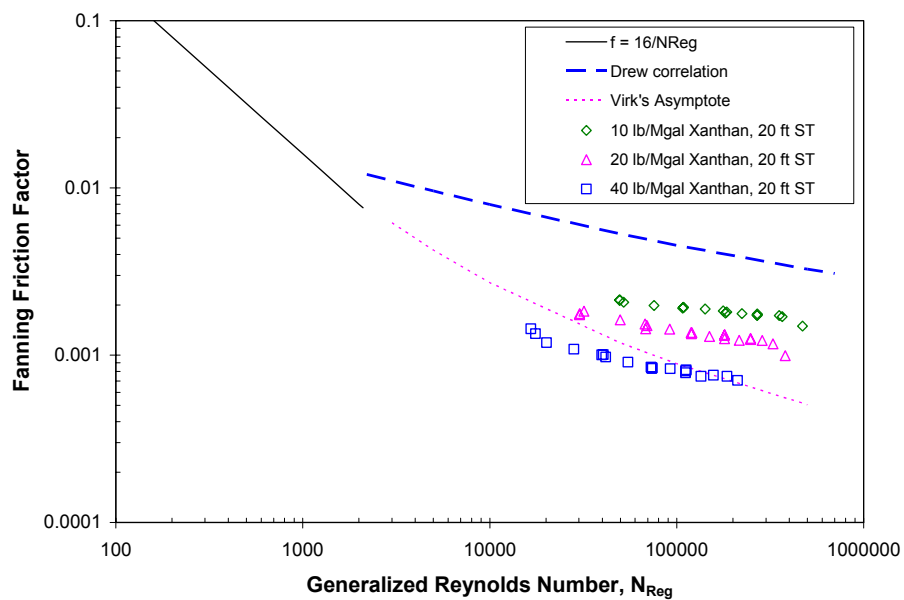
Fig. 6.12—Friction factor behavior of 10, 20, and 40 lb/Mgal xanthan in 1-in. straight tubing.

137
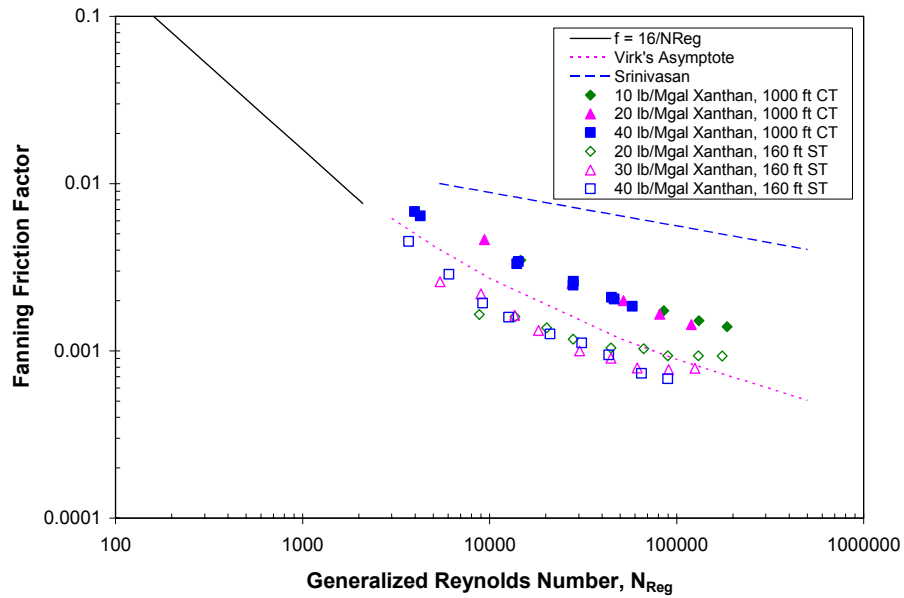
Fig. 6.13—Friction factor behavior of 10, 20, 30, and 40 lb/Mgal xanthan in 1-1/2-in. straight and coiled tubing.
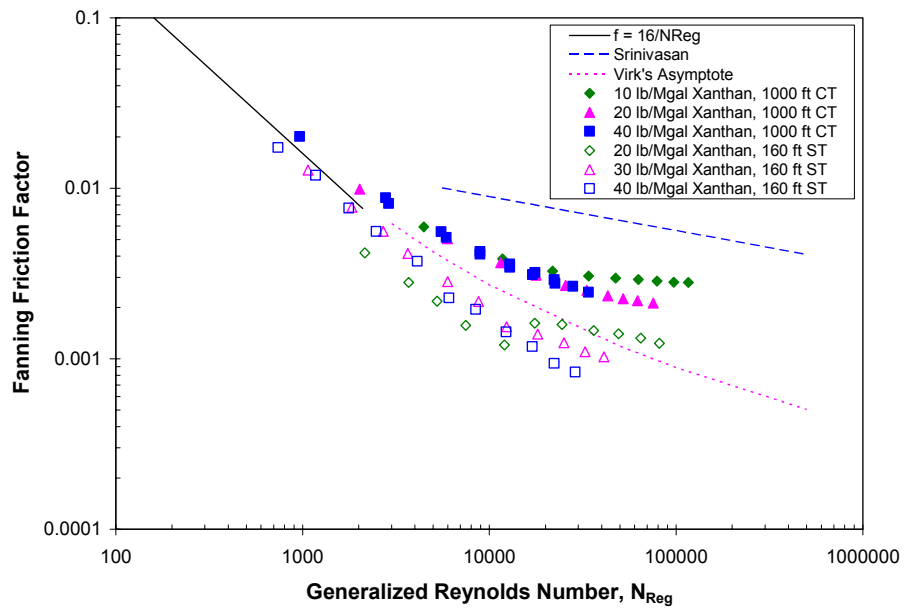
Fig. 6.14—Friction factor behavior of 10, 20, 30, and 40 lb/Mgal xanthan in 2-3/8-in. straight and coiled tubing.

138

(f = 16/N_{Reg}) for straight laminar tubing flow, Srinivasan correlation for turbulent Newtonian flow in coiled pipe [Eq. (6.12)], and Virk's maximum drag reduction asymptote for dilute polymer solutions in straight tubing flow which is given below:

$$1/\sqrt{f} = 19.0 \log_{10} N_{Re} \sqrt{f} - 32.4 \, .$$ ....(6.14)

where f is Fanning friction factor and N_{Re} is Reynolds number. For clarity, the friction factor data of xanthan fluids in 1-in. coiled tubing and straight tubing are plotted separately in Figs. 6.11 and 6.12. Several features can be observed from these plots.

First, straight tubing versus coiled tubing. The most significant feature of coiled tubing flow is that its friction factor is much higher than that of straight tubing. The difference in friction factor can be between 20% to 170%, depending on the generalized Reynolds number and polymer concentration. At low polymer concentration, the maximum difference in friction factor is smaller than at higher polymer concentration.

Second, the effect of polymer concentration on friction factor of straight and coiled tubing. For straight tubing (Fig. 6.12), as xanthan polymer concentration increases from 10 to 40 lb/Mgal, the friction factor decreases drastically. The more concentrated xanthan polymer solution tends to result in lower friction. The trend of straight tubing data approaching horizontal lines indicates that friction in 1-in. tubing at high Reynolds number is affected by tubing roughness. In coiled tubing, the effect of polymer concentration is not as important as in straight tubing except at the lowest

xanthan concentration of 10 lb/Mgal. At 10 lb/Mgal, the data points turn to be flat, implying that the roughness is playing a bigger role.

Third, by comparing the friction factor of the 500 ft and 1000 ft CT, we can see that the friction factor of the 500 ft CT is consistently higher than that of the 1000 ft CT. The difference is due to the effect of curvature ratio and can be as much as 20%. Recall that the 500 ft CT reel has a larger curvature ratio, therefore, it produces greater friction factor than the loosely spooled 1000 ft CT reel.

Fourth, the data points of coiled tubing in turbulent regime are all significantly lower than the Srinivasan correlation, indicating that the xanthan fluids exhibit significant drag reduction. More detailed discussion on drag reduction in coiled tubing will be made in Chapter 7.

In Figs. 6.13 and 6.14, the straight tubing data were from the 200 ft long straight tubing sections (with 160 ft DP measurement length). In Figs. 6.13 and 6.14, we see that there can be regions where the difference in friction factor between coiled tubing and straight tubing is the most significant. At a generalized Reynolds number of about 28,800, the friction factor in the 2-3/8-in. coiled tubing is 185% higher than that in straight tubing. As the generalized Reynolds number decreases, the difference in friction factor between coiled tubing and straight tubing becomes smaller. The flow of xanthan polymer solutions in straight tubing exhibits significantly extended laminar flow for generalized Reynolds number up to 10,000 or 20,000, see Fig. 6.14. Therefore, the friction factor in straight tubing is much lower than what would be expected for Newtonian fluid in turbulent flow at this high Reynolds number. On the

140

other hand, the friction factor of coiled tubing flow deviates early from the $f = 16/N_{Reg}$ line. Even at low Reynolds number, the friction factor in coiled tubing is higher than predicted from $f = 16/N_{Reg.}$ This is due to the secondary flow effect in coiled tubing. Only in very slow motion, the secondary flow effect can be neglected. As Reynolds number increases, the effect of secondary flow becomes stronger, resulting in more flow resistance in coiled tubing. The net result of the two different mechanisms in straight and coiled tubing – extended laminar flow in straight tubing and the secondary flow effect in coiled tubing – is that the difference in friction factor would reach a maximum after which the difference will become smaller as the Reynolds number increases. This is because when the Reynolds number is high enough, turbulence and tubing roughness will play more important role in the flow resistance in both straight and coiled tubing. It is logical to believe that at very high Reynolds number, the difference in friction factor between coiled and straight tubing will be even smaller and will be mainly dominated by the roughness of the tubing. We have seen this behavior in water data analysis. For example, the difference in friction factor of water in 1-in. coiled tubing is only about 8 and 22% higher than that of straight tubing for the 1000 ft and 500 ft CT respectively. In the case of water flow in 1-in. tubing, the Reynolds number is from 90,000 to 260,000. The feature that xanthan fluids display most significant friction difference in certain Reynolds number region has significant impact on the CT hydraulics calculations because most field coiled tubing injection operations will be performed at similar flow rates to what we have investigated.

6.3.2 Flow Tests of PHPA Fluids

The friction factor behavior of 20 and 40 lb/Mgal PHPA fluids in 1, 1-1/2, and 2-3/8-in. coiled and straight tubing are shown in Figs. 6.15 to 6.17 respectively. In general, the friction factor behavior is similar to that of xanthan fluids. The friction factor in coiled tubing is seen to be significantly higher than in straight tubing. The difference can be more pronounced for the larger pipe size, as seen in Fig. 6.17. Due to the higher viscosity of PHPA fluids, the maximum Reynolds number investigated is lower than in the case of xanthan fluids. For the 1-in. straight tubing, the friction factor stays close to the Virk's maximum drag reduction (MDR) asymptote. This is different from the xanthan fluids where the friction factor becomes higher than the Virk's MDR asymptote when xanthan concentration is decreased from 40 lb/Mgal to 20 and 10 lb/Mgal. This indicates that PHPA fluids can retain good drag reduction performance in straight tubing even at Reynolds number as high as 100,000. At conditions of low generalized Reynolds number, both coiled tubing and straight tubing approach the Hagen-Poiseuille equation, see Fig. 6.17.

6.3.3 Flow Tests of Guar Fluids

Figs. 6.18 to 6.21 show the plots of Fanning friction factor of guar fluids in three tubing sizes respectively. In Figs. 6.18 and 6.19, the maximum friction factor difference between coiled tubing and straight tubing can be as high as 134% for the 500 ft CT and 53% for the 1000 ft CT. Again, the coiled tubing and straight tubing display quite different behavior. In coiled tubing, the effect of guar concentration is
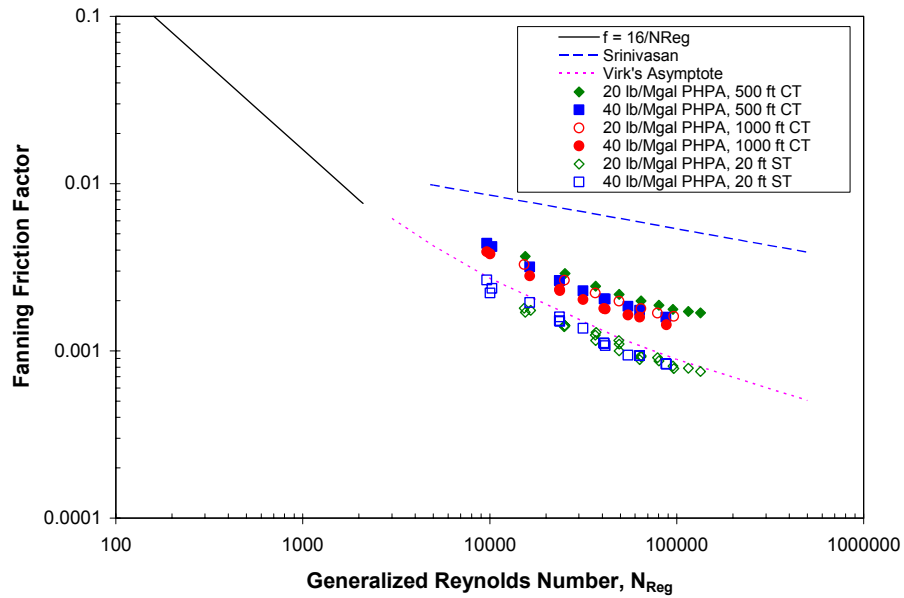
Fig. 6.15—Friction factor behavior of 20 and 40 lb/Mgal PHPA in 1-in. straight and coiled tubing.
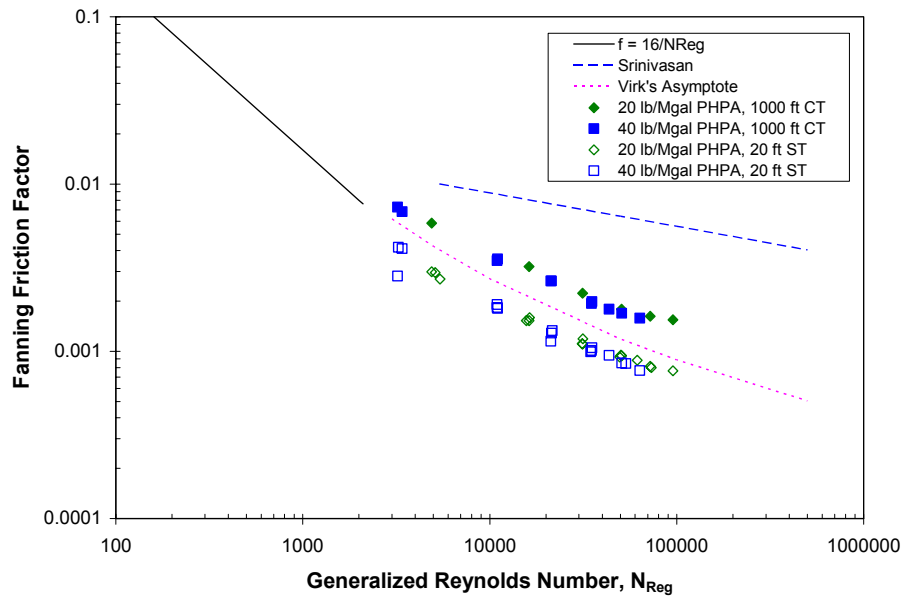
Fig. 6.16—Friction factor behavior of 20 and 40 lb/Mgal PHPA in 1-1/2-in. straight and coiled tubing.

143
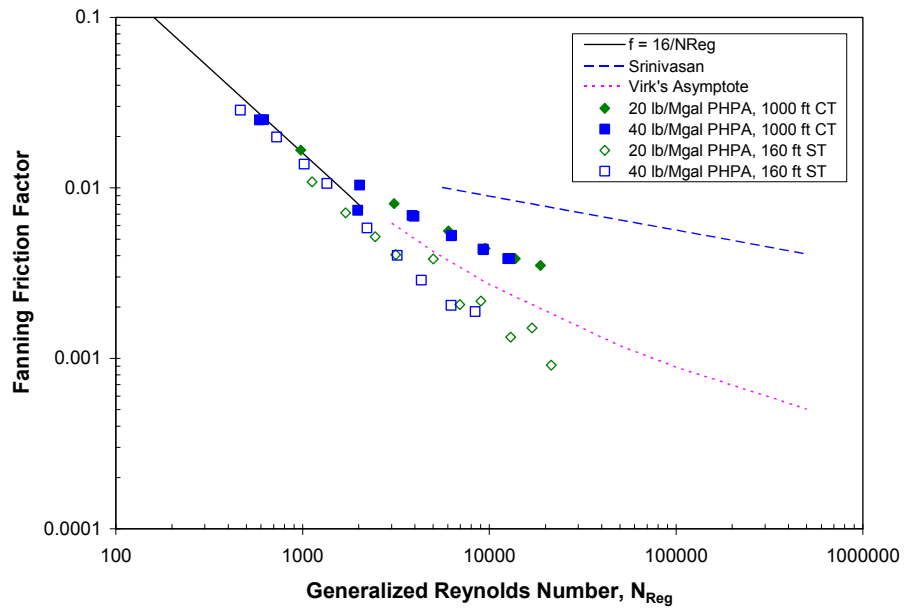
Fig. 6.17—Friction factor behavior of 20 and 40 lb/Mgal PHPA in 2-3/8-in. straight and coiled tubing.
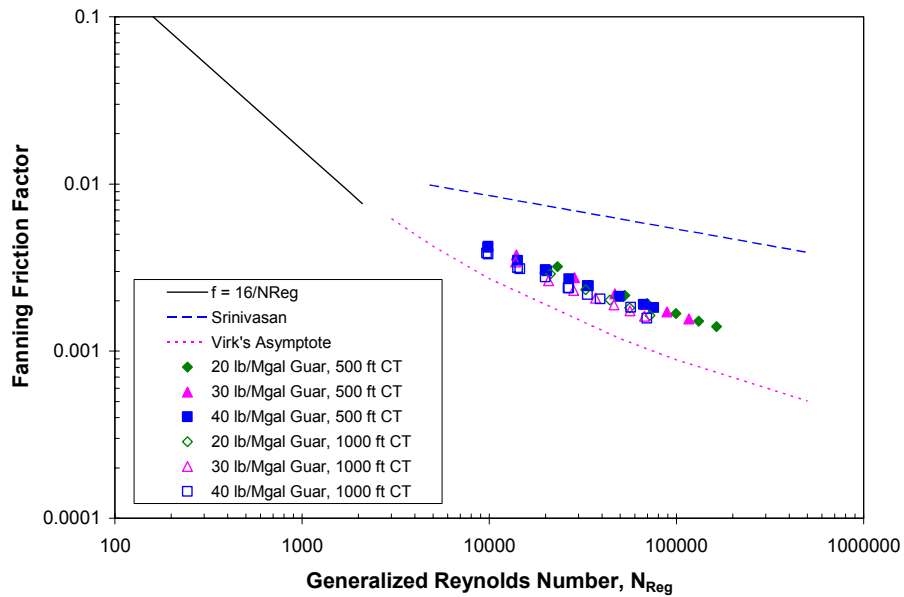
Fig. 6.18—Friction factor behavior of 20, 30, and 40 lb/Mgal guar in 1-in. coiled tubing.

144
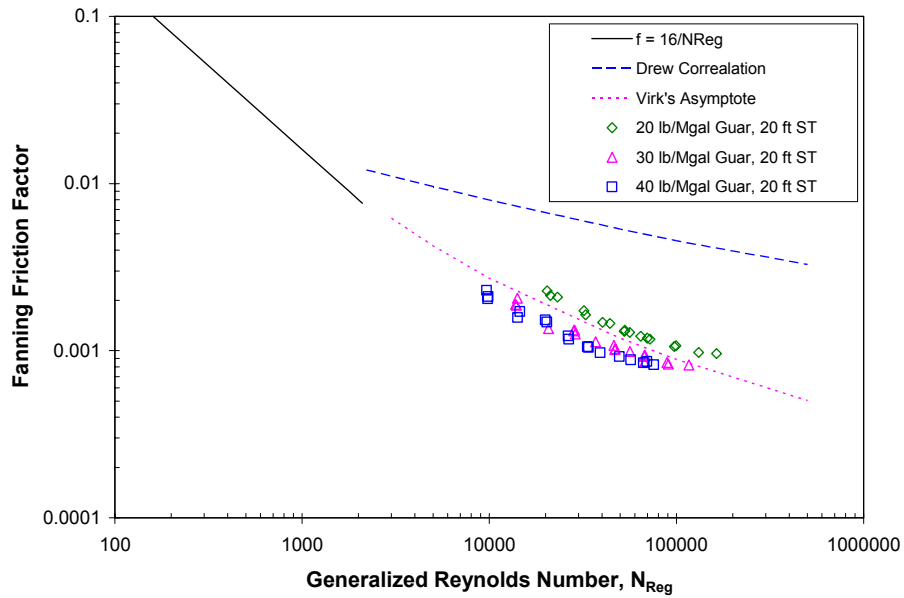
Fig. 6.19—Friction factor behavior of 20, 30, and 40 lb/Mgal guar in 1-in. straight tubing.
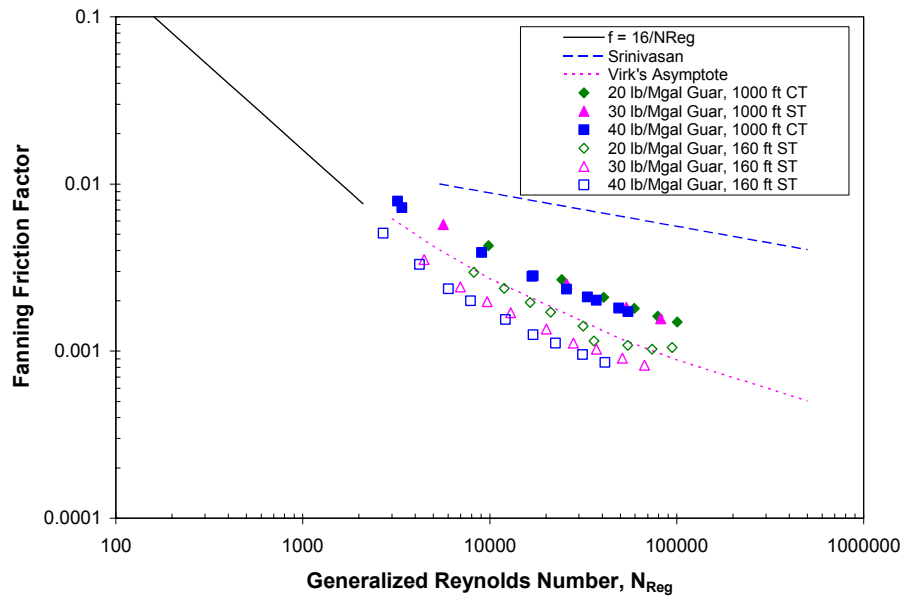
Fig. 6.20—Friction factor behavior of 20, 30, and 40 lb/Mgal guar in 1-1/2-in. straight tubing and coiled tubing.
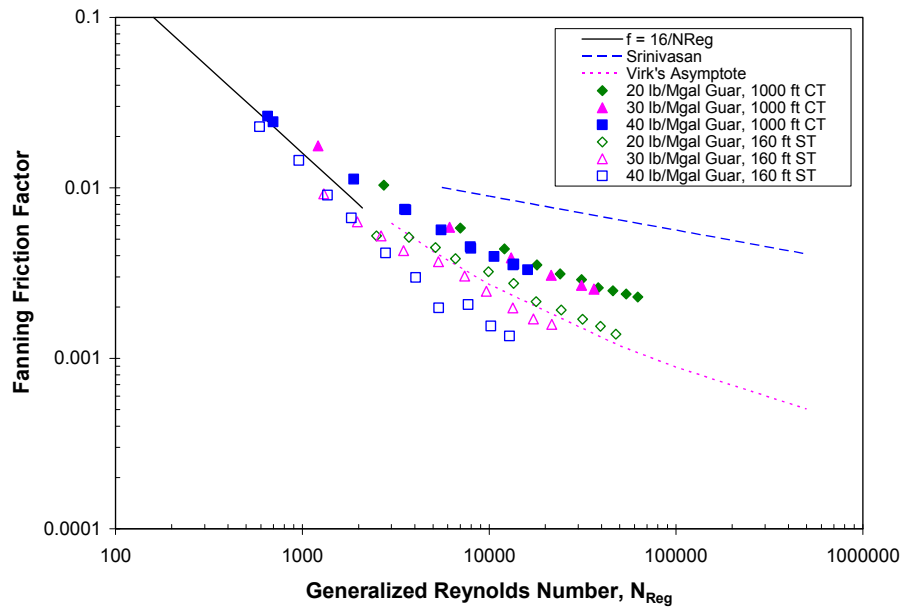
Fig. 6.21—Friction factor behavior of 20, 30, and 40 lb/Mgal guar in 2-3/8-in. straight and coiled tubing.

not significant on the plots of friction factor vs. generalized Reynolds number. In straight tubing, the friction factor of the 20 lb/Mgal guar is significantly higher than the 30 and 40 lb/Mgal guar. In Fig. 6.21, we see bigger effect of guar concentration for straight tubing than for coiled tubing. Similar to both xanthan and PHPA fluids, the big difference between coiled tubing and straight tubing occurs at Reynolds number above 1000. At very low Reynolds number, the difference between straight and coiled tubing is smaller.

6.3.4   Flow Tests of HEC Fluids

Figs. 6.22 to 6.25 show the friction factor versus generalized Reynolds number for HEC fluids in 1, 1-1/2, and 2-3/8-in. tubing systems. The friction factor behavior of coiled tubing shows similar characteristics to the other three polymer types, that is,

the friction factor in coiled tubing is significantly higher than in straight tubing. The friction factor of coiled tubing deviates early from the line of $f = 16/N_{Reg}$ at low Reynolds number. As Reynolds number increases, the friction factor in coiled tubing keeps turning to more horizontal. The friction factor in straight tubing, on the other hand, first follows the extended laminar flow behavior (that is, $f = 16/N_{Reg}$), then at Reynolds number of about 20,000 (for 1-in. tubing), the friction factor takes a relatively sharp turn toward horizontal. This behavior is obvious in the flow data of the 1-in. tubing. In larger tubing sizes, the flow rate is not high enough to display the behavior of friction factor turning to horizontal. Note that in Fig. 6.24, the data from the 20-ft straight tubing were used since no tests were performed through the 200-ft straight tubing sections for HEC fluids.
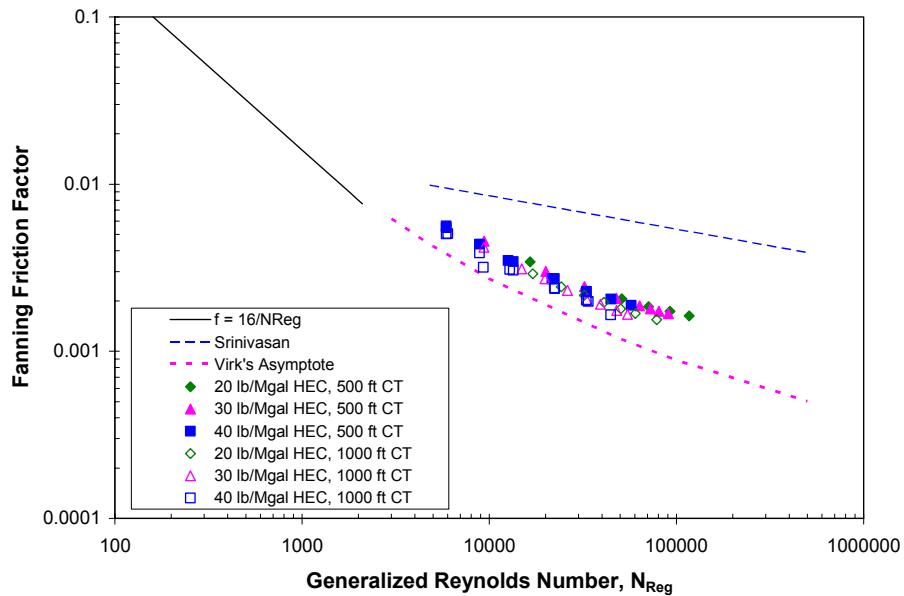
Fig. 6.22—Friction factor behavior of 20, 30, and 40 lb/Mgal HEC in 1-in. coiled tubing.
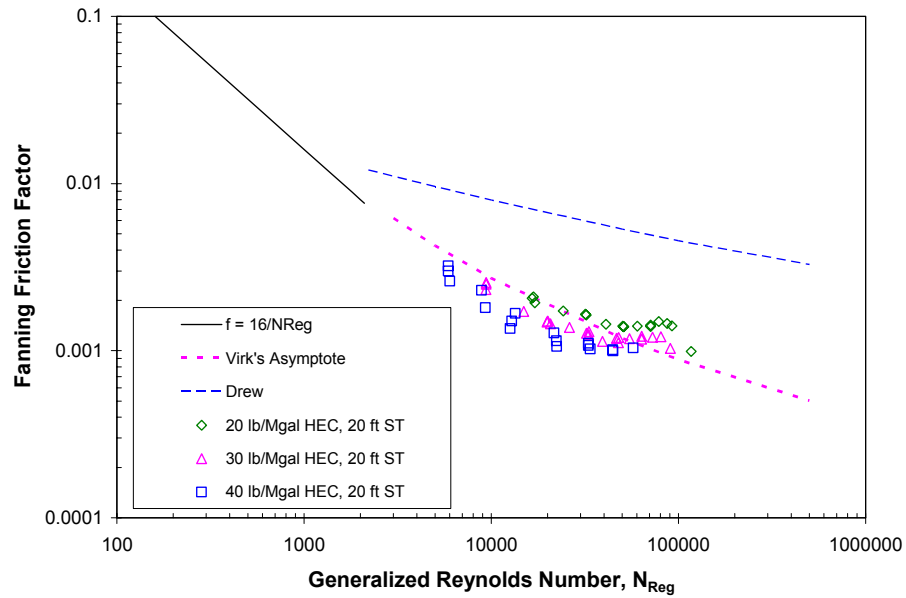
Fig. 6.23—Friction factor behavior of 20, 30, and 40 lb/Mgal HEC in 1-in. straight tubing.
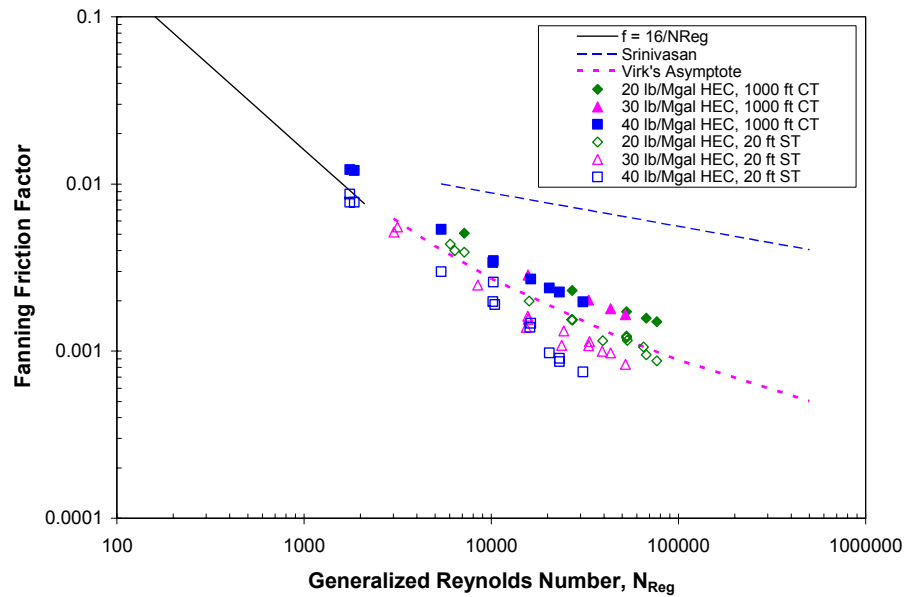
Fig. 6.24—Friction factor behavior of 20, 30, and 40 lb/Mgal HEC in 1-1/2-in. straight and coiled tubing.
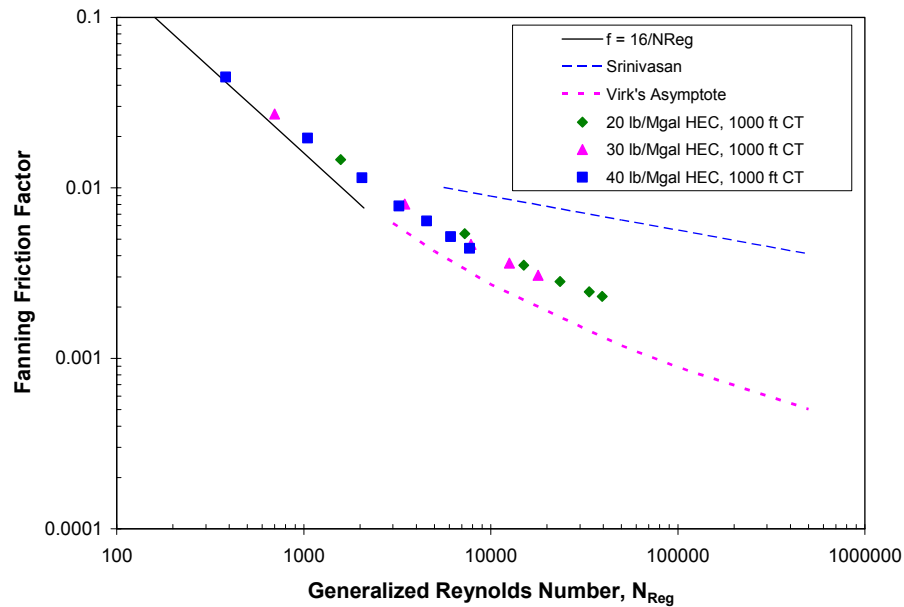
Fig. 6.25—Friction factor behavior of 20, 30, and 40 lb/Mgal HEC in 2-3/8-in. coiled tubing.

6.3.5   Development of Friction Factor Correlations

To make the above full-scale experimental data and observations useful to the engineering design calculations, empirical correlations of friction factor of xanthan, PHPA, guar, and HEC fluids have been developed. In order to obtain such correlations, the friction factor data were plotted as Fanning friction factor versus generalized Dean number as defined previously by Eq. (3.70).

Figs. 6.26 to 6.29 show such plots for guar, HEC, PHPA, and xanthan fluids respectively. In preparing these plots, only those data points whose generalized Reynolds number is greater than the corresponding critical Reynolds number as predicted by the Srinivasan correlation [Eq. (2.13)] were included. The reason is that the effect of curvature for laminar flow in coiled tubing is relatively small and can be estimated using laminar correlations such as our theoretical correlation for laminar

149

flow. In fact, the vast majority of our data points from the field-size flow loop are at high Reynolds number (higher than the critical Reynolds number predicted by Srinivasan correlation). Therefore, only very few outlying data points were excluded. Yet excluding these few data points would improve the correlation quality.

Several observations can be made and will be useful for selecting the appropriate correlations. First, all fluids except 10 lb/Mgal xanthan show well-behaved data trend when plotted as Fanning friction factor versus generalized Dean number.
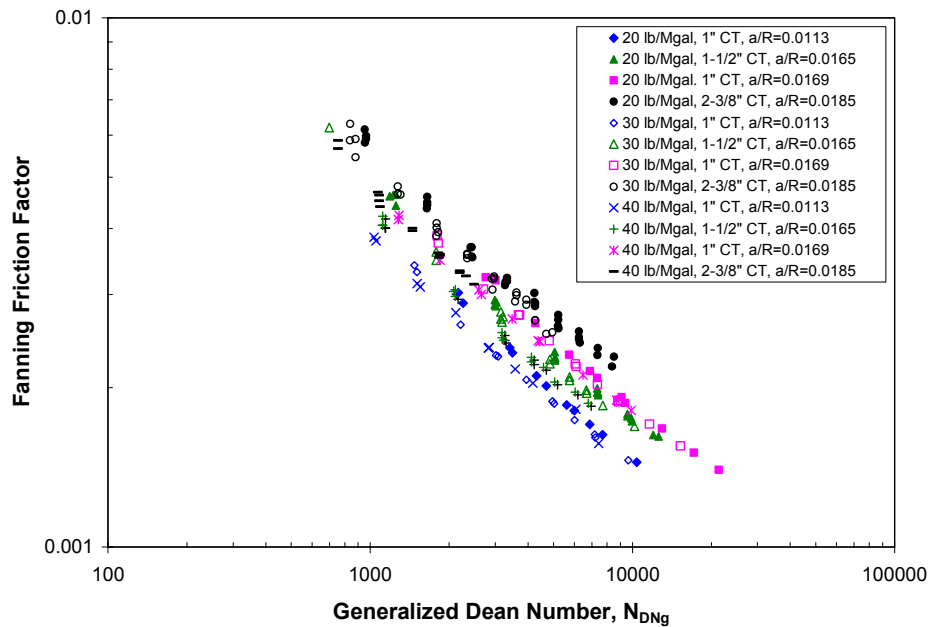
Fig. 6.26—Composite plot of Fanning friction factor vs. generalized Dean number for guar fluids.
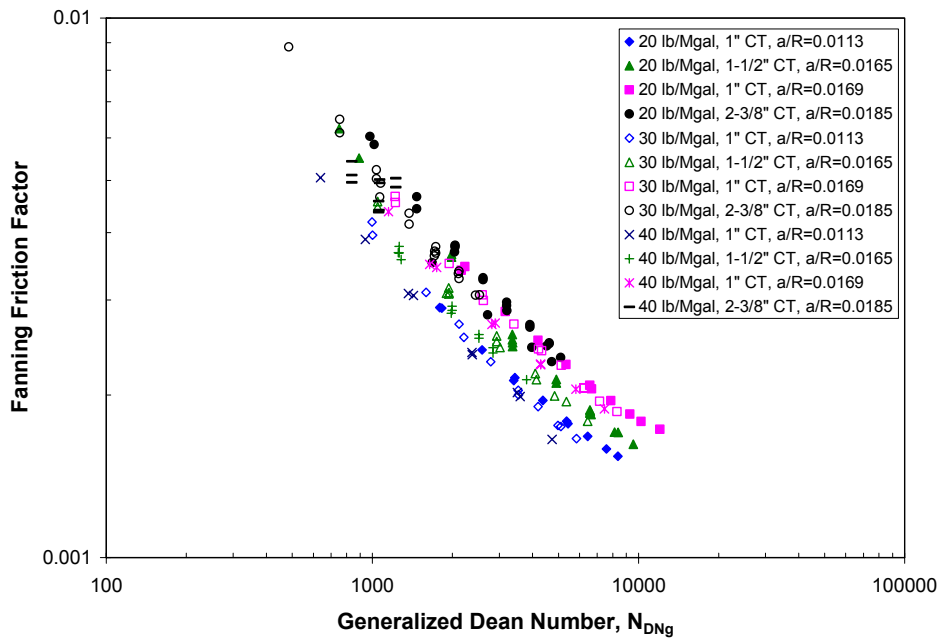
Fig. 6.27—Composite plot of Fanning friction factor vs. generalized Dean number for HEC fluids.
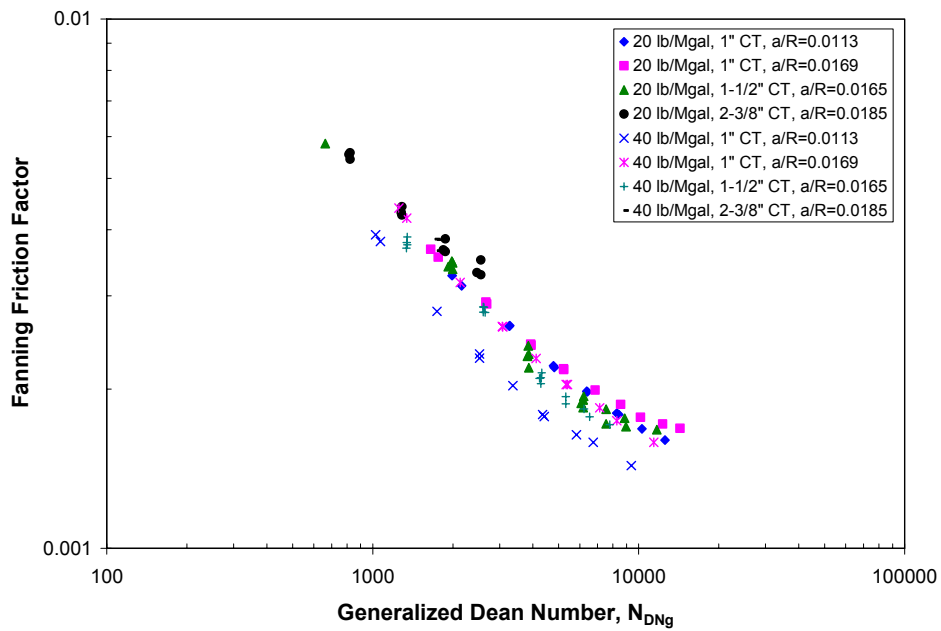
Fig. 6.28—Composite plot of Fanning friction factor vs. generalized Dean number for PHPA fluids.

151
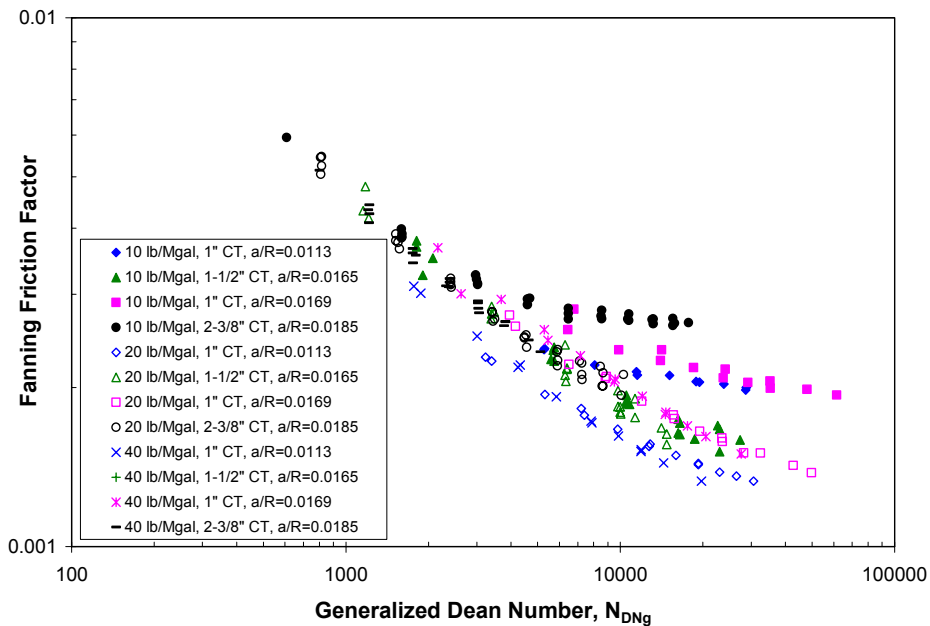
Fig. 6.29—Composite plot of Fanning friction factor vs. generalized Dean number for xanthan fluids.

The data points of guar fluids seem to give straight lines with similar slopes over wide range of generalized Dean number. For other types of fluids, data points can be approximated as straight lines only over narrower ranges of generalized Dean number. If the range of the generalized Dean number is expanded to include all data points, the data display certain degree of curvature.

Second, the vertical separation in these plots is largely due to difference in curvature ratio. For clarity, we use four different colors to identify data sets of different curvature ratios. We also chose consistent marker convention so that it will be easier to distinguish between different polymer concentrations within each data set of a given curvature ratio. It can be easily seen that the data sets form color bands representing four curvature ratios. Within each color band, the minor separation

152

between sub-sets of data indicates that the effect of polymer concentration is slight on these plots.

Based on the above observations, it is concluded that a two-parameter type correlation such as the Srinivasan correlation for Newtonian turbulent flow in coiled pipe is not sufficient to describe the friction behavior of non-Newtonian fluid turbulent flow in coiled tubing, since a two-parameter correlation of the Srinivasan type can only be a straight line relationship on the log-log coordinates of f vs. N_{DNg}. In this case, a three-parameter correlation of the following form will be required:

$$f_M = \frac{A}{N_{DNg}^{B}} + C \quad \text{...(6.15)}$$

where f_M is the friction factor of mean curve, A, B, and C are correlation constants. This form of correlation has been successfully used by Shah[124] for obtaining friction factor correlation of non-Newtonian fluid flow in straight tubing.

For each type of polymer fluids, we apply Eq. (6.15) to all data points to get a mean curve for all data of the polymer type. Table 6.1 summarizes the correlation constants A, B, and C for each type of fluids.

Table 6.1—Correlation Constants of the Mean Curve

Fluid	A	B	C
Xanthan	0.32669	0.64877	0.00102
PHPA	0.43054	0.67836	0.00078
Guar	0.53349	0.70666	0.00100
HEC	1.48075	0.86895	0.00119

The feature of each of these mean curves is that they are more or less parallel to each sub-set of data for a given tubing size (and curvature ratio) and fluid concentration. Then, by shifting the data set of each fluid by a factor of M, we can get a least-square fit with the mean curve. The shift factors thus obtained are shown in Tables 6.2 to 6.5.

Table 6.2—Shift Factors to Match the Mean Curve (Guar Fluids)

Fluid	n	K_p, $lb_f s^n/ft^2$	a/R	M
20 lb/Mgal Guar	0.719	0.00098	0.0113	1.1670
	0.686	0.00136	0.0165	1.0073
	0.719	0.00098	0.0169	0.9622
	0.641	0.00204	0.0185	0.8567
30 lb/Mgal Guar	0.552	0.00566	0.0113	1.2316
	0.537	0.00676	0.0165	1.0377
	0.552	0.00566	0.0169	0.9747
	0.527	0.00793	0.0185	0.9139
40 lb/Mgal Guar	0.483	0.01410	0.0113	1.2442
	0.454	0.01935	0.0165	1.1176
	0.483	0.01410	0.0169	1.0074
	0.432	0.02428	0.0185	1.0285

Table 6.3—Shift Factors to Match the Mean Curve (HEC Fluids)

Fluid	n	K_p, $lb_f s^n/ft^2$	a/R	M
20 lb/Mgal HEC	0.657	0.00211	0.0113	1.1477
	0.668	0.00236	0.0165	0.9868
	0.657	0.00211	0.0169	0.9095
	0.599	0.00442	0.0185	0.8708
30 lb/Mgal HEC	0.545	0.00847	0.0113	1.1843
	0.515	0.01321	0.0165	1.0489
	0.545	0.00847	0.0169	0.9341
	0.494	0.01690	0.0185	0.9351
40 lb/Mgal HEC	0.443	0.03036	0.0113	1.2553
	0.424	0.04003	0.0165	1.1163
	0.443	0.03036	0.0169	0.9873
	0.420	0.04572	0.0185	0.9959

Table 6.4—Shift Factors to Match the Mean Curve (PHPA Fluids)

Fluid	n	K_p, $lb_f s^n/ft^2$	a/R	M
20 lb/Mgal PHPA	0.363	0.02083	0.0113	0.9680
	0.355	0.02231	0.0165	0.9955
	0.363	0.02083	0.0169	0.9384
	0.384	0.01978	0.0185	0.9212
40 lb/Mgal PHPA	0.322	0.04567	0.0113	1.2222
	0.305	0.04732	0.0165	1.0539
	0.322	0.04567	0.0169	0.9889
	0.308	0.04659	0.0185	0.9510

Table 6.5—Shift Factors to Match the Mean Curve (Xanthan Fluids)

Fluid	n	K_p, $lb_f s^n/ft^2$	a/R	M
20 lb/Mgal Xanthan	0.381	0.00950	0.0113	1.1235
	0.439	0.00710	0.0165	0.9931
	0.381	0.00950	0.0169	0.9421
	0.422	0.00818	0.0185	0.9706
40 lb/Mgal Xanthan	0.293	0.03284	0.0113	1.1517
	0.277	0.04519	0.0165	0.9949
	0.293	0.03284	0.0169	0.9260
	0.343	0.02682	0.0185	0.9960

The M factors in Tables 6.2 to 6.5 were then plotted against a/R and n for possible correlation. It is found that there is good correlation between M and a/R. Table 6.6 summarizes the correlations of shift factor M as functions of a/R and correlation constants. It should be noted that the behavior of the 10 lb/Mgal xanthan deviated remarkably from the main data trend and therefore the data of 10 lb/Mgal xanthan were not included in the correlation.

The final friction factor correlation as functions of generalized Dean number becomes:

$$f = \left(\frac{A}{N_{DNg}^B} + C \right) \frac{1}{M} , \dots\dots\dots\dots\dots\dots\dots\dots\dots(6.16)$$

where A, B, and C are given in Table 6.1, and M can be calculated according to Table 6.6.

Table 6.6—Correlation Constants for the Shift Factor

Fluid	Correlation for Shift Factor	c_0	c_1	c_2
Xanthan	$M = \left[c_1 + c_2 \big/ \left(a/R\right)^2\right]^{0.5}$		0.6983	7.498×10^{-5}
PHPA	$M = c_0 + c_1 n + c_2 \left(a/R\right)$	1.8840	-1.5937	-21.304
Guar	$M = \left[c_1 + c_2 \left(a/R\right)\right]^{0.5}$		2.4500	-85.633
HEC	$M = \left[c_1 + c_2 \left(a/R\right)\right]^{0.5}$		2.3293	-80.094

6.3.6   Evaluation of the New Friction Factor Correlations

To evaluate the performance of the developed empirical correlations given in Eq. (6.16), the experimental friction factors were compared with the predictions of the above correlations. The results of this comparison are shown in Figs. 6.30 through 6.33.

It can be seen that the correlations could adequately match the experimental data. Majority of the predictions are within ±5%. The ±10% lines are drawn on the plots to show that only a few data points are outside the ±10% lines.

The following examples may provide further evaluation on the accuracy of the above empirical correlations.
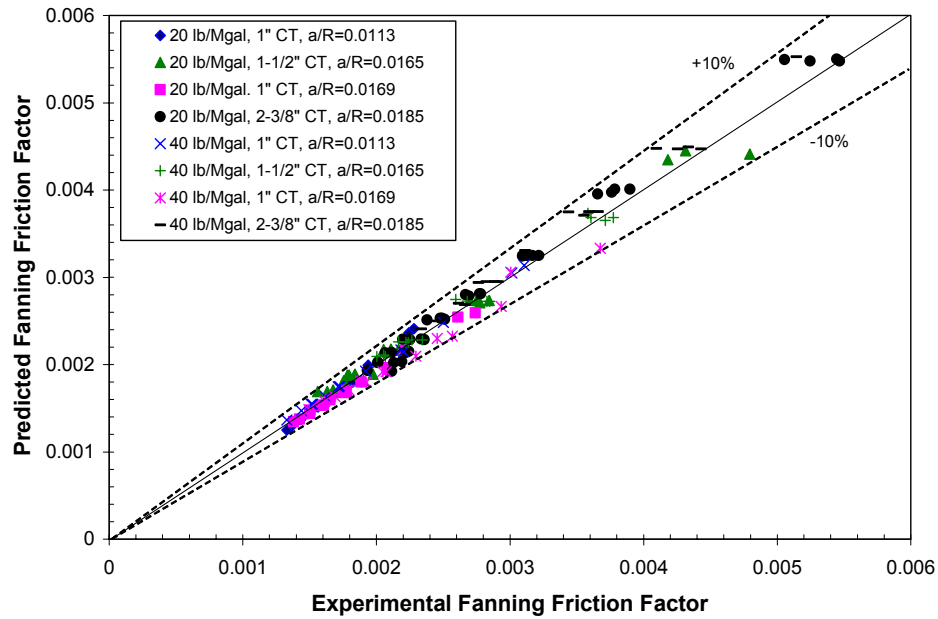
Fig. 6.30—Comparison between experimental and predicted friction factors of xanthan data.
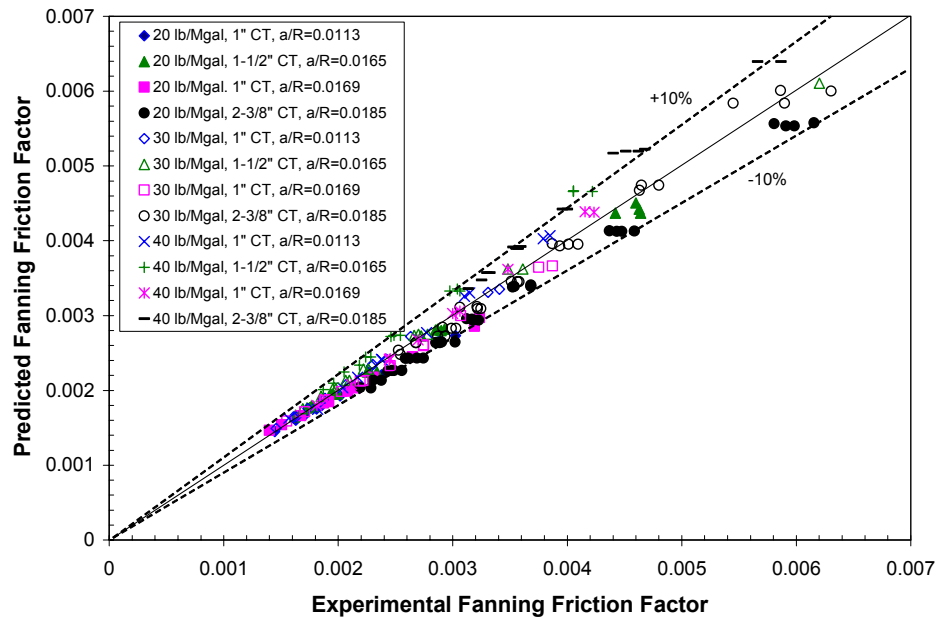
Fig. 6.31—Comparison between experimental and predicted friction factors of guar data.

157
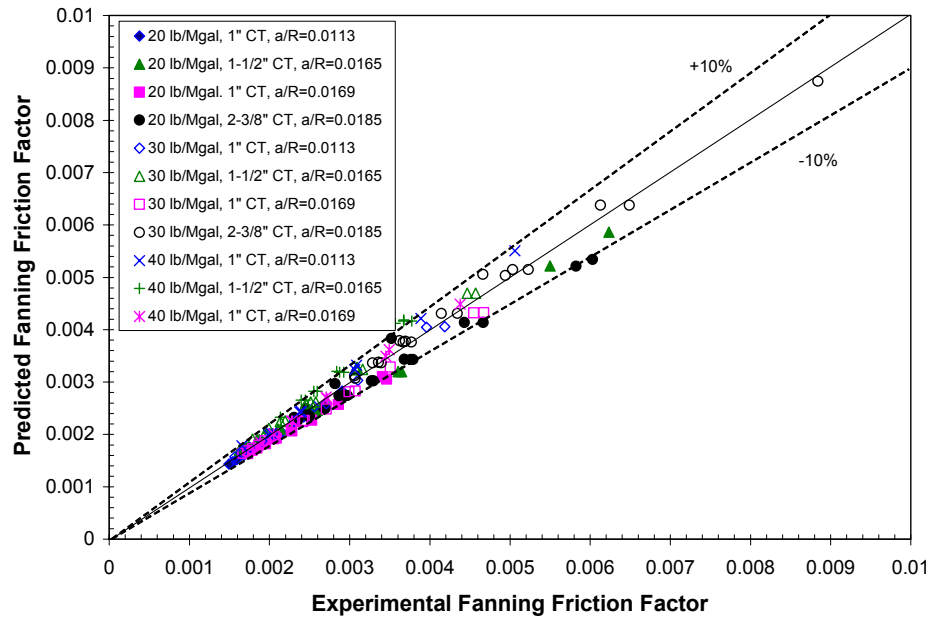
Fig. 6.32—Comparison between experimental and predicted friction factors of HEC data.
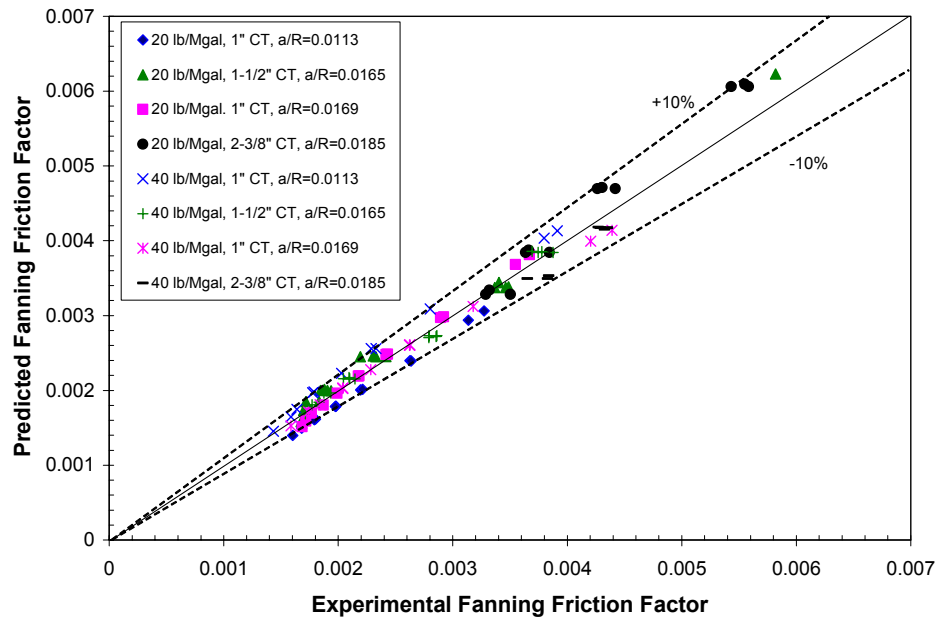
Fig. 6.33—Comparison between experimental and predicted friction factors of PHPA data.

158

Example 1—Turbulent flow of 35 lb/Mgal guar gel in 2-3/8-in. CT. 35 lb/Mgal clean (proppant-free) guar gel was pumped through the 1000 ft, 2-3/3-in. coiled tubing. The rheological properties of the guar gel were: n = 0.444 and K_p = 0.01755 $lb_f s^n/ft^2$. Fig. 6.34 compares the measured and predicted friction factors from the new empirical correlation for guar fluids. The agreement between the measured data and the predictions are reasonably good. Over the wide range of generalized Reynolds number (N_{Reg} = 3790 – 24,792), the deviations for majority of data points are within 5%. Only at the highest flow rate (N_{Reg} = 24,792), the correlation underestimated the data by 10.5%.
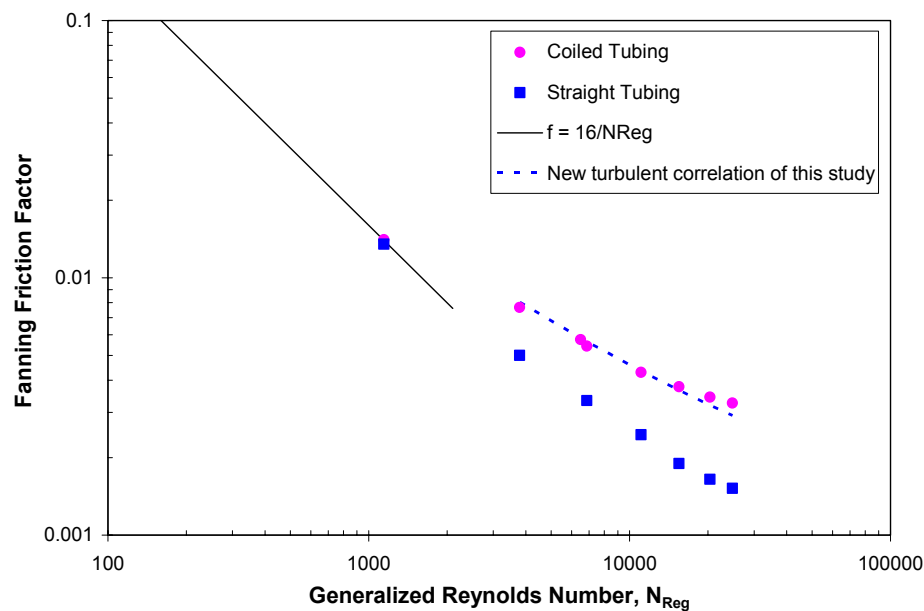
Fig. 6.34—Comparison of measured and predicted friction factors using the new friction factor correlation for guar in coiled tubing – 35 lb/Mgal guar in 2-3/8-in. CT.

Example 2—2 lb/bbl xanthan + 1 lb/bbl starch fluid in the 2-3/8-in. coiled tubing reel. Since a concentration of 2 lb/bbl is equivalent to 47.6 lb/Mgal, we first

compared the friction data of this xanthan + starch mixture with the friction data of 40 lb/Mgal xanthan fluid. It was found that adding 1 lb/bbl starch to 2 lb/bbl xanthan does not change the general behavior of xanthan on the plot of Fanning friction factor vs. generalized Reynolds number. Fig. 6.35 shows the comparison between measured and predicted friction factors using the new empirical correlation for xanthan fluids. It can be seen that there is close agreement between the measured data and the estimated friction factors. Over the Reynolds number range of 4019 to 29,562, the largest deviation between correlation and data is 3.5%. The average deviation is 1.6%.
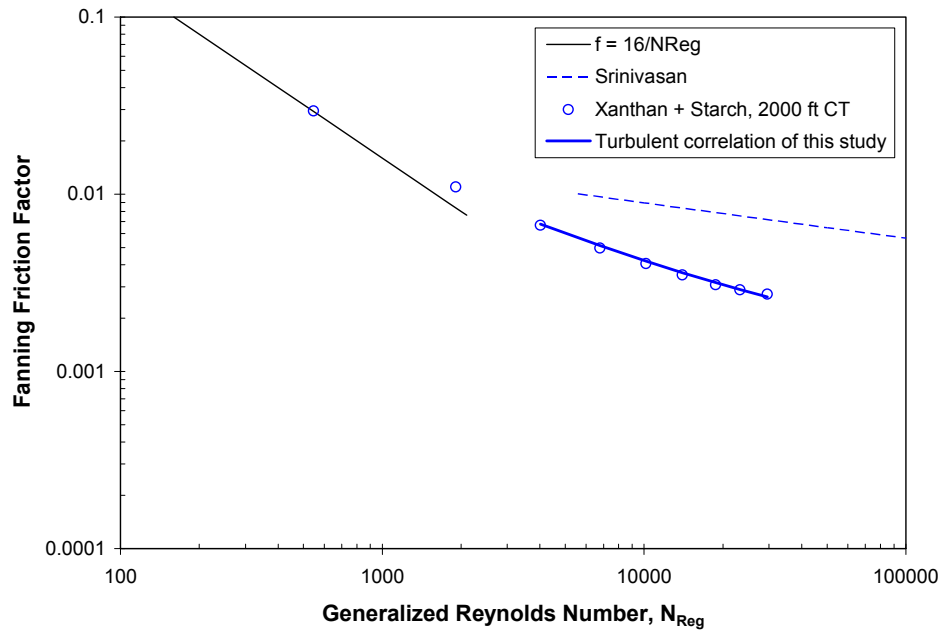
Fig. 6.35—Comparison of measured and predicted friction factors using the new friction factor correlation for xanthan in coiled tubing – 2 lb/bbl xanthan + 1 lb/bbl starch in 2-3/8-in. CT.

Comparison with data of lab-scale tests. Figs. 6.36 and 6.37 compare the friction factors of 20 lb/Mgal guar in the ½-in. coiled tubing with curvature ratio of 0.01 and 0.019 with the new correlation respectively. It can be seen that generally the new correlation matches the data reasonably well for both cases. The biggest deviation between the new correlation with data is about 11% for 20 lb/Mgal guar in the coil with a/R = 0.01. For 30 lb/Mgal guar in the coil of a/R = 0.019, the biggest deviation between the correlation and the data is only 8%. The new correlation for guar fluids somehow underestimates the friction factor data of the ½-in. coiled tubing.
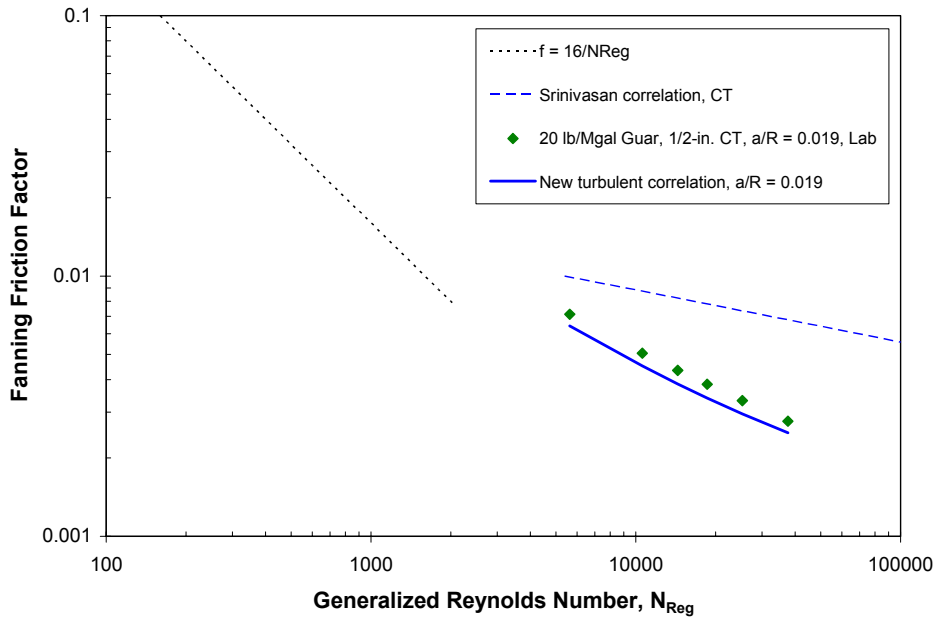
Fig. 6.36—Comparison of new turbulent correlation with experimental data in the ½-in. coiled tubing (20 lb/Mgal guar).

161
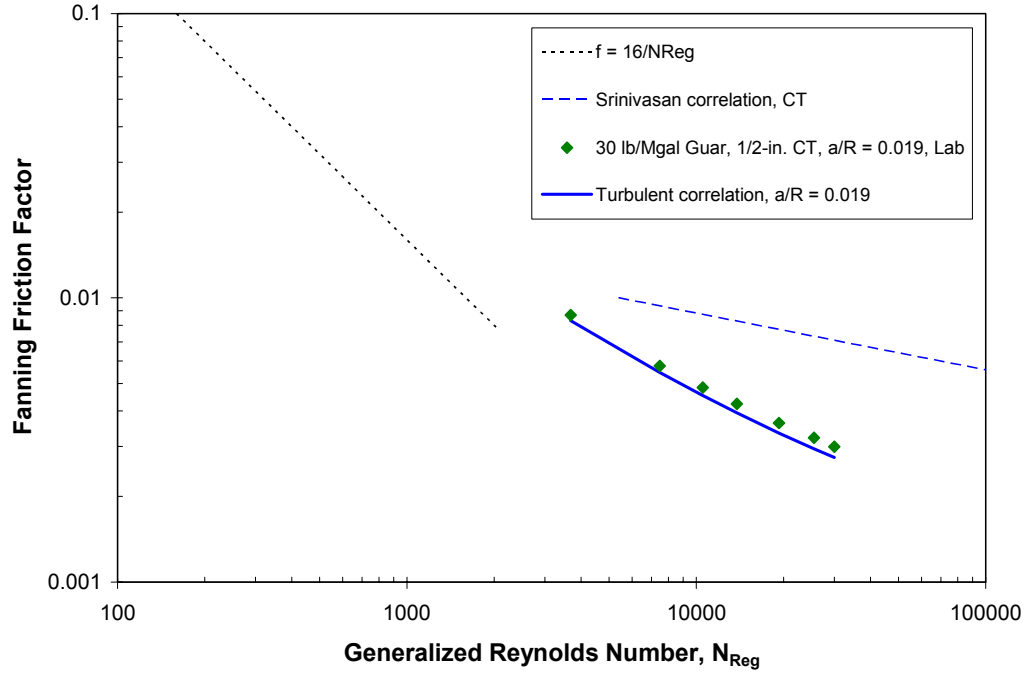
Fig. 6.37—Comparison of new turbulent correlation with experimental data in the ½-in. coiled tubing (30 lb/Mgal guar).

Fig. 6.38 may be helpful to explain the possible reason for the underestimation of the new correlation to the ½-in. coiled tubing data. Fig. 6.38 compares friction factor data of 20 lb/Mgal guar in ½, 1, and 1-1/2-in. coiled tubing. Intuitively, we would expect higher friction in the 1-in. and 1-1/2-in. coiled tubing than in the ½-in. coiled tubing since the 1-in. and 1-1/2-in. coiled tubing reels have roughness and the ½-in. coiled tubing is made of stainless steel and is smoother than the carbon steel coiled tubing. One of the possible reasons for the relatively lower friction in 1 and 1-1/2-in. coiled tubing is due to the welding seam in these tubings. Instead of acting as an added roughness, the seam might have altered the turbulence spectrum by damping

162

the high turbulence frequencies and thus causing a decrease in the turbulent friction pressure drop. This behavior has been observed in a previous study.[101]
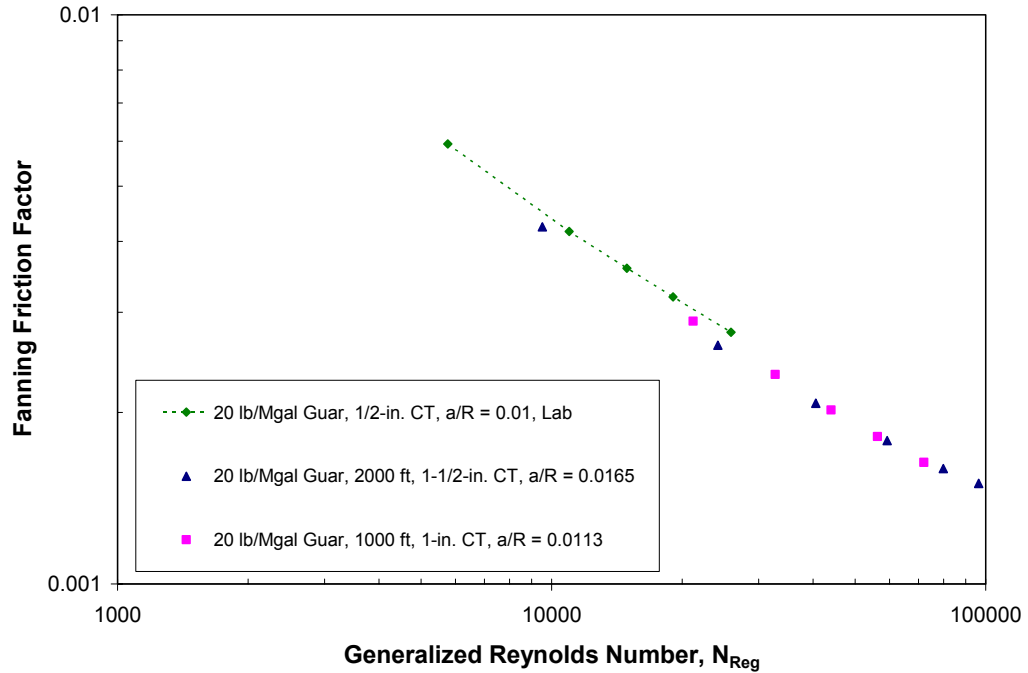
Fig. 6.38—Comparison of friction factors of 20 lb/Mgal guar in lab-scale ½-in. tubing and field-scale 1 and 1-1/2-in. tubing.

6.4 Flow Tests of Non-Newtonian Fluids in Lab-Scale Flow Loop

The advantage of the lab-scale flow loop is that the coils represent a wide range of curvature ratio – 0.01, 0.019, 0.031, and 0.076. Therefore, the effect of curvature can be more easily investigated. Another advantage of the lab-scale flow loop is that the coiled tubing and straight tubing sections are made of stainless steel. Water tests have

revealed that they can be treated as smooth tubing. Therefore, the effect of roughness can be excluded in the data analysis.

As shown in Table 5.7, three types of polymer solutions have been tested with the lab-scale flow loop: 10, 15, 20, and 30 lb/Mgal xanthan; 10, 20, and 30 lb/Mgal guar; and 10, 20, and 30 lb/Mgal HPG.

6.4.1   Effect of Curvature Ratio on Friction Factor

Figs. 6.39 to 6.42 show the plots of Fanning friction factor versus generalized Reynolds number of 10, 15, 20, and 30 lb/Mgal xanthan solutions respectively. Similar plots for 10, 20, and 30 lb/Mgal HPG solutions are given in Figs. 6.43 to 6.45 respectively.

Several important observations can be made from these plots. The first and most important feature of these plots is that as the curvature ratio increases, the friction factor increases. This is true for all the curvature ratios including the straight tubing as a special case (zero curvature ratio) and for all fluids tested. Therefore, the effect of curvature ratio on the friction factor of coiled tubing is firmly established. Physically, as curvature ratio increases, the secondary flow is enhanced and therefore, there is more flow resistance.

Secondly, the effect of curvature ratio on friction factor is not uniform. Unless at very low polymer concentration such as the 10 lb/Mgal xanthan, the friction factor differences between zero curvature ratio (the straight tubing) and the curvature ratio of 0.01, and between a/R = 0.01 and a/R = 0.019 are much larger than those between higher curvature ratios, such as the difference between a/R =0.031 and 0.076.
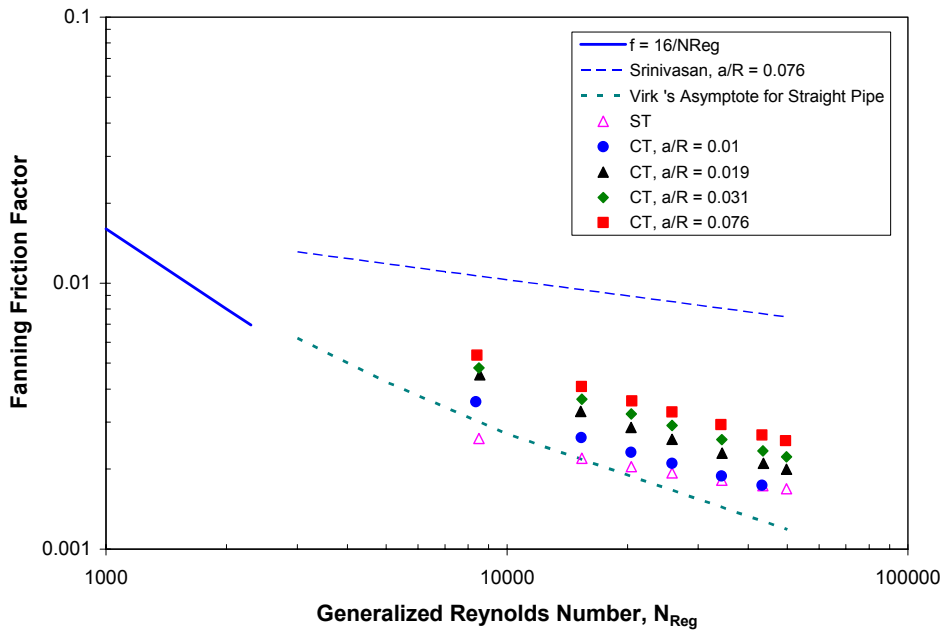
Fig. 6.39—Friction factor versus generalized Reynolds number of 10 lb/Mgal xanthan in ½-in. coiled and straight tubing.
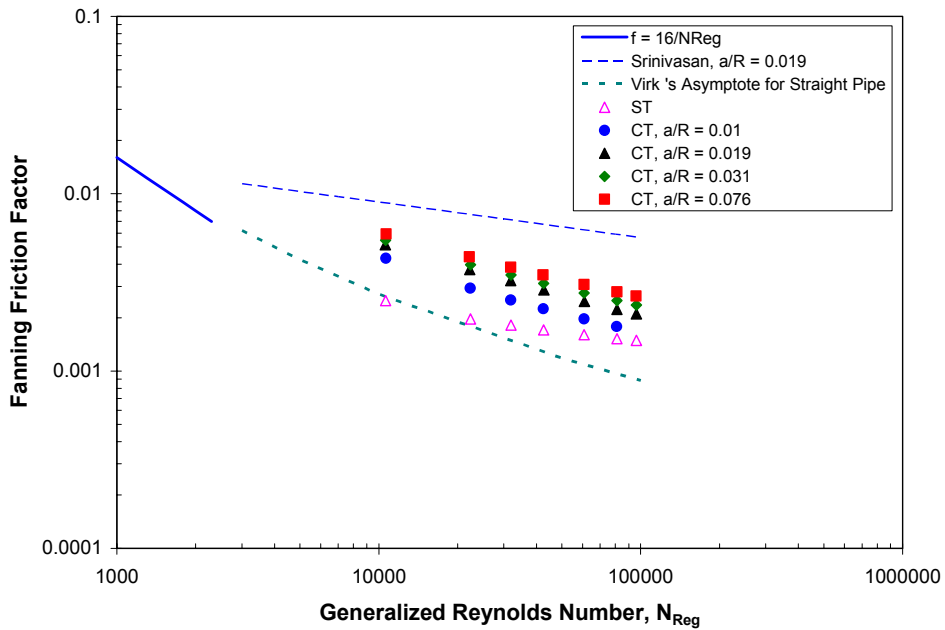
Fig. 6.40—Friction factor versus generalized Reynolds number of 15 lb/Mgal xanthan in ½-in. coiled and straight tubing.
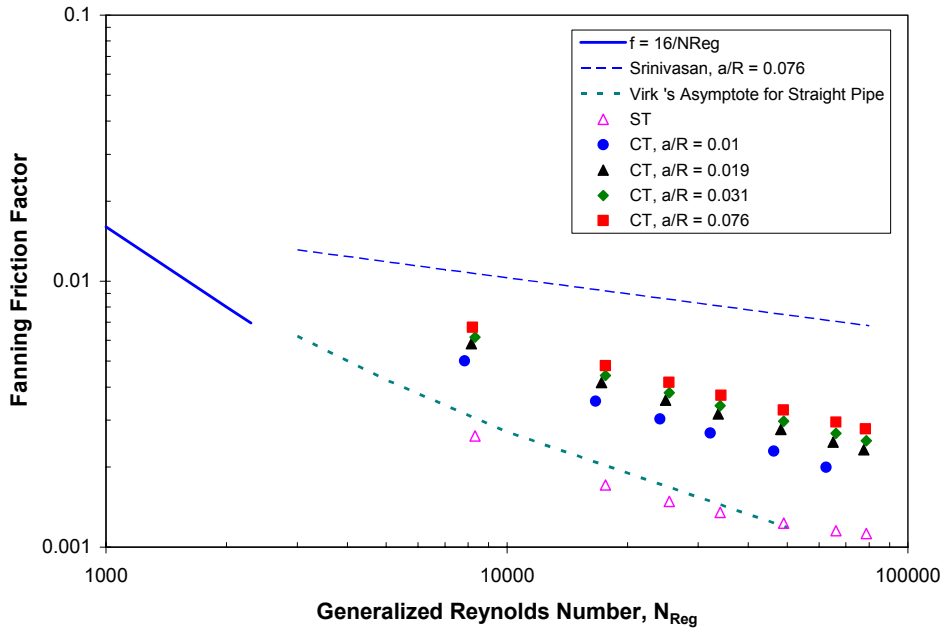
Fig. 6.41—Friction factor versus generalized Reynolds number of 20 lb/Mgal xanthan in ½-in. coiled and straight tubing.
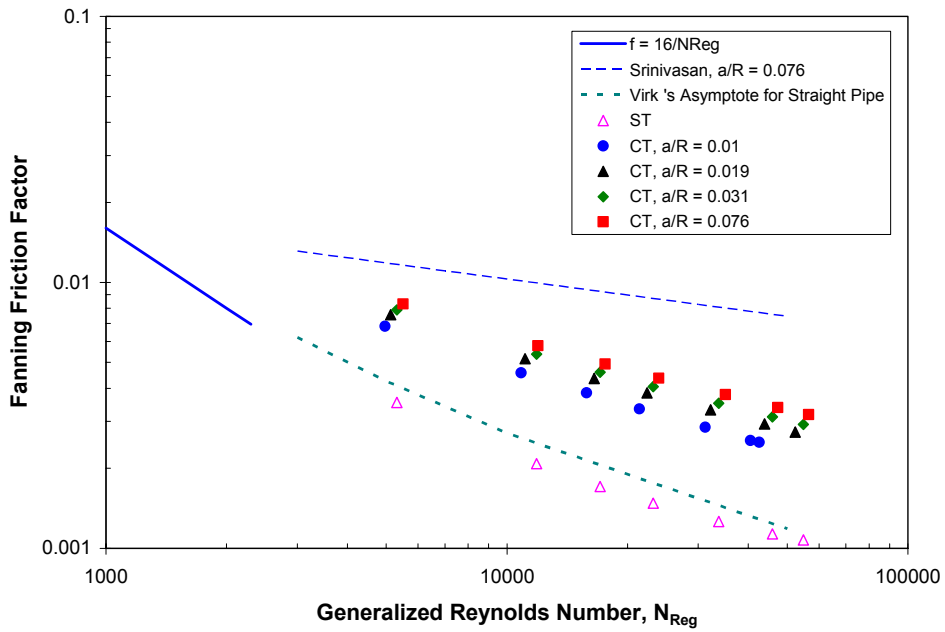
Fig. 6.42—Friction factor versus generalized Reynolds number of 30 lb/Mgal xanthan in ½-in. coiled and straight tubing.

166
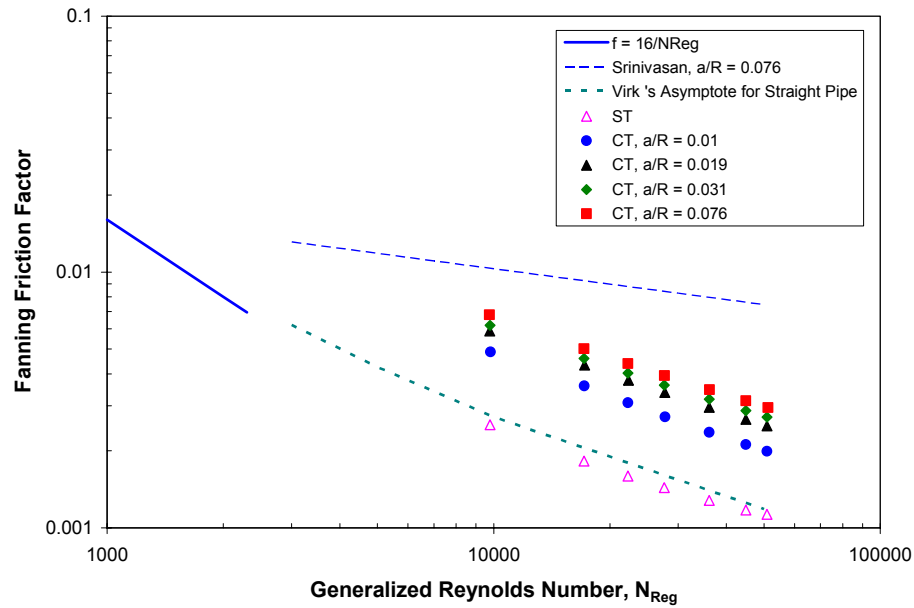
Fig. 6.43—Friction factor versus generalized Reynolds number of 10 lb/Mgal HPG in ½-in. coiled and straight tubing.
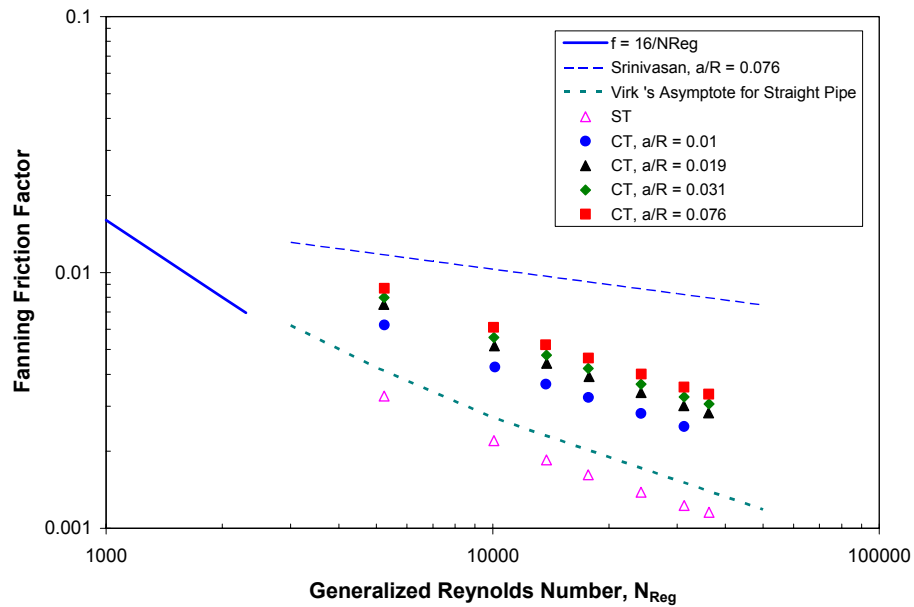
Fig. 6.44—Friction factor versus generalized Reynolds number of 20 lb/Mgal HPG in ½-in. coiled and straight tubing.

167
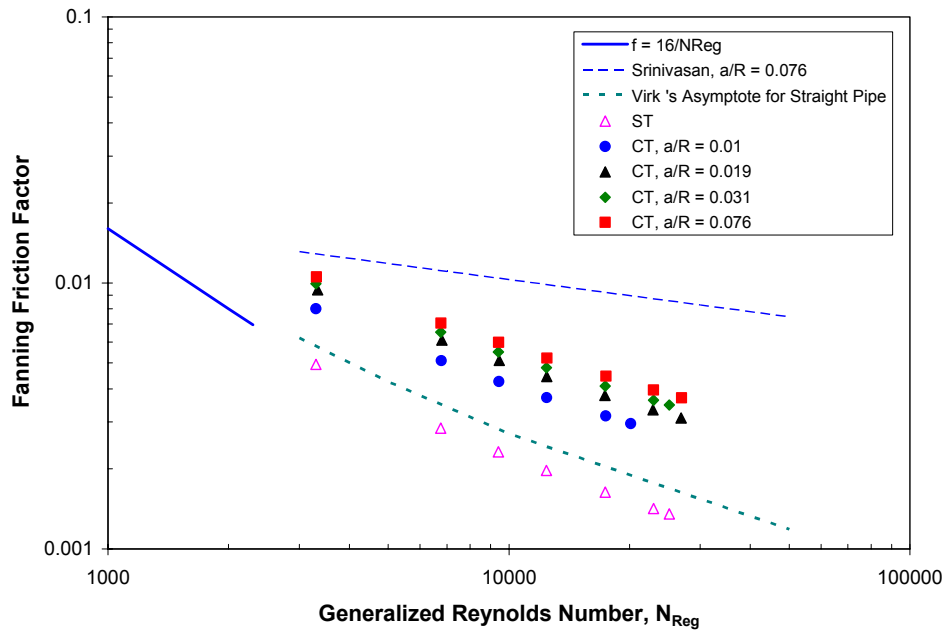
Fig. 6.45—Friction factor versus generalized Reynolds number of 30 lb/Mgal HPG in ½-in. coiled and straight tubing.

The effect of curvature ratio is also dependent on the polymer concentration. At high concentration, the difference between coiled tubing and straight tubing is greater than at low concentration, for the same reason as we have discussed for the analysis of the field-scale flow tests. For more concentrated polymer solutions, as Reynolds number increases, the friction factor of straight tubing will tend to follow the extended line of laminar flow, whereas the friction factor of coiled tubing follows a curved line, gradually reaching an asymptotic value.

6.4.2 Effect of Polymer Concentration

To more easily investigate the effect of polymer concentration on friction factor behavior, we can make composite plots of friction factor at various polymer

concentrations for each curvature ratio. For example, Figs. 6.46 and 6.47 show such plots for xanthan fluids at curvature ratios of 0.01 and 0.031 respectively. Figs. 6.48 and 6.49 show similar results for the HPG fluids at a/R = 0.01 and 0.031 respectively.

It is interesting that at concentrations of 20 and 30 lb/Mgal, the friction factor is not sensitive to the concentration change. This is true for all the polymer types and for coiled tubing and straight tubing. The friction behavior of the low concentration, i.e., 10 lb/Mgal, fluid is worth some discussion. From Figs. 6.46 and 6.47, it can be seen that the 10 lb/Mgal xanthan fluid has the lowest friction factor in coiled tubing, but the highest friction factor in straight tubing. In straight tubing, the friction factor of 15 lb/Mgal xanthan is close to that of 10 lb/Mgal xanthan. At 20 and 30 lb/Mgal, the friction factor of xanthan fluids in straight tubing is significantly lower. This indicates that in straight tubing, the xanthan polymer concentration should be higher than 10 or 15 lb/Mgal to minimize the friction pressure. But, for coiled tubing, 10 lb/Mgal xanthan seems to be more favorable than the 20 or 30 lb/Mgal xanthan fluid in reducing friction pressure.

In this respect, the guar and HPG fluids display different behavior. The 10 lb/Mgal guar shows higher friction than 20 and 30 lb/Mgal guar, in both straight and coiled tubing. The friction factor of 10 lb/Mgal HPG is just slightly higher than that of 20 and 30 lb/Mgal HPG in both straight and coiled tubing, as shown in Figs. 6.48 and 6.49. Apparently, polymers at this low concentration (10 lb/Mgal) exhibit drastic change in flow behavior. We have seen the significant change of flow behavior of the 10 lb/Mgal xanthan fluid in the 1, 1-1/2, and 2-3/8-in coiled tubing, see Figs. 6.11 to
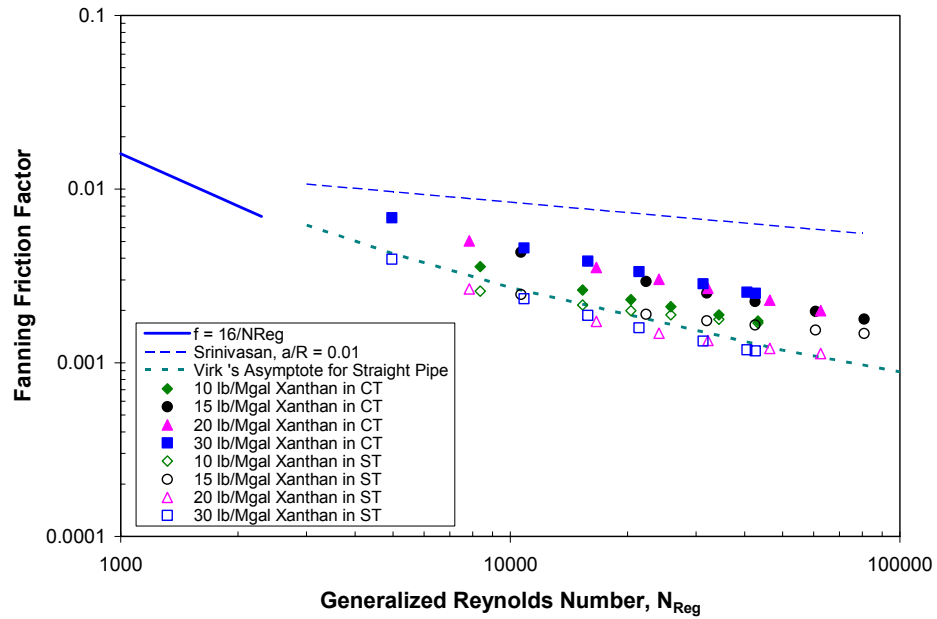
Fig. 6.46—Effect of polymer concentration on friction factor of xanthan fluids in straight and coiled tubing (a/R = 0.01).
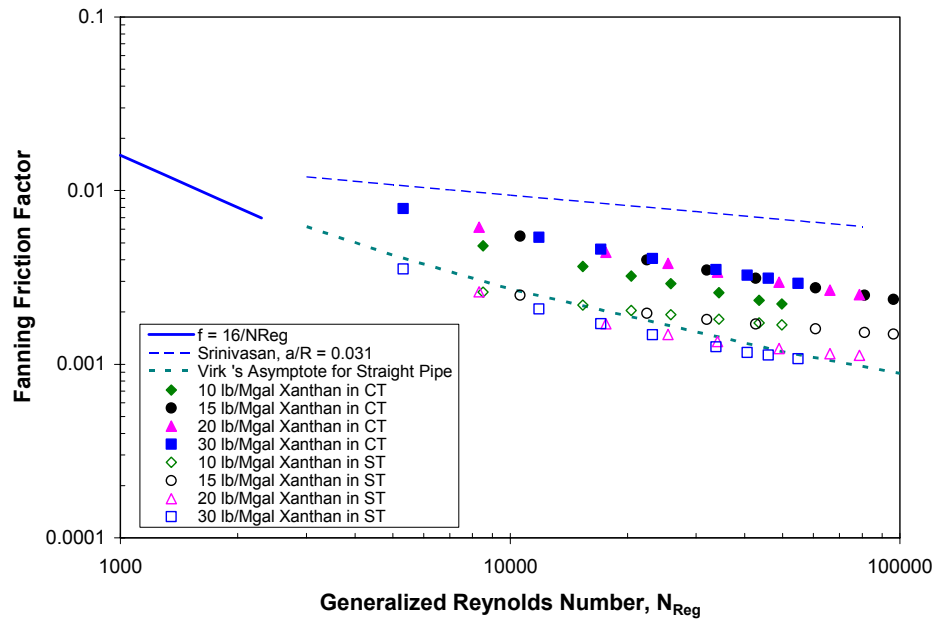
Fig. 6.47—Effect of polymer concentration on friction factor of xanthan fluids in straight and coiled tubing (a/R = 0.031).

170
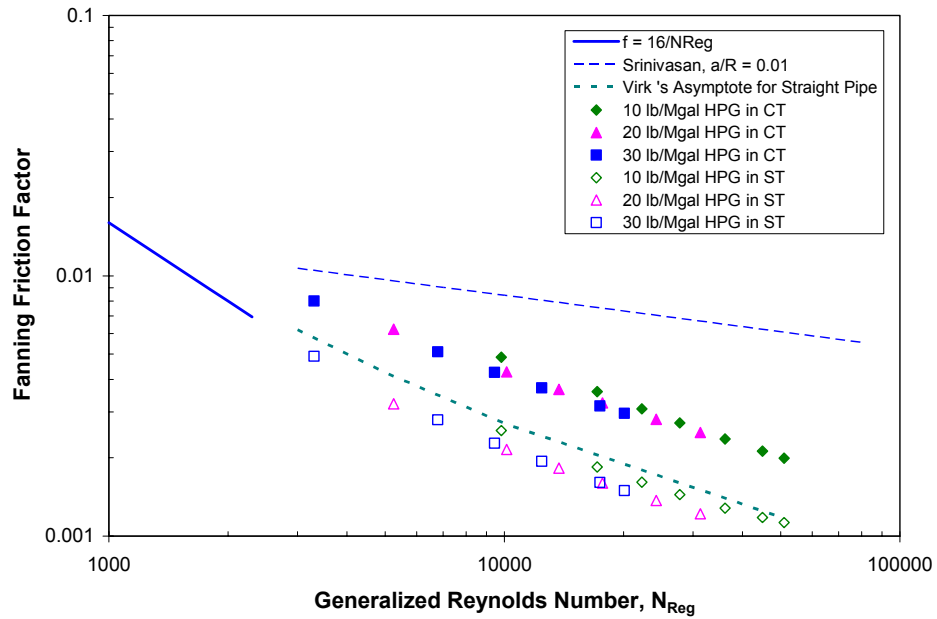
Fig. 6.48—Effect of polymer concentration on friction factor of HPG fluids in straight and coiled tubing (a/R = 0.01).
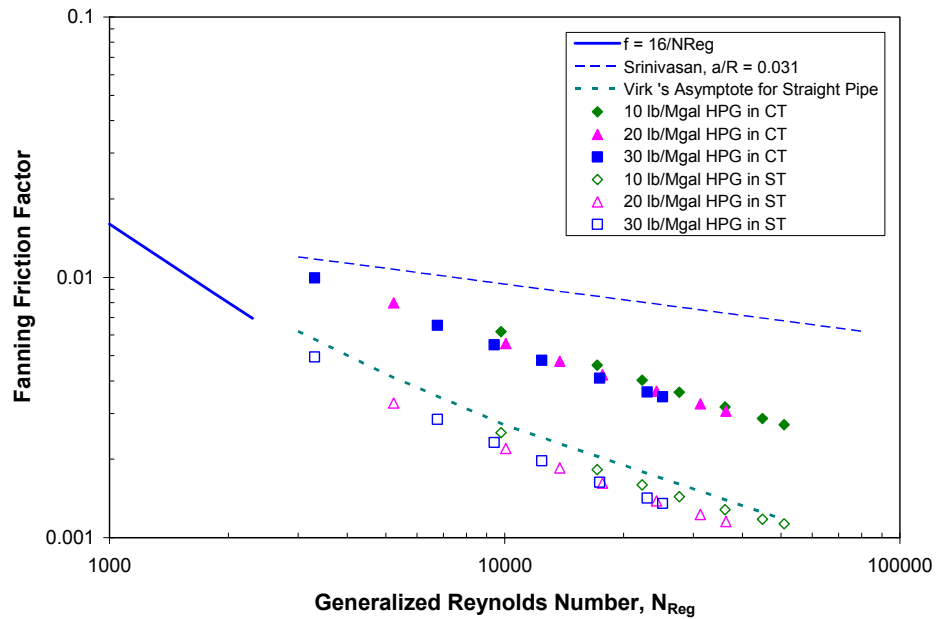
Fig. 6.49—Effect of polymer concentration on friction factor of HPG fluids in straight and coiled tubing (a/R = 0.031).

171

6.14 where an abnormally high friction factor has been observed for the 10 lb/Mgal xanthan fluid. In future research, more systematic tests at these low concentrations may provide more insights into the mechanisms for drastic flow change at certain low polymer concentrations.

6.5   Summary

Water tests through coiled tubing and straight tubing in both field-scale and lab-scale flow loops have indicated that friction in coiled tubing is significantly higher than in straight tubing. The difference in friction factor can be as high as 30%. For polymeric fluids, the difference in friction factor between straight and coiled tubing is more pronounced. In the range of generalized Reynolds number investigated, the biggest difference in friction factor can be as much as 185%. This is due to two different friction mechanisms for polymer fluids – extended laminar flow in straight tubing and secondary flow in coiled tubing.

Friction factor correlations for turbulent flow in coiled tubing have been developed based on the field-scale flow tests. They can be used in the hydraulics design of CT operations. The test data of the ½-in. lab-scale flow loop have clearly shown the significant effect of curvature ratio on friction factor in coiled tubing. As curvature ratio is increased, the friction factor in coiled tubing increases.

CHAPTER 7

CHARACTERISTICS OF DRAG REDUCTION IN

COILED TUBING

7.1   Introduction

Frictional pressure in turbulent flow in straight pipes can be drastically reduced by adding small quantities of certain long-chain polymers to the solvent, such as water. This phenomenon is called drag reduction. Credit is generally given to Toms[125] for being the first to observe this phenomenon. There have been tremendous studies of drag reduction in straight pipe. Several papers have provided extensive reviews on this topic, such as Lumley,[126] Hoyt,[127,128] Virk,[129] and Berman.[130] Although the drag reduction phenomena have been extensively investigated in recent decades, the underlying mechanisms producing drag reduction is not yet fully understood. Many tentative explanations have been offered to explain the phenomenon, but none of them is entirely convincing. Kostic[131] summarized these theories or hypotheses of drag reduction which include: shear thinning, visco-elasticity, molecular stretching, decreased turbulence production, etc.

In contrast, the information in the literature on drag reduction in coiled pipes is very scarce. Kelkar and Mashelkar[132] ran tests of aqueous solutions of polyacrylamide through a single coiled tube of 1.25 cm inside diameter and proposed a correlation of reduced friction factor (defined as ratio of the friction factor of polymer solution and the friction factor of the purely viscous solvent) as a function of Deborah number.

Another relevant research effort was reported by Yokoyama and Tomita[133] who preformed tests of dilute aqueous solutions of polyethylene oxide in 360° bends with curvature ratios of 0.021, 0.029, and 0.053. It was found that the drag reduction was reduced with increase of curvature ratio.

During the analysis of friction behavior in coiled and straight tubing in Chapter 6, we have seen that all the polymeric fluids are highly drag-reducing fluids, i.e., their friction factors are much lower than what would be expected for Newtonian fluids in turbulent flow. For coiled tubing, friction factor of polymer fluids is lower than predicted by Scrinivasan correlation for Newtonian turbulent flow. For straight tubing, the friction factor of polymer fluids is lower than the Drew correlation.

There are reasons to believe that the behavior of polymer solutions in coiled tubing may be substantially different from that in straight tubing, because there is secondary flow in coiled tubing which may alter the flow structure.

In this study, we follow the original definition of Savins[134] and define the drag reduction, DR, as the following:

$$DR = 1 - \left(\frac{dp}{dl}\right)_p \bigg/ \left(\frac{dp}{dl}\right)_s, \dots\dots\dots\dots\dots\dots\dots\dots\dots\dots\dots\dots\dots\dots\dots\dots\dots\dots\dots\dots\dots\dots\dots\dots\dots(7.1)$$

in which $(dp/dl)_p$ and $(dp/dl)_s$ are the frictional pressure gradients for polymer solution and the solvent under the same flow conditions, respectively. Assuming that the density of the polymer solution is the same as the density of the solvent, the following equation is applicable:

$$DR = 1 - f_p/f_s ,\dots\dots\dots\dots\dots\dots\dots\dots\dots\dots\dots\dots\dots\dots\dots\dots\dots\dots\dots\dots(7.2)$$

in which f_p and f_s are the Fanning friction factors of the polymer solution and the solvent, respectively. DR is usually expressed in percentage. The Fanning friction factors, f_p and f_s, can be calculated from the Eqs. (6.6) and (6.7). Therefore, once the frictional pressure drop for a certain tubing length at a pump rate is obtained from a flow test, the DR can be calculated with the above equations.

Kostic[131] called the definition given by Eq. (7.1) as the "pressure-drop drag reduction," and the definition given by Eq. (7.2) as the "friction factor drag reduction." There has been confusion about these two definitions in the drag reduction literature.[128,130,131] There could be confusion if the friction factors, f_s and f_p, are calculated at the "same Reynolds number." As pointed out by Kostic, if DR is calculated at the "same Reynolds number" using Eq. (7.2), the two definitions will not be the same unless with very dilute polymer solutions with viscosity of solutions equal to that of solvent. In this study, we want to stress that the definitions given by Eqs. (7.1) and (7.2) are consistent as long as the friction factors, f_s and f_p, are calculated at the "same flow rate."

In this chapter, we will mainly use the lab-scale test data to discuss the drag reduction behavior in coiled tubing since the lab-scale flow loop has wider range of curvature ratio and effect of tubing roughness can be excluded.

7.2 Drag Reduction and Onset of Drag Reduction in Coiled Tubing

Figs. 7.1 to 7.3 show the plots of drag reduction versus generalized Reynolds number for 10, 20, and 30 lb/Mgal HPG solutions in the four coils and straight section of ½-in. diameter. The effect of curvature ratio on drag reduction can be seen clearly. The drag reduction in straight tubing is significantly higher than in coiled tubing. The tighter the coil was spooled, the lower the drag reduction in that coil. In literature, we only found the results of Yokoyama and Tomita[133] that can be compared with our results. Their results of drag reduction in coiled tube are shown in Fig. 7.4. The fluids they used were 1 ppm to 100 ppm aqueous solutions of polyethylene oxide. They used a single turn (360° bend) of copper pipes of 1.4 cm inside diameter. The curvature ratios were a/R = 0.021, 0.029, and 0.053 or R/a = 47.3, 34.3, and 18.7. Their results showed that as curvature ratio (a/R) was increased, the drag reduction was decreased. But, compared to our results, their data is less systematic and quite limited.

Another value of plots like Figs. 7.1 to 7.3 is that they can provide information about the onset of drag reduction. This can be understood by examining Figs. 7.2 and 7.3. The interceptions of the data with the zero-drag reduction line should correspond to the generalized Reynolds number at the onset of drag reduction. Figs. 7.2 and 7.3 clearly indicate that as curvature ratio increases, the onset of drag reduction is obviously delayed.

176
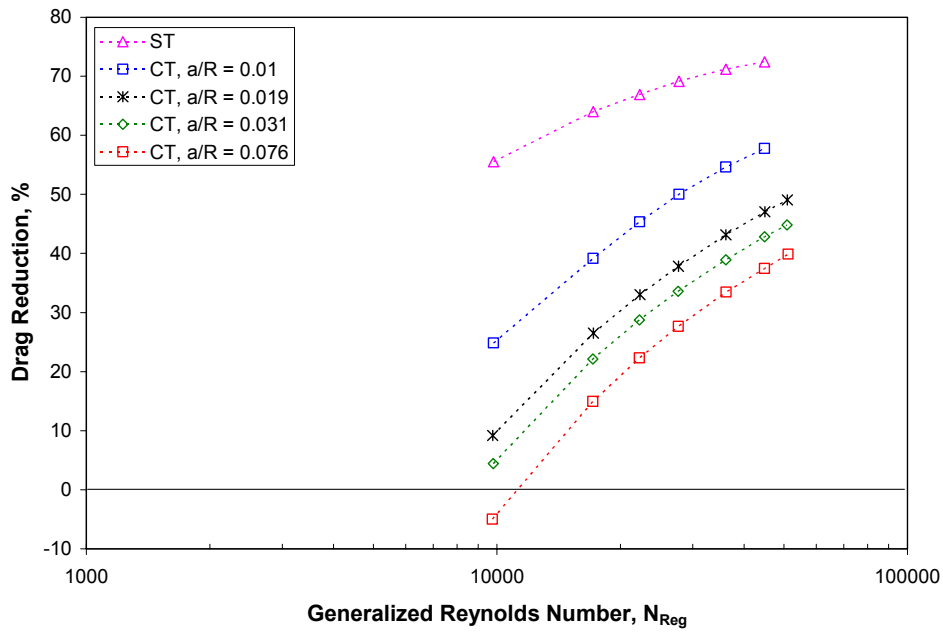
Fig. 7.1—Drag reduction of 10 lb/Mgal HPG in ½-in. straight and coiled tubing.
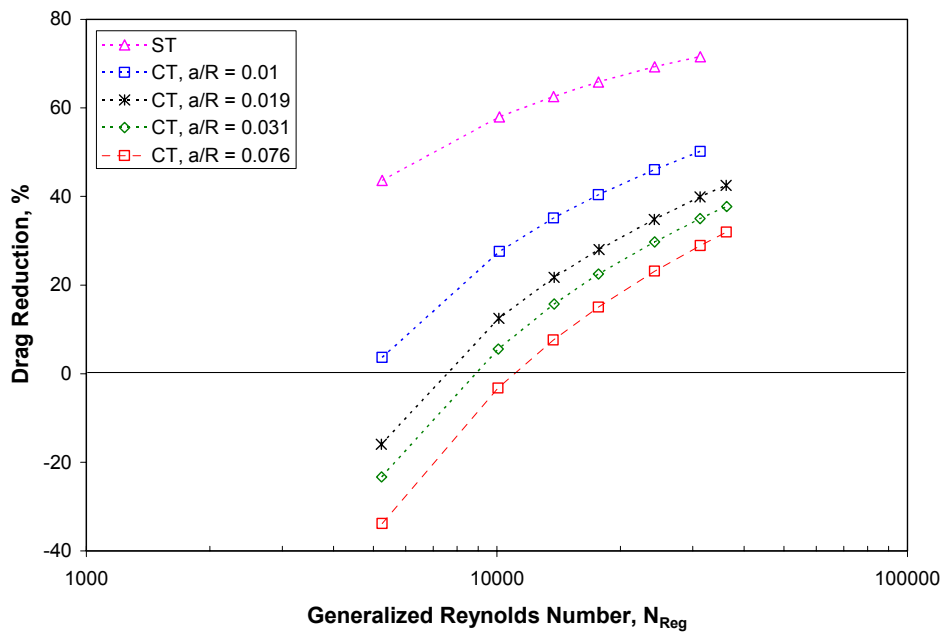
Fig. 7.2—Drag reduction of 20 lb/Mgal HPG in ½-in. straight and coiled tubing.

177
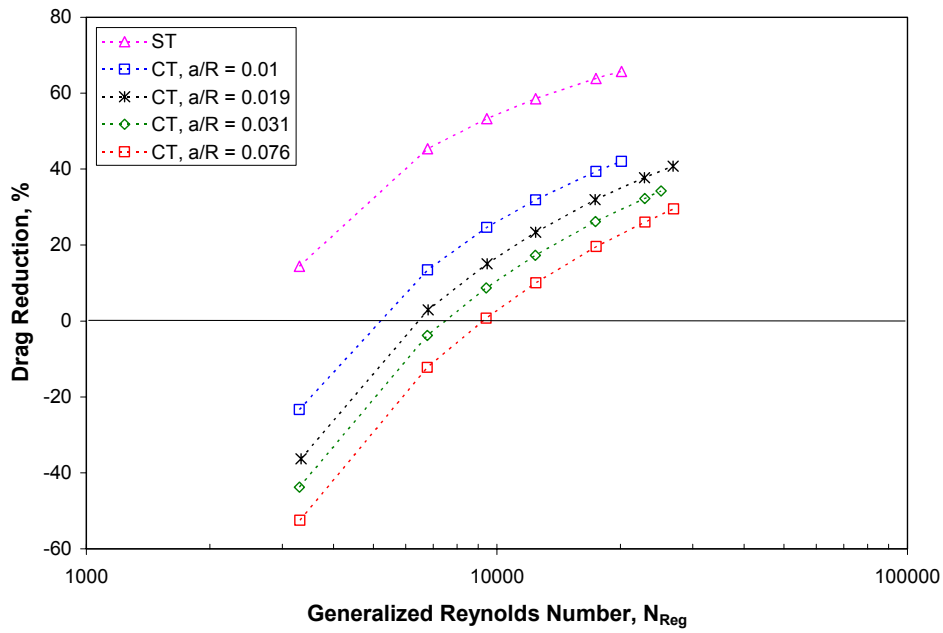
Fig. 7.3—Drag reduction of 30 lb/Mgal HPG in ½-in. straight and coiled tubing.
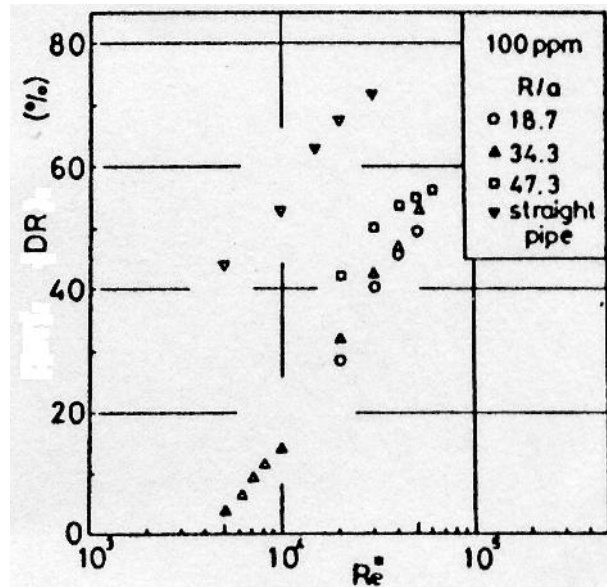
Fig. 7.4—Effect of curvature ratio on drag reduction studied by Yokoyama and Tomita.[133]

In contrast, the drag reduction in straight tubing has been always present in these tests, even at the lowest flow rate and more concentrated polymer solutions. Therefore, drag reduction in straight tubing occurs much earlier than in coiled tubing. Table 7.1 summarizes the generalized Reynolds number at the onset of drag reduction for the three types of polymer solutions in the ½-in. tubing. In Table 7.1, the values of critical Reynolds number predicted by the Srinivasan correlation [Eq. (2.13)] for the Newtonian laminar-turbulent transition in coiled tubing are also included for comparison. It can be seen that the generalized Reynolds number at the onset of drag reduction is higher than the critical Reynolds number for Newtonian turbulent flow in coiled tubing (except 20 lb/Mgal xanthan in the coil with a/R = 0.01). Based on the data in Table 7.1, an empirical correlation can be obtained for the critical generalized Reynolds number at onset of drag reduction for flow in coiled tubing:

$$N^*_{\mathrm{Re}g} = c_1 - \frac{c_2}{(a/R)^{0.5}} , \dots\dots\dots\dots\dots\dots\dots\dots\dots\dots\dots\dots\dots\dots\dots\dots\dots\dots(7.3)$$

where $c_1 = 13172$, $c_2 = 835.33$, and a/R = curvature ratio.

Table 7.1—Generalized Reynolds Number at Onset of Drag Reduction in ½-in. Coiled Tubing

Fluid	Curvature ratio			
	0.01	0.019	0.031	0.076
20 lb/Mgal Xanthan	3700	6800	7300	9200
30 lb/Mgal Xanthan	5800	8000	9300	11500
20 lb/Mgal HPG	4800	7500	9000	11000
30 lb/Mgal HPG	5200	6400	7300	9300
20 lb/Mgal Guar	4800	7200	8500	10500
30 lb/Mgal Guar	4800	7100	8000	10000
$N_{\mathrm{Re}c}$ by Srinivasan	4620	5574	6537	9047

The above correlation for onset Reynolds number can be compared with the results of tests in the field-size flow loop. We choose the test data of xanthan and guar fluids in the 2-3/8-in. tubing for our analysis, since flow in smaller tubing sizes doesn't show onset of drag reduction (drag reduction is always present even at low flow rates). Figs. 7.5 and 7.6 show the plots of drag reduction versus generalized Reynolds number for xanthan and guar solutions in the 2-3/8-in. tubing respectively. From the interception points of the data with the zero-drag reduction line, the onset Reynolds number for xanthan in this tubing size is roughly estimated as 5200 and 5700 (corresponding to 20 and 40 lb/Mgal xanthan). These values are lower than what is predicted by Eq. (7.3) which gives $N_{Reg}^* = 7031$ for a/R = 0.0185 with the 2-3/8-in coiled tubing. The observed values of 5200 and 5700 are actually quite close to the critical Reynolds number for Newtonian turbulent flow with this coiled tubing. Srinivasan correlation predicted the critical Reynolds number $N_{Rec} = 5528$ for a/R = 0.0185. On the other hand, Fig. 7.6 indicates that the observed onset of drag reduction for guar fluids in the 2-3/8-in. coiled tubing occurs at $N_{Reg}^* = 7900$ which is close to 7031, as predicted by Eq. (7.3). The variances in observed onset Reynolds number are probably due to the nature of drag reduction onset. Since drag reduction is a phenomenon associated with turbulence, the variance in onset Reynolds number can be related to the uncertainties in the laminar-turbulent flow regime transition.
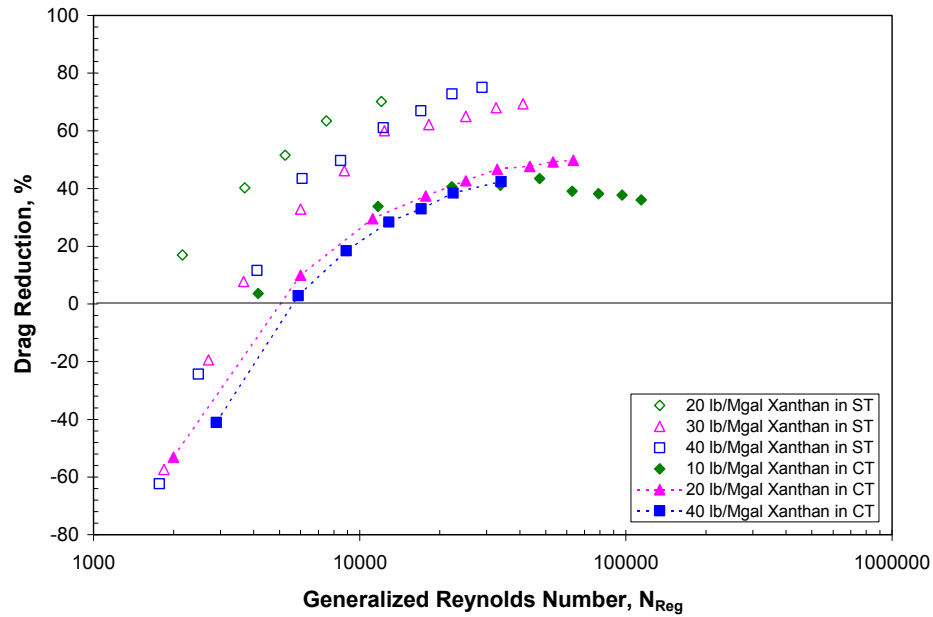
Fig. 7.5—Drag reduction of xanthan fluids in 2-3/8-in. straight and coiled tubing.
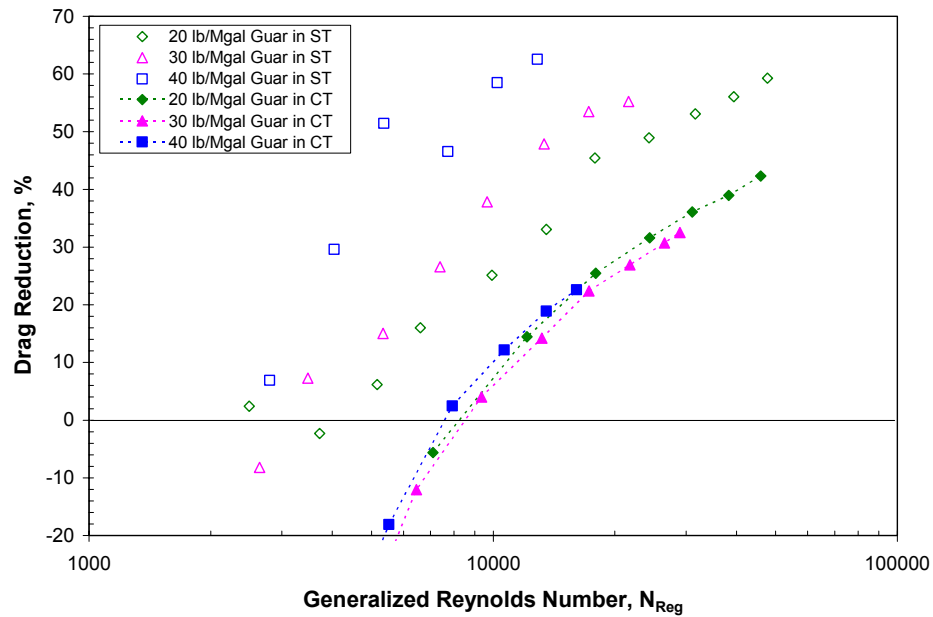
Fig. 7.6—Drag reduction of guar fluids in 2-3/8-in. straight and coiled tubing.

7.3   Maximum Drag Reduction Asymptote in Coiled Tubing

For turbulent flow of dilute polymer solutions in straight pipes, Virk et al.[135] proposed an ultimate drag reduction asymptote as given by Eq. (6.14). This correlation is a mean curve of maximum drag reduction data from 9 sources with total of 235 data points, as shown in Fig. 7.7.   The maximum scatter of the data is ± 15%. This maximum drag reduction correlation has been referenced by numerous authors in literature on drag reduction or has been used as a reference line for friction pressure analysis of drag-reducing fluids.
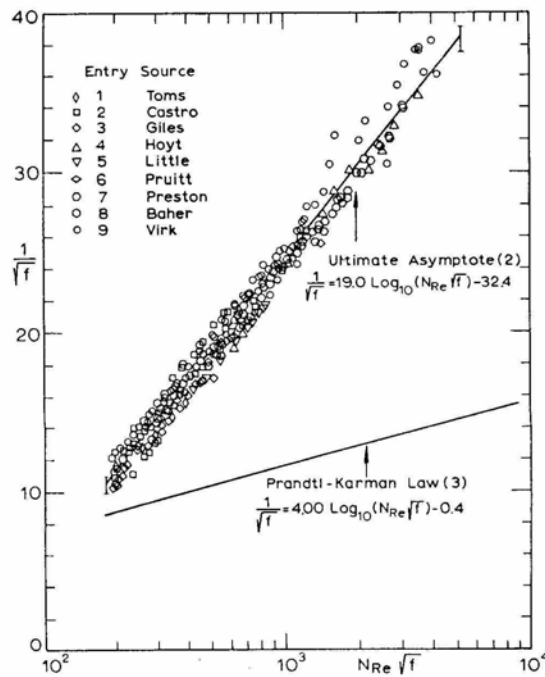
Fig. 7.7—Virk's correlation of drag reduction ultimate asymptote on Prandtl coordinates, $1/\sqrt{f}$ versus $N_{Re}\sqrt{f}$.[135]

Our previous analysis of friction behavior of polymeric fluids has indicated that the friction factor in straight tubing can be close to or even below the Virk's

182

asymptote. The friction factor of more concentrated polymer solutions in straight tubing can be below the Virk's asymptote because they are more shear-thinning than the dilute polymer solutions. But, it is evident that the friction factor in coiled tubing has never reached the Virk's asymptote. As a matter of fact, the friction factor in coiled tubing is bounded by lines that are functions of curvature ratio. These bounding lines are called the drag reduction asymptotes in coiled tubing. Virk's asymptote is just a limiting case of the curved tubing asymptotes. In the following, we develop equations for these asymptotes in coiled tubing.

Development of maximum drag reduction asymptote for coiled tubing. First, for each curvature ratio (corresponding to each coil in the lab-scale tests), plot the friction factor data of all fluids at all concentrations on the same plot of Fanning friction factor versus generalized Reynolds number. Then, compare the data points and remove those data points that show high friction factor and keep those that show the minimum friction factor. Repeat this procedure for each curvature ratio and four data sets of minimum friction factor corresponding to four curvature ratios were obtained. Then, these four data sets were plotted in the Prandtl-Karman coordinates, as shown in Fig. 7.8.

Clearly, these data sets are straight lines which can be curve-fitted with the following equation:

$$\frac{1}{\sqrt{f}} = A\log\left[N_{\text{Reg}}\sqrt{f}\right] + B \dots\dots\dots\dots\dots\dots\dots\dots\dots\dots\dots\dots\dots\dots\dots\dots\dots\dots(7.4)$$

The values of correlation constants A and B are given in Table 7.2.
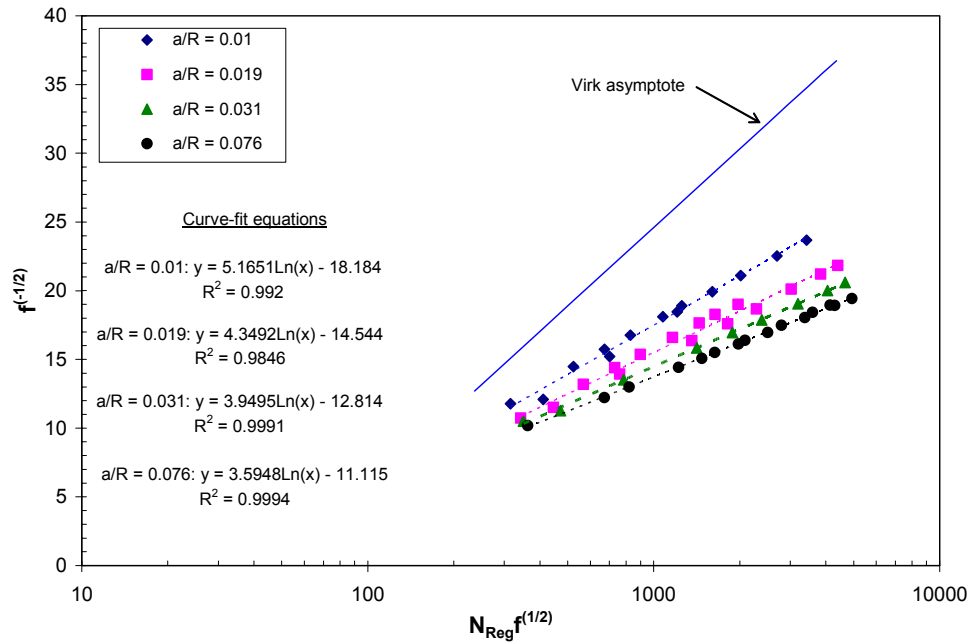
Fig. 7.8—Friction factors at maximum drag reduction for CT on Prandtl-Karman coordinates, $1/\sqrt{f}$ **versus** $N_{Reg}\sqrt{f}$ **.**

Table 7.2—Correlation Constants of the Maximum Drag Reduction Asymptotes in CT

a/R	A	B
0	19.0	32.4
0.010	11.893	18.184
0.019	10.014	14.544
0.031	9.094	12.814
0.076	8.277	11.115

The correlation constants of the Virk's asymptote are also included in Table 7.2 as a special case with a/R = 0 for straight tubing. Constants A and B have strong correlations with curvature ratio and can be correlated as follows:

$$A = \left[c_1 + c_2 \left(\frac{a}{R} \right)^{0.5} \right]^{-1} , \dots\dots\dots\dots\dots\dots\dots\dots\dots\dots\dots\dots\dots\dots\dots(7.5)$$

where c_1 = 0.053109965 and c_2 = 0.29465004 with correlation coefficient R^2 = 0.9814.

$$B = \left[c_3 + c_4 \left(\frac{a}{R} \right)^{0.5} \right]^{-1} , \dots\dots\dots\dots\dots\dots\dots\dots\dots\dots\dots\dots\dots\dots\dots(7.6)$$

where c_3 = 0.0309447 and c_4 = 0.245746 with correlation coefficient R^2 = 0.9924.

Therefore, the maximum drag reduction asymptotes for coiled tubing can be written as:

$$\frac{1}{\sqrt{f}} = \frac{1}{0.05311 + 0.29465 \left(\frac{a}{R} \right)^{0.5}} \log_{10} \left[N_{Reg} \sqrt{f} \right] + \frac{1}{0.03094 + 0.24575 \left(\frac{a}{R} \right)^{0.5}} .(7.7)$$

When a/R = 0, A = 18.83 and B = 32.32. These values of A and B are very close to Virk's constants of 19.0 and 32.4 respectively for straight tubing. Therefore, Eq. (7.7) reduces to the Virk asymptote for straight tubing.

7.4   Drag Reduction Envelope for Coiled Tubing

Parallel to the work of Virk et al.,[135] we can construct the drag reduction envelope for coiled tubing as follows. Drag reduction in coiled tubing will be bounded by three lines – the laminar flow correlation, the maximum drag reduction (MDR) asymptote for CT, the zero-drag reduction line which can be represented by the Srinivasan correlation for Newtonian turbulent flow in coiled tubing. For laminar flow regime,

we choose the correlation of Liu and Masliyah[97] based on its performance of predicting laminar friction factor in coiled tubing, as reviewed in Chapter 2. Fig. 7.9 shows an example of drag reduction envelope for coiled tubing.
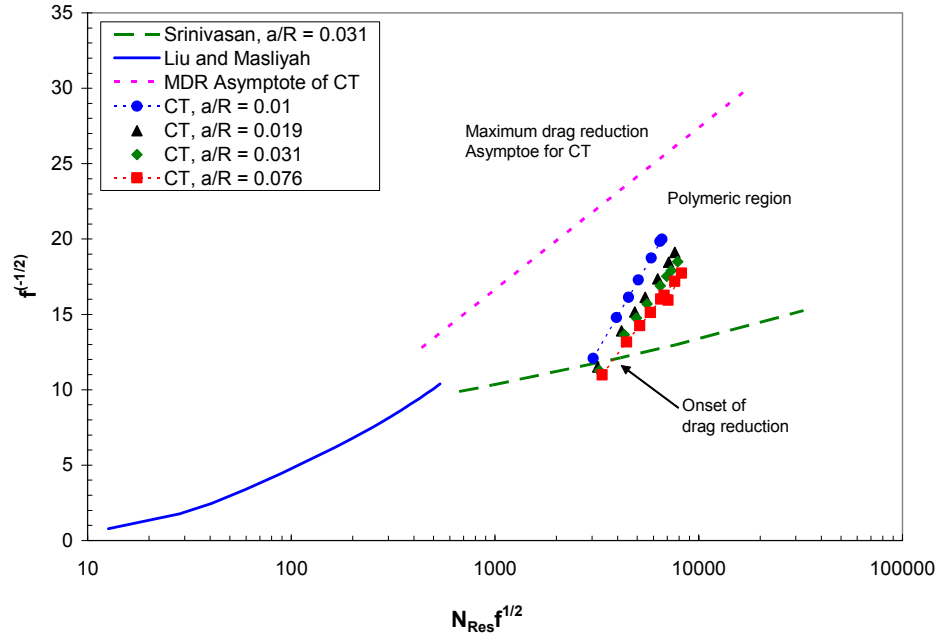
Fig. 7.9—Drag reduction envelope showing the drag reduction behavior of 30 lb/Mgal xanthan in ½-in. CT.

It should be noted that all three bounding lines in the drag reduction envelope are functions of curvature ratio. This is different from the Virk's drag reduction envelope where the bounding lines – Hagen-Poiseuille law, Prandtl-Karman law, and Virk asymptote – are fixed.

7.5 Application of CT Drag Reduction Envelope

7.5.1 Effect of Curvature Ratio

As an example, Figs. 7.10 to 7.12 show the drag reduction behavior of 10, 20, and 30 lb/Mgal HPG fluids on the drag reduction envelope of coiled tubing. In constructing

these envelopes, a curvature ratio of a/R = 0.019 was used with the Srinivasan correlation, Liu and Masliyah correlation, and the new MDR asymptote for CT. Several observations can be made based on Figs. 7.10 to 7.12. First, the data appear to be more or less straight lines. The slopes of these lines are increased slightly with decreasing curvature ratio. The smaller the curvature ratio, the closer the data lines are to the maximum drag reduction asymptote. Second, the intersection points of the data lines and the zero-drag reduction line represent the onset of drag reduction. It can be seen that increasing curvature ratio delays the onset of drag reduction. Careful observation of Figs. 7.10 to 7.12 indicates that the onset points from these plots are consistent with what were shown in Figs. 7.1 to 7.3. Similar drag reduction plots for xanthan fluids in the ½-in. tubing systems are shown in Figs. 7.13 to 7.16.
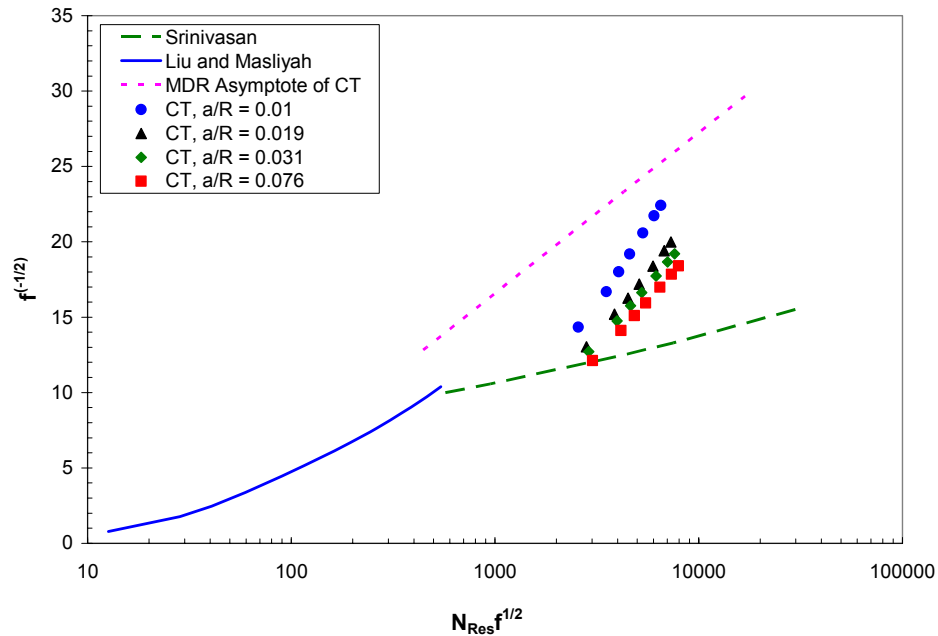
Fig. 7.10—Effect of curvature ratio on DR of 10 lb/Mgal HPG in ½-in. coiled tubing.
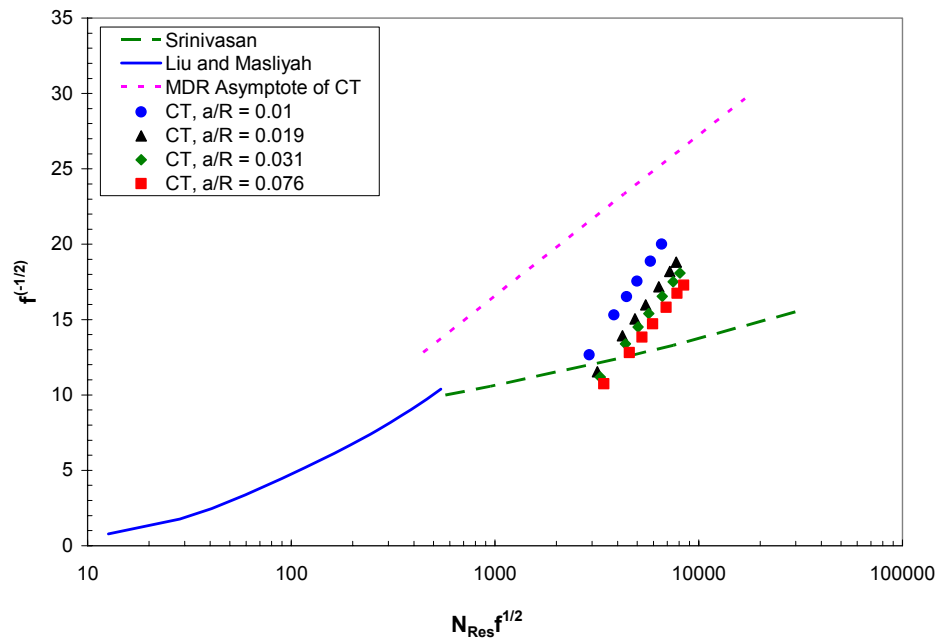
Fig. 7.11—Effect of curvature ratio on DR of 20 lb/Mgal HPG in ½-in. coiled tubing.
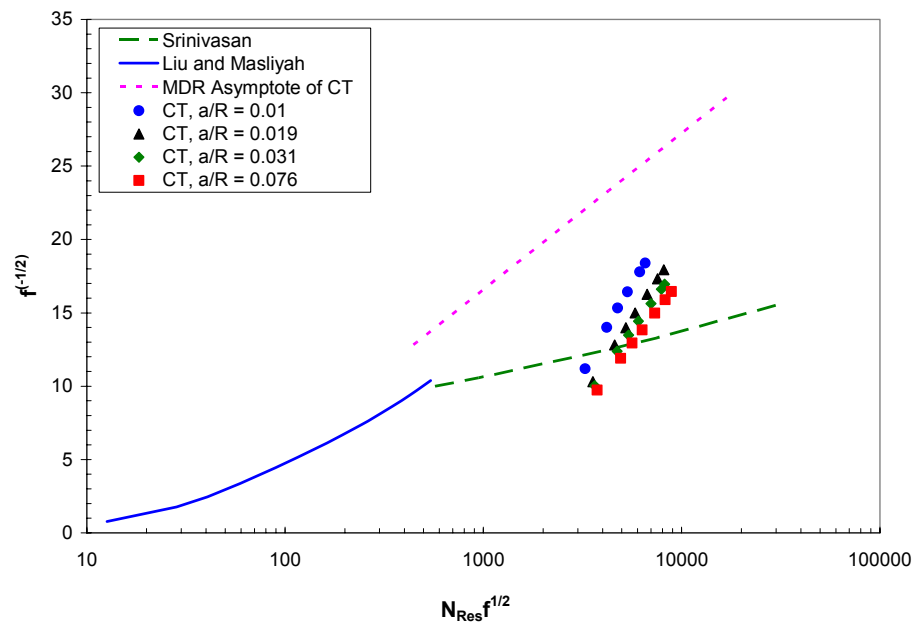
Fig. 7.12—Effect of curvature ratio on DR of 30 lb/Mgal HPG in ½-in. coiled tubing.
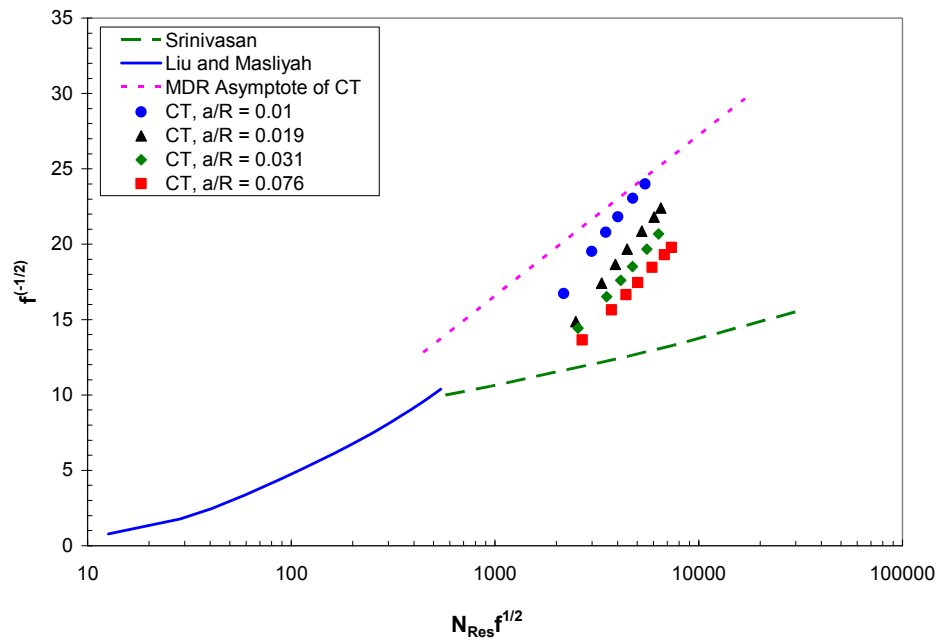
Fig. 7.13—Effect of curvature ratio on DR of 10 lb/Mgal xanthan in ½-in. coiled tubing.
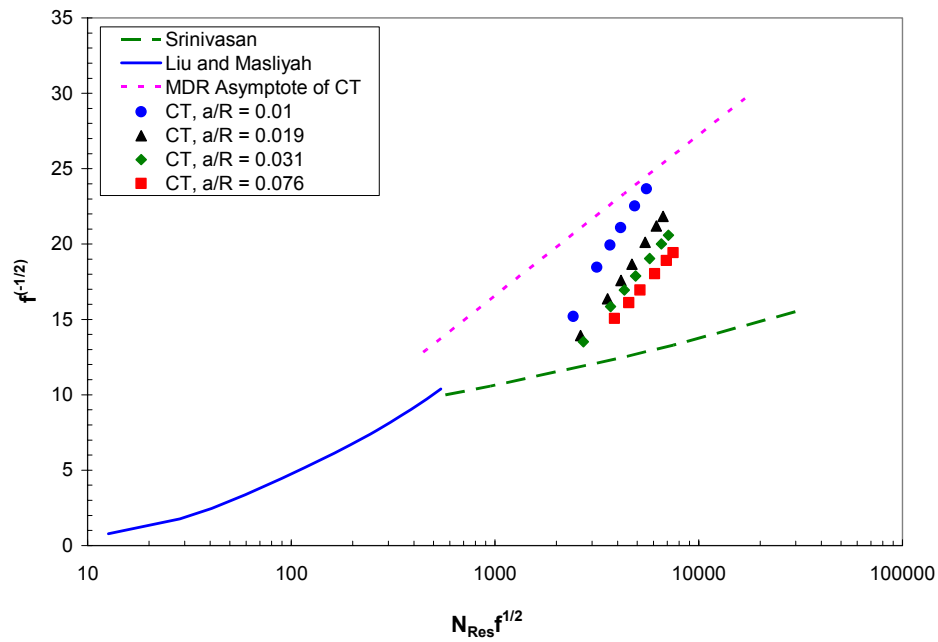
Fig. 7.14—Effect of curvature ratio on DR of 15 lb/Mgal xanthan in ½-in. coiled tubing.
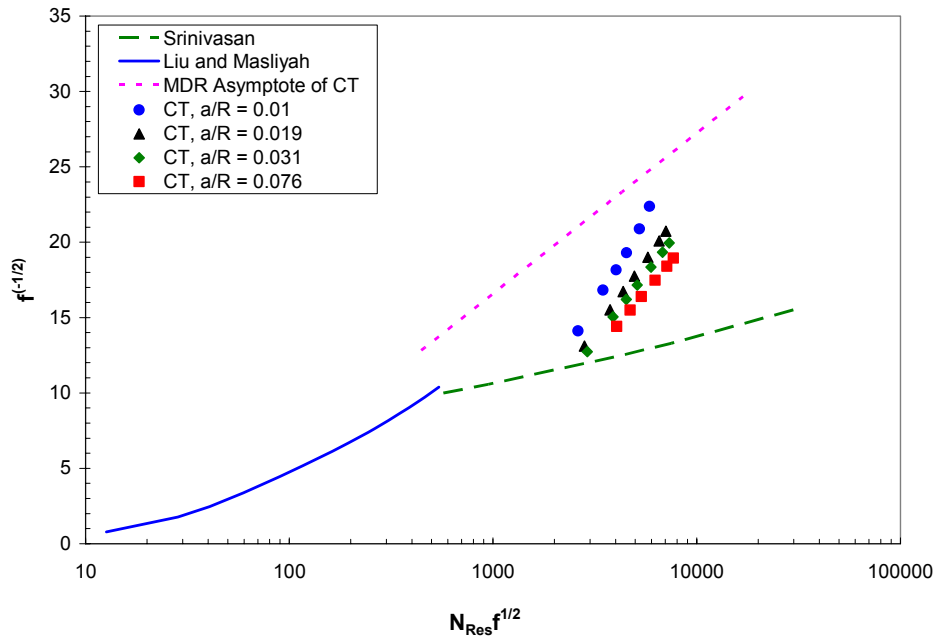
Fig. 7.15—Effect of curvature ratio on DR of 20 lb/Mgal xanthan in ½-in. coiled tubing.
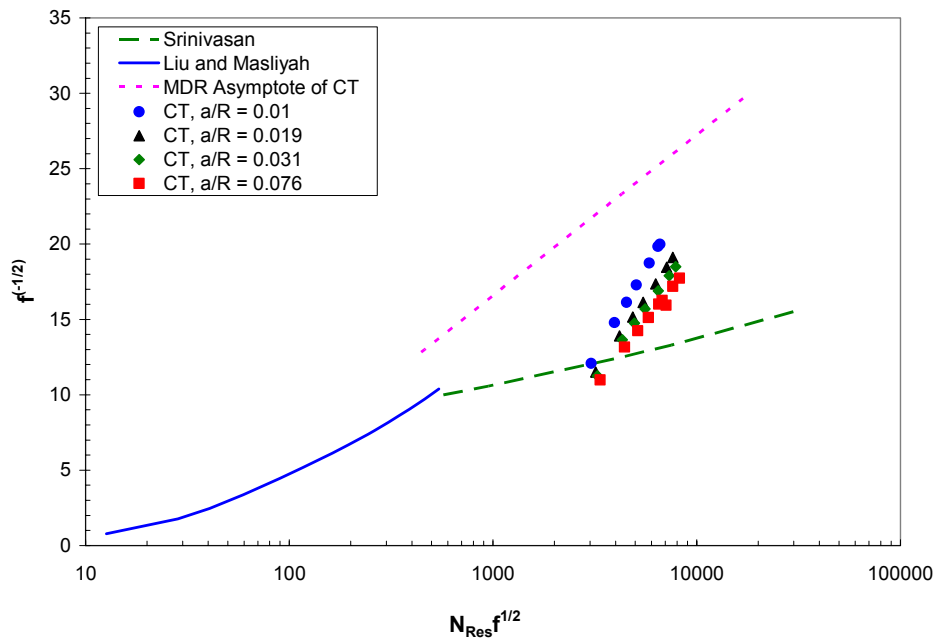
Fig. 7.16—Effect of curvature ratio on DR of 30 lb/Mgal xanthan in ½-in. coiled tubing.

7.5.2 Effect of Polymer Concentration on Drag Reduction

Figs. 7.17 and 7.18 show the effect of polymer concentration on the drag reduction behavior of HPG fluids in straight tubing and a coiled tubing with curvature ratio of 0.019, respectively. It can be observed from Fig. 7.17 that as HPG polymer concentration increases, the slopes of the data also increases. This is in agreement with Virk's study.[129] In contrast, for coiled tubing, the slopes of the data do not seem to be affected by the HPG concentration. In fact, the difference in drag reduction behavior between straight and coiled tubing can be more clearly seen from the results of xanthan fluids. Figs. 7.19 and 7.20 compare the behavior of xanthan fluids in straight and coiled tubing respectively. Again, for xanthan fluids in coiled tubing, xanthan concentration has little effect on the slopes of the data lines. We only see slight decrease in slope in the case of a/R = 0.019. But, for flow in straight tubing, on the other hand, the slopes of the data lines change drastically. After 20 lb/Mgal concentration, further decreasing xanthan concentration reduces the slopes and the vertical position of the data lines of the 10 and 15 lb/Mgal xanthan solutions. This explains why we saw increased friction factors in Figs. 6.46 and 6.47 when the xanthan concentration was reduced to 10 and 15 lb/Mgal. Therefore, the drag reduction envelope can serve as a useful tool in selecting the optimum polymer concentration for drag reduction.
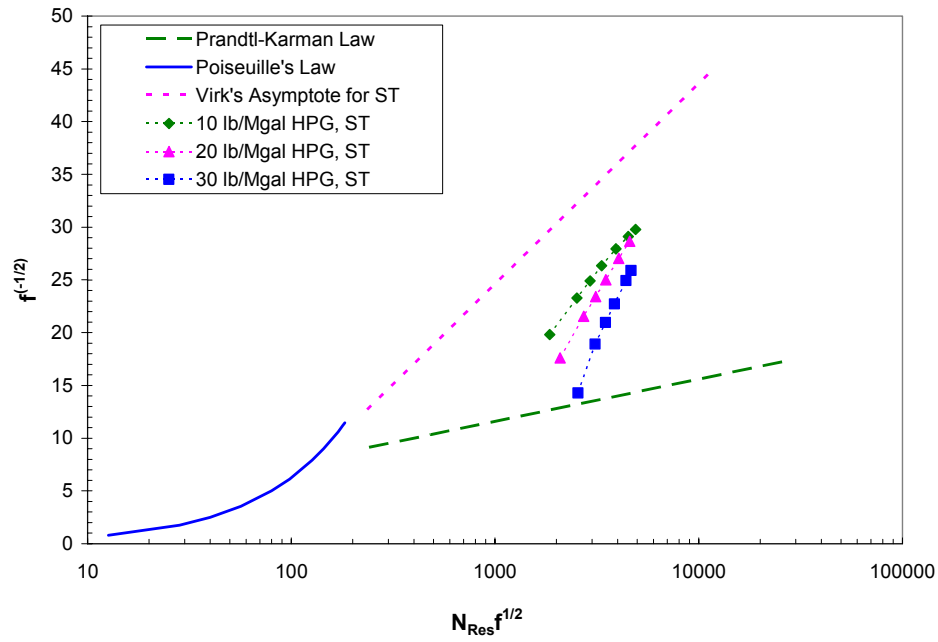
Fig. 7.17—Effect of HPG concentration on DR in ½-in. straight tubing.
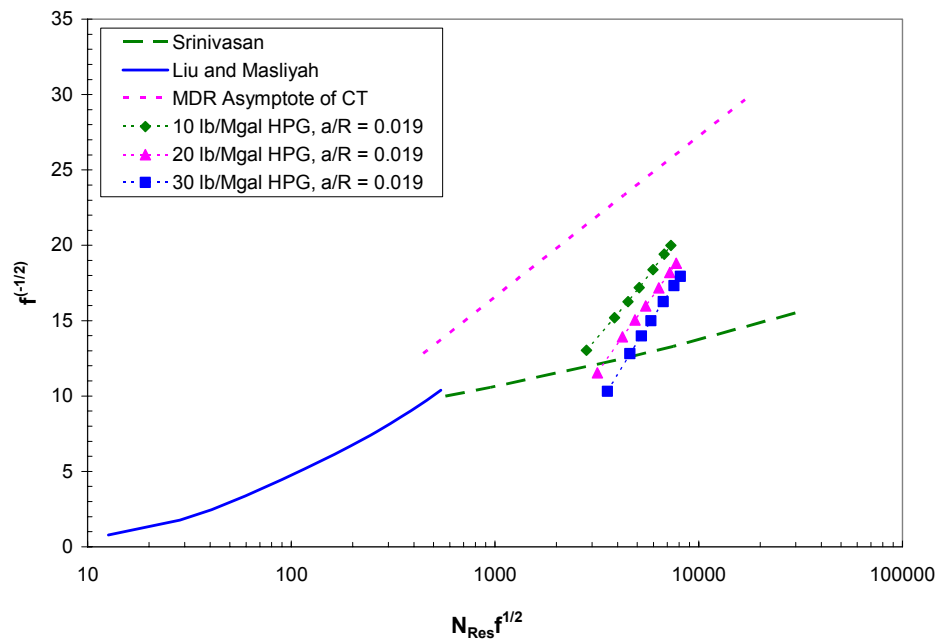
Fig. 7.18—Effect of HPG concentration on DR in ½-in. coiled tubing with curvature ratio a/R = 0.019.
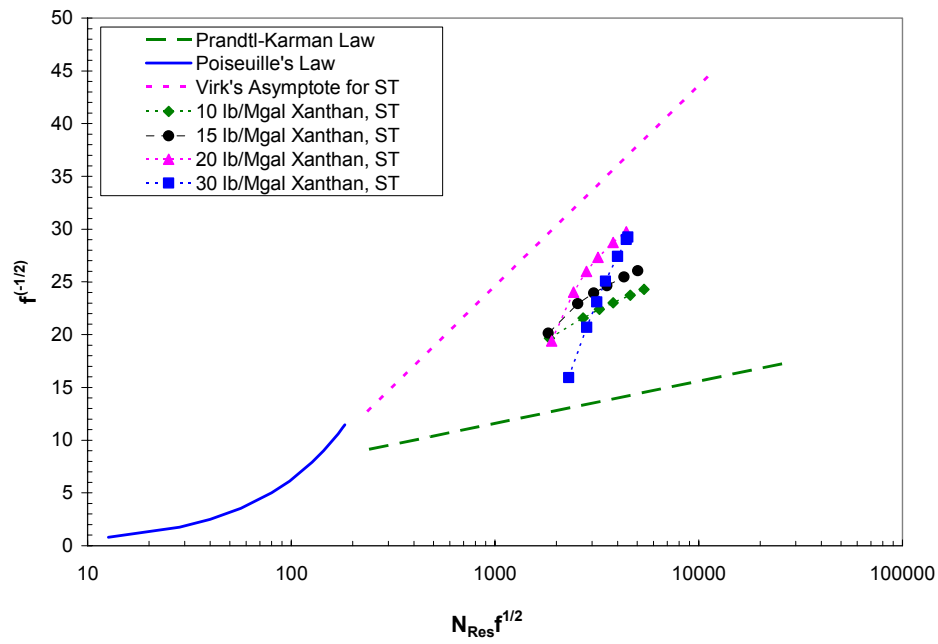
Fig. 7.19—Effect of xanthan concentration on DR in ½-in. straight tubing.
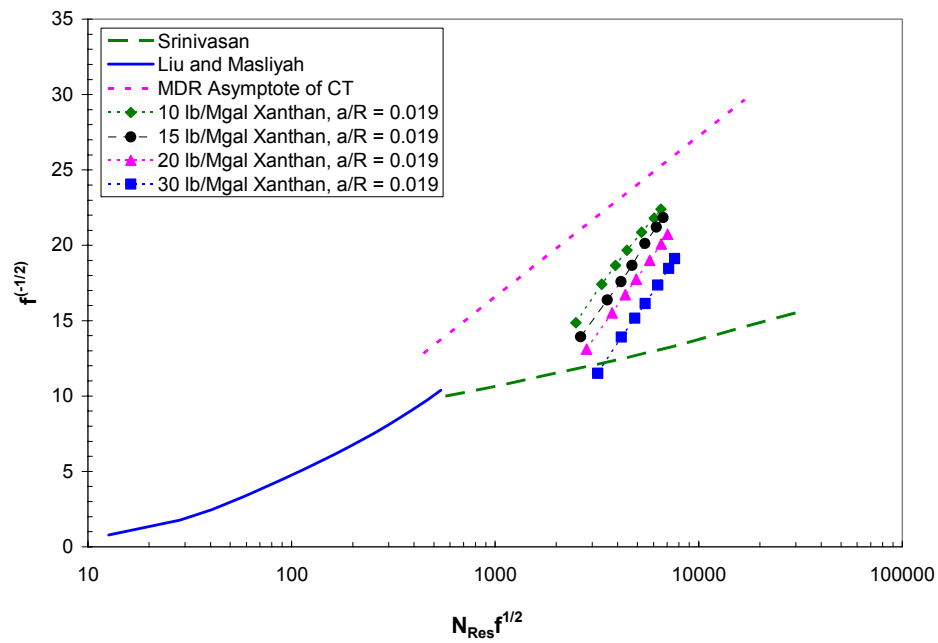
Fig. 7.20—Effect of xanthan concentration on DR in ½-in. coiled tubing with curvature ratio a/R = 0.019.

To further illustrate the application of the drag reduction envelope, we can examine the friction results of xanthan fluids tested using the field-size flow loop. Figs. 7.21 and 7.22 show the results of 10, 20, and 40 lb/Mgal xanthan fluids in the 1-in. and 2-3/8-in. coiled tubing respectively. For the 10 lb/Mgal xanthan in the 2-3/8-in. tubing, the data slope is changed when $(N_{Res}f^{1/2})$ is increased. At low flow rate (low $N_{Res}f^{1/2}$), the slope is large, implying that higher drag reduction can be achieved by increasing flow rate. But beyond a certain value of $N_{Res}f^{1/2}$, the data of the 10 lb/Mgal xanthan turn toward the zero-drag reduction line. This behavior is even more pronounced in the smaller tubing size (1-in.). In the case of 1-in. coiled tubing, the slope of data points of the 10 lb/Mgal xanthan has been small at all flow rates. Therefore, there would be no further gain in drag reduction for the 10 lb/Mgal xanthan if flow rate is increased. The practical value of the drag reduction analysis in this case is that with the 10 lb/Mgal xanthan, the maximum drag reduction could not be reached. Higher xanthan concentration should be considered.
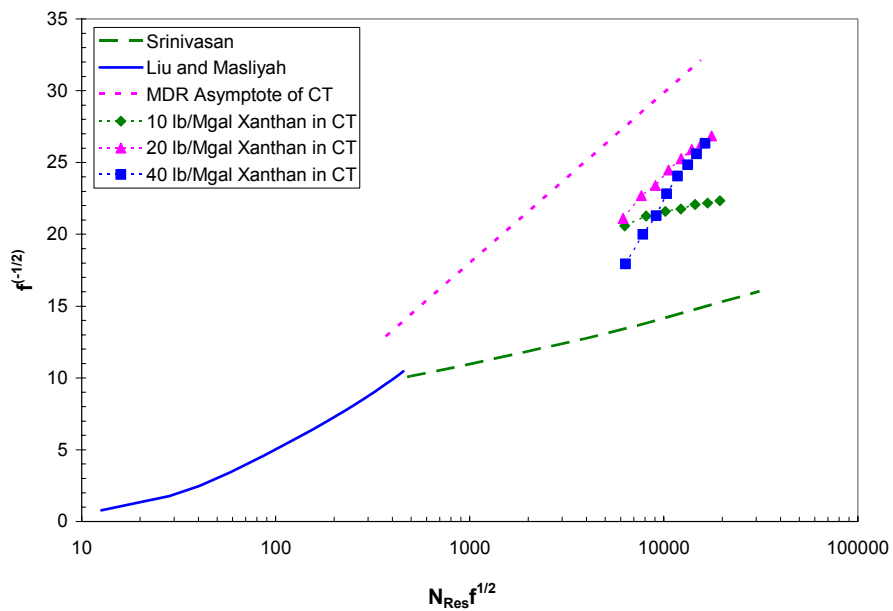
Fig. 7.21—Effect of xanthan concentration on DR in 1-in. coiled tubing with curvature ratio a/R = 0.0113.
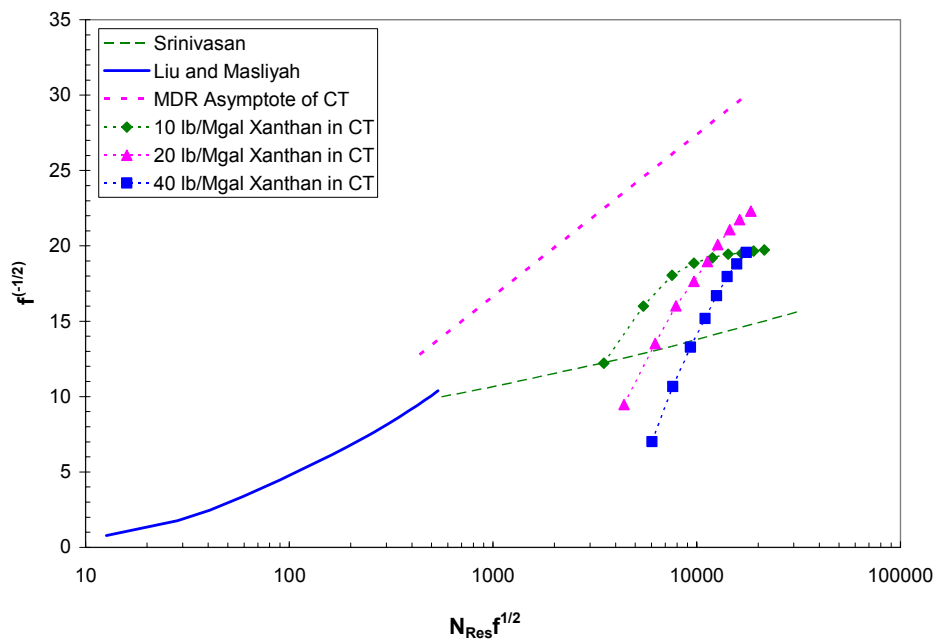
Fig. 7.22—Effect of xanthan concentration on DR in 2-3/8-in. coiled tubing with curvature ratio a/R = 0.0185.

195

7.6   Summary

The polymer fluids tested in this study displayed significant drag reduction properties in both straight and coiled tubing. It was found that coiled tubing curvature reduced the drag reduction and delayed the onset of drag reduction of polymer fluids in coiled tubing.

Based on the drag reduction data of the ½-in. lab-scale flow loop which has wider range of curvature ratio, a new correlation of maximum drag reduction (MDR) asymptote for polymeric fluid fluids in coiled tubing has been developed. When curvature ratio is set to zero, this new correlation reduces to the Virk's MDR asymptote for dilute polymer solutions in straight pipes. Therefore, this new correlation is more universal than the well-known Virk's MDR asymptote for straight pipe.

A new drag reduction envelope for fluid flow in coiled tubing was also proposed. Examples have shown that the drag reduction envelope was a useful tool for analyzing the drag reduction behavior of polymer fluids in coiled tubing.

CHAPTER 8

CFD SIMULATION OF FLUID FLOW IN COILED TUBING

8.1   Introduction

Fluid flow in coiled tubing is featured by the secondary flow that is caused by the centrifugal forces in the curved geometry. As we have seen in Chapter 2, since Dean's classical work, numerous studies on coiled pipe flow have been reported in the literature. These various studies can be categorized according to the factors considered in each study. These factors can be geometrical effects (curvature ratio, helicity, and torsion), Reynolds number, Dean number, and flow regime (laminar or turbulent) as well as fluid properties (Newtonian and non-Newtonian). If the curvature and helicity are involved, the flow in coiled pipe would become more complex to solve. Previous studies often simplified the coiled pipe geometry. For example, the curvature ratio can be assumed small or the torsion effect can be neglected. As far as the fluid is concerned, most previous studies investigated Newtonian fluids, only a few[5,86,100,136] considered non-Newtonian fluids. The review of Chapter 2 indicates that the vast majority of previous research efforts have dealt with Newtonian laminar flow in small-curvature-ratio coiled pipes. The main reason is believed to be due to the difficulties involved for the complex geometry and coordinate systems. Fortunately, FLUENT,[137] as a powerful CFD software, can

overcome the difficulty due to the coiled pipe geometry. FLUENT is especially useful in simulating complex fluid flow geometries.

The objective of the present study is to initiate an effort on CFD modeling of both Newtonian and non-Newtonian fluid flow in a real-size coiled tubing geometry and also to understand the fundamental flow behavior and frictional pressure in coiled tubing flow.

8.2   About Fluent

FLUENT is one of the state-of-the-art computational fluid dynamics softwares for modeling fluid flow and heat transfer in complex geometries. FLUENT provides complete mesh flexibility, solving flow problem with both structured and unstructured meshes with relative ease. The FLUENT software package includes the solver (FLUENT), the preprocessors (such as GAMBIT[138]) for geometry modeling and mesh generation, and translators (filters) for import of surface and volume meshes from CAD/CAE packages. FLUENT solvers are based on the finite volume method. The flow domain is discretized into a finite set of control volumes or cells. The general conservation (transport) equations for mass, momentum, energy, etc., are discretized into algebraic equations which are solved to render the flow field.

8.3   Model Geometry and Grid Generation

8.3.1   Model Geometry

GAMBIT$^{®}$ has been a useful tool for building the model geometry and meshing the model. In the present work, a 2-3/8-in. coiled tubing on a reel of 111-in. drum

diameter is considered. Before the simulation domain is determined, one consideration on the geometry is to simplify the model geometry. Notice that the coiled tubing has a long and thin geometry. We will model only one turn of the tubing string and assume that the flow will reach fully-developed flow within this turn. Furthermore, since the coiled tubing is tightly coiled (wall-to-wall contact between each turns), the pitch of the helical coil is the tubing OD, i.e., 2.375 in. This results in a dimensionless pitch of 0.0067 << 1. Previous studies[70,73] on the torsion effect have shown that effects of such a small torsion can be assumed negligible. Therefore, the model geometry can be simplified as a torus. Notice further that flow in a torus would be symmetric about the central plane which is normal to the torus axis. Therefore, it is sufficient to model only one half of the torus. This immediately reduces the meshing and computational efforts significantly. A slot is made in the half torus to form the inlet and outlet by cutting out a very thin slice (for example, 0.001 in. thick).

8.3.2   Grid Generation

FLUENT is an unstructured solver. For a 3D problem, various types of cells can be used – hexahedral, tetrahedral, pyramid, and wedge cells as well as hybrid cells. Selection of mesh type depends on the setup time, computational expenses, and numerical accuracy (diffusion). For complex geometries, it is advantageous to use unstructured grids employing triangular or tetrahedral cells for saving setup time. But, for the present study, our concerns are mainly computational expenses and numerical accuracy.

Considering the dimensions of coiled tubing diameter (2.063 in. ID) and its length (356 in.), the geometry is a long and thin duct. Therefore, the cell lengths in the axial direction can not be too small. Meanwhile, to model the secondary flow feature (anticipated for curved pipe flow), moderately fine grids are needed in the tubing cross-section. These considerations lead us to select a hexahedral grid. With hexahedral cells, when the flow is aligned with the grid, high-aspect-ratio cells can be used. But with tetrahedral cells, a large aspect ratio will invariably affect the skewness of the cells, which is undesirable as it may impede accuracy and convergence. Also, for the tubing geometry considered, a mesh of hexahedral cells is expected to result in better numerical accuracy (less diffusion) and faster convergence.

Another consideration in the model meshing is the boundary layer. Finer cells are created near the tubing wall in order to provide more details on the secondary flow which is expected to occur close to the tubing wall.

The meshing procedures are as follows. After the geometry is built, mesh the circular edges on the end faces with uniform intervals. Then, mesh the boundary layer for these edges by specifying the first row height, growth factor, and total rows for the boundary layer. For the circular area in the center on the two end faces, specify the mesh interval size and apply Quad/Pave scheme to finish the meshing of the end faces. Next, mesh the edges in the axial direction into uniform segments by specifying the number of intervals (e.g., 720). Finally, apply the Cooper scheme to the whole volume since the geometry is a logical cylinder with both end faces as the

caps (source faces) and the tubing wall and the central plane (symmetry plane) forming the barrel.

For grid-independence study, several grids with different mesh sizes were generated. They are: $14(r) \times 20(\theta) \times 720(\phi)$, $23(r) \times 30(\theta) \times 720(\phi)$, $23(r) \times 40(\theta) \times 720(\phi)$, and $16(r) \times 30(\theta) \times 540(\phi)$ meshes. Figs. 8.1 and 8.2 show the meshes of Grid 3. The four grids are all non-uniform in the radial direction (r). Grid 1 has a boundary layer of 5 rows with the first row being 0.04 in. and a growth factor of 1.2. Both Grid 2 and Grid 3 each have a boundary layer of 6 rows with the first row being 0.02 in. and the growth factor of 1.2. By comparing the key flow features of different grids, it was found that there is no obvious difference between Grid 2 and Grid 3. It was then qualitatively decided to use Grid 3 for all laminar flow simulations. For turbulence modeling, Grid 4 was used. Grid 4 has the same boundary layer as Grid 3, but has coarser grid for the central core. This is because it is expected that the changes of flow variables are relatively small in turbulent flow and fine grids are not needed. Also, a coarser grid can reduce time requirement for turbulence simulation.

8.3.3 Simulation Procedure

The basic procedures in a typical CFD analysis involves: (1) problem identification, (2) solver execution, and (3) post-processing. After the modeling goals are defined and the model domain is identified, the model geometry is constructed and grid or mesh is generated. The grid is then imported into the solver. Within the solver, appropriate physical models such as laminar, turbulent or multiphase flow models need to be selected. The properties of the materials – fluid, solid, and/or mixture, are

defined. The boundary conditions at all the boundary zones are specified. To start the solver execution (iteration), an initial solution has to be provided. The discretized conservation equations are solved iteratively until convergence is reached when changes in solution variables from one iteration to the next are negligible (within convergence criteria). FLUENT provides useful tools, such as residual plots, to help monitor the convergence process.
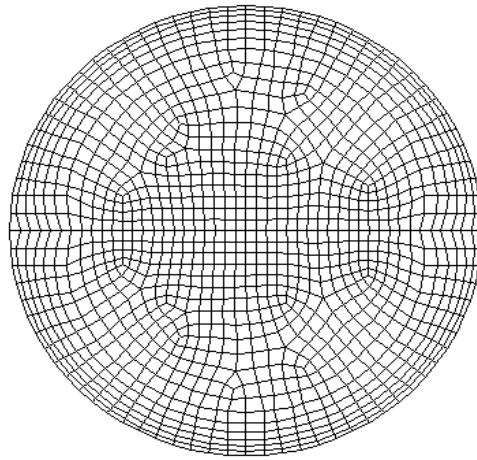
Fig. 8.1—Grid of the tubing cross-section (Grid 3).
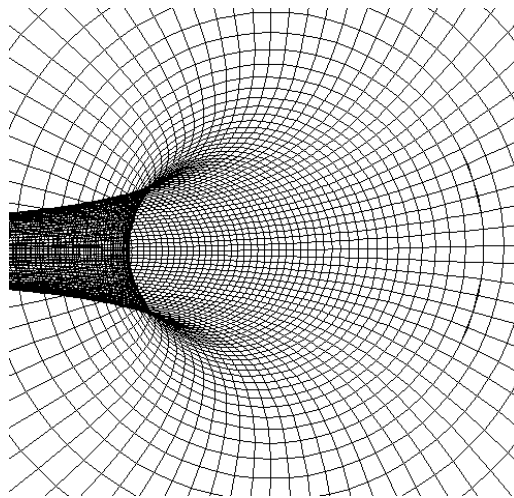
Fig. 8.2—Inside view of the grid on the tubing wall (Grid 3).

To obtain converged solutions, the first order numerical scheme is generally selected first. The under-relaxation factors are kept small. After a number of iterations, increase the under-relaxation factors to speed up the convergence. Finally, switch to second order scheme to get more accurate solutions. Therefore, the solutions in this modeling study are all second order accurate.

In the post-processing stage, the converged solutions are examined visually and numerically to obtain information on the overall flow patterns, key flow features and to extract useful engineering data. The converged solutions need to be checked for accuracy. Revisions to the physical models and modifications (such as grid adaption) to the grid may be considered.

8.4   Results and Discussion

8.4.1   Newtonian Laminar Flow

Figs. 8.3 through 8.6 show the simulation results of water flow in 2-3/8-in. coiled tubing at flow rate of 0.5, 1, and 2 gpm (these rates perhaps are unpractically low, since water has low viscosity and flow rate has to be kept low for laminar regime). The axial velocity (in ft/s) contours reveal unique features of curved pipe flow. It can be observed that in all the cases, the contours are distorted from the counterparts in straight tubings, i.e., co-axial circles. The high velocity region is shifted toward the outer side of the tubing due to centrifugal forces. This will cause the secondary flow. It is interesting and maybe surprising to note that in cases 1 (q = 0.5 gpm) and 3 (q = 2 gpm), there is only one maximum axial velocity value and it occurs on the axis of symmetry, but in case 2 (q = 1 gpm), there are twin maxima of the axial velocity

symmetrically placed with respect to the axis of symmetry. This result is actually in agreement with Dennis and Ng[68] who found that for Dean number D < 956 [Here, D is defined as $D = (2a/R)^{1/2} Ga^3/\mu v$, and is related to N_{De} by $D = 4\sqrt{2} N_{De}$, as discussed in Chapter 2], only one solution (single-maximum) can be obtained. For D > 956, dual solutions (twin maxima) are obtained. The secondary flow of the single maximum solution has one pair of counter-rotating vortices, while the secondary flow of the dual solutions has four-vortex pattern consisting of two vortex pairs. The Dean numbers for these three cases are: D = 584, 1168, and 2237 respectively. Though D = 2237 > 956 for the case 3, it has a single-maximum solution, this is contrary to Dennis and Ng.[68] This is probably because at high Reynolds (Dean) numbers, a multiple vortex solution is unstable and a two-vortex solution will be re-established.
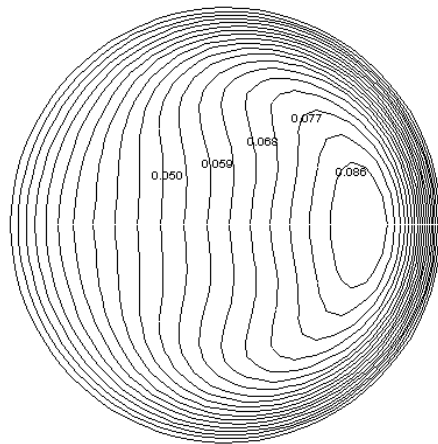
Fig. 8.3—Contours of axial velocity (water in 2-3/8-in. CT, q = 0.5 gpm).
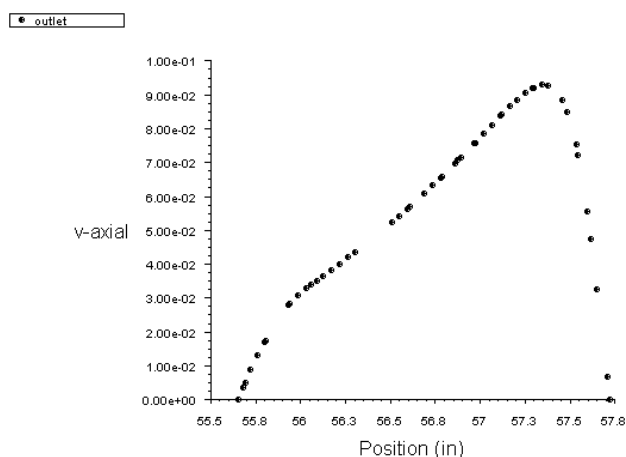
Fig. 8.4—Axial velocity profile (water in 2-3/8-in. CT, q = 0.5 gpm).
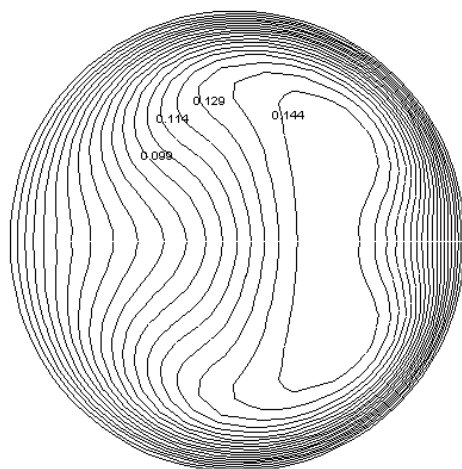
Fig. 8.5—Contours of axial velocity (water in 2-3/8-in. CT, q = 1 gpm).

Fig. 8.7 compares the results of friction pressure gradients by the CFD simulations and the Ito correlation[4] which was obtained for Newtonian laminar flow using the boundary layer approximation method. It can be seen that the CFD result is in close agreement with the Ito correlation.

205
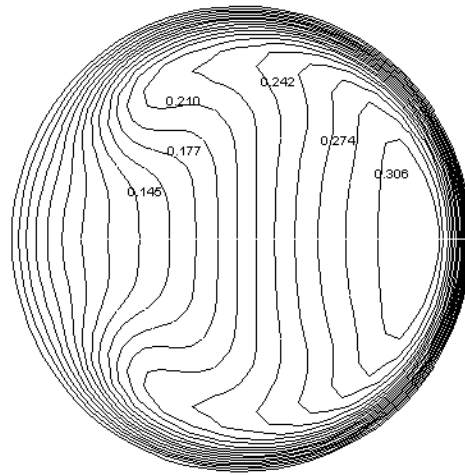
Fig. 8.6—Contours of axial velocity (water in 2-3/8-in. CT, q = 2 gpm).
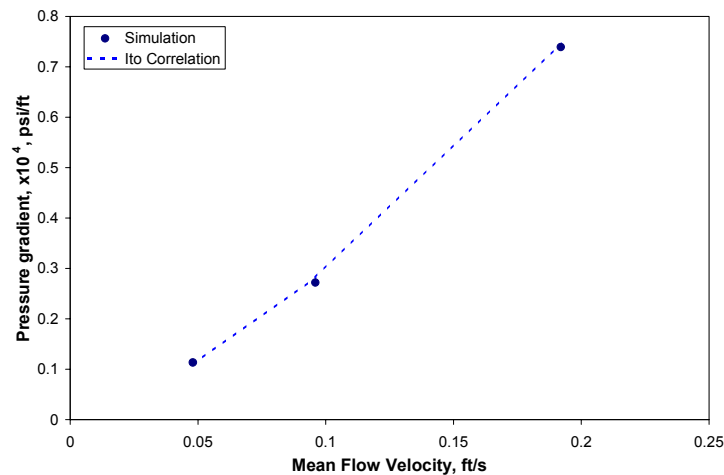
Fig. 8.7—Frictional pressure gradient vs. mean flow velocity (water, laminar).

8.4.2   Newtonian Turbulent Flow

Fig. 8.8 and Fig. 8.9 show the axial velocity contours of water flow in 2-3/8-in. coiled tubing at rates of 30.5 and 119.2 gpm. At these flow rates the flow regime is turbulent. In the simulation, $k\text{-}\varepsilon$ model was chosen as the turbulence model. From Fig.

206

8.10 it can seen that the axial velocity is more uniform than in laminar flow. The large

axial velocity gradients only occur in a very thin layer close to the wall boundary.
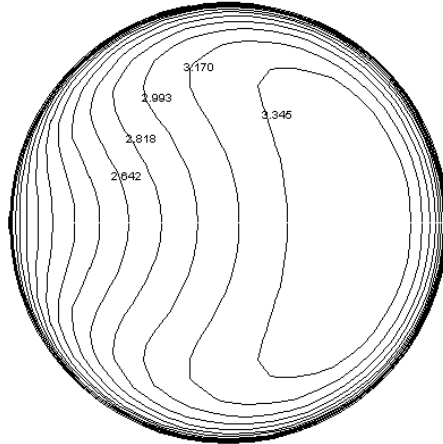
Fig. 8.8—Contours of axial velocity (water in 2-3/8-in. CT, q = 30.5 gpm).
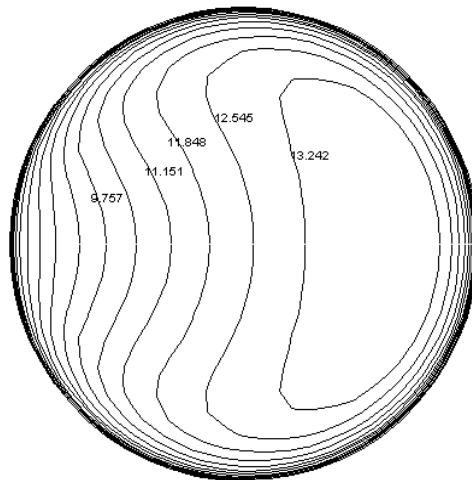
Fig. 8.9—Contours of axial velocity (water in 2-3/8-in. CT, q = 119.2 gpm).
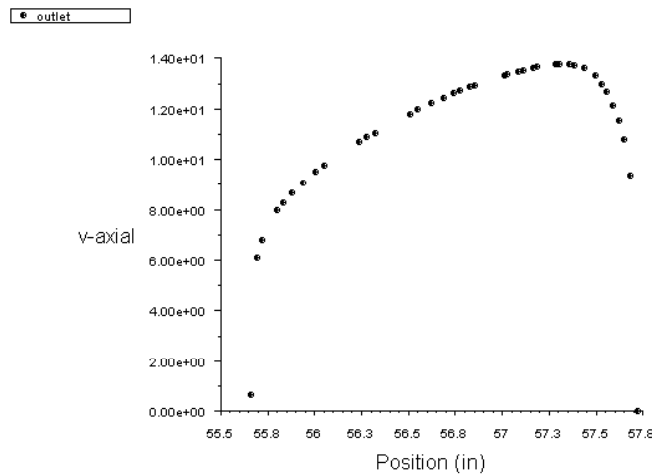
Fig. 8.10—Axial velocity profile (water in 2-3/8-in. CT, q = 119.2 gpm).

Fig. 8.11 compares the friction pressure gradients predicted by CFD simulation and the experimental data. Both Ito[83] and Srinivasan *et al.*[90] correlations are compared with the CFD results. The two correlations are lower than the experimental data. This is probably because the correlations were developed based on tests run with smooth pipes. In the CFD modeling, a pipe roughness of 0.0004 in. was found to match the experimental data well.

8.4.3 Non-Newtonian Laminar Flow

The flow of 40 lb/Mgal Guar fluid in 2-3/8-in. coiled tubing is modeled for flow rates of 30.5, 60.0, 90.4, and 119.2 gpm (these are the rates used in the experiments). Under these flow rates, the flow in 2-3/8-in. coiled tubing is expected to be in laminar regime. Rheologically, this fluid can be described by a power law model with flow behavior index $n = 0.432$ and consistency index $k_p = 0.0243$ $lb_f\text{-}s^n/ft^2$.
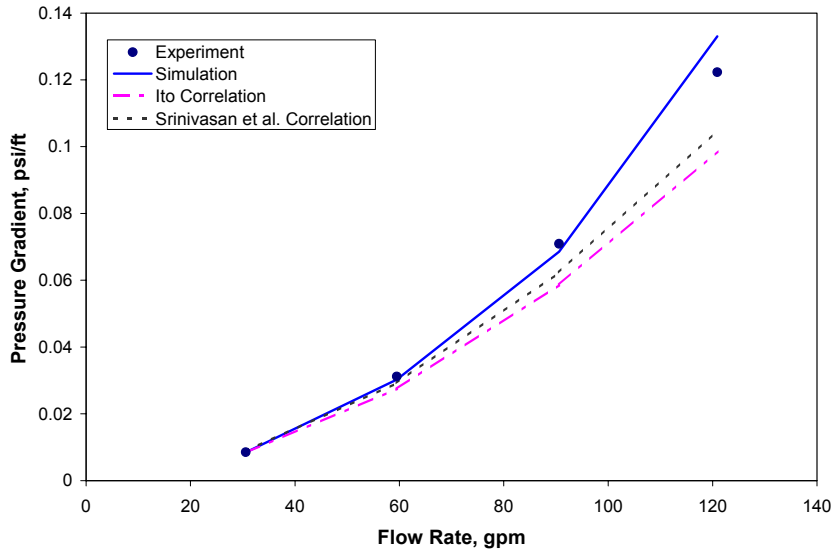
Fig. 8.11—Frictional pressure gradient vs. flow rate (water, turbulent).

Fig. 8.12 shows the axial velocity contours of 40 lb/Mgal guar flowing through 2-3/8-in. coiled tubing at 60 gpm. Fig. 8.13 shows the corresponding axial velocity profile along the tubing diameter. The feature of these contours and profile is similar to the case of laminar Newtonian flow, i.e., the velocity profile is distorted from the counterpart of straight tubing flow.
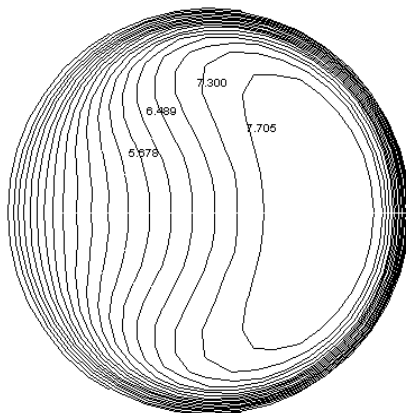
Fig. 8.12—Contours of axial velocity (40 lb/Mgal guar in 2-3/8-in. CT, q = 60 gpm).
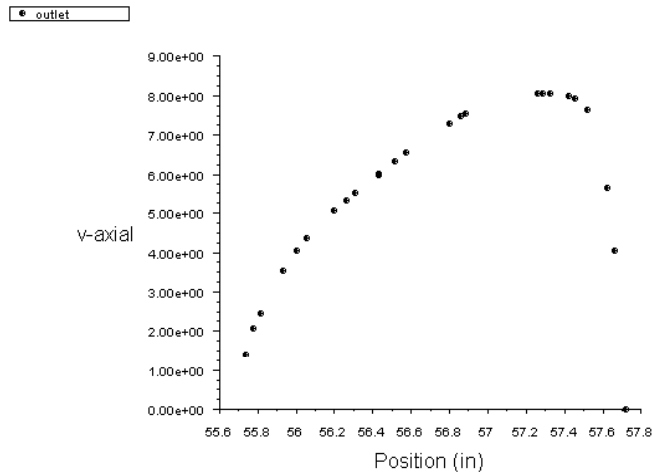
Fig. 8.13—Axial velocity profile (40 lb/Mgal guar in 2-3/8-in. CT, q = 60 gpm).

Fig. 8.14 evaluates the friction pressure gradient predicted by the CFD simulation with the experimental data. Generally, the agreement is rather good. The pressure gradients by the CFD modeling are slightly higher than the experimental values.

The current version of FLUENT used in this work does not provide the capability of modeling non-Newtonian turbulent flow. Therefore, turbulent flow of the 40 lb/Mgal guar fluid was not simulated in this study.
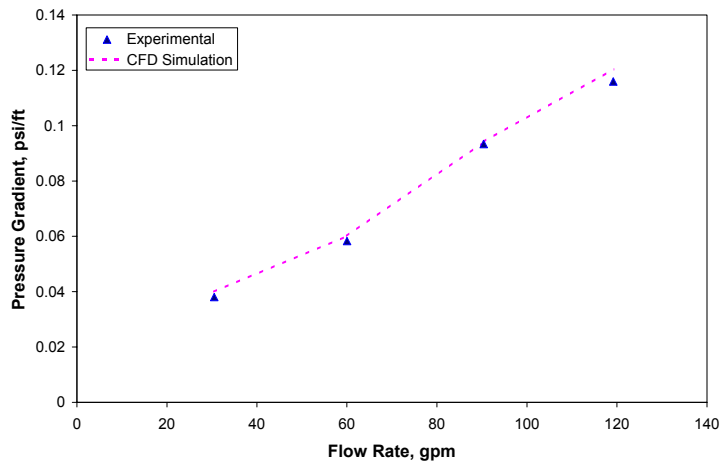
Fig. 8.14—Frictional pressure gradient vs. flow rate (40 lb/Mgal guar, laminar).

8.5　Summary

The flow patterns revealed by the CFD simulations agree well with the previous theoretical and numerical studies. The axial velocity profile in coiled tubing is distorted from the counterpart of straight tubing flow. The high velocity region is shifted toward the outer side of the tubing. Flow regimes affect the axial velocity profiles. In laminar flow of Newtonian fluid, the velocity profile is very different from the parabolic one as in straight tubing; while in turbulent flow, the velocity profile is relatively uniform and the difference between straight and coiled tubing is not as significant as for laminar flow. This is because the turbulence eddies tend to mix the fluid and lead to more uniform flow. As the Reynolds (Dean) number increases, the secondary flow is largely confined to a thin boundary layer close to the tubing wall. Large changes of axial velocity occur mainly in the boundary layer. This supports the basic assumptions of the boundary layer theory for coiled pipe flow. The friction pressure gradients of Newtonian turbulent flow and non-Newtonian laminar flow predicted by the CFD modeling agree well with the flow data of full-scale coiled tubing experiments. The simulation result of friction pressure gradients of Newtonian laminar flow was also verified with the published correlations.

CHAPTER 9

CONCLUSIONS AND RECOMMENDATIONS

9.1   Conclusions

1. Under flow conditions of high Dean number and small curvature ratio (a/R), viscous effect in coiled tubing is important only in a thin boundary layer near the tubing wall. Therefore, the boundary layer approximation method can be applied to the analysis of both laminar and turbulent flow of power-law fluid in coiled tubing. The present study not only corrected the errors in the Mashelkar and Devarajan's correlation, but also extended the work of Mashelkar and Devarajan to wider range of fluids with flow behavior index from 0.25 to 1.0.

2. There is an excellent agreement between the new friction factor correlation of this study for non-Newtonian laminar flow in coiled tubing and the experimental data from experiments using full-scale flow loop. The new correlation matches well with the Ito correlation for Newtonian laminar flow in coiled pipe. It is recommended that the new correlation for laminar flow in coiled tubing should be used for generalized Dean number greater than 100.

3. A new friction factor correlation for non-Newtonian turbulent flow in coiled tubing has been developed based on boundary layer approximation analysis and numerical solutions. The new correlation was found to match

experimental data well under certain conditions and within certain range of generalized Reynolds number. But the accuracy and range of applicability of this new correlation should be further evaluated in future with non-drag reducing fluids.

4. The frictional pressure behavior of four types of polymer fluids – xanthan, PHPA, guar, and HEC have been investigated using field-scale flow loop. It is found that friction factor of polymer solutions in coiled tubing is significantly higher than in straight tubing. The biggest difference in friction factor between coiled tubing and straight tubing can be as high as 185%. As generalized Reynolds number increases, the friction factors in coiled tubing and straight tubing were seen to diverge. This is because of two different flow mechanisms – extended laminar flow in straight tubing and secondary flow effect in coiled tubing.

5. Empirical correlations of friction factor as functions of generalized Dean number for polymer solutions in turbulent flow have been developed based on field-scale experimental data. Evaluation of these correlations indicated that for most data points used for the development of the correlations, the deviations between correlations and the experimental data were within 5%. The accuracy of the correlations was also verified with experimental data from independent tests.

6. Flow of polymer fluids in coiled tubing exhibits different characteristics of drag reduction than in straight tubing. Drag reduction in coiled tubing was

found significantly lower than in straight tubing. The coiled tubing curvature delays the onset of drag reduction.

7. A correlation of maximum drag reduction (MDR) asymptote for coiled tubing has been developed. This correlation reduces to the well-known Virk's asymptote for dilute polymer solutions in straight pipes. A new drag reduction envelope, which is composed of the new CT MDR asymptote, Liu and Masliyah correlation, and Srinivasan correlation, has been proposed to provide useful insights into the drag reduction behavior in coiled tubing.

8. CFD simulation is an effective approach of studying fluid flow in coiled tubing. Simulation results of Newtonian laminar and turbulent flow, and non-Newtonian laminar in a 2-3/8-in. coiled tubing revealed essential flow features in coiled tubing, such as secondary flow and shift of higher velocity toward the outside wall. The friction pressures from CFD simulations also match the correlations and experimental data well.

9. Water tests with field-scale coiled tubing reels and the ½-in. lab-scale flow loop have shown that the water friction factor in coiled tubing can be higher than in straight tubing by as much as 30%. A new correlation of friction factor has been proposed for Newtonian turbulent flow in coiled tubing with roughness effect. Comparison with experimental data indicated that the new correlation could adequately describe the effect of roughness in coiled tubing.

9.2   Recommendations for Future Research

1. Conduct additional flow tests with non-drag reducing fluids in coiled tubing to further verify the newly developed friction factor correlation for non-Newtonian turbulent flow in coiled tubing. An example of non-drag reducing fluids is carbopol solutions at different concentrations.

2. Surfactant fluids have been used in recent coiled tubing applications due to their unique drag reduction property. Their flow behavior in coiled tubing is expected to be different than polymer based fluids. It is therefore suggested to perform systematic tests on friction pressure of surfactant-based fluids in the present flow loops.

3. Conduct flow tests of drag reducers in coiled tubing. Since over 95% CT operations involve pumping slick water (water with drag reducers), it would be of great benefits to the industry to experimentally study the drag reducing behavior of drag reducers. Currently, there is no correlation available to predict friction pressure of these fluids.

4. Conduct further flow tests of polymer fluids at higher flow rates. In some field pumping operations such as CT fracturing, the pump rates can be much higher than the maximum flow rates we had achieved in this study. The friction pressure behavior at these high flow rates is not known. It is expected that at high enough rates, the difference in friction factor between coiled tubing and straight tubing should decrease and fluids may lose their drag reducing

properties. Additional tests are needed to investigate the friction behavior at higher flow rate conditions.

5. Conduct CFD simulations on the effect of tubing roughness on friction factor. Since there are no available correlations to calculate roughness effect in coiled tubing, and physically building coiled tubing with controlled roughness is not practically feasible, the approach of CFD simulations should be adopted. A range of tubing roughness can be chosen in the simulation of water flow in CT. Based on the simulation results, a correlation of friction factor in coiled tubing with roughness is expected to be developed which should include the effect of curvature ratio and relative roughness.

6. Considering the rapid increase of CT application in hydraulic fracturing, studies in multiphase flow in coiled tubing should be conducted. Under typical fracturing through CT conditions, the centrifugal acceleration in coiled tubing can be much higher than gravitational acceleration (say 30 g). Under the effect of this strong centrifugal force, phase separation would be expected. Experiments at various flow velocities, different curvature ratios, and different solid concentrations should be conducted to develop flow regime maps. These flow regime maps are expected to have significant potential applications in the multiphase flow studies in coiled tubing.

NOMENCLATURE

a   =   radius of coiled tubing

a' =   coefficient in Eq. (3.67); coefficient of McCann and Islas friction factor correlation in Table 2.3

a/R   =   curvature ratio

A   =   constant in Eq. (4.13); correlation constant in Eqs. (6.15) and (7.4)

b' =   coefficient in Eq. (3.67); coefficient of McCann and Islas friction factor correlation in Table 2.3

B   =   constant in Eq. (4.13); correlation constant in Eqs. (6.15) and (7.4)

$c_0, c_1, \ldots, c_6$ =   coefficients of empirical correlations used in Eqs. (3.66). (3.69), (4.66), (4.67), (7.3), (7.5), and (7.6), and in Table 6.6

C   =   axial pressure gradient, Eqs. (3.5) and (4.5); correlation constant in Eq. (6.15)

CT   =   coiled tubing

d   =   inside diameter of pipe

D   =   Dean number, Eq. (2.9); characteristic angular velocity, Eq. (4.35)

D_e =   for Newtonian fluid, $D_e = N_{Re}(a/R)^{1/2}$; for non-Newtonian, $D_e = \dfrac{(2a)^n v_m^{2-n} \rho}{K}\sqrt{a/R}$, Eqs. (2.14) and (3.48)

D_o =   dimensionless characteristic angular velocity, Eq. (4.49)

D_{o1}, D_{o3} =   expansion coefficients of dimensionless characteristic angular velocity (D_o), Eq. (4.58)

DR   =   drag reduction, defined in Eqs. (7.1) and (7.2)

f   =   Fanning friction factor

$f_1(n)$ to $f_5(n)$	=	functions of flow behavior index (n), defined in Eqs. (4.42) to (4.46)
f_M	=	Fanning friction factor of mean curve, Eq. (6.15)
f_p	=	Fanning friction factor of polymer solution
f_{rough}	=	Fanning friction factor in rough coiled tubing
f_s	=	Fanning friction factor of solvent
$F(x)$	=	function of x, Eqs. (3.11) and (4.12)
$F'(x)$	=	dF/dx
g	=	gravitational acceleration
$g(\eta)$	=	function defined in Eq. (3.41)
gpm	=	gallon per minute
G	=	pressure gradient, Eqs. (2.5) and (2.9)
h	=	the pitch of the coil (the distance between axes of two adjacent turns of coiled tubing on the reel)
h_r	=	tubing roughness projection
$h(\eta)$	=	function defined in Eq. (3.42)
$k(\eta)$	=	function defined in Eq. (3.43)
K	=	consistency index of power law fluid; Dean number, Eq. (2.7)
K_p	=	consistency index of power law fluid from pipe viscometer, $lb_f s^n/ft^2$
K_v	=	consistency index of power law fluid from Fann Model 35 viscometer, $lb_f s^n/ft^2$
L	=	tubing length over which the pressure drop Δp is measured
M	=	shift factor, Eq. (6.16)
MDR	=	maximum drag reduction
n	=	flow behavior index, dimensionless
N	=	spring factor of Fann Model 35 viscometer, Eq. (6.2)
N_{De}	=	Dean number for Newtonian fluid, Eq. (2.8)
N_{De2}	=	$N_{Re2}(a/R)^{0.5}$

N_{DNg}	=	generalized Dean number, Eq. (3.70)
N_{Re}	=	Reynolds number ($= dv\rho/\mu$)
N'_{Reg}	=	generalized Reynolds number, Eq. (3.49)
N^0_{Re}	=	generalized Reynolds number, the same as N^0_{Reg}
N_{Re2}	=	Reynolds number based on pseudoshear viscosity[91]
N^0_{Reg}	=	generalized Reynolds number [$= \dfrac{(2a)^n v_m^{2-n}\rho}{K}$], Eq. (4.51)
N_{Rec}	=	critical Reynolds number, Eqs. (2.12) and (2.13)
N_{Red}	=	Reynolds number based on differential viscosity[91]
N_{Reg}	=	generalized Reynolds number [$= d^n v^{2-n}\rho/(K_p 8^{n-1})$]
$N_{Reg}{}^*$	=	generalized Reynolds number at onset of drag reduction, Eq. (7.3)
N_{Res}	=	Reynolds number based on solvent viscosity ($= dv\rho/\mu_s$)
p	=	pressure
$(dp/dl)_p$	=	frictional pressure gradient of polymer solution
$(dp/dl)_s$	=	frictional pressure gradient of solvent
Δp	=	frictional pressure drop over tubing length of L
q	=	flow rate
Q	=	flow rate, Eq. (3.61)
Q_c	=	flow rate in coiled pipe, Eq. (2.6)
Q_s	=	flow rate in straight pipe, Eq. (2.6)
r	=	radial co-ordinate
r_B	=	radius at Point B in Fig. 4.2
R	=	radius of coiled tubing reel
R_b	=	radius of bob of viscometer
R_c	=	radius of cup (the rotor) of viscometer
RPM	=	rotational speed of rotor of viscometer in revolutions per minute, Eq. (6.1)
s	=	R_c/R_b, Eq. (6.5)

S	=	shape factor of v-velocitycomponent, Eq. (3.39)
S_o	=	dimensionless form of variable S, Eq. (3.46)
S_{o1}, S_{o3}	=	expansion coefficients of S_o, Eq. (3.55)
ST	=	straight tubing
u	=	velocity component in r direction
U	=	total velocity scale very near to the pipe wall, Eq. (4.39)
v	=	velocity component in θ direction of Figs. 3.1 and 4.1 (or in α direction of Fig. 2.8)
v_m	=	mean velocity
w	=	velocity in axial direction
W_0	=	maximum axial velocity in pipe cross-section, Eq. (2.7)
$w_0, w_1, w_2, \ldots$	=	series coefficients, Eq. (2.10)
w_1	=	axial velocity component at the edge of the boundary layer
w_{10}	=	value of w_1 axial velocity component at the edge of the boundary layer at $\theta = 0$
w_o	=	dimensionless axial velocity at the boundary layer edge $(=w_1/w_{10})$
w_{o2}	=	expansion coefficient of dimensionless variable w_o, Eq. (3.56)
x	=	horizontal Cartesian coordinate, Figs. 3.2 and 4.2
y	=	vertical Cartesian coordinate, Figs. 3.2 and 4.2
Y	=	variable defined in Eq. (3.69)
z	=	Cartesian coordinate in the direction of coil axis, Figs. 2.8, 3.1, and 4.1

Greek Symbols

α	=	variable defined in Eq. (3.53); coefficient in Dodge-Metzner friction factor correlation, Eq. (4.36); angle, Fig. 2.8
α^*	=	variable defined in Eqs. (4.55) and (4.56)

β	=	variable defined in Eq. (3.64); coefficient in Dodge-Metzner friction factor correlation, Eq. (4.36)
γ	=	variable defined in Eq. (3.65)
γ_1	=	$K8^{n-1}\left(\dfrac{3n+1}{4n}\right)^n$, Eqs. (4.37) and (4.38)
$\dot{\gamma}_w$	=	shear rate at the bob, Eq. (6.1)
δ	=	boundary layer thickness
δ_o	=	dimensionless boundary layer thickness
δ_{o0}, δ_{o2}	=	expansion coefficients of dimensionless variable δ_o, Eqs. (3.54) and (4.57)
η	=	dimensionless coordinate ($= \xi/\delta$)
θ	=	angular coordinate
θ_i	=	dial reading at "i" rpm of viscometer, Eq. (6.2)
λ	=	variable defined in Eq. (6.4)
μ	=	dynamic viscosity
μ_s	=	solvent viscosity
ν	=	kinematic viscosity
ξ	=	a - r
ρ	=	density
τ	=	shear stress
τ_w	=	wall shear stress
ϕ	=	angular coordinate in axial direction
ψ	=	stream function
$\psi_1, \psi_2, \ldots$	=	series coefficients, Eq. (2.11)

Overline:

$-$	=	time-averaged

Subscripts

1	=	at the edge of the boundary layer
A	=	at Point A of Figs. 3.2 and 4.2
B	=	at Point B of Figs. 3.2 and 4.2
CL	=	laminar flow in coiled pipe
CT	=	turbulent flow in coiled pipe
o	=	dimensionless
p	=	polymer solution
rr	=	in r direction in plane normal to r
rθ	=	in θ direction in plane normal to r
rϕ	=	in ϕ direction in plane normal to r
s	=	solvent
SL	=	laminar flow in straight pipe
ST	=	turbulent flow in straight pipe
w	=	at pipe wall
$\theta\theta$	=	in θ direction in plane normal to θ

REFERENCES

1. ICoTA: "An Introduction to Coiled Tubing: History, Applications, and Benefits," www.icota.com /publications/.

2. Lang, K.: "Coiled Tubing Reaches for Areas of Growth," *Petroleum Technology Transfer Council Network News* (2002) **8**, No. 2, pp. 7–9.

3. Barua, S.N.: "On Secondary Flow in Stationary Curved Pipes," *Q. J. Mech. Appl. Math.*(1963) **16**, pp. 61–77.

4. Ito, H.: "Laminar Flow in Curved Pipes," *Z. Angew. Math. Mech.*(1969) **49**, pp. 653–63.

5. Mashelkar, R. A. and Devarajan, G. V.: "Secondary Flows of Non-Newtonian Fluids: Part I – Laminar Boundary Layer Flow of a Generalized Non-Newtonian Fluid in a Coiled Tube," *Trans. Instn. Chem. Eng.* (1976) **54**, pp. 100–107.

6. Wright, T. R. Jr. and Sas-Jaworsky II, A.: *Coiled Tubing Handbook*, 3rd edition, World Oil, Gulf Publishing Company, Houston, Texas (1998).

7. Sas-Jaworsky II, A.: "Coiled Tubing … Operations and Services, Part 5, Unloading Wells with Lighter Fluids," World Oil's *Coiled Tubing Handbook*, 1993, pp. 36–43.

8. Sas-Jaworsky II, A.: "Coiled Tubing … Operations and Services, Part 6, Tubing Assisted Logging and Perforating," World Oil's *Coiled Tubing Handbook*, 1993, pp. 45–50.

9. Adams , L.S. and Marsili, D.L.: "Design and Installation of a 20,500 ft Coiled Tubing Velocity String in the Gomez Field, Pecos County, Texas," paper SPE 24792 presented at the 1992 SPE Annual Technical Conference and Exhibition, Washington, DC, Oct. 4–7.

10. Sas-Jaworsky II, A.: "Coiled Tubing … Operations and Services, Part 4, Sands and Solids Washing," World Oil's *Coiled Tubing Handbook*, 1993, pp. 28–33.

11. Anderson, G.W. and Hutchinson, S.O.: "How to Efficiently Wash Sand from Deviated Wellbores," *World Oil* (December 1978) **187**, No. 7, pp. 75-84.

12. Pursell, J.C. and Moore, B.K.: "How to Wash Large Tubulars with Coiled Tubing," *Petroleum Engineer International* (August 1992), pp. 42–45.

13. Appah, D. and Ichara, M.: "Empirical Model Determines Energy Required to Clean Sand from Wellbore," *Oil and Gas Journal* (February 28, 1994) **92**, No. 9, p. 36.

14. Walton, I.C.: "Computer Simulator of Coiled Tubing Wellbore Cleanouts in Deviated Wells Recommends Optimum Pump Rate and Fluid Viscosity," paper SPE 29491 presented at the 1995 SPE Production Operations Symposium, Oklahoma City, OK, April 2–4, 1995.

15. Gu, H. and Walton, I.C.: "Development of a Computer Wellbore Simulator for Coiled Tubing Operations," paper SPE 28222 presented at the SPE Petroleum Computer Conference held in Dallas, Texas, USA, 31 July–3 August 1994.

16. Gary, S.C., Walton, I.C., and Gu, H.: "Two New Design Tools Maximize Safety and Efficiency for Coiled Tubing Pumping Treatments," paper SPE 29267 presented at the SPE Asia pacific Oil & Gas Conference held in Kuala Lumpur, Malaysia, 20–22 March 1995.

17. Bhalla, K. and Walton, I.C.: "The Effect of Fluid Flow on Coiled Tubing Reach," paper SPE 36464 presented at the 1995 SPE Annual Technical Conference held in Denver, Colorado, USA, 6–9 October 1996.

18. Gu, H.: "Transient Aspects of Unloading Oil and Gas Wells with Coiled Tubing," paper SPE 29541 presented at the SPE Production Operations Symposium held in Oklahoma City, OK, 2–4 April, 1995.

19. Misselbrook, J. and Falk, K.: "A Novel Method Using Coiled Tubing for Dewatering Gas Wells," paper SPE presented at the 2005 SPE/ICoTA Coiled Tubing Conference and Exhibition held in the Woodlands, TX, 12–13 April 2005.

20. Moore, B.K. et al.: "Rigless Completions: A Spoolable Coiled Tubing Gas-lift System," paper OTC 7321 presented at the 25th Annual OTC in Houston, Texas, USA, 3–6 May 1993.

21. Misselbrook, J., Wilde, G., and Falk, K.: "The Development and Use of a Coiled Tubing Simulation for Horizontal Applications," paper SPE 22822 presented at 66th Annual Conference and Exhibition of SPE held in Dallas, TX, October 6–9, 1991.

22. "Coiled Tubing: State of the Industry and Role for NETL," Topical Report prepared for U.S. Department of Energy by National Energy Technology Laboratory, Contract No. DE-AD26-00NT00612, June 2005.

23. Snyder, R.E.: "US Firms Could Follow Canada's Lead in Coiled Tubing Drilling," World Oil (February 2005) **226**, No. 2, www.worldoil.com/magazine/.

24. "Introduction to Coiled Tubing Drilling," LEAding Edge Advantage International Ltd., 2002, www.lealtd.com/pdfs/.

25. Williams, T., Deskins, G., Ward, S.L., and Hightower, M.: "Sound Coiled-Tubing Drilling Practices," Final Report to DOE National Energy Technology Laboratory and U.S. Department of the Interior Minerals Management Service, DOE/NETL-2002/1170, ww.maurertechnology.com/NewsEvents/publications/.

26. Courville, P.W. and Maddox, S.D.: "Rigless Slimhole Drilling," paper OTC 7331 presented at the 25th Annual OTC in Houston, Texas, 3–6 May 1993.

27. Ramos Jr. A.B. et al.: "Horizontal Slim-hole Drilling with Coiled Tubing: An Operator's Experience," paper SPE 23875 presented at the 1992 IADC/SPE Drilling Conference held in New Orleans, Feb. 18–21.

28. Wu, J. and Juvkam-Wold, H.C.: "Drilling and Completing Horizontal Wells with Coiled Tubing," paper SPE 26366 presented at the 68th Annual Technical Conference and Exhibition of SPE held in Houston, Texas, Oct. 3 – 6, 1993.

29. Gavin, W.G.: "Fracturing though Coiled Tubing – Recent Developments and Case Histories," paper SPE 60690 presented at the 2000 SPE/ICoTA Coiled Tubing Roundtable, Houston, TX, USA, 5–6 April 2000.

30. Spady, D.W., Udick, T.H., and Zemlak,, W.M.: "Enhancing Production in Multizone Wells Utilizing Fracturing through Coiled Tubing," paper SPE 57435 presented at the 1999 SPE Eastern Regional Meeting held in Charleston, West Virginia, USA, 21–22 October.

31. Gulrajani, S.N., and Olmstead, C.C.: "Coiled Tubing Conveyed Fracture Treatments: Evolution, Methodology, and Field Application," paper SPE 57432 presented at the 1999 SPE Eastern Regional Meeting, Charleston, West Virginia, USA, 21–22 October.

32. Rodvelt, G., Toothman, R., and Willis, S.: "Multiseam Coal Stimulation Using Coiled-tubing Fracturing and a Unique Bottomhole Packer Assembly," paper SPE 72380 presented at the SPE Eastern Regional Meeting, Canton, OH, USA, 17–19 October 2001.

33. Economides, M.J., Ben-Naceur, K., and Klem, R.C.: "Matrix Stimulation Method for Horizontal Wells," paper SPE 19719 presented at the 64th Annual

Technical Conference and Exhibition of SPE held in San Antonio, TX, October 8–11, 1989.

34. Thomas, R.L. and Milne, A.: "The Use of Coiled Tubing during Matrix Acidizing of Carbonate Reservoirs," paper SPE presented at SPE Asia Pacific Oil & Gas Conference held in Kuala Lumpur, Malaysia, 20–22 March 1995.

35. Frick, T.P. and Economides, M.J.: "State of the Art in the Matrix Stimulation of Horizontal Wells," paper SPE 26997 presented at the Latin American Petroleum Engineering Conference held in Buenos Aires, Argentina, 27–29 April 1994.

36. Mauro Tambini: "An Effective Matrix Stimulation Technique for Horizontal Wells," paper SPE 24993 presented at the European Petroleum Conference held in Cannes, France, 16–18 November 1992.

37. Bunnell, F.D. and Daud, M.M.: "Coiled Tubing Stimulations Eliminate Hole Failures & Condensate Losses in Arun Field," paper SPE 30681 presented at the SPE Annual meeting in Dallas, USA, 22–25 October 1995.

38. Pleasants, C.W., Head, D.W., and de Ruiter, J.: "Design, Testing, and Field Use of a New Selective Reeled Tubing Well Stimulation System," paper SPE 22826 presented at the 66th Annual Technical Conference and Exhibition of SPE held in Dallas, TX, USA, October 6–9, 1991.

39. Loveland, K.R. and Bond, A.J.: "Recent Applications of Coiled Tubing in Remedial Wellwork at Prudhoe Bay," paper SPE 35587 presented at the SPE Western Regional Meeting held in Anchorage, Alaska, 22–24 May 1996.

40. Mirza, T., Budiman, M., Cannan, W.L., and Bordelon, T.P.: "Coiled Tubing Workovers in Deep, Hot Wells," paper SPE 20427 presented at the 65th Annual Technical Conference and Exhibition of the Society of Petroleum Engineers held in New Orleans, LA, September 23–26, 1990.

41. Vidick, B., Nash, F.D. and Hartley, I.: "Cementing Through Coiled Tubing and Its Influence on Slurry Properties," paper SPE 20959 presented at Europec 90, the Hague, Netherlands, 22–24, October, 1990.

42. Harrison, T.W. and Blount, C.G.: "Coiled Tubing Cement Squeeze Technique at Prodhoe Bay, Alaska," paper SPE 15104 presented at the 1986 California Regional Meeting of the SPE, Oakland, April 2–4.

43. Hornbrook, P.R. and Mason, C.M.: "Improved Coiled Tubing Squeeze Cementing Techniques at Prodhoe Bay," paper SPE 19543 presented at the 1989 Annual Technical Conference and Exhibition of the SPE, San Antonio, Oct. 8–11.

44. Carpenter, R.B.: "New Technologies Address the Problem Areas of Coiled Tubing Cementing," paper SPE 20426 presented at the 1990 SPE Annual Technical Conference and Exhibition, New Orleans, Sept. 23–26.

45. Nowak, T.W., Patout, T.S., and Buzarde, C.B.: "Rigless Multi-zone Recompletion Using a Cement Packer Placed with Coiled Tubing: A Case History," paper SPE 35613 presented at the Gas Technology Conference held in Calgary, Alberta, Canada, April 28 – May 1, 1996.

46. Hoyer, C.W.J., Chassagne, A., Vidick, B., and Hartley, I.P.: "A Platform Abandonment Program in the North Sea Using Coiled Tubing," paper SPE 23110 presented at the Offshore Europe Conference held in Aberdeen, 3–6 September 1991.

47. Newman, K. R., Haver, N. A., Stone, L. R., and Tong, D.: "Development of a Coiled Tubing Cable Installation System," paper SPE 30679 presented at the SPE Annual Technical Conference and Exhibition held in Dallas, Oct. 22 – 25, 1995.

48. Hilts, R.L., Fowler Jr., S.H., and Pleasants, C.W.: "Fishing with Coiled Tubing," paper SPE 25499 presented at the Production Operations Symposium held in Oklahoma City, OK, USA, March 21–23, 1993.

49. Mullin, M. A., McCarty, S. H., and Plante, M. E.: "Fishing with 1.5 and 1.75 inch Coiled Tubing at Western Prudhoe Bay, Alaska," paper SPE 20679 presented at the International Arctic Technology Conference, Anchorage, AK, May 29 – 31, 1991.

50. Welch, J. L. and Stephens, R. K.: "Coiled Tubing … Operations and Services, Part 9 – Fishing," *World Oil*'s *Coiled Tubing Handbook*, 1993, pp. 67-71.

51. Stadwiser, J., Best, J., and Wilson, D., and Bloor, B.: "Coiled Tubing Fishing Operation on a Deep, High Pressure, Sour Gas Well," *J. Cdn. Pet. Tech.* (Jan. 1994), pp.16–21.

52. Dean, W.R.: "Note on the Motion of Fluid in a Curved Pipe," *Philos. Mag.* (July 1927) **20**, pp. 208–23.

53. Dean, W.R.: "The Streamline Motion of Fluid in a Curved Pipe," *Philos. Mag.* (April 1928) **30**, pp. 673–93.

54. Van Dyke, M.: "Extended Stokes Series: Laminar Flow through a Loosely Coiled Pipe," *J. Fluid Mech.* (1978) **86**, part 1, pp.129–145.

55. Berger, S.A., Talbot, L., and Yao, L.S.: "Flow in Curved Pipes," *Ann. Rev. Fluid Mech.* (1983) **15**, pp. 461–512.

56. McConalogue, D.J. and Srivastava, R.S.: "Motion of a Fluid in a Curved Tube," *Proc. Roy. Soc. A*. (1968) **307**, pp. 37–53.

57. Eustice, J.: "Flow of Water in Curved Pipes," *Proc. Roy. Soc. London Ser. A* (June 1910) **84**, pp. 107–18.

58. Eustice, J.: "Experiments of Streamline Motion in Curved Pipes," *Proc. Roy. Soc. London Ser. A* (February 1911) **85**, pp. 119–31.

59. Adler, M.: "Flow in Curved Pipes," *Z. Angew. Math. Mech.*(October 1934) **14**, pp. 257–75.

60. Collins, W.M. and Dennis, S.C.R.: "The Steady Motion of a Viscous Fluid in a Curved Tube," *Q. J. Mech. Appl. Math.* (1975) **28**, pp. 133–56.

61. Jones, J.R.: "Flow of a Non-Newtonian Liquid in a Curved Pipe," *Q. J. Mech. Appl. Math.* (1960) **13**, pp. 428–43.

62. Thomas, R.H. and Walters, K.: "On the Flow of an Elastico-viscous Liquid in a Curved Pipe under a Pressure Gradient," *J. Fluid Mech.* (1963) **16**, pp. 228–242.

63. Thomas, R.H. and Walters, K.: "On the Flow of an Elastico-viscous Fluid in a Curved Pipe of Elliptic Cross-section under a Pressure Gradient," *J. Fluid Mech.*(1965) **21**, pp. 173–82.

64. Larrain, J. and Bonilla, C.F.: "Theoretical Analysis of Pressure Drop in the Laminar Flow of Fluid in a Coiled Pipe," *Trans. Soc. Rheol.* (1970) **14**, pp. 135–47.

65. Topakoglu, H.C.: "Steady laminar Flows of an Incompressible Viscous Fluid in Curved Pipes," *J. Math. Mech.*(1967) **16**, No. 12, pp. 1321–1337.

66. Robertson, A.M. and Muller, S.J.: "Flow of Oldroyd-B Fluids in Curved Pipes of Circular and Annular Cross-section," *Int. J. Non-Linear Mech.*(1996) **31**, No. 1, pp. 1–20.

67. Jayanti, S. and Hewitt, G.F.: "On the Paradox Concerning Friction Factor Ratio in Laminar Flow in Coils," *Proc. R. Soc. Lond. A.*(1991) **432**, pp. 291–99.

68. Dennis, S.C.R. and Ng, M.: "Dual Solutions for Steady Laminar Flow through a Curved Tube," *Q. J. Mech. Appl. Math.* (1982) **35**, pp. 305–324.

69. Daskopoulos, P. and Lenhoff, A.M.: "Flow in Curved Ducts: Bifurcation Structure for Stationary Ducts," *J. Fluid Mech.* (1989) **203**, pp.125–148.

70. Germano, M.: "On the Effect of Torsion on a Helical Pipe," *J. Fluid Mech.*(1982) **125**, pp. 1–8.

71. Germano, M.: "The Dean Equations Extended to a Helical Pipe Flow," *J. Fluid Mech.* (1989) **203**, pp. 289–305.

72. Kao, H.C.: "Torsion Effect on Fully Developed Flow in a Helical Pipe," *J. Fluid Mech.* (1987) **184**, pp. 335–356.

73. Trusedell, L.C., Jr. and Adler, R.J.: "Numerical Treatment of Fully Developed Laminar Flow in Helically Coiled Tubes," *AIChE J.* (November 1970), pp. 1010–1015.

74. Greenspan, D.: "Secondary Flow in a Curved Tube," *J. Fluid Mech.* (1973) **57**, pp. 167–76.

75. Patankar, S.V., Pratap, V.S., and Spalding, D.B.: "Prediction of Laminar Flow and Heat Transfer in Helically Coiled Pipes," *J. Fluid Mech.* (1974) **62**, part 3, pp. 539–551.

76. Joseph, B., Smith, E.P., and Adler, R.J.: "Numerical Treatment of Laminar Flow in Helically Coiled Tubes of Square Cross Section. Part I. Stationary Helically Coiled Tubes," *AIChE J.* (September 1975) **21**, pp. 965–74.

77. Dennis, S.C.R.: "Calculation of the Steady Flow through a Curved Tube Using a New Finite-Difference Method," *J. Fluid Mech.* (1980) **99**, pp. 449–467.

78. Hsu, C.F. and Patankar, S.V.: "Analysis of Laminar Non-Newtonian Flow and Heat Transfer in Curved Tubes," *AIChE J.* (July 1982) **28**, pp. 610–616.

79. Soh, W.Y. and Berger, S.A.: "Fully Developed Flow in a Curved Pipe of Arbitrary Curvature Ratio," *Intl. J. Num. Meth. Fluids* (1987) **7**, pp. 733–755.

80. Austin, L.R. and Seader, J.D.: "Fully Developed Viscous Flow in Coiled Circular Pipes," *AIChE J.* (January 1973) **19**, No. 1, pp. 85–94.

81. Patankar, S.V., Pratap, V.S., and Spalding, D.B.: "Prediction of Turbulent Flow in Helically Coiled Pipes," *J. Fluid Mech.* (1975) **67**, part 3, pp. 583–595.

82. Lai, Y.G., So, R.M.C., and Zhang, H.S.: "Turbulence-Driven Secondary Flows in a Curved Pipe," *Theoret. Comput. Fluid Dynamics* (1991) **3**, pp. 163–180.

83. Ito, H.: "Friction Factors for Turbulent Flow in Curved Pipes," *J. Basic Eng.* (June 1959), pp. 123–134.

84. Mori, Y. and Nakayama, W.: "Study on Forced Convective Heat Transfer in Curved Pipes (1st Report)," *Int. J. Heat Mass Transfer* (1965) **8**, pp. 67–82.

85. Mashelkar, R. A. and Devarajan, G. V.: "Secondary Flows of Non-Newtonian Fluids: Part II Frictional Losses in Laminar Flow of Purely Viscous and Viscoelastic Fluids through Coiled Tubes," *Trans. Instn. Chem. Eng.* (1976) **54**, pp. 108–114.

86. Mashelkar, R. A. and Devarajan, G. V.: "Secondary Flows of Non-Newtonian Fluids: Part III – Turbulent Flow of Visco-inelastic Fluids in Coiled Tubes: A Theoretical Analysis and Experimental Verification," *Trans. Instn. Chem. Eng.* (1977) **55**, pp. 29–37.

87. Riley, N.: "Unsteady Fully-developed Flow in a Curved Pipe," *J. Engineering Mathematics* (1998) **34**, pp. 131–141.

88. White, C.M.: "Streamline Flow through Curved Pipes," *Proc. Roy. Soc. London Ser. A* (February 1929) **123**, pp. 645–63.

89. Taylor, G.I.: "The Criterion for Turbulence in Curved Pipes," *Proc. Roy. Soc. London Ser. A* (1929) **124**, pp. 243–49.

90. Srinivasan, P. S., Nandapurkar, S.S., and Holland, F.A.: "Friction Factors for Coils," *Trans. Instn. Chem. Engr.* (1970) **48**, pp. T156–T161.

91. Mishra, P. and Gupta, S.N.: "Momentum Transfer in Curved Pipes. I. Newtonian Fluids, II. Non-Newtonian," *Ind. Eng. Chem. Process Des. Dev.* (1979) **18**, pp. 130–42.

92. Shah, S.N. and Zhou, Y.: "An Experimental Study of Drag Reduction of Polymer Solutions in Coiled Tubing," *Journal of SPE Production & Facilities* (November 2003) **18**, No. 4, pp. 280–287.

93. Sreenivasan, K.R. and Strykowski, P.J.: "Stabilization Effects in Flow through Helically Coiled Pipes," *Experiments in Fluids* (1983) **1**, pp. 31–36.

94. Webster, D.R. and Humphrey, J.A.C.: "Experimental Observations of Flow Instability in a Helical Coil," *Trans., ASME* (September 1993) **115**, pp. 436–443.

95. Hasson, D.: "Streamline Flow in Coils," *Res. Corresp.* (1995) **1**, pp. S1.

96. Mujawar, B.A. and Rao, M.R.: "Flow of Non-Newtonian Fluids through Helical Coils," *Ind. Eng. Chem. Process Des. Dev.* (1978) **17**, No. 1, pp. 22–27.

97. Liu, S. and Masliyah, J.H.: "Axially Invariant Laminar Flow in Helical Pipes with a Finite Pitch," *J. Fluid Mech.* (1993) **251**, pp. 315–353.

98. Barnes, H.A. and Walters, K.: "On the Flow of Viscous and Elastico-Viscous Liquids through Straight and Curved Pipes," *Proc. Roy. Soc. A.* (1969) **314**, pp. 85–109.

99. Jones, W.M. and Davies, O.H.: "The Flow of Dilute Aqueous Solutions of Macromolecules in Various Geometries: III. Bent Pipes and Porous Materials," *J. Phys. D: Appl. Phys.* (1976) **9**, pp. 753–770.

100. Tsang, H.Y. and James, D.F.: "Reduction of Secondary Motion in Curved Tubes by Polymer Additives," *J. Rehol.* (1980) **24**, pp. 589–601.

101. Azouz, I., Shah, S.N., Vinod, P.S., and Lord, D.L.: "Experimental Investigation of Frictional Pressure Losses in Coiled Tubing," paper SPE 37328 presented at the 1996 SPE Eastern Regional Meeting held in Columbus, Ohio, 23–25 October 1996.

102. McCann, P.C. and Islas, C.G.: "Frictional Pressure Loss during Turbulent Flow in Coiled Tubing," paper SPE 36345 presented at the SPE/ICoTA North American Coiled Tubing Roundtable held in Montgomery, Texas, 26–28 February 1996.

103. Shah, S.N., Zhou, Y., and Goel, N.: "Flow Behavior of Fracturing Slurries in Coiled Tubing," paper SPE 74811 presented at the SPE/ICoTA Coiled Tubing Conference held in Houston, TX, 9–10 April 2002.

104. Devarajan, G.V.: "Secondary Flows of Non-Newtonian Fluids," PhD Dissertation, University of Salford, Salford, UK (1975).

105. Perry, R.H.: *Perry's Chemical Engineers' Handbook*, 7th edition, McGraw-Hill, New York (1997), Chapter 5.

106. Dodge, D. W. and Metzner, A. B.: "Turbulent Flow of Non-Newtonian Systems," *AIChE J.* (June 1959) **5**, pp. 189–204.

107. Skelland, A.H.P.: *Non-Newtonian Flow and Heat Transfer*, John Wiley & Sons, Inc., New York, 1967.

108. Zhou, Y. and Shah, S.N.: "Rheological Properties and Frictional Pressure Loss of Drilling, Completion, and Stimulation Fluids in Coiled Tubing," *Journal of Fluids Engineering* (2003) **126**, No. 2, pp. 153-161.

109. Lipton, D. and Burnett, D.B.: "Comparisons of Polymers Used in Workover and Completion Fluids," paper SPE 5872 presented at the 46th Annual California Regional Meeting of SPE, April 8–9, 1976.

110. Whitcomb, P.J. and Macosko, C.W.: "Rheology of Xanthan Gum," *Journal of Rheology* (1978) **22**, No. 5, pp. 493–505.

111. Rochefort, W.E. and Middleman, S.: "Rheology of Xanthan Gum: Salt, Temperature, and Strain Effects in Oscillatory and Steady Shear Experiments," *Journal of Rheology* (1987) **31**, No. 4, pp. 337–369.

112. Garcia-Ochoa, F., Santos, V.E., Casas, J.A., and Gomez, E.: "Xanthan Gum: Production, Recovery, and Properties," *Biotechnology Advances* (2000) **18**, pp. 549–579.

113. Chillingarian, G.V. and Vorabutr, P.: *Drilling and Drilling Fluids*, Elsevier Scientific Publishing Company, Amsterdam (1981).

114. Kadaster, A.G., Gulld, G.J., Hanni, G.L., and Schmidt, D.D.: "Field Applications of PHPA Muds," *SPEDE* (1992) **7**, No. 3, pp. 191–199.

115. Economides, M.J. and Nolte, K.G.: *Reservoir Stimulation*, New York, John Wiley & Sons Ltd, 2000

116. Naik, S.C., Pittman, J.F.T., and Richardson, J.F.: "The Rheology of Hydroxyethyl Cellulose Solutions," *Journal of Rheology* (1976) **20**, No. 4, pp. 639–649.

117. API *RP39*, *Standard Procedures for Evaluation of Hydraulic Fracturing Fluids,* American Society of Institute, Washington, D.C. (1983).

118. Shah, S.N.: Lecture Note for Non-Newtonian Fluid Mechanics, University of Oklahoma, Norman, USA, 1998.

119. Drew, T.B., Koo, E.C., and McAdams, W.H.: "The Friction Factor for Clean Round Pipes," *Trans. AIChE* (1932) **28**, pp. 56–72.

120. Chen, N.H.: "An Explicit Equation for Friction Factors in Pipe," *Ind. Eng. Chem. Fundam.* (1979) **18**, No. 3, 296.

121. Colebrook, C.F.: "Turbulent Flow in Pipes, with Particular Reference to the Transition Region between the Smooth and Rough Pipe Laws," *Journal of the Institution of Civil Engineers* (1938–1939) **11**, p133–156.

122. Yaws, C.L.: *Chemical Properties Handbook*, 1999, p501.

123. Moody, L.F.: "Friction Factors for Pipe Flow," *Trans. ASME* (November 1944) **66**, pp. 671–684.

124. Shah, S.N.: "Correlations Predict Friction Pressures of Fracturing Gels," *Oil & Gas Journal* (Jan. 16, 1984) **82**, No. 3, pp. 92–98.

125. Toms, B. A.: "Some Observations on the Flow of Linear Polymer Solutions through Straight Tubes at Large Reynolds Numbers," *Proc. First Intern. Congr. On Rheology*, Vol. II, pp. 135–141, North Holland, Amsterdam (1948).

126. Lumley, J.L.: "Drag Reduction by Additives," *Annual Review of Fluid Mechanics* (1969) **1**, pp. 367–384, Annual Reviews Inc., Palo Alto, Calif.

127. Hoyt, J.W.: "The Effect of Additives on Fluid Friction," *ASME Journal of Basic Engineering* (1972) **94**, No. 2, p. 258.

128. Hoyt, J.W.: "Drag Reduction by Polymers and Surfactants," *Viscous Drag Reduction in Boundary Layers*, D.M. Bushnell and J.N. Hefner (eds.), American Institute of Aeronautics and Astronautics, Washington, D.C. (1990).

129. Virk, P. S.: "Drag Reduction Fundamentals," *AIChE J.* (July 1975) **21**, No. 4, pp. 625–656.

130. Berman, N.S.: "Drag Reduction by Polymers," *Annual Review of Fluid Mechanics* (1978) **10**, pp. 47–64, Annual Reviews Inc., Palo Alto, Calif.

131. Kostic, M.: "On Turbulent Drag and Heat Transfer Reduction Phenomena and Laminar Heat Transfer Enhancement in non-Circular Duct Flow of Certain non-Newtonian Fluids," *Int. J. Heat Mass Transfer* (1994) **37**, Suppl. 1, pp. 133–147.

132. Kelkar, J.V. and Mashelkar, R.A.: "Drag Reduction in Dilute Polymer Solutions," *Journal of Applied Polymer Science* (1972) **16**, pp. 3047–3046.

133. Yokoyama, T. and Tomita, Y.: "Flow of Dilute Polymer Solutions through Curved Bends," *Bulletin of JSME* (June 1986) **29**, No. 252, pp. 1740–1745.

134. Savins, J.G.: "Drag Reduction Characteristics of Solutions of Macromolecules in Turbulent Pipe Flow," *SPEJ* (September 1964) **203**; *Trans.*, AIME, **231**.

135. Virk, P.S., Mickley, H.S., and Smith, K.A.: "The Ultimate Asymptote and Mean Flow Structure in Tom's Phenomenon," *ASME Journal of Applied Mechanics* (June 1970) **37**, pp. 488–493.

136. Fan, Y., Tanner, R.I., and Phan-Thien, N.: "Fully Developed Viscous and Viscoelastic Flows in Curved Pipes," *J. Fluid Mech.* (2001) **440**, pp. 327–357.

137. FLUENT 6.0 Users Guide, Fluent Inc. (December 2001).

138. "Modeling Guide, GAMBIT$^{®}$ 2.0 Documentation," Fluent Inc. (December 2001).

APPENDIX A

DERIVATION OF FRICTION FACTOR OF NON-NEWTONIAN LAMINAR FLOW IN COILED TUBING

From Eqs. (3.59) and (3.32), we have

$$f = \frac{\left[-\left(\frac{\partial p}{R\partial \phi}\right)\right](2a)}{4\left(\frac{1}{2}\rho v_m^2\right)} = \frac{\frac{2a}{R}C}{4\left(\frac{1}{2}\rho v_m^2\right)} = \frac{2}{\pi \rho v_m}\int_0^\pi \tau_{r\phi}\big|_{\xi=0}\, d\theta \quad \text{.............................(A.1)}$$

For power-law fluid,

$$\tau_{r\phi}\big|_{\xi=0} = K\left(-\frac{dw}{dr}\right)^n\Bigg|_{r=a} \quad \text{.......................................(A.2)}$$

From Eq. (3.40), we can have

$$\frac{dw}{dr} = -\frac{3}{2}\frac{w_1}{\delta}\left(1-\eta^2\right) \quad \text{...(A.3)}$$

Therefore, Eq. (A.2) can be written as:

$$\tau_{r\phi}\big|_{\xi=0} = K\left[\frac{3}{2}\frac{w_1}{\delta}\left(1-\eta^2\right)\right]^n\Bigg|_{\eta=0} = K\left(\frac{3}{2}\right)^n\frac{w_1^n}{\delta^n} \quad \text{.....................(A.4)}$$

or

$$\tau_{r\phi}\big|_{\xi=0} = \left(\frac{2}{3}\right)^{-n}\frac{w_1^n}{\delta^n}K \quad \text{.......................................(A.5)}$$

Using Eqs. (3.45) and (3.47), we can have

$$\frac{1}{\rho}\int_0^\pi \tau_{r\phi}\big|_{\xi=0}\, d\theta = \left(\frac{2}{3}\right)^{-n}\frac{K}{\rho}\int_0^\pi \frac{w_o^n w_{10}^n}{\delta_o^n a^n D_{e0}^{-n/(n+1)}}\, d\theta = \left(\frac{2}{3}\right)^{-n}\int_0^\pi \frac{w_o^n}{\delta_o^n}\, d\theta\, \frac{w_{10}^n K}{\rho a^n D_{e0}^{-n/(n+1)}}$$

$$= \frac{\pi}{2} \alpha D_{e0}^{-n/(n+1)} w_{10}^2 (a/R)^{1/2} \quad \text{...(A.6)}$$

where

$$\alpha = \frac{2}{\pi} \left(\frac{2}{3}\right)^{-n} \int_0^\pi \frac{w_o^n}{\delta_o^n} d\theta \quad \text{...(3.53)}$$

Therefore, Eq. (A.1) becomes

$$f = \frac{2}{\pi} \frac{1}{v_m^2} \frac{\pi}{2} \alpha D_{e0}^{-1/(n+1)} w_{10}^2 (a/R)^{1/2} \quad \text{...(A.7)}$$

or

$$f = \alpha D_{e0}^{-1/(n+1)} \left(\frac{v_m}{w_{10}}\right)^{-2} (a/R)^{1/2} \quad \text{...(A.8)}$$

If D_e is defined as:

$$D_e = \frac{(2a)^n v_m^{2-n} \rho}{K} \quad \text{...(A.9)}$$

then

$$D_{e0} = 2^{-n} D_e \left(\frac{v_m}{w_{10}}\right)^{n-2} \quad \text{...(A.10)}$$

Eq. (A.8) then becomes:

$$f = \alpha 2^{\frac{n}{n+1}} (a/R)^{1/2} D_e^{-1/(n+1)} \left(\frac{v_m}{w_{10}}\right)^{-\frac{3n}{n+1}} \quad \text{...(A.11)}$$

Eq. (A.11) is the same as Eq. (3.60).

APPENDIX B

DERIVATION OF FRICTION FACTOR OF NON-NEWTONIAN TURBULENT FLOW IN COILED TUBING

The Fanning friction factor is defined as:

$$f = \frac{\left(-\dfrac{\partial \overline{p}}{R \partial \phi}\right)a}{\rho v_m^2} = \frac{C\left(\dfrac{a}{R}\right)}{\rho v_m^2} \quad \text{..(4.62)}$$

The pressure gradient, C is already derived as:

$$C = -\frac{\partial \overline{p}}{\partial \phi} = \frac{2R}{\pi a}\int_0^\pi \overline{\tau}_{r\phi}\Big|_{\xi=0} d\theta \quad \text{..(4.64)}$$

Inserting Eq. (4.64) into Eq. (4.62) gives:

$$f = \frac{2}{\pi}\frac{1}{\rho v_m}\int_0^\pi \overline{\tau}_{r\phi}\Big|_{\xi=0} d\theta \quad \text{..(B.1)}$$

From Eq. (4.38), we can approximately have

$$\overline{\tau}_{r\phi}\Big|_{\xi=0} \approx \frac{\alpha(0.817)^{2-\beta(2-n)}}{2^{\beta n+1}}\gamma_1^\beta \rho^{1-\beta}\delta^{-\beta n}\overline{w}_1^{2-\beta(2-n)}$$

$$= \frac{\alpha(0.817)^{2-\beta(2-n)}}{2^{\beta n+1}}\left[8^{n-1}\left(\frac{3n+1}{4n}\right)^n\right]^\beta K^\beta \rho^{1-\beta}\delta^{-\beta n}\overline{w}_1^{2-\beta(2-n)} \quad \text{...................................(B.2)}$$

Inserting Eq. (B.2) into Eq. (B.1) gives:

$$f = \frac{\alpha(0.817)^{2-\beta(2-n)}}{2^{\beta n+1}}\left[8^{n-1}\left(\frac{3n+1}{4n}\right)^n\right]^\beta \frac{K^\beta \rho^{1-\beta}}{\rho v_m^2}\int_0^\pi \delta^{-\beta n}\overline{w}_1^{2-\beta(2-n)} d\theta$$

or

$$f = \frac{2}{\pi}f_5(n)\frac{K^\beta \rho^{-\beta}}{v_m^2}\int_0^\pi \delta^{-\beta n}\overline{w}_1^{2-\beta(2-n)} d\theta \quad \text{..(B.3)}$$

where

$$f_5(n) = \frac{\alpha(0.817)^{2-\beta(2-n)}}{2^{\beta n+1}}\left[8^{n-1}\left(\frac{3n+1}{4n}\right)^n\right]^\beta$$ ....(4.46)

Replacing δ and $\overline{w}_1$ with δ_o and w_o through Eqs. (4.48) and (4.50), we have

$$f = \frac{2}{\pi}f_5(n)\frac{K^\beta}{\rho^\beta v_m^2}a^{-\beta n}N_{Reg}^0{}^{\frac{\beta^2 n}{\beta n+1}}\left(\frac{a}{R}\right)^{\frac{\beta n}{2(\beta n+1)}}\int_0^\pi \delta_o^{-\beta n}w_o^{2-\beta(2-n)}d\theta$$

$$= \frac{2}{\pi}f_5(n)\frac{(2a)^{\beta n}a^{-\beta n}}{\frac{\rho^\beta v_m^{\beta(2-n)}(2a)^{\beta n}}{K^\beta}}N_{Reg}^0{}^{\frac{\beta^2 n}{\beta n+1}}\left(\frac{a}{R}\right)^{\frac{\beta n}{2(\beta n+1)}}\int_0^\pi \delta_o^{-\beta n}w_o^{2-\beta(2-n)}d\theta$$

$$= \frac{2}{\pi}f_5(n)\frac{(a/R)^{1/2}}{\left[N_{Reg}^0\left(\frac{a}{R}\right)^{\frac{1}{2\beta}}\right]^{\beta/(\beta n+1)}}\int_0^\pi \delta_o^{-\beta n}w_o^{2-\beta(2-n)}d\theta$$

or

$$f = \frac{\alpha^*(a/R)^{1/2}}{\left[N_{Reg}^0(a/R)^{1/(2\beta)}\right]^{\beta/(\beta n+1)}}$$ ....(B.4)

where

$$\alpha^* = f_5(n)2^{\beta n+1}\pi^{-1}\int_0^\pi w_o^{2-\beta(2-n)}\delta_o^{-\beta n}d\theta$$ ....(4.56)

N_{Reg}^0 and the generalized Reynolds number, N_{Reg} are related by the following

equation:

$$N_{Reg}^0 = 2^{3(n-1)}\left(\frac{3n+1}{4n}\right)^n N_{Reg}$$ ....(B.5)

Therefore, Eq. (B.4) becomes:

$$f = \frac{\alpha^* (a/R)^{1/2}}{\left[2^{3(n-1)} \left(\dfrac{3n+1}{4n} \right)^n N_{\mathrm{Reg}} (a/R)^{1/(2\beta)} \right]^{\beta/(\beta n+1)}} \quad \dots\dots\dots\dots\dots\dots\dots\dots\dots\dots\dots\dots\dots\dots\dots\dots\dots (B.6)$$

Eq. (B.6) is the same as Eq. (4.65).

APPENDIX C

FLUID MIXING PROCEDURES

In preparing the test fluids, the procedures from the material provider have been followed. The following briefly describes the general procedure for each category of fluids.

Mixing Procedure for Guar:

- Fill water to the desired level for the amount of guar needed.

- Add Biocide and mix.

- Add caustic and mix. This should raise the pH to 9.

- Add guar and mix till homogeneous.

- Add fumaric acid. This will cause guar to hydrate. (lower pH to 7).

- Add D-air after mixture has begun to hydrate.

- Mixture needs to hydrate for at least one hour. Measure rheology.

Mixing Procedure for Xanthan:

- Add 1 gallon household bleach per 100 bbl of water

- Add Xanvis to the desired concentration.

- Add biocide.

- Circulate tank for 1 hour. Check rheology.

- Allow to stand overnight.

- Circulate tank for 15 minutes. Check rheology.

Mixing Procedure for HEC:

- Lower mixing water pH to 4 with HCl (@ 0.5 gal 15% HCl).

- Mix in HEC, similar to Guar or HPG.

- Allow to mix for a few minutes. Then use caustic to adjust pH to 9.

APPENDIX D

POWER LAW PARAMETERS FROM FANN

VISCOMETERS

Table D.1—Rheological Properties of Xanthan Fluids Based on Fann Viscometers

Fluid Sample for Test with Fann Model 35	n	K lb_fs^n/ft^2	K_v lb_fs^n/ft^2	K_p lb_fs^n/ft^2
40 lb/Mgal Xanthan before 3000 ft 2-3/8-in. CT	0.308	2.81E-02	2.93E-02	3.22E-02
40 lb/Mgal Xanthan after 3000 ft 2-3/8-in. CT	0.344	2.35E-02	2.45E-02	2.69E-02
40 lb/Mgal Xanthan after 2000 ft 2-3/8-in. CT	0.355	2.18E-02	2.27E-02	2.49E-02
40 lb/Mgal Xanthan after 1000 ft 2-3/8-in. CT	0.364	2.03E-02	2.12E-02	2.32E-02
40 lb/Mgal Xanthan before 1-1/2-in. CT test	0.256	4.91E-02	5.15E-02	5.65E-02
40 lb/Mgal Xanthan after 1-1/2-in. CT test	0.285	3.79E-02	3.97E-02	4.36E-02
40 lb/Mgal Xanthan before 1500 ft 1-in. CT	0.293	2.94E-02	3.07E-02	3.38E-02
40 lb/Mgal Xanthan after 1500 ft 1-in. CT	0.282	3.09E-02	3.23E-02	3.55E-02
40 lb/Mgal Xanthan after 1000 ft 1-in. CT	0.287	2.93E-02	3.07E-02	3.37E-02
20 lb/Mgal Xanthan before 3000 ft 2-3/8-in. CT	0.396	8.24E-03	8.56E-03	9.37E-03
20 lb/Mgal Xanthan after 3000 ft 2-3/8-in. CT	0.431	6.87E-03	7.12E-03	7.77E-03
20 lb/Mgal Xanthan after 2000 ft 2-3/8-in. CT	0.434	6.80E-03	7.05E-03	7.69E-03
20 lb/Mgal Xanthan after 1000 ft 2-3/8-in. CT	0.428	6.98E-03	7.24E-03	7.90E-03
20 lb/Mgal Xanthan after 3000 ft 1-1/2-in. CT	0.391	9.24E-03	9.60E-03	1.05E-02
20 lb/Mgal Xanthan before 1500 ft 1-in. CT	0.386	8.20E-03	8.52E-03	9.33E-03
20 lb/Mgal Xanthan after 1500 ft 1-in. CT	0.383	8.29E-03	8.62E-03	9.44E-03
20 lb/Mgal Xanthan after 1000 ft 1-in. CT	0.368	8.81E-03	9.17E-03	1.00E-02
20 lb/Mgal Xanthan after 500 ft 1-in. CT	0.386	8.08E-03	8.40E-03	9.19E-03
10 lb/Mgal Xanthan before 3000 ft 2-3/8-in. CT	0.503	2.32E-03	2.40E-03	2.60E-03
10 lb/Mgal Xanthan after 3000 ft 2-3/8-in. CT	0.482	2.66E-03	2.75E-03	2.98E-03
10 lb/Mgal Xanthan after 2000 ft 2-3/8-in. CT	0.471	2.72E-03	2.81E-03	3.06E-03
10 lb/Mgal Xanthan after 1000 ft 2-3/8-in. CT	0.499	2.32E-03	2.39E-03	2.59E-03
10 lb/Mgal Xanthan before 3000 ft 1-1/2-in. CT	0.489	2.61E-03	2.70E-03	2.92E-03
10 lb/Mgal Xanthan before 1500 ft 1-in. CT	0.483	2.40E-03	2.48E-03	2.69E-03
10 lb/Mgal Xanthan after 1500 ft 1-in. CT	0.480	2.45E-03	2.54E-03	2.75E-03
10 lb/Mgal Xanthan after 1000 ft 1-in. CT	0.462	2.67E-03	2.76E-03	3.01E-03
10 lb/Mgal Xanthan after 500 ft 1-in. CT	0.462	2.67E-03	2.76E-03	3.01E-03

Table D.2—Rheological Properties of PHPA Fluids Based on Fann Viscometers

Fluid Sample for Test with Fann Model 35	n	K $lb_f s^n/ft^2$	K_v $lb_f s^n/ft^2$	K_p $lb_f s^n/ft^2$
40 lb/Mgal PHPA before 3000 ft 2-3/8-in. CT	0.401	2.20E-02	2.28E-02	2.50E-02
40 lb/Mgal PHPA after 3000 ft 2-3/8-in. CT	0.375	2.77E-02	2.88E-02	3.15E-02
40 lb/Mgal PHPA after 2000 ft 2-3/8-in. CT	0.374	2.79E-02	2.90E-02	3.18E-02
40 lb/Mgal PHPA after 1000 ft 2-3/8-in. CT	0.366	2.82E-02	2.94E-02	3.22E-02
40 lb/Mgal PHPA before 3000 ft 1-1/2-in. CT	0.376	2.82E-02	2.93E-02	3.21E-02
40 lb/Mgal PHPA after 3000 ft 1-1/2-in. CT	0.355	3.04E-02	3.17E-02	3.47E-02
40 lb/Mgal PHPA after 2000 ft 1-1/2-in. CT	0.351	3.11E-02	3.24E-02	3.55E-02
40 lb/Mgal PHPA after 1000 ft 1-1/2-in. CT	0.329	3.46E-02	3.60E-02	3.96E-02
40 lb/Mgal PHPA before 1500 ft 1-in. CT	0.514	1.55E-02	1.60E-02	1.73E-02
40 lb/Mgal PHPA after 1500 ft 1-in. CT	0.358	2.96E-02	3.08E-02	3.38E-02
40 lb/Mgal PHPA after 1000 ft 1-in. CT	0.352	3.14E-02	3.27E-02	3.59E-02
40 lb/Mgal PHPA after 500 ft 1-in. CT	0.343	3.26E-02	3.40E-02	3.73E-02
20 lb/Mgal PHPA before 3000 ft 2-3/8-in. CT	0.551	6.93E-03	7.13E-03	7.68E-03
20 lb/Mgal PHPA after 3000 ft 2-3/8-in. CT	0.437	1.26E-02	1.30E-02	1.42E-02
20 lb/Mgal PHPA after 2000 ft 2-3/8-in. CT	0.444	1.18E-02	1.22E-02	1.33E-02
20 lb/Mgal PHPA after 1000 ft 2-3/8-in. CT	0.423	1.29E-02	1.34E-02	1.46E-02
20 lb/Mgal PHPA before 3000 ft 1-1/2-in. CT	0.416	1.38E-02	1.43E-02	1.56E-02
20 lb/Mgal PHPA after 3000 ft 1-1/2-in. CT	0.404	1.45E-02	1.50E-02	1.64E-02
20 lb/Mgal PHPA after 2000 ft 1-1/2-in. CT	0.391	1.56E-02	1.62E-02	1.78E-02
20 lb/Mgal PHPA after 1000 ft 1-1/2-in. CT	0.389	1.56E-02	1.62E-02	1.77E-02
20 lb/Mgal PHPA before 1500 ft 1-in. CT	0.400	1.46E-02	1.51E-02	1.66E-02
20 lb/Mgal PHPA after 1500 ft 1-in. CT	0.391	1.53E-02	1.59E-02	1.75E-02
20 lb/Mgal PHPA after 1000 ft 1-in. CT	0.395	1.51E-02	1.57E-02	1.71E-02
20 lb/Mgal PHPA after 500 ft 1-in. CT	0.397	1.48E-02	1.54E-02	1.68E-02

Table D.3—Rheological Properties of Guar Fluids Based on Fann Viscometers

Fluid Sample for Test with Fann Model 35	n	K lb_fs^n/ft^2	K_v lb_fs^n/ft^2	K_p lb_fs^n/ft^2
40 lb/Mgal Guar before 3000 ft 2-3/8-in. CT	0.427	2.18E-02	2.26E-02	2.47E-02
40 lb/Mgal Guar after 3000 ft 2-3/8-in. CT	0.428	2.22E-02	2.30E-02	2.51E-02
40 lb/Mgal Guar after 2000 ft 2-3/8-in. CT	0.432	2.14E-02	2.22E-02	2.42E-02
40 lb/Mgal Guar after 1000 ft 2-3/8-in. CT	0.442	2.05E-02	2.12E-02	2.31E-02
40 lb/Mgal Guar before 3000 ft 1-1/2-in. CT	0.453	1.78E-02	1.84E-02	2.01E-02
40 lb/Mgal Guar after 3000 ft 1-1/2-in. CT	0.449	1.77E-02	1.84E-02	2.00E-02
40 lb/Mgal Guar after 2000 ft 1-1/2-in. CT	0.455	1.70E-02	1.76E-02	1.92E-02
40 lb/Mgal Guar after 1000 ft 1-1/2-in. CT	0.461	1.61E-02	1.67E-02	1.82E-02
40 lb/Mgal Guar before 1500 ft 1-in. CT	0.482	1.28E-02	1.32E-02	1.43E-02
40 lb/Mgal Guar after 1500 ft 1-in. CT	0.481	1.29E-02	1.33E-02	1.45E-02
40 lb/Mgal Guar after 1000 ft 1-in. CT	0.484	1.24E-02	1.28E-02	1.39E-02
40 lb/Mgal Guar after 500 ft 1-in. CT	0.485	1.22E-02	1.26E-02	1.37E-02
30 lb/Mgal Guar before 3000 ft 2-3/8-in. CT	0.514	7.90E-03	8.14E-03	8.81E-03
30 lb/Mgal Guar after 3000 ft 2-3/8-in. CT	0.514	7.90E-03	8.14E-03	8.81E-03
30 lb/Mgal Guar after 2000 ft 2-3/8-in. CT	0.527	7.12E-03	7.34E-03	7.93E-03
30 lb/Mgal Guar after 1000 ft 2-3/8-in. CT	0.528	6.94E-03	7.15E-03	7.72E-03
30 lb/Mgal Guar before 3000 ft 1-1/2-in. CT	0.534	6.46E-03	6.66E-03	7.18E-03
30 lb/Mgal Guar after 3000 ft 1-1/2-in. CT	0.536	6.13E-03	6.32E-03	6.81E-03
30 lb/Mgal Guar after 2000 ft 1-1/2-in. CT	0.540	5.90E-03	6.07E-03	6.54E-03
30 lb/Mgal Guar after 1000 ft 1-1/2-in. CT	0.537	5.84E-03	6.02E-03	6.49E-03
30 lb/Mgal Guar before 1500 ft 1-in. CT	0.563	4.86E-03	5.00E-03	5.37E-03
30 lb/Mgal Guar after 1500 ft 1-in. CT	0.542	5.40E-03	5.56E-03	6.00E-03
30 lb/Mgal Guar after 1000 ft 1-in. CT	0.546	5.31E-03	5.47E-03	5.89E-03
30 lb/Mgal Guar after 500 ft 1-in. CT	0.554	4.86E-03	5.00E-03	5.38E-03
20 lb/Mgal Guar before 3000 ft 2-3/8-in. CT	0.634	2.01E-03	2.05E-03	2.19E-03
20 lb/Mgal Guar after 3000 ft 2-3/8-in. CT	0.645	1.84E-03	1.88E-03	2.00E-03
20 lb/Mgal Guar after 2000 ft 2-3/8-in. CT	0.637	1.90E-03	1.95E-03	2.07E-03
20 lb/Mgal Guar after 1000 ft 2-3/8-in. CT	0.650	1.75E-03	1.79E-03	1.90E-03
20 lb/Mgal Guar before 3000 ft 1-1/2-in. CT	0.708	1.18E-03	1.20E-03	1.27E-03
20 lb/Mgal Guar after 3000 ft 1-1/2-in. CT	0.684	1.26E-03	1.29E-03	1.36E-03
20 lb/Mgal Guar after 2000 ft 1-1/2-in. CT	0.684	1.26E-03	1.29E-03	1.36E-03
20 lb/Mgal Guar after 1000 ft 1-1/2-in. CT	0.667	1.34E-03	1.37E-03	1.45E-03

Table D.4—Rheological Properties of HEC Fluids Based on Fann Viscometers

Fluid Sample for Test with Fann Model 35	n	K $lb_f s^n/ft^2$	K_v $lb_f s^n/ft^2$	K_p $lb_f s^n/ft^2$
40 lb/Mgal HEC, Initial Sample	0.410	4.50E-02	4.67E-02	5.11E-02
40 lb/Mgal HEC, after 3000 ft 2-3/8-in.	0.429	3.78E-02	3.92E-02	4.28E-02
40 lb/Mgal HEC, after 2000 ft 2-3/8-in CT	0.411	4.37E-02	4.54E-02	4.96E-02
40 lb/Mgal HEC, after 1000 ft 2-3/8-in CT	0.401	4.42E-02	4.59E-02	5.02E-02
40 lb/Mgal HEC, before 3000 ft 1-1/2-in. CT	0.420	3.85E-02	3.99E-02	4.35E-02
40 lb/Mgal HEC, after 3000 ft 1-1/2-in. CT	0.424	3.48E-02	3.61E-02	3.94E-02
40 lb/Mgal HEC, after 2000 ft 1-1/2-in. CT	0.434	3.20E-02	3.32E-02	3.62E-02
40 lb/Mgal HEC, after 1000 ft 1-1/2-in. CT	0.418	3.61E-02	3.75E-02	4.09E-02
40 lb/Mgal HEC, after 1500 ft 1-in. CT	0.443	2.69E-02	2.79E-02	3.04E-02
40 lb/Mgal HEC, after 1000 ft 1-in. CT	0.459	2.59E-02	2.68E-02	2.91E-02
40 lb/Mgal HEC, after 500 ft 1-in. CT	0.466	2.36E-02	2.44E-02	2.65E-02
30 lb/Mgal HEC, before 3000 ft 2-3/8-in. CT	0.503	1.37E-02	1.42E-02	1.53E-02
30 lb/Mgal HEC, after 3000 ft 2-3/8-in. CT	0.486	1.54E-02	1.59E-02	1.73E-02
30 lb/Mgal HEC, after 2000 ft 2-3/8-in. CT	0.499	1.44E-02	1.49E-02	1.62E-02
30 lb/Mgal HEC, after 1000 ft 2-3/8-in. CT	0.531	1.18E-02	1.22E-02	1.32E-02
30 lb/Mgal HEC, before 3000 ft 1-1/2-in. CT	0.507	1.30E-02	1.34E-02	1.45E-02
30 lb/Mgal HEC, after 3000 ft 1-1/2-in. CT	0.507	1.30E-02	1.34E-02	1.45E-02
30 lb/Mgal HEC, after 2000 ft 1-1/2-in. CT	0.527	1.04E-02	1.08E-02	1.16E-02
30 lb/Mgal HEC, after 1000 ft 1-1/2-in. CT	0.518	1.09E-02	1.13E-02	1.22E-02
30 lb/Mgal HEC, before 1500 ft 1-in. CT	0.530	9.26E-03	9.54E-03	1.03E-02
30 lb/Mgal HEC, after 1500 ft 1-in. CT	0.545	7.64E-03	7.86E-03	8.47E-03
30 lb/Mgal HEC, after 1000 ft 1-in. CT	0.562	6.73E-03	6.92E-03	7.44E-03
30 lb/Mgal HEC, after 500 ft 1-in. CT	0.567	6.31E-03	6.49E-03	6.97E-03
20 lb/Mgal HEC, before 3000 ft 2-3/8-in. CT	0.592	4.21E-03	4.32E-03	4.62E-03
20 lb/Mgal HEC, after 3000 ft 2-3/8-in. CT	0.599	4.03E-03	4.13E-03	4.42E-03
20 lb/Mgal HEC, after 2000 ft 2-3/8-in CT	0.631	3.28E-03	3.36E-03	3.58E-03
20 lb/Mgal HEC, after 1000 ft 2-3/8-in CT	0.629	3.23E-03	3.31E-03	3.52E-03
20 lb/Mgal HEC, before 3000 ft 1-1/2-in. CT	0.608	3.49E-03	3.57E-03	3.82E-03
20 lb/Mgal HEC, after 3000 ft 1-1/2-in. CT	0.672	2.22E-03	2.27E-03	2.40E-03
20 lb/Mgal HEC, after 2000 ft 1-1/2-in. CT	0.672	2.22E-03	2.27E-03	2.40E-03
20 lb/Mgal HEC, after 1000 ft 1-1/2-in. CT	0.661	2.11E-03	2.16E-03	2.28E-03
20 lb/Mgal HEC, before 1500 ft 1-in. CT	0.648	2.26E-03	2.31E-03	2.45E-03
20 lb/Mgal HEC, after 1500 ft 1-in. CT	0.657	1.95E-03	1.99E-03	2.11E-03
20 lb/Mgal HEC, after 1000 ft 1-in. CT	0.659	1.85E-03	1.89E-03	2.01E-03
20 lb/Mgal HEC, after 500 ft 1-in. CT	0.684	1.52E-03	1.55E-03	1.64E-03